Quantitative NO-LIF measurements of thermal-NO in methane and hydrogen flames - the uncertain predictions of a seemingly well-established pathway

Marie Meulemans

Department of Mechanical Engineering
McGill University, Montréal

December 2024

A thesis submitted to McGill University in partial fulfillment of the requirements of the degree of

Doctor of Philosophy

In Memoriam

Je dédie cette thèse à mon papa, Pierre Meulemans, qui était fier de mon parcours, qui avait lui aussi des idées pour revolutioner la transition énergétique, mais qui n'aura pas eu le temps de me voir diplômée.

Table of Contents

Abstract

In the context of the energy transition that is urgently required to limit the effects of climate change on the environment, hydrogen emerges as a strong candidate as an alternative to fossil fuels. When produced in a sustainable manner, hydrogen can lead to significantly reduced greenhouse gas emissions compared to the production and combustion of fossil fuels. The combustion of hydrogen in gas turbines is facilitated by their current design philosophies that promote fuel flexibility. Therefore, the transition from the combustion of natural gas to hydrogen in gas turbines could be performed without the need for a complete redesign of these technologies, thus, accelerating the implementation of this solution into the energy mix.

The accurate design and implementation of hydrogen combustion is, however, only feasible if a precise understanding of the chemistry at play in such flames is obtained. Measurements performed in the literature show that, despite its simplicity, the chemistry involved in hydrogen combustion remains mispredicted by most thermochemical models. More specifically, the NO formation predictions in flames, either produced using natural gas or hydrogen fuels, are not able to accurately reproduce measurements performed in a variety of conditions. Preliminary results show that the thermal NO pathway, dominant in most gas turbine combustor conditions, could play an important role in bridging the gap between the predicted and measured NO concentration, if it was accurately modelled. This is especially true since the NNH and N_2O pathways, historically less dominant in the formation of NO, gain significance as NO mitigation strategies are progressively implemented in gas turbine combustor design.

The work performed in this thesis focuses particularly on the formation of NO in conditions promoting the dominance of the thermal pathway. To do so, measurements are performed using NO-Laser Induced Fluorescence (NO-LIF), a highly-resolved non-intrusive diagnostic technique, which enables the measurement of NO concentration in flames, from those producing several hundred ppm down to sub-ppm levels. A comprehensive experimental review of several calibration techniques used in the literature is conducted to ensure measurements are of low uncertainty and high accuracy, to obtain quantitative NO concentration measurements. Two distinct experimental campaigns are then completed to investigate the key contributors to the NO mispredictions made by existing thermochemical models. In the first campaign, atmospheric stagnation methane-air flames are produced in high-temperature conditions, aiming to replicate gas turbine conditions, and its NO concentrations are measured. Discrepancies are found between the NO prediction of several models when compared to the experimentally measured NO. Analysis indicates that inaccu-

racies in both the core hydrogen-oxidation chemistry and the NO formation chemistry, particularly the thermal and prompt pathways, contribute to the observed discrepancies. Based on these results, a follow-up study is performed in high-temperature hydrogen flames to focus on the thermal pathway and the core chemistry by eliminating the contribution of the prompt pathway. In this study, major discrepancies were still found, not only in the prediction of NO formation, but also in the prediction of flame characteristics. This is consistent with the results of the methane-air campaign, which also found that both the thermal NO pathway and the core hydrogen-oxidation chemistry, the basis of any hydrocarbon flame modelling, remain inaccurate.

These results show that the combustion chemistry governing both the flame kinetics and NO formation in either methane or hydrogen flames still requires significant improvement. Improved predictive models would enable faster implementation of hydrogen combustion in current state-of-the-art technologies, particularly gas turbines, and therefore accelerate the energy transition.

Résumé

Dans le contexte de la transition énergétique qui s'impose d'urgence pour limiter les effets du changement climatique sur l'environnement, l'hydrogène apparaît comme un candidat sérieux comme alternative aux énergies fossiles. Lorsqu'il est produit de manière durable, l'hydrogène peut entraîner une réduction significative des émissions de gaz à effet de serre par rapport à la production et à la combustion de carburants fossiles. La combustion de l'hydrogène dans les turbines à gaz est facilitée par leurs philosophies de conception actuelles qui favorisent la flexibilité du carburant. Ainsi, la transition de la combustion du gaz naturel à l'hydrogène dans les turbines à gaz pourrait s'effectuer sans nécessiter une refonte complète de ces technologies, accélérant ainsi la mise en oeuvre de cette solution dans le portfolio énergétique.

La conception et la mise en oeuvre de la combustion de l'hydrogène ne sont toutefois possibles que si une compréhension précise de la chimie en jeu dans de telles flammes est obtenue. Les mesures réalisées dans la littérature montrent que, malgré sa simplicité, la chimie impliquée dans la combustion de l'hydrogène reste mal prédite par la plupart des modèles thermochimiques. Plus précisément, les prédictions de la formation de NO dans les flammes produites à l'aide de gaz naturel ou d'hydrogène ne sont pas en mesure de reproduire avec précision les mesures effectuées dans des conditions expérimentales diverses. Les résultats préliminaires montrent que la voie thermique du NO, dominante dans la plupart des conditions de combustion des turbines à gaz, pourrait combler l'écart entre la concentration de NO prédite et mesurée, si elle était modélisée avec précision. Cela est particulièrement vrai puisque les voies NNH et N_2O, historiquement moins dominantes dans la formation de NO, gagnent en importance à mesure que des stratégies d'atténuation du NO sont progressivement mises en oeuvre dans la conception des chambres de combustion des turbines à gaz.

Les travaux réalisés dans cette thèse se concentrent particulièrement sur la formation de NO dans des conditions favorisant la dominance de la voie thermique. Pour ce faire, les mesures sont effectuées à l'aide de NO-LIF (Fluorescence de NO Induite par Laser), une technique de diagnostic non intrusive à haute résolution, qui permet de mesurer la concentration de NO dans les flammes, de celles produisant plusieurs centaines de ppm jusqu'à celles produisant seulement quelques ppm. Une revue expérimentale complète de plusieurs techniques de calibration utilisées dans la littérature est menée pour garantir que les mesures sont d'une faible incertitude et d'une grande précision, afin d'obtenir des mesures quantitatives de concentration de NO. Deux campagnes expérimentales distinctes sont ensuite réalisées pour étudier les principaux contributeurs aux erreurs de prédiction

du NO faites par les modèles thermochimiques existants. Au cours de la première campagne, des flammes de stagnation atmosphérique méthane-air sont produites dans des conditions de températures élevées, dans le but de reproduire les conditions d'une turbine à gaz, et dans lesquelles la concentration de NO est mesurée. Des divergences sont constatées entre la prédiction du NO de plusieurs modèles, par rapport au NO mesuré expérimentalement. L'analyse indique que les inexactitudes dans la chimie de base de l'oxydation de l'hydrogène et dans la chimie de la formation de NO, en particulier les voies thermique et rapide, contribuent aux écarts observés. Sur la base de ces résultats, une étude de suivi est réalisée dans des flammes d'hydrogène à haute température pour se concentrer sur la voie thermique et la chimie de base en éliminant la contribution de la voie rapide. Dans cette étude, des divergences majeures ont encore été trouvées, non seulement dans la prédiction de la formation de NO, mais également dans la prédiction des caractéristiques de la flamme. Cela concorde avec les résultats de la campagne méthane-air, qui a également révélé que la voie thermique du NO et la chimie de base de l'oxydation de l'hydrogène, base de toute modélisation des flammes d'hydrocarbures, restent inexactes.

Ces résultats montrent que la chimie de la combustion régissant à la fois la cinétique de la flamme et la formation de NO dans les flammes de méthane ou d'hydrogène nécessite encore des améliorations significatives. Des modèles prédictifs améliorés permettraient une mise en oeuvre plus rapide de la combustion de l'hydrogène dans les technologies de pointe actuelles, notamment les turbines à gaz, et accéléreraient donc la transition énergétique.

Acknowledgements

I would like to express my heartfelt gratitude to my supervisor, Prof. Jeffrey M. Bergthorson, for his continuous academic and personal support throughout the years. I am particularly grateful for the opportunities and advice he shared countless times, which allowed me to grow and succeed in my degree.

I would also like to thank my co-supervisor, Dr. Gilles Bourque. His industrial expertise was key to helping me contextualise and propagate my research to the community.

I deeply thank my colleague and friend, Dr. Antoine Durocher, with whom I spent endless hours in the lab or on the phone, to discuss, debate, argue, and laugh about professional and personal topics.

I also extends to extend my thanks to Dr. Philippe Versailles. His rigour and dedication to science is something I deeply admire, and helped me publish two quality manuscripts.

I appreciate the many members, past and present, of the Alternative Fuels Laboratory, with whom I had the pleasure of working and collaborating. Special thanks to the friends I made along the way, through obstacles and struggles, particularly Asst. Prof. Keena Trowell, Dihia Idrici, Kartik Mangalvedhe, Samson Bowen-Bronet, and Dr. Jan Palečka.

My gratitude also goes to the people that convinced me, years ago, to follow this academic path. Specifically, Asst. Prof. Joshua Lacey and Dr. Robert Gordon, with whom I worked at the University of Melbourne through a research internship.

Je désire également remercier ma famille et mes amis en France qui m'ont soutenue de loin, mais aussi de plus près grâce à leurs visites. My thanks extend to the Australian side of my family and friends as well.

Above all, my deepest gratitude goes to Jacob, without whom I would not have finished this degree. His support and belief in me was beyond measure. I will be eternally grateful to have met you.

Finally, I would not be who I am today without the help of Murphy's laws, COVID, and unreliable suppliers. Their endeavour to challenge my patience and determination to finish this degree ultimately forged my resilience.

Contribution to original knowledge

Through the research described in this thesis, several contributions are made to the field of gaseous combustion. They are summarised as follows:

- Providing the experimental research community with a comprehensive comparison of several calibration methodologies to obtain quantitative NO measurements using Laser-Induced Fluorescence. The comparison is performed on a set of experimental data to demonstrate the applicability of each technique with their associated uncertainties. Its aim is to guide researchers in choosing the calibration technique that fits their experimental conditions. Making this work available to the community facilitates the use of LIF measurements to improve the thermochemical models.

- Providing the modelling community with a complete set of 1D velocity, temperature, and NO concentration profiles in high-temperature methane-air flames and high-temperature hydrogen-air flames. Both experimental datasets aim to diversify the existing dataset available to the modelling community, thereby reducing bias in modelling towards low-temperature and low-pressure hydrocarbon flames.

- Providing the industrial and modelling communities with insights regarding the thermal NO pathway. It is found that the modelling of this pathway remains significantly inaccurate, with considerable implications for the design of gas turbines aiming for lower NO_x emissions.

- Providing the modelling community with insights regarding the hydrogen oxidation core chemistry. An in-depth investigation into the discrepancies of thermal NO predictions indicated that the core chemistry, common to any combustion modelling, is still misunderstood. This major finding implies that the modelling of any other combustion subset (hydrocarbon and pollutant reactions) would necessarily be impacted. Hence, the current modelling of gas turbines running on sustainable fuels such as hydrogen still carries significant uncertainty which comprise the ability to guide the development in an effective manner.

To facilitate the dissemination of these contributions to the community, the work presented in each published manuscript was made available for free access through the AFL website. Furthermore, close collaboration between the research group and others, as well as industrial partners, is maintained to ensure the practical relevance of the experimental findings.

Contribution of Authors

This thesis is presented as a collection of three manuscripts of which I am the first author. Note that these publications are listed chronologically, but are organised differently within the thesis for improved understanding and readability. The contribution of each author is listed below:

Chapter IV – **M. Meulemans**, A. Durocher, P. Versailles, G. Bourque, and J. M. Bergthorson. "How well do we know thermal-NO? An investigation of NO formation in flames over a wide temperature range". In: *Proceeding of the Combustion Institute*, volume 39, Issue 1, 2023, pages 521–529.

This was my first publication resulting from my first experimental campaign. The aim was to study the thermal NO formation in methane-air high temperature flames. For this work, I planned and conducted the experiments and simulations, I analysed and interpreted the results, and I wrote the manuscript. I was guided experimentally by Dr. Antoine Durocher, a fellow Ph.D. student at the time, who assisted me throughout this time. The apparatus and experimental methods were already designed and available, mostly from the work of a former Ph.D. student, Dr. Philippe Versailles, who also contributed to the manuscript through the review and editing. Dr. Gilles Bourque and Prof. Jeffrey M. Bergthorson, my co- and main supervisors, were responsible for supervising the research, reviewing, and editing the manuscript.

Chapter V – **M. Meulemans**, A. Durocher, G. Bourque, and J. M. Bergthorson. "NO measurements in high temperature hydrogen flames: The crucial role of the hydrogen oxidation chemistry for accurate NO predictions". In: *Combustion and Flame*, volume 261, 2024, 113279.

This manuscript resulted from my second experimental campaign. The aim was to further investigate the findings made in the first experimental campaign by using hydrogen flames. For this manuscript, I planned and conducted the experiments and simulations, I analysed and interpreted the results, and I wrote the manuscript. Dr. Durocher assisted in the analysis and interpretation of the results, and the reviewing and editing of the manuscript. Dr. Bourque and Prof. Bergthorson were responsible for supervising the research, reviewing, and editing the manuscript.

Chapter III – **M. Meulemans**, A. Durocher, P. Versailles, G. Bourque, and J. M. Bergthorson. "Calibration techniques for quantitative NO measurement using Laser-Induced Fluorescence". In: *Journal of Quantitative Spectroscopy and Radiative Transfer*, volume 330, 2025, 109221.

This was my last publication resulting from the work performed between both experimental campaigns. Several experimental issues arose during my first experimental campaign that pushed me to gather much more data points that what was needed in order to review the methodology we were using for calibration of the NO-LIF experimental results. It was then decided to use these experimental struggles and turn them into a meaningful dataset and a manuscript that could be used as a guide by researchers using NO-LIF. For this work, I planned and conducted the experiments and simulations, I analysed and interpreted the results, and I wrote the manuscript. Dr. Durocher and Dr. Versailles participated in the reviewing and editing of the manuscript. Dr. Bourque and Prof. Bergthorson were responsible for supervising the research, reviewing and editing the manuscript.

Throughout my degree, I also assisted, trained, and mentored other students in their researches, for which I am credited as co-authors in their manuscripts:

A. Durocher, **M. Meulemans**, G. Bourque, and J. M. Bergthorson. "Nitric oxide concentration measurements in low-temperature, premixed hydrogen-air stagnation flames at elevated pressures". In: *Proceeding of the Combustion Institute*, volume 39, Issue 1, 2023, pages 541−550.

A. Durocher, **M. Meulemans**, G. Bourque, and J. M. Bergthorson. "Measurements of the laminar flame speed of premixed, hydrogen-air-argon stagnation flames". In: *Applications in Energy and Combustion Science*, volume 7, 2021, 100028.

A. Durocher, **M. Meulemans**, P. Versailles, G. Bourque, and J. M. Bergthorson. "Back to basics − NO concentration measurements in atmospheric lean-to-rich, low-temperature, premixed hydrogen–air flames diluted with argon". In: *Proceeding of the Combustion Institute*, volume 38, Issue 2, 2021, pages 2093−2100.

List of Figures

List of Tables

Chapter I. Introduction

I.1 Hydrogen combustion: a strong candidate to tackle the energy transition

In 2022, the world energy consumption was 604 EJ, of which 82% was produced using fossil fuels (oil, gas, and coal), 4% *via* nuclear, and 14% *via* renewables [1]. In order to meet the commitments of the 196 signatory countries of the Paris climate agreement, an energy transition from fossil fuels to renewables is necessary and urgent. Not only are fossil fuels strong contributors to the greenhouse effect, but their quantities are approaching their limit [2]. Thus, sustainable alternative technologies are necessary to meet the continuously growing energy demand and maintain our quality of life. In order to compete with the current use of fossil fuels, these technologies must be carbon-free for their entire life cycle (extraction, use, recycling), be globally marketable, and be abundantly available [3]. Above all, the proposed solutions must be applicable to the fields of transportation and energy production, the main consumers of fossil fuels.

Despite being carbon-free, several challenges arise with the use of renewable energies, especially those that are climate-dependent, such as wind or solar power. Their energy production is generally unpredictable and unreliable due to intermittency and seasonality. Due to this inconsistent power delivery, and in order to meet the energy demand, these technologies must be coupled to energy storage systems, such as batteries [4]. These systems, however, possess a very low storage density compared to traditional energy systems. Furthermore, Life Cycle Assessment (LCA) of batteries show that they represent an environmental burden due to their substantial energy requirements (extraction, production, and end of life) and associated carbon emissions [5, 6]. Moreover, wind, solar, and more specifically hydro-power rely on natural landscape that are often remote and inaccessible from where they are the most needed. Hence, while climate-dependent renewable energies are integral to the energy transition portfolio, they cannot solely be relied upon. Sustainable alternative technologies to fossil fuels and climate-dependent renewable energies remain required to complete the energy transition mix.

A promising alternative is the use of hydrogen [7]. Its primary advantage is its lack of carbon molecules. As a result, its use, through combustion or in fuel cells, does not produce CO_2 emissions, a major contributor to the greenhouse effects. Additionally, hydrogen's Lower Heating Value (LHV), defining the chemical energy potential of the fuel by weight, is two to three time

larger than those of fossil fuels. Its volumetric density, however, is several times lower than those of fossil fuels. Thus, to maintain the same power output as fossil fuels, less mass, but more volume, of hydrogen is required. While the reduction of fuel mass is advantageous for the transportation field, like in rocket or aviation applications, the extra space required to store it can be unfavorable. Moreover, the storage and transportation of hydrogen is known to present safety challenges. It is the smallest molecule and is highly diffusive and is extremely difficult to store safely. As such, extensive efforts are required to develop hydrogen storage methods, especially in its gaseous form. Its low volumetric density presents further concerns as significant energy and cost are required to pump and compress hydrogen to a denser form for more efficient storage. Finally, as hydrogen is not readily available in the atmosphere, it needs to be produced. Depending on the production method, they can be more or less energy and carbon intensive, with a spectrum of colour used to describe its carbon footprint [8]. The production of blue, grey, brown, or black hydrogen is obtained *via* the reforming and gasification of fossil fuels. These technologies are potentially more carbon-emitting than the direct combustion of fossil fuels. Therefore, blue, grey, brown, or black hydrogen is not a sustainable alternative to fossil fuels. On the contrary, sustainable hydrogen, or green hydrogen, is obtained from the use of renewable energies to split H_2 molecules from H_2O *via* electrolysis. Other production methods, such as the production of hydrogen through the reaction of metal and water in supercritical conditions [9] present an alternative to green hydrogen. In such example, hydrogen can be produced *in situ* allowing its transportation through the form of metal, posing minimal safety concerns.

Nevertheless, the use of hydrogen through combustion, whilst recognised as a strong sustainable alternative solution, presents significant challenges that remain to be addressed.

I.2 Transition from the combustion of fossil fuels to hydrogen

A significant portion of the energy production, especially for the industrial sector, is through the use of Gas Turbines (GTs). For industries whose demand in energy cannot be supplied by the grid, GTs are often used as an energy source because of their relatively low pollutant emissions, high efficiency, and high responsiveness to changing loads [10]. Some examples of these are remote mining sites, gas compression stations, or off-shore platforms. Gas turbines are also a much more flexible source of energy, relative to climate-dependent renewable energies, as they can be used according to the energy demand without the need for electricity storage.

Climate concerns have led GT manufacturers to shift their design and operating conditions to burn natural gas instead of heavier hydrocarbon fuels in the 1970s. The shift to natural gas, whose composition varies per region but is mainly composed of methane, achieved a significant reduction of pollutant emissions and led to the concept of fuel flexibility in gas turbines using diffusion

combustion [11]. Per this concept, GTs are designed with a level of flexibility to accommodate different fuel composition or operating conditions, typically described by the Wobbe Index. This index indicates how two fuels of different composition vary in the heat they produce for a given combustor condition. Two fuels of similar Wobbe Index are more likely to be interchangeable. As such, GTs designed for the diffusion combustion of natural gas could have a flexibility that may accommodate pure hydrogen combustion, as the Wobbe Index of pure hydrogen is $40.7\,\mathrm{MJ.m^{-3}}$ compared to $47.9\,\mathrm{MJ.m^{-3}}$ for pure methane[1] [12]. In theory and in a vacuum, this similarity implies that switching fuels, in a diffusion combustion setting, would not require significant modifications of existing GT designs, and therefore, would accelerate the energy transition. To further decrease emissions, the GTs industry has also favored the development of premixed combustors, as opposed to diffusion combustors, switching the combustion to lean conditions, significantly reducing NO_x emissions, at the cost of flame stability [11].

Despite a similar Wobbe index, the widespread use of premixed combustion systems challenges the full implementation of hydrogen in current GTs. In particular, the properties of hydrogen combustion are significantly different than those of natural gas. The laminar flame speed (S_L), a fundamental flame characteristic, describes the speed at which the flame propagates and is a good indicator of this difference of properties between the two fuels. The maximum flame speed of hydrogen ($\sim 3\,\mathrm{m.s^{-1}}$) is one order of magnitude larger than that of methane ($\sim 0.35\,\mathrm{m.s^{-1}}$) [13]. Such a difference leads to flames that are much more difficult to stabilise for a given flow rate. This may lead to dangerous flashbacks where the flame propagates upstream past the nozzle or injector, towards the fuel reservoir, where uncontrolled and undesirable combustion events could occur, in addition to potential hardware damage. The flame temperature of hydrogen combustion is also higher than methane combustion, at the same equivalence ratio, by almost 150 K. This leads to increased pollutant formation, such as Nitric Oxide (NO) through the thermal-NO pathway, and increases the thermal stresses endured by components downstream of a GT combustor. The ignition delay of hydrogen mixtures is also greatly reduced compared to methane, for temperatures above 1000 K [14, 15]. This leads to potentially dangerous ignition events in unwanted regions, especially with GT combustors that use premixing. Furthermore, hydrogen leads to a strong heat diffusivity over mass diffusivity in lean flames, and the contrary effect in rich flames [16]. This ratio, also known as the effective Lewis number ($\mathrm{Le_{eff}}$), is ~ 0.3 in lean and ~ 2.3 in rich hydrogen-air flames, compared to ~ 1 for the entire equivalence ratio range of methane-air flames. Consequently, hydrogen-air flames are more prone to differential diffusion, exhibited by flame diffusive instabilities through wrinkling. This effect can result in greater difficulties of hydrogen flame stabilisation, increased hot regions in combustion, and increased potential for thermo-acoustic instabilities, relative to methane flames in a natural gas-based combustor design. In summary, even

[1] For the sake of clarity, natural gas is approximated to pure methane.

with the similarity in Wobbe index, the fundamentally different combustion behaviour of hydrogen poses intricate design challenges, complicating the transition to alternative fuels.

Despite these challenges, hydrogen combustion presents some advantages. Due to their high diffusivity, hydrogen flames have significantly wider flammability limits relative to methane flames [17]. Thus, hydrogen-air flames can be sustained in an equivalence ratio range of $\sim 0.1-7.1$, compared to $\sim 0.4-1.6$ for methane-air flames. This extended flammability in lean conditions allows burning hydrogen at the same output power as methane, but at a lower equivalence ratio, reducing its laminar flame speed and combustion temperature. This may lead to similar, if not reduced, NO emissions. Additionally, as discussed previously, hydrogen combustion does not contain carbon-based species. This removes the production of several major pollutant species, such as CO, CO_2, soot, unburnt hydrocarbons (UHC), or particle matter (PM), all of which are both harmful and heavily regulated. Finally, hydrogen combustion occurs through a relatively small set of species and reactions, leading to the simplest combustion chemical process to model. This focuses the study of the reactions and species at play to a very small subset relative to fossil-fuel combustion allowing an improved assessment of their role and behaviours. It also facilitates the design and development of combustor design through reduced numerical simulation time.

I.3 The chemistry of hydrogen oxidation

The hydrogen-oxidation chemistry is at the heart of any combustion mechanism. It fundamentally governs the radical pool formation, thereby shaping the flame characteristics such as the laminar flame speed, the adiabatic flame temperature, and the flammability range. As the foundation of any flame modelling, it ultimately regulates both the breakdown of hydrocarbons and the generation of pollutants. It is therefore crucial to obtain a sufficient understanding of the chemistry at play to correctly consider the combustion chemistry of other fuels.

The first works identifying the reaction rates of hydrogen oxidation (H_2/O_2) chemistry were produced in the 1930s by Hinshelwood *et al.* [18] and Semenov [19]. Since then and up to the present day, numerous studies have delved into comprehending the chemistry, primarily through the acquisition of experimental data. Sánchez *et al.* [13] compiled these efforts in a review study. Hydrogen oxidation can be described with as few as 8 species and 20 elementary reactions. These reactions can be categorised according to their role in the events leading to the different explosion limits [20].

I.3.1 H_2-O_2 chain reactions

The following reactions compose the set of hydrogen-oxygen chain reactions, also called shuffle reactions, describing the rapid inter-conversion of radicals:

$$H + O_2 \leftrightarrow O + OH, \quad (R_{H_2/O_2\text{-}1})$$
$$O + H_2 \leftrightarrow H + OH, \quad (R_{H_2/O_2\text{-}2})$$
$$OH + H_2 \leftrightarrow H + H_2O, \quad (R_{H_2/O_2\text{-}3})$$
$$O + H_2O \leftrightarrow OH + OH. \quad (R_{H_2/O_2\text{-}4})$$

This set of reactions drive the radical pool formation, composed of O, H, and OH species. The reactions lead to a greater rate of formation in high temperatures, such as in the flame front. Thus, the radical pool is mainly associated with this region.

An increased reaction rate of ($R_{H_2/O_2\text{-}2}$) and ($R_{H_2/O_2\text{-}3}$) relative to ($R_{H_2/O_2\text{-}1}$), leads to an increased formation rate of H radicals relative to O and OH. Thus, ($R_{H_2/O_2\text{-}1}$) is the rate limiting reaction of this reaction set, and is of central importance in the description of the radical pool of hydrogen flames, and by extension, of any flames. Despite its crucial role, the reaction rate of ($R_{H_2/O_2\text{-}1}$) contains significant uncertainty in the literature [13, 21–24].

I.3.2 H_2-O_2 dissociation/recombination reactions

The following reactions compose the set of radical-radical recombination reactions, directly competing with the reactions describing their formation in Section I.3.1:

$$H + H\ (+M) \leftrightarrow H_2\ (+M), \quad (R_{H_2/O_2\text{-}5})$$
$$H + OH\ (+M) \leftrightarrow H_2O\ (+M), \quad (R_{H_2/O_2\text{-}6})$$
$$O + O\ (+M) \leftrightarrow O_2\ (+M), \quad (R_{H_2/O_2\text{-}7})$$
$$O + H\ (+M) \leftrightarrow OH\ (+M). \quad (R_{H_2/O_2\text{-}8})$$

These reactions lead to the reduction of the radical pool concentration through recombination collisions, especially through ($R_{H_2/O_2\text{-}5}$) and ($R_{H_2/O_2\text{-}6}$). The reverse of ($R_{H_2/O_2\text{-}5}$), and ($R_{H_2/O_2\text{-}7}$) to a lesser degree, also play a role in the decomposition of the initial H_2 and O_2 contained in the mixture, also participating in the greater concentration of radicals. Thus, the accurate determination of ($R_{H_2/O_2\text{-}5}$) is of importance in the description of H_2/O_2 chemistry. This reaction contains one of the largest uncertainties in the rates recommended by Baulch *et al.* [21]. Beyond these, no more recent measurements quantifying this reaction rate have been conducted.

I.3.3 Formation and consumption of HO_2

The following reactions compose the set controlling the formation and consumption of hydroperoxyl (HO_2):

$$H + O_2\ (+M) \leftrightarrow HO_2\ (+M), \qquad (R_{H_2/O_2\text{-}9})$$

$$HO_2 + H \leftrightarrow H_2 + O_2, \qquad (R_{H_2/O_2\text{-}10})$$

$$HO_2 + H \leftrightarrow OH + OH, \qquad (R_{H_2/O_2\text{-}11})$$

$$HO_2 + H \leftrightarrow H_2O + O, \qquad (R_{H_2/O_2\text{-}12})$$

$$HO_2 + O \leftrightarrow OH + O_2, \qquad (R_{H_2/O_2\text{-}13})$$

$$HO_2 + OH \leftrightarrow H_2O + O_2. \qquad (R_{H_2/O_2\text{-}14})$$

The formation of hydroperoxyl occurs through ($R_{H_2/O_2\text{-}9}$), directly competing with ($R_{H_2/O_2\text{-}1}$). The fast formation of the radical pool in the high temperatures of the flame front, however, quickly reduces the concentration of HO_2 through ($R_{H_2/O_2\text{-}10}$)-($R_{H_2/O_2\text{-}14}$). Thus, HO_2 is more prone to be found in large quantities during the ignition process, where the radical pool is still at low concentrations. Explosion occurs when the H-radicals are not reduced fast enough through ($R_{H_2/O_2\text{-}9}$). Its exothermicicty leads to the acceleration of ($R_{H_2/O_2\text{-}1}$), further encouraging the explosivity of the mixture. The reaction rate of ($R_{H_2/O_2\text{-}9}$), while of significant importance in the explosivity limit, still contains fairly large uncertainty [13, 23, 24].

I.3.4 Formation and consumption of H_2O_2

The last subset intervening in the H_2/O_2 chemistry consists of the hydrogen peroxide (H_2O_2) reaction subset:

$$HO_2 + HO_2 \leftrightarrow H_2O_2 + O_2, \qquad (R_{H_2/O_2\text{-}15})$$

$$H_2O_2\ (+M) \leftrightarrow OH + OH\ (+M), \qquad (R_{H_2/O_2\text{-}16})$$

$$H_2O_2 + H \leftrightarrow H_2O + OH, \qquad (R_{H_2/O_2\text{-}17})$$

$$H_2O_2 + H \leftrightarrow H_2 + HO_2, \qquad (R_{H_2/O_2\text{-}18})$$

$$H_2O_2 + O \leftrightarrow OH + HO_2, \qquad (R_{H_2/O_2\text{-}19})$$

$$H_2O_2 + OH \leftrightarrow H_2O + HO_2. \qquad (R_{H_2/O_2\text{-}20})$$

The formation of hydrogen peroxide occurs through the recombination of two hydroperoxyl species *via* ($R_{H_2/O_2\text{-}15}$). These reactions are mostly active in low temperatures and high pressures, where large concentrations of HO_2 is produced. It is then possible to omit this set when modelling at-

mospheric high temperature combustion. At high pressures, the recombination of the hydrogen peroxide species through ($R_{H_2/O_2\text{-}16}$)-($R_{H_2/O_2\text{-}20}$) leads to the formation of radicals, further encouraging the formation of HO_2, leading to the third explosion limit. While ($R_{H_2/O_2\text{-}15}$)-($R_{H_2/O_2\text{-}17}$) play the most significant role in this subset of reactions, only few measurements, especially at low temperatures, have been performed [23].

I.4 The chemistry of Nitrogen Oxide emissions

NO_x emissions encompass any nitrogen-based pollutant that is the result of a reaction between nitrogen and oxygen: nitric oxide (NO), nitrogen dioxide (NO_2), and nitrous oxide (N_2O). Their emissions have been increasingly monitored and regulated throughout the last decades due to their impact on the environment and health [25, 26]. NO_x is principally composed of NO, thus NO formation is the focus of both this study, and the literature. NO formation is generally the result of a combustion process, as large energies are required to break the triple bond of the nitrogen molecule before bonding with oxygen atoms. Its formation is quasi-inevitable in practical combustion processes as they often employ atmospheric air, in which nitrogen is the main component. The formation of NO is exacerbated if the fuel also contains N species (called Fuel-N), such as ammonia, coal, or biomass. Nevertheless, strategies can be employed to mitigate its production rate and concentration. To employ such strategies, the precise understanding of its formation mechanism is required. NO forms by following specific pathways which describe how the N-containing species (N_2 or Fuel-N) decomposes to form NO, as shown in Fig. I.1. Several pathways have been identified in the literature [27, 28], which are more or less active in the formation of NO depending on the condition in which the flame is produced.

I.4.1 The thermal pathway

The thermal pathway, alternatively referred to as the Zel'dovich pathway in honor of its initial discoverer [29], is the first NO formation pathway to have been identified. This pathway, represented by two red arrows in Fig. I.1, is the primary contributor to NO formation in practical combustion systems. It is mostly active in the post-flame region of high temperature and lean to stoichiometric flames. NO formation through this pathway is the result of three chain reactions. First, the oxygen atom attacks the triple bond of the nitrogen molecule, producing NO and N ($R_{\text{thermal-1}}$). Then, the produced nitrogen atom is quickly oxidized with either OH ($R_{\text{thermal-2}}$) or O_2 ($R_{\text{thermal-3}}$) to produce

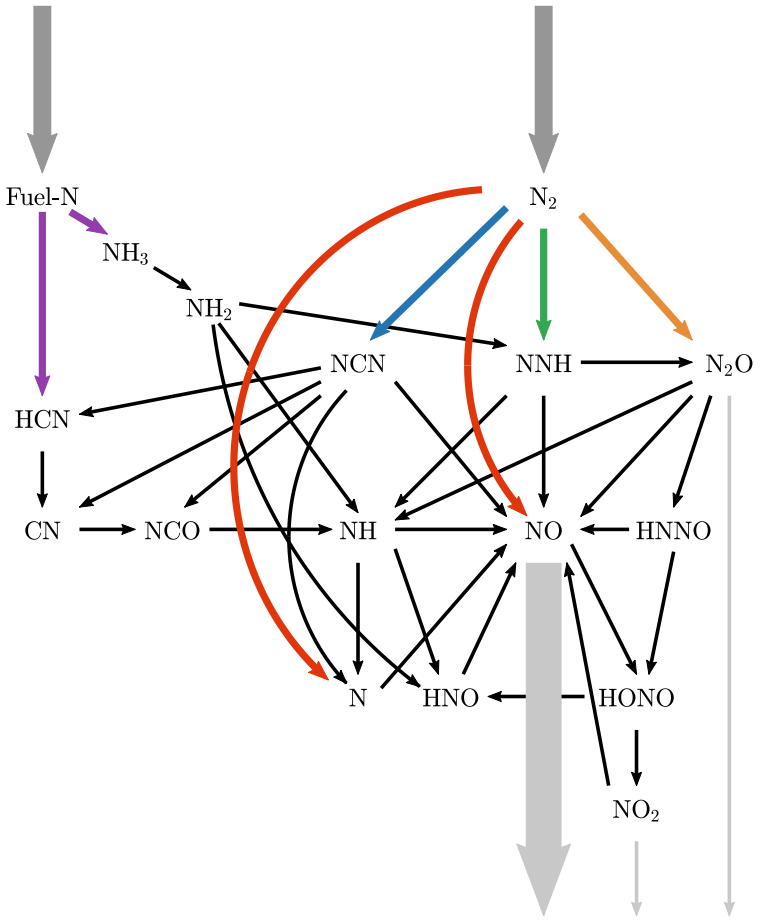

Figure I.1: Simplified schematics of the possible decomposition and recombination of the N-containing species to later form NO_x. Five NO formation pathways are identified: thermal (red), prompt (blue), N_2O (orange), NNH (green), fuel-N (purple). Arrows are indicative (not quantitative) of possible paths between species.

NO and radicals (O, H):

$$N_2 + O \leftrightarrow N + NO, \qquad (R_{\text{thermal-1}})$$

$$N + OH \leftrightarrow H + NO, \qquad (R_{\text{thermal-2}})$$

$$N + O_2 \leftrightarrow O + NO. \qquad (R_{\text{thermal-3}})$$

As ($R_{\text{thermal-1}}$) requires a high activation energy, it is the rate limiting step in thermal NO formation. The thermal formation pathway has been extensively studied as it is the pathway that is dominant in practical combustion systems. It can also be easily mitigated through a reduction of the combustion temperature or residence time. Despite the extensive research, recent studies have shown discrepancies in the prediction of NO formation where the thermal pathway is dominant [30–33]. Inaccuracies in the rate of the thermal pathway initiation or subsequent reactions could result in

significant flaws in the design of gas turbine combustors that heavily rely on accurate modelling of this pathway in particular.

I.4.2 The prompt pathway

The prompt pathway, also called the Fenimore pathway after the researcher that first identified it [34], is a complex NO formation mechanism driven by the fast (prompt) hydrocarbon fuel decomposition reactions. The initiation of the prompt pathway occurs through the reaction of N_2 with the CH radicals originating from the decomposition of the hydrocarbon fuel C_mH_n. The decomposition of the fuel species is the first mechanism occurring in the flame, in the flame front, and is therefore also where the prompt pathway dominates. This pathway remains active until the fuel species are fully consumed and is therefore mostly active in rich flames. Fenimore [34] initially proposed that $N_2 + CH$ would react to form $HCN + N$. Moskaleva [35] proposed through *ab initio* calculations that the reaction would, instead, form $NCN + H$ through the spin-conserved reaction:

$$N_2 + CH \leftrightarrow NCN + H. \qquad (R_{\text{prompt-1}})$$

While many studies supported this finding, some widely used thermochemical models still use the spin-forbidden formulation of the prompt pathway, such as GRI v.3.0 [36] or CRECK v.1412 [37].

As presented in Fig. I.1, where the prompt pathway is represented by the blue arrow, once NCN is formed it either leads to the direct formation of NO through several reactions with oxygen-containing species:

$$NCN + O \leftrightarrow CN + NO, \qquad (R_{\text{prompt-2}})$$

$$NCN + OH \leftrightarrow HCN + NO, \qquad (R_{\text{prompt-3}})$$

$$NCN + O_2 \leftrightarrow NCO + NO, \qquad (R_{\text{prompt-4}})$$

or leads to the indirect formation of NO through further reaction and recombination of NCN, through species such as HCN, CN, NCO, N, or HNO.

With the significance of this pathway in hydrocarbon flames, many studies have also focused their interest in the accurate measurement of its reaction rates or specie concentration [38–44]. Despite the extensive efforts spent on deriving the reaction rate of ($R_{\text{prompt-1}}$) [28], significant prediction discrepancies remain when comparing to measurements of NO formed in conditions that favour the prompt pathway [39, 42]. This led to the development of tools using Bayesian inference to constrain the inaccuracies in the CH chemistry modelling [45].

I.4.3 The N_2O pathway

The N_2O pathway, shown through the orange arrow in Fig. I.1, is the result of a third-body collision initiating the recombination of N_2 with atomic oxygen, forming N_2O ($R_{N2O\text{-}1}$) [46]. The N_2O molecules then react with radicals to form NO:

$$N_2 + O \ (+M) \leftrightarrow N_2O \ (+M), \qquad (R_{N2O\text{-}1})$$

$$N_2O + H \leftrightarrow NH + NO, \qquad (R_{N2O\text{-}2})$$

$$N_2O + O \leftrightarrow NO + NO. \qquad (R_{N2O\text{-}3})$$

This route, in contrast to the prompt and thermal pathways, is counterbalanced by the recycling of the nitrogen molecules through:

$$N_2O + H \leftrightarrow OH + N_2, \qquad (R_{N2O\text{-}4})$$

$$N_2O + O \leftrightarrow O_2 + N_2. \qquad (R_{N2O\text{-}5})$$

This recycling effect limits the net N_2O formation through the N_2O pathway in typical hydrocarbon flames, but can become dominant in high pressure hydrogen flames, as seen by Durocher *et al.* [47].

The N_2O pathway is more likely to occur in lean conditions at high pressure and moderate temperatures. A recent study, however, has demonstrated that the N_2O pathway could be coupled to the thermal pathway through ($R_{N2O\text{-}3}$) [32]. Indeed, this pathway is in direct competition with the thermal pathway through the availability of the O radicals in ($R_{N2O\text{-}1}$) and ($R_{thermal\text{-}1}$), demonstrating a strong interaction between the two rates. Advanced combustion technologies, such as Dry Low Emissions (DLE) systems, are seeing an increased contribution from the N_2O pathway as these systems rely on lean and moderate temperature combustion, which attempts to mitigate the thermal and prompt pathways. The relatively recent focus on this pathway leads to a lack of experimental data measuring the rates of the subset of reactions [28]. Consequently, studies comparing NO predictions in conditions which favour the N_2O pathway demonstrate major mispredictions relative to measurements [48–51].

I.4.4 The NNH pathway

The NNH pathway, identified in Fig. I.1 by the green arrow, is also the result of a third-body collision initiating the recombination of N_2 with atomic hydrogen [52, 53]. It forms NNH ($R_{NNH\text{-}1}$)

and is followed by its oxidation by oxygen radicals to form NO:

$$N_2 + H \ (+M) \leftrightarrow NNH \ (+M), \qquad (R_{NNH\text{-}1})$$

$$NNH + O \leftrightarrow NH + NO. \qquad (R_{NNH\text{-}2})$$

The NNH pathway also strongly interacts with the N_2O pathway as it can directly produce N_2O:

$$NNH + O \leftrightarrow H + N_2O, \qquad (R_{NNH\text{-}3})$$

therefore directly competing with ($R_{NNH\text{-}2}$). Furthermore, similarly to the N_2O pathway, the NNH pathway is counterbalanced by reactions recycling the NNH species back to N_2 through:

$$NNH + O_2 \leftrightarrow HO_2 + N_2, \qquad (R_{NNH\text{-}4})$$

$$NNH + H \leftrightarrow H_2 + N_2, \qquad (R_{NNH\text{-}5})$$

$$NNH + OH \leftrightarrow H_2O + N_2, \qquad (R_{NNH\text{-}6})$$

$$NNH + O \leftrightarrow OH + N_2. \qquad (R_{NNH\text{-}7})$$

This pathway is rarely dominant in current and typical combustion systems, and is, therefore, the least studied in the literature [28]. Nevertheless, this pathway has been identified as the sole contributor of NO formation in low pressure and low temperature hydrogen flames, especially for rich stoichiometry [47, 50, 53–55].

I.4.5 Other pathways

The fuel-N pathway, represented by the purple arrows in Fig. I.1, only occurs when the fuel specie contains the N molecule, such as in biofuels. In contrast to the previously discussed "traditional" pathways where the N_2 of the air is the source of atomic N, in the fuel-N pathway, the N contained in the fuel becomes the source (as it is more easily broken down than the triple bond of N_2) and forms NH_3 and HCN through the flame front. In N-containing fuels, this pathway generally dominates and leads to significant NO production, typically several order of magnitude larger than NO produced in hydrocarbon or hydrogen fuels [56]. This pathway is gaining increased attention due to the interest in NH_3-containing fuels, which is another promising alternative to current fossil fuels [57].

Finally, a new potential formation pathway was presented by Burke's research group [58, 59]. This pathway would result from the formation of HNNO from the reaction $N_2O+H \ (+M)$ and later breaking the N_2 bond to form NO. This pathway would be active at low temperatures and moderate to elevated pressures. This discovery would imply that additional pathway interactions may play

a role in the formation of NO at some conditions, and therefore potentially explain mispredictions from current thermochemical models.

While both these pathways are relevant to the combustion and gas turbine community, this work focuses only on the four traditional NO formation pathways.

I.4.6 NO_x mitigation in practical combustion systems

In order to limit the NO production in practical combustion systems, gas turbine manufacturers have employed strategies targeting individual pathways [60]. To decrease the contribution of the thermal pathway, a simple reduction of the combustion temperature and residence time is required. To do so, dilution strategies, such as Exhaust Gas Recirculation (EGR), or a decrease of equivalence ratio (on the lean side), lead to an improvement of NO emissions, but generally at the expense of an increase of CO emissions [10, 11]. The decrease in the contribution of the prompt pathway is possible with the use of fuels with shorter hydrocarbon chains [31]. Conveniently, in hydrogen fuels, the complete lack of C-species leads to a null contribution of the prompt pathway. Furthermore, the decrease of the equivalence ratio mitigates the production of CH-radicals directly linked to the prompt-NO production, as well as the production of H radicals linked to the NNH pathway. Finally, it was demonstrated that the implementation of premixing significantly improves NO emissions through the reduction of flame temperatures [61]. It improves mixedness and avoids the formation of hot regions favoring thermal NO. It also facilitates operating at lean equivalence ratios, where the prompt, the NNH, and the thermal pathway contributions are reduced.

It is becoming common to see such strategies employed by industrial gas turbines. One example is DLE systems which use both premixing and lean equivalence ratios (both globally and locally). In such systems, the formation of NO is not simply dependent on a single dominant pathway, but rather, on the interaction and co-dependence of several pathways.

I.4.7 Pathway contributions

As discussed, state-of-the-art combustion technologies, using natural gas (substituted as pure methane in this study) or potentially hydrogen, can have up to four pathways that alternate in dominance depending on the combustion conditions. This is illustrated in Fig. I.2, which compares the significance of each pathway for different pressures, temperatures, and fuels. This figure presents the NO formation in laminar free flames modelled using Cantera and the Galway [62] thermochemical model, one of the most comprehensive model available in the literature. 633 methane-air and 677 hydrogen-air flames were modelled for which initial conditions were varied. The inlet pressure was varied from 1 atm to 36 atm in steps of 1 atm. The flames were modelled to reach adiabatic flame temperatures ranging from 1600 K to 2500 K by varying the equivalence ratio between an

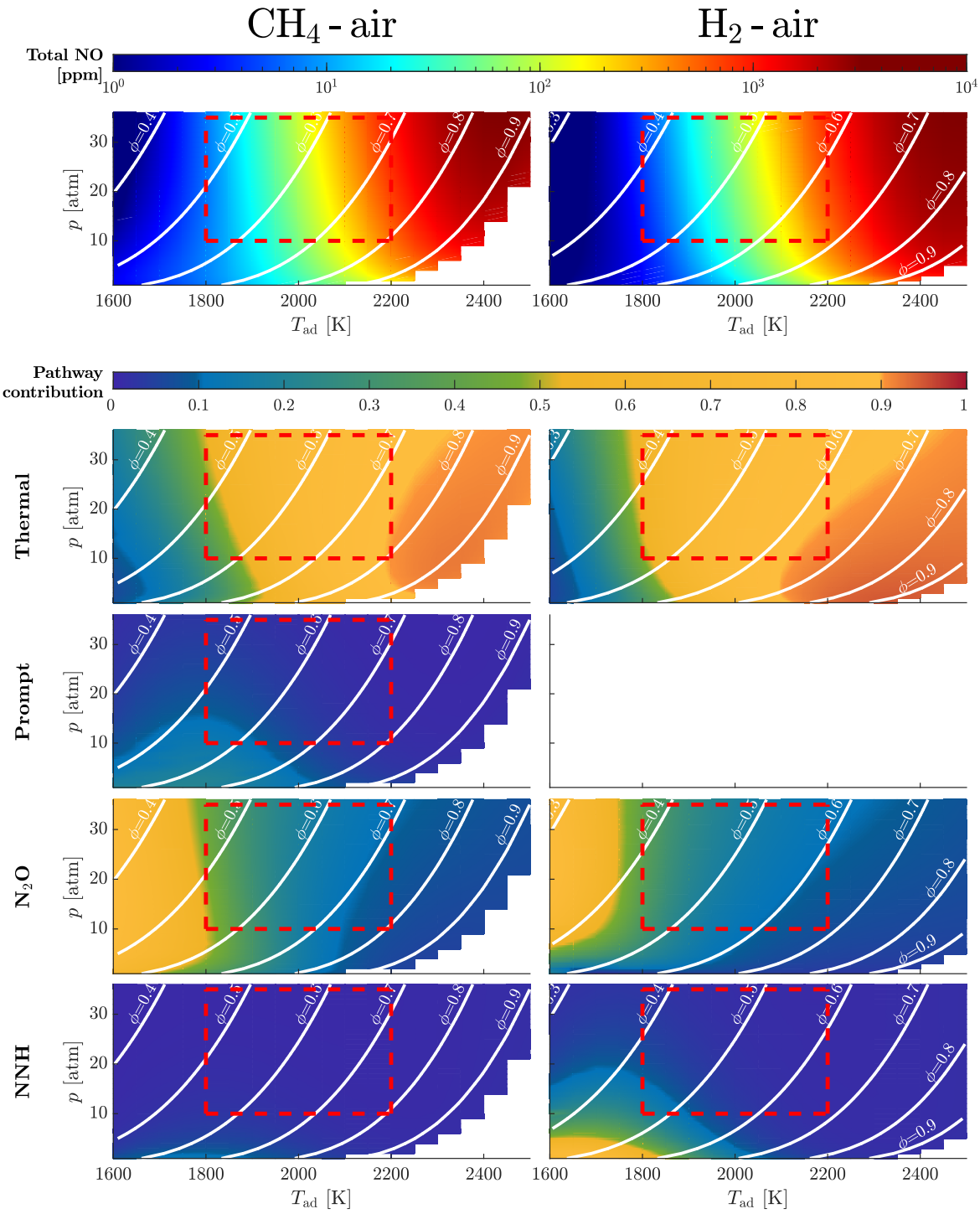

Figure I.2: Pathway contribution assessment at 10 ms residence time of 633 CH_4-air (left) and 677 H_2-air (right) laminar free flames in varying inlet conditions: pressure varying from 1 to 36 atm and equivalence ratio varying from 0.20 to 0.99 to reach adiabatic flame temperatures from 1600 to 2500 K. The red dashed square represents typical GT running conditions.

allowed lean range of 0.20 to 0.99. These conditions represent the full map of possible gas turbine combustion conditions in which a flame could be sustained, at either full- or part-load. The NO concentration and the contribution of its formation pathways were analysed at a consistent residence time of 10 ms post-flame (identified from the point of peak heat release rate), comparable to residence times in practical gas turbines [10]. The formation mechanism of NO is determined using a Reaction Pathway Analysis (RPA) [63] by tracking the flux of atomic nitrogen reacting with other species, from the inlet to the outlet of the domain. The contribution of each NO-formation route is assessed by probing the decomposition of N_2 into different species: N/NO (thermal pathway), NCN (prompt pathway), NNH (NNH pathway), and N_2O (N_2O pathway). Results are presented for both CH_4-air and H_2-air flames on the left and right sides, respectively, of Fig. I.2. Note that the absence of data in the low-pressure and high-temperature region is due to the limit of the analysis to lean equivalence ratios. As such, more flames could be studied using hydrogen than using methane fuel.

For CH_4-air flames, a large variation of NO concentration can be seen throughout the map, from a few ppm at low adiabatic flame temperatures, to several thousands of ppm at high temperatures and pressures. As expected, the total concentration of NO at 10 ms increases with the increase of the adiabatic temperature, while an increase of pressure has a minor effect. When looking at the contribution of each pathway, it is evident that the thermal pathway is dominant for most of the map. At 10 ms, for most of the flames conditions used in this analysis, the thermal pathway had enough time to develop and gain in dominance over the other pathways. The prompt pathway is more significant in low pressure and low temperatures conditions as these flames are slower and with greater flame thickness, leading to a larger and longer prompt formation region. The N_2O pathway is mostly dominant in low temperatures, where the thermal pathway is not active. Finally, the contribution of the NNH pathway is mostly null on the entire map, with a slight contribution at low pressures and moderate temperatures. The analysis of the pathway contribution show that, for methane-air flames, the four pathways play a role in the formation of NO, with the thermal and N_2O pathways being the most significant.

For H_2-air flames, the overall production of NO is of the same order of magnitude as for the CH_4-air flames. Additionally, matching the same temperature range as the CH_4-air flames results in generally lower H_2-air equivalence ratios, going beyond the flammability limits of CH_4-air flames. Despite similarities in the total production of NO at 10 ms, the pathway contribution is different for both fuels. First, with the lack of C-species in the H_2-air flames, the contribution of the prompt pathway is completely removed. The thermal and N_2O pathways, however, behave similarly to the methane-air flames. The thermal pathway is fully dominant in typical GT conditions and an increase of the adiabatic flame temperature leads to an increase of its contribution. For the N_2O contribution, its dominance is clearly limited to the high pressures and low temperatures region.

The main difference stems from the contribution of the NNH pathway, which Fig. I.2 shows is far more significant for H_2-air flames compared to CH_4-air flames. It is clearly dominant at low pressure and low-temperature conditions. Its contribution decreases significantly when pressures beyond ~ 10 atm, and temperatures greater than 1900 K, are reached.

The direct comparison of both fuels at constant pressure is presented in Fig. I.3, which shows two isobaric slices of Fig. I.2, at atmospheric pressure (a) and elevated pressure (b). The contribution of each pathway is plotted in coloured curves using the left-hand side vertical axis, and the concentration of NO is plotted using black curves and the right-hand side of the vertical axis.

At atmospheric pressure, seen in Fig. I.3a, the contribution to the overall NO production is shared between three and four pathways, for hydrogen and methane respectively. As discussed previously, the thermal contribution increases significantly above 1800 K for both fuels. Note that the curves for methane flames stop at ~ 2100 K due to the limit of the analysis to lean equivalence ratios. The prompt contribution, unique to the methane flames, decreases with temperature as thermal is gaining importance. The N_2O pathway is mostly dominant in low temperature methane flames while mostly negligible in hydrogen flames. On the contrary, the NNH pathway is dominant in low temperature hydrogen flames and leads to a minor contribution in methane flames. The total concentration of NO at 10 ms is similar for both fuels, going from few ppm to several hundreds of ppm from low to high temperatures.

At high pressure, seen in Fig. I.3b, the contribution is only shared by two pathways: thermal and N_2O. The dominance alternates from the N_2O pathway in low temperatures to the thermal pathway in temperatures above 1800 K. Interestingly, the contribution of the prompt pathway for the methane flames and the contribution of the NNH pathway for the hydrogen flames are behaving in the same manner, while negligible. Finally, the total concentration of NO at 10 ms is once

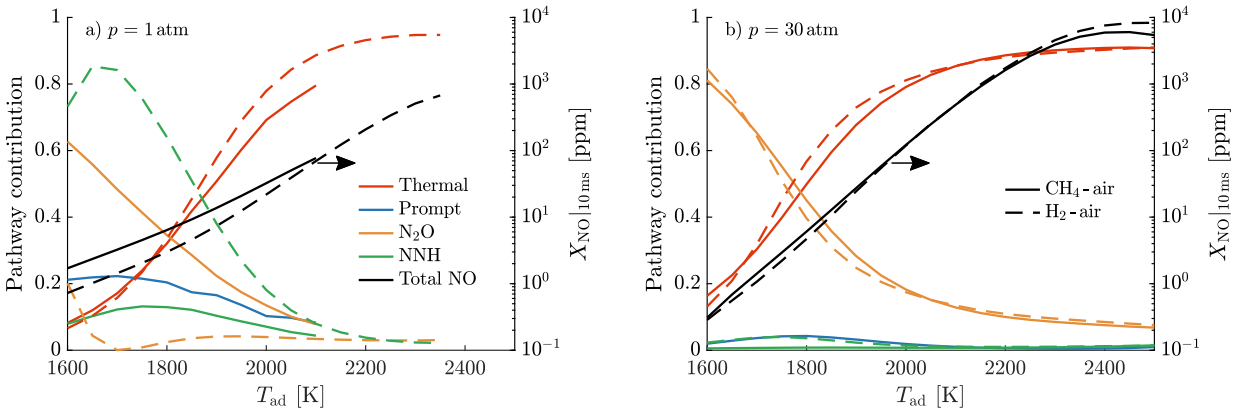

Figure I.3: Pathway contribution assessment at 10 ms residence time of CH_4-air flames (–) and H_2-air flames (- -) at adiabatic flame temperatures ranging from 1600 to 2500 K and inlet pressures of: a) 1 atm and b) 30 atm.

again similar for both fuels, but spanning a larger range than at atmospheric conditions, from sub-ppm levels to several thousands of ppm produced from low to high temperatures. These results indicate that the accurate prediction of both the N_2O and thermal pathways is crucial for improved mitigation strategies. Furthermore, at high pressure, the behaviour of the pathway contribution is the same for both fuels, for the thermal pathway, as well as for the N_2O pathway. Similar behaviour is also present for the thermal pathway at atmospheric pressure. Regardless of the fuel, the thermal pathway is dominant and behaving in a similar manner. Therefore, a study of the accuracy of prediction of the thermal-NO pathway in either methane-air or hydrogen-air flames is key for thermochemical model development of both fuels. It is interesting to note that the thermal pathway remains dominant with similar contributions regardless of the pressure, at adiabatic flame temperatures above 1800 K. Thus, a study of the accuracy of prediction of the thermal-NO pathway in atmospheric conditions would also be representative at higher pressures, which are more relevant for GT conditions. Finally, Fig. I.3 shows that at high temperatures, this pathway is almost entirely dominant, with it comprising of up to 90% of total NO production at temperatures beyond 2100 K. Therefore, these conditions can be used to study the behaviour of this pathway in isolation, forming a baseline to then examine the pathway interactions at other conditions.

As discussed, it is evident that the thermal-NO pathway plays an important role in practical combustion systems. Furthermore, recent discoveries regarding the role, contribution, rates, and interactions of the other pathways might lead to a shift in the understanding of the thermal pathway. Indeed, interactions and sharing of species can occur between the pathways. The change of the rate of a pathway might lead to a change in the radical pool availability or to a different competition of the rates themselves. Therefore, a study of the thermal-NO pathway in the current context is required. The previous analysis has demonstrated that this pathway could be investigated in methane and hydrogen flames, by going to high adiabatic flame temperatures. These conditions would also be representative of typical GT conditions, leading to a direct possible comparison of experimental results with thermochemical model predictions.

I.5 Prediction capabilities and model development

The design and optimisation of gas turbines combustors use thermochemical models to predict flame behaviour at different operating conditions. These models describe the transport and thermodynamic mechanisms of the species, as well as the chemical reactions occurring during combustion. While the thermodynamic and transport properties of each specie is generally well known, it is principally through the chemical reactions that each model differ. These differences depend on the choice of which specie to include in the model, as well as the choice of which reaction and which rate. The greater number of specie and reaction is generally indicative of a more com-

prehensive model, developed and optimised to target a more expansive set of flame conditions. While often opaque, the development of a thermochemical model is often performed similarly to the process described by Curran [64].

The optimisation of a model is generally conducted through the adjustment of the reaction rates. Each reaction rate is described following the modified Arrhenius formulation, in which the pre-exponential factor A, the temperature exponent b, and the activation energy E_a parameters need to be specified. Other parameters, such as the collider partners and their efficiencies, as well as the pressure-dependent parameters, or the transport parameters, are also crucial for a complete description of the chemical process occurring during combustion. During development and optimisation of a thermochemical model, these parameters are adjusted to meet specific validation targets. These targets can be a direct measurement of a reaction rate obtained with shock tubes, flow reactors, or *ab initio* calculations. In these, only one reaction is studied at a time in controlled conditions to measure its fundamental kinetic parameters. This methodology, while being more precise and accurate, cannot be performed for all reactions that might occur in a combustion process. This is because, in addition to being time-consuming as it requires a high level of experimental "cleanliness", it also cannot physically recreate every specie and reaction that might be happening in a flame, especially for short-lived species. Other targets, or indirect measurements, can be used to derive one or several kinetic rates through the flame as a whole, such as ignition time, flame speed, or speciation. Indirect validation targets are usually obtained in burners, in flow or jet-stirred reactors. In these, each reaction rate cannot be isolated and are inherently impacted by the chemistry of the entire domain. Therefore, the rate of several reactions are determined by what leads to the best fit on the indirect measurements. This implies that some rates might be misrepresented and might be concealing errors in other reaction rates.

Thermochemical models are usually developed following two approaches: global and hierarchical. In the global approach, all reactions are specified in the model in no precise order or importance. All reactions are then used to optimise the best fit for all required validation targets. In contrast, in the hierarchical manner, the model is divided in subsets of decreasing levels of importance. The first level being the hydrogen oxidation chemistry (H_2/O_2), the core of any flame chemical reactions and of critical importance, as previously discussed. The subsequent levels model C_1 species (CO, CH_4), and then heavier hydrocarbons (C_{2+}). In this structure each upper level depends on all the lower levels, but not otherwise. Thus, the model can be developed by subset, with a stronger importance given to the validation of the H_2/O_2 chemistry. Pollutant formation (NO_x, soot) can also be represented by a subset, usually the last one of a model.

Regardless of the validation target and the model structure, the optimisation process can be performed in a brute-force manner, the reactions parameters are adjusted "by hand" and individually to meet the validation target, or in a more global and robust approach achieved through the

use of optimisation tools in which the uncertainty of the validation target is also accounted through statistical or Bayesian inference [65–67]. The use of optimisation tools has become more prevalent in the development and optimisation of thermochemical models, leading to higher confidence in such models.

Given these unique developmental characteristics, it becomes clear how the predictive capabilities of each thermochemical model can differ. With the importance of the NO thermal pathway in gas turbine conditions, variability in the prediction of thermochemical models could be negatively impactful for the development and distribution of ultra-low NO_x emitting gas turbines.

I.6 Scope of the thesis

The focus of the thesis is on the thermal NO formation pathway, as it dominates NO formation in gas turbine combustor conditions. Extensive studies were performed to find strategies mitigating the impact of the thermal pathway in practical combustion systems. As such, the reduction of the flame temperature, the residence time, and the equivalence ratio of the combusting mixture led to a significant decrease of NO formation. Through these mitigation strategies, NO transitioned from being predominantly formed via the thermal pathway to being formed through the contribution of several pathways. Due to the increased contribution of the pathways other than thermal, recent studies have focused their interest in accurately describing the reaction rates and activation conditions of the N_2O and NNH pathways. These have shed a new light on the pathway behaviours and have shown that interaction could occur in certain conditions between multiple pathways. The pathway inter-dependence, not historically taken into account in the development of NO_x models, as well as the increased contribution of the N_2O and NNH pathways relative to the prompt and thermal pathways, questions the accuracy of current NO prediction models. Additionally, variability in the modelling of reactions rates involved in the several NO formation pathways, as well as in the hydrogen-oxidation core chemistry, indicate that the chemistry at play is still not comprehended with low uncertainty. These uncertainties have the potential to significantly affect future combustor designs, potentially causing the initially predicted levels to deviate considerably from the actual NO emissions.

The investigation focuses particularly on the thermal pathway as it is dominant in most flame conditions. Its accurate description could result in a better description of the other pathways through interaction. To effectively study the thermal pathway, its isolation from other pathways is required. The analysis of the contribution of the NO formation pathways under a wide variation of gas turbine inlet conditions show that NO measurements in high-temperature, atmospheric, lean, premixed flames, would allow to isolate the thermal pathway while mitigating the contribution of the other ones. Therefore, NO measurements performed in these conditions would be mainly rep-

resentative of the NO formation behaviour through the thermal pathway. Thus, the comparison of the experimental results with the prediction capabilities of several state-of-the-art thermochemical models would allow to map out the current state of understanding of the combustion chemistry. Any misprediction would therefore be indicative of an inaccurate representation of the thermal NO formation pathway, or be a result of a deeper modelling issue through, for example, the modelling of the hydrogen-oxidation chemistry.

The first goal of this thesis is to dive into the modelling chemistry of NO formation in conditions that are representative of practical combustion systems. This thesis aims to outline the state of the current understanding of NO formation in conditions that particularly promote the thermal pathway. The second goal of this thesis is to provide the modelling community with a full set of data (velocity, temperature, and NO concentration profiles) of flames in gas turbine representative conditions. These data, obtained with high level of confidence, are needed to help modeller constrain their model and diversify their validation targets, to obtain a better numerical representation of potential future solutions for the production of energy *via* alternative fuels.

To address these goals, the thesis is organised in three main sections, all associated with the publication of a journal article.

First, a detailed methodology section presents the experimental setup and diagnostic techniques used to provide high accuracy and low uncertainty velocity, temperature, and NO concentration measurements in premixed, laminar, atmospheric stagnation flames. The focus is brought on the diagnostic technique for quantitative NO measurements. NO profiles are measured using Laser Induced Fluorescence (LIF), an advanced laser diagnostic allowing high levels of accuracy, precision, and low uncertainty. In order to achieve such levels of accuracy in flames producing from sub-ppm to several hundreds ppm of NO, a comprehensive comparison of several calibration techniques using LIF is performed, and published in *Journal of Quantitative Spectroscopy and Radiative Transfer* [68]. This study was designed to help researchers, especially those starting in the LIF measurement field, to select a suitable methodology for the quantitative measurement of specie concentration.

The second study, published in the *Proceedings of the Combustion Institute* [69], is conducted to measure NO in high temperature methane-air flames. This study aims to replicate the thermal pathway in gas turbine conditions by using methane as a fuel, and compares the prediction behaviours of several thermochemical models. Discrepancies in the prediction of NO in regions where the thermal pathway dominates indicate that either the thermal-NO pathway, the prompt pathway, or the H_2/O_2 chemistry description by the models is not accurate.

A follow-up and third study, published in *Combustion and Flame* [70], is conducted to measure NO in hydrogen flames, once again by reaching high flame temperatures. The elimination of the prompt pathway contribution leads to a better focus on the thermal NO contribution, as well as

on the hydrogen-oxidation core chemistry. NO measurements performed in the lean, atmospheric, high-temperature hydrogen-air flames, present even stronger prediction discrepancies by the models than for the methane study. In this study, clear mispredictions in the flame characteristics other than NO concentration (velocity and temperature) show that the flame core chemistry is still not accurately described and understood by any of the eleven thermochemical models tested.

These results in both methane and hydrogen-air flames indicate that important efforts are still required to improve the combustion chemistry understanding. This would enable a more accurate representation of, not only the NO formation, but also the overall flame behaviour, in current and future combustor designs. This improved comprehension is paramount for an effective, cost and time-wise, integration of alternative fuels into a diverse energy mix.

References

[1] Energy Insitute. *Statistical Review of World Energy*. Tech. rep. 2023.

[2] G. Maggio and G. Cacciola. "When will oil, natural gas, and coal peak?" In: *Fuel* 98.2012 (2012), pp. 111–123.

[3] J. M. Bergthorson. "Recyclable metal fuels for clean and compact zero-carbon power". In: *Progress in Energy and Combustion Science* 68 (2018), pp. 169–196.

[4] E. Rahimi, A. Rabiee, J. Aghaei, K. M. Muttaqi, and A. Esmaeel Nezhad. "On the management of wind power intermittency". In: *Renewable and Sustainable Energy Reviews* 28 (2013), pp. 643–653.

[5] M. C. McManus. "Environmental consequences of the use of batteries in low carbon systems: The impact of battery production". In: *Applied Energy* 93 (2012), pp. 288–295.

[6] A. R. Dehghani-Sanij, E. Tharumalingam, M. B. Dusseault, and R. Fraser. "Study of energy storage systems and environmental challenges of batteries". In: *Renewable and Sustainable Energy Reviews* 104 (2019), pp. 192–208.

[7] T. Capurso, M. Stefanizzi, M. Torresi, and S. M. Camporeale. "Perspective of the role of hydrogen in the 21st century energy transition". In: *Energy Conversion and Management* 251 (2022), p. 114898.

[8] J. Incer-Valverde, A. Korayem, G. Tsatsaronis, and T. Morosuk. ""Colors" of hydrogen: Definitions and carbon intensity". In: *Energy Conversion and Management* 291 (2023), p. 117294.

[9] K. A. Trowell, S. Goroshin, D. L. Frost, and J. M. Bergthorson. "The use of supercritical water for the catalyst-free oxidation of coarse aluminum for hydrogen production". In: *Sustainable Energy and Fuels* (2020), pp. 5628–5635.

[10] A. H. Lefebvre and D. R. Ballal. *Gas Turbine Combustion: alternative fuels and emissions*. CRC Press, 2010.

[11] T. C. Lieuwen and V. Yang. *Gas Turbine Emissions*. 2013.

[12] P. Griebel. “Gas Turbines and Hydrogen”. In: *Hydrogen Science and Engineering: Materials, Processes, Systems and Technology*. Vol. 2. Wiley VCH, 2016, pp. 1011–1032.

[13] A. L. Sánchez and F. A. Williams. “Recent advances in understanding of flammability characteristics of hydrogen”. In: *Progress in Energy and Combustion Science* 41 (2014), pp. 1–55.

[14] J. Herzler and C. Naumann. “Shock-tube study of the ignition of methane/ethane/hydrogen mixtures with hydrogen contents from 0% to 100% at different pressures”. In: *Proceedings of the Combustion Institute* 32 (2009), pp. 213–220.

[15] S. Panigrahy, A. A. E. S. Mohamed, P. Wang, G. Bourque, and H. J. Curran. “When hydrogen is slower than methane to ignite”. In: *Proceedings of the Combustion Institute* 39.1 (2023), pp. 253–263.

[16] C. J. Sun, C. J. Sung, L. He, and C. K. Law. “Dynamics of weakly stretched flames: Quantitative description and extraction of global flame parameters”. In: *Combustion and Flame* 118 (1999), pp. 108–128.

[17] G. S. Jackson, R. Sai, J. M. Plaia, C. M. Boggs, and K. T. Kiger. “Influence of H_2 on the response of lean premixed CH_4 flames to high strained flows”. In: *Combustion and Flame* 132 (2003), pp. 503–511.

[18] C. Hinshelwood and A. Williams. “The reaction between hydrogen and oxygen”. In: *The Oxford Press* (1934).

[19] N. Semenov. “Chemical kinetics and chain reactions”. In: *The Oxford Press* (1935).

[20] C. K. Law. *Combustion Physics*. Cambridge. 2006.

[21] D. L. Baulch et al. “Evaluated Kinetic Data for Combustion Modeling: Supplement II”. In: *Journal of Physical and Chemical Reference Data* 34 (2005), pp. 757–1397.

[22] A. A. Konnov. “Remaining uncertainties in the kinetic mechanism of hydrogen combustion”. In: *Combustion and Flame* 152 (2008), pp. 507–528.

[23] M. P. Burke, M. Chaos, Y. Ju, F. L. Dryer, and S. J. Klippenstein. “Comprehensive H_2/O_2 kinetic model for high-pressure combustion”. In: *International Journal of Chemical Kinetics* 44 (2012), pp. 444–474.

[24] A. A. Konnov. “Yet another kinetic mechanism for hydrogen combustion”. In: *Combustion and Flame* 203 (2019), pp. 14–22.

[25] G. Lammel and H. Graßl. “Greenhouse effect of NO_x”. In: *Environmental Science and Pollution Research* 2 (1995), pp. 40–45.

[26] M. W. Frampton and I. A. Greaves. *NO_x - NO_x: Who’s there?* 2009.

[27] J. A. Miller and C. T. Bowman. “Mechanism and modeling of nitrogen chemistry in combustion”. In: *Progress in Energy and Combustion Science* 15 (1989), pp. 287–338.

[28] P. Glarborg, J. A. Miller, B. Ruscic, and S. J. Klippenstein. "Modeling nitrogen chemistry in combustion". In: *Progress in Energy and Combustion Science* 67 (2018), pp. 31–68.

[29] Y. B. Zeldovich. "The oxidation of nitrogen in combustion and explosions". In: *Acta Physiochimica* 21 (1946), pp. 577–628.

[30] M. Abián, M. U. Alzueta, and P. Glarborg. "Formation of NO from N_2/O_2 mixtures in a flow reactor: Toward an accurate prediction of thermal NO". In: *International Journal of Chemical Kinetics* 47 (2015), pp. 518–532.

[31] G. M. G. Watson, P. Versailles, and J. M. Bergthorson. "NO formation in premixed flames of C_1-C_3 alkanes and alcohols". In: *Combustion and Flame* 169 (2016), pp. 242–260.

[32] N. A. Buczkó, T. Varga, I. G. Zsély, and T. Turányi. "Formation of NO in high-temperature N_2/O_2/H_2O mixtures: re-evaluation of rate coefficients". In: *Energy and Fuels* 32 (2018), pp. 10114–10120.

[33] X. Han, M. Lubrano Lavadera, C. Brackmann, Z. Wang, Y. He, and A. A. Konnov. "Experimental and kinetic modeling study of NO formation in premixed CH_4+O_2+N_2 flames". In: *Combustion and Flame* 223 (2021), pp. 349–360.

[34] C. P. Fenimore. "Formation of nitric oxide in premixed hydrocarbon flames". In: *Symposium (International) on Combustion* 13 (1971), pp. 373–380.

[35] L. Moskaleva and M. C. Lin. "The spin-conserved reaction CH + N_2 → H + NCN: A major pathway to prompt NO studied by quantum/statistical theory calculations and kinetic modeling of rate constant". In: *Proceedings of the Combustion Institute,* 28 (2000), pp. 2393–2401.

[36] G. P. Smith et al. "GRI-Mech 3.0". In: (1999).

[37] E. Ranzi, A. Frassoldati, R. Grana, A. Cuoci, T. Faravelli, A. P. Kelley, and C. K. Law. "Hierarchical and comparative kinetic modeling of laminar flame speeds of hydrocarbon and oxygenated fuels". In: *Progress in Energy and Combustion Science* 38 (2012), pp. 468–501.

[38] J. A. Sutton, B. A. Williams, and J. W. Fleming. "Investigation of NCN and prompt-NO formation in low-pressure C_1-C_4 alkane flames". In: *Combustion and Flame* 159.2 (2012), pp. 562–576.

[39] N. Lamoureux, P. Desgroux, A. El Bakali, and J. F. Pauwels. "Experimental and numerical study of the role of NCN in prompt-NO formation in low-pressure CH_4-O_2-N_2 and C_2H_2-O_2-N_2 flames". In: *Combustion and Flame* 157 (2010), pp. 1929–1941.

[40] N. Lamoureux, H. E. Merhubi, L. Pillier, S. de Persis, and P. Desgroux. "Modeling of NO formation in low pressure premixed flames". In: *Combustion and Flame* 163 (2016), pp. 557–575.

[41] P. Versailles, G. M. G. Watson, A. C. A. Lipardi, and J. M. Bergthorson. "Quantitative CH measurements in atmospheric-pressure, premixed flames of C_1-C_4 alkanes". In: *Combustion and Flame* 165 (2016), pp. 109–124.

[42] G. M. Watson, P. Versailles, and J. M. Bergthorson. "NO formation in rich premixed flames of C_1-C_4 alkanes and alcohols". In: *Proceedings of the Combustion Institute* 36 (2017), pp. 627–635.

[43] S. J. Klippenstein, M. Pfeifle, A. W. Jasper, and P. Glarborg. “Theory and modeling of relevance to prompt-NO formation at high pressure”. In: *Combustion and Flame* 195 (2018), pp. 3–17.

[44] N. Lamoureux, P. Desgroux, M. Olzmann, and G. Friedrichs. “The story of NCN as a key species in prompt-NO formation”. In: *Progress in Energy and Combustion Science* 87 (2021), p. 100940.

[45] A. Durocher, G. Bourque, and J. M. Bergthorson. “Bayesian calibration of kinetic parameters in the CH chemistry toward accurate prompt-NO modelling”. In: *Journal of Engineering for Gas Turbines and Power* 145 (2022), p. 021014.

[46] P. C. Malte and D. T. Pratt. “Measurement of atomic oxygen and nitrogen oxides in jet-stirred combustion”. In: *Symposium (International) on Combustion* 15 (1975), pp. 1061–1070.

[47] A. Durocher, M. Meulemans, G. Bourque, and J. M. Bergthorson. “Nitric oxide concentration measurements in low-temperature, premixed hydrogen-air stagnation flames at elevated pressures”. In: *Proceedings of the Combustion Institute* 39 (2023), pp. 541–550.

[48] P. Versailles, A. Durocher, G. Bourque, and J. M. Bergthorson. “Nitric oxide formation in lean, methane-air stagnation flames at supra-atmospheric pressures”. In: *Proceedings of the Combustion Institute* 37 (2019), pp. 711–718.

[49] P. Versailles, A. Durocher, G. Bourque, and J. M. Bergthorson. “Effect of high pressures on the formation of nitric oxide in lean, premixed flames”. In: *Journal of Engineering for Gas Turbines and Power* 143 (2021), p. 051029.

[50] A. Durocher, M. Meulemans, P. Versailles, G. Bourque, and J. M. Bergthorson. “Back to basics - NO concentration measurements in atmospheric lean-to-rich, low-temperature, premixed hydrogen-air flames diluted with argon”. In: *Proceedings of the Combustion Institute* 38 (2021), pp. 2093–2100.

[51] S. de Persis, L. Pillier, M. Idir, J. Molet, N. Lamoureux, and P. Desgroux. “NO formation in high pressure premixed flames: Experimental results and validation of a new revised reaction mechanism”. In: *Fuel* 260 (2020), p. 116331.

[52] J. W. Bozzelli and A. M. Dean. “O + NNH: A possible new route for NO_x formation in flames”. In: *International Journal of Chemical Kinetics* 27 (1995), pp. 1097–1109.

[53] M. S. Day, J. B. Bell, X. Gao, and P. Glarborg. “Numerical simulation of nitrogen oxide formation in lean premixed turbulent $H_2/O_2/N_2$ flames”. In: *Proceedings of the Combustion Institute* 33 (2011), pp. 1591–1599.

[54] S. J. Klippenstein, L. B. Harding, P. Glarborg, and J. A. Miller. “The role of NNH in NO formation and control”. In: *Combustion and Flame* 158 (2011), pp. 774–789.

[55] A. B. Sahu and R. V. Ravikrishna. “Quantitative LIF measurements and kinetics assessment of NO formation in H_2/CO syngas–air counterflow diffusion flames”. In: *Combustion and Flame* 173 (2016), pp. 208–228.

[56] M.-C. Chiong, C. T. Chong, J. H. Ng, S. Mashruk, W. W. F. Chong, N. A. Samiran, G. R. Mong, and A. Valera-Medina. "Advancements of combustion technologies in the ammonia-fuelled engines". In: *Energy Conversion and Management* 244 (2021), p. 114460.

[57] H. Kobayashi, A. Hayakawa, K. D. K. A. Somarathne, and E. C. Okafor. "Science and technology of ammonia combustion". In: *Proceedings of the Combustion Institute* 37 (2019), pp. 109–133.

[58] J. Lee, M. C. Barbet, Q. Meng, R. E. Cornell, and M. P. Burke. "Experimental support for a new NO_x formation route via an HNNO intermediate". In: *Combustion and Flame* (2023).

[59] Q. Meng, L. Lei, J. Lee, and M. P. Burke. "On the role of HNNO in NO_x formation". In: *Proceedings of the Combustion Institute* 39 (2023), pp. 551–560.

[60] G. E. Andrews. "Ultra-low nitrogen oxides (NO_x) emissions combustion in gas turbine systems". In: *Modern Gas Turbine Systems: High Efficiency, Low Emission, Fuel Flexible Power Generation*. Woodhead Publishing Limited, 2013, pp. 715–790.

[61] C. H. Cho, G. M. Baek, C. H. Sohn, J. H. Cho, and H. S. Kim. "A numerical approach to reduction of NO_x emission from swirl premix burner in a gas turbine combustor". In: *Applied Thermal Engineering* 59 (2013), pp. 454–463.

[62] Y. Wu et al. "Understanding the antagonistic effect of methanol as a component in surrogate fuel models: A case study of methanol/*n*-heptane mixtures". In: *Combustion and Flame* 226 (2021), pp. 229–242.

[63] P. Versailles. "CH formation in premixed flames of C_1-C_4 alkanes: assessment of current chemical modelling capability against experiments". PhD. McGill University, 2017.

[64] H. J. Curran. "Developing detailed chemical kinetic mechanisms for fuel combustion". In: *Proceedings of the Combustion Institute* 37 (2019), pp. 57–81.

[65] T. Varga et al. "Optimization of a hydrogen combustion mechanism using both direct and indirect measurements". In: *Proceedings of the Combustion Institute* 35 (2015), pp. 589–596.

[66] H. Wang and D. A. Sheen. "Combustion kinetic model uncertainty quantification, propagation and minimization". In: *Progress in Energy and Combustion Science* 47 (2015), pp. 1–31.

[67] J. Bell, M. Day, J. Goodman, R. Grout, and M. Morzfeld. "A Bayesian approach to calibrating hydrogen flame kinetics using many experiments and parameters". In: *Combustion and Flame* 205 (2019), pp. 305–315.

[68] M. Meulemans, A. Durocher, P. Versailles, G. Bourque, and J. M. Bergthorson. "Calibration techniques for quantitative NO measurement using Laser-Induced Fluorescence". In: *Journal of Quantitative Spectroscopy and Radiative Transfer* 330 (2025), p. 109221.

[69] M. Meulemans, A. Durocher, P. Versailles, G. Bourque, and J. M. Bergthorson. "How well do we know thermal-NO? An investigation of NO formation in flames over a wide temperature range". In: *Proceedings of the Combustion Institute* 39 (2023), pp. 521–529.

[70] M. Meulemans, A. Durocher, G. Bourque, and J. M. Bergthorson. “NO measurements in high temperature hydrogen flames : The crucial role of the hydrogen oxidation chemistry for accurate NO predictions”. In: *Combustion and Flame* 261 (2024), p. 113279.

Chapter II. Methodology

The investigation of the thermal pathway is performed in methane and hydrogen flames, enabling the differentiation of the contribution of the core chemistry, the NO formation pathways, and their interactions in the context of the experimental results. For each flame condition examined, three measurements are conducted: velocity, temperature, and NO concentration. Each of these measurements provide insights into specific aspects of the flame chemistry: the velocity of the flame directly reflects the core chemistry involved; the temperature reflects the thermodynamics of the flame; and the NO concentration measurement reflects the NO formation mechanisms as well as the core chemistry. Each flame is produced using a stagnation flame burner, such that a complete 1D profile is obtained, for each measured parameter, from the inlet of the unburnt gas to the stagnation plate, upon which the burnt gases impinge. In contrast to single-point measurements, spatial- or time-resolved measurements are indispensable to understand how the upstream chemistry would impact the behaviour downstream. This is particularly helpful for NO formation, where some pathways are active in distinct regions of the domain. Finally, each flame condition produced experimentally is modelled using a variety of thermochemical models. The comparison of the numerical and experimental results, by using a variety of numerical investigation tools, reveals the gap in the current understanding of both the NO formation and core flame chemistry.

II.1 Experimental setup

Experiments carried out in the Alternative Fuels Laboratory (AFL) consist of producing stagnation flames in a variety of conditions, and on which non-intrusive optical diagnostics are performed. The experimental setup used in this work is similar to those of previous studies of the group [1–8].

II.1.1 Stagnation flame burner

Premixed, laminar, atmospheric flames are produced using a water-cooled stagnation plate burner. This type of burner leads to flames that are flat, symmetric, stretched, detached, and lifted, suited for optical diagnostics and comparison to simulations. This burner configuration is ideal to isolate any influence of the burner on the flame, leading to flame behaviour that is only dependent on the fundamental properties of the unburnt mixture. The lifted flame also facilitates the use of non-intrusive optical diagnostics on the entire flow domain. Additionally, profiles obtained from

stagnation flame burner measurements can be compared to predictions by a quasi-one-dimensional model (quasi-1D) [9, 10], saving computational time and enabling detailed chemistry. Finally, the measurement of the flame properties can be correlated to the induced stretch and extrapolated to an unstretched flame, approximating an idealised case called a laminar free flame. Such results in simplified flames are particularly useful when developing and optimizing thermochemical models, and thus when testing their performance.

Figure II.1 displays the schematic of the stagnation burner in which two types of flames were successively produced: a methane-air-argon flame (left, blue coloured), and a hydrogen-air flame (right, white-reddish coloured). The blue colour of the methane flame is indicative of the CH radical breakdown, and the white-reddish colour of the hydrogen flame (only captured on camera using a long exposure time of 4 s) is due to the OH and H_2O chemiluminescence emissions [11].

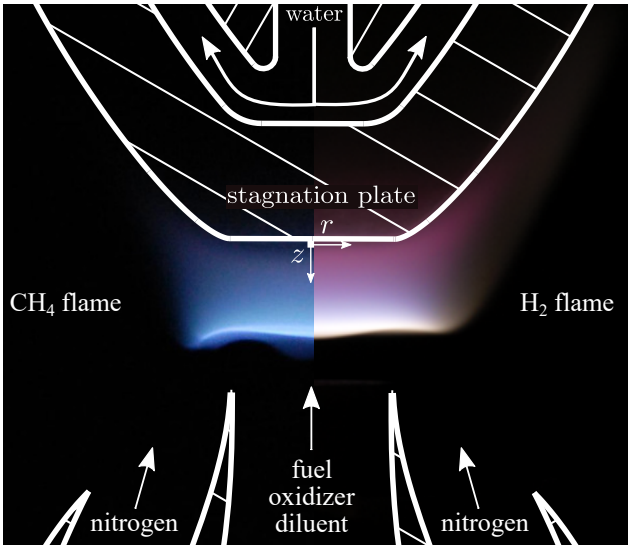

Figure II.1: Schematic of the stagnation flame burner on which the photo of two flames were superimposed: left - a lean ($\phi = 0.9$) methane-air-argon flame at $T_{\text{ad}} \sim 2100$ K; right - a stoichiometric hydrogen-air flame at $T_{\text{ad}} \sim 2100$ K.

The flame is produced using a mixture of combustible gases: a fuel, an oxidizer, and in some instances a diluent. The selected gases flow through a set of Mass Flow Controllers (MFC), controlling the mass flow rate of each gas, generating unburnt gas compositions with desired equivalence ratio (ϕ), oxygen-to-nitrogen ratio (O_2-to-N_2), and diluent mass fraction (X_{diluent}). The mixture is premixed in a mixing tank upstream of the burner inlet to ensure composition homogeneity. The mixture then flows through the burner nozzle (throat diameter of 10.2 mm) containing laminarization beads to ensure a low Reynolds number flow. The flow is guided towards the stagnation plate (same diameter than the nozzle) at ~ 9.5 mm from the nozzle exit plane. By impinging on the stagnation plate, the flow decelerates to a non-slip boundary condition. The stagnation plate is maintained at a constant moderate temperature throughout the experiments to help flame stabilisa-

tion and to avoid surface reactions [12]. This is done by choking the flow of cold water passing through the plate to slow down or accelerate cooling. Once the flame is stabilised, the plate temperature is generally very stable and does not require to be adjusted during a measurement. The temperature of the plate is monitored using a thermocouple inserted into the stainless steel plate but very close to the surface ($\sim$0.7 mm from the surface) such that it does not disturb the flow. The flame, once ignited, stabilises where the flow velocity matches the reference flame speed. To facilitate optical diagnostics, the flow inlet velocity is varied to stabilise the flame at mid-distance of the nozzle-plate distance to maximise the NO developed through the post-flame region. The flow is shielded using a coflowing mixture of an inert gas, nitrogen, avoiding the reaction of the oxygen contained in the air with the combustible mixture, and improving the flame stability [13].

Each flame is carefully monitored during each measurement. The flame position, indicative of any change in the flow inlet velocity and/or flame composition, is tracked through the use of cameras. A LabVIEW interface tracks the various MFC flow rates, as well as the temperature at several points in the burner, inserted in such a manner to not disturb the flow. The temperature of the stagnation plate (T_{wall}) and of the mixture at the inlet (T_{in}) are measured using type-K thermocouples within $\pm\,5$ K and $\pm\,2$ K respectively. These are used as boundary conditions in the corresponding numerical simulations. Additionally, before an experimental campaign, each MFC (Bronkhorst El-Select F-201 and F-211) is calibrated using a dry-piston calibrator (DryCal MF-500-44 and ML-500-10), reaching flow rate uncertainties of of $\pm\,0.40\%$ for each MFC. These measures ensure that there is low uncertainty on experimental boundary conditions, and limits the uncertainty propagation to measured profiles or numerical simulations. The flames are highly stable and can be sustained for several hours. They are also very consistent, resulting in low random uncertainties. This enables the non-simultaneous measurement of multiple flow properties with high repeatability.

II.1.2 Optical diagnostics

The laboratory is equipped with two optical diagnostic setups: a visible green laser and camera setup for velocity measurements, and a UV laser and camera setup for temperature and specie concentration measurements. Each measurement leads to a two-dimensional description of the flow, from which the information at the centerline is extracted and transformed into a 1D profile. The measurements are performed for each flame, sequentially, and several times to ensure repeatability.

II.1.2.1 Particle Tracking Velocimetry

Velocity measurements are performed using Particle Tracking Velocimetry (PTV), as shown in Fig. II.2. This technique provides velocity measurements with minimal disturbance to the flow, in

contrast to Particle Image Velocimetry (PIV). This is made possible through the use of temporally stable flames, allowing the capture of hundreds to thousands of images to obtain a complete description of the flow field using low-density seeding. The setup comprises of a class IV, pulsed, high-power ($I \sim 20$ mJ/pulse), visible ($\lambda = 527$ nm), double-head Nd:YLF laser (Litron LDY303) capable of reaching frequencies of 10 kHz on each head. The frequency and delay of each laser head is controlled using a Digital Delay Generator (SRS DG535) enabling frequencies of up to 20 kHz. The laser beam is shaped, using a set of borosilicate glass lenses (N-BK7), into a thin (~ 1 mm) focused sheet above the center axis of the burner, whose height (~ 9 mm) spans from just above the nozzle to just below the plate to avoid surface reflections.

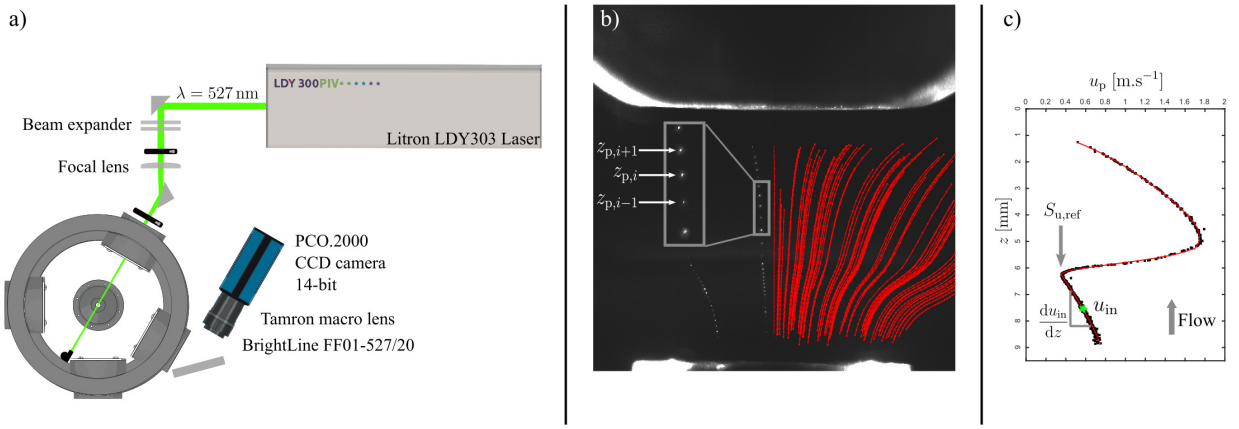

Figure II.2: Particle Tracking Velocimetry methodology: a) schematic of the experimental setup; b) image obtained for a single exposure (100 ms) and multiple laser pulses through a flame (left) and assembled streaks from the post-processing of hundreds of images (right); c) resulting particle velocity profile extracted around the centerline of the nozzle.

A tank, filled with alumina (Al_2O_3) particles of $\sim 1\,\mu$m diameter is placed upstream of the mixing tank. When needed, the air stream is diverted to pass through the particle tank to seed the flow with the alumina particles [14]. A manual valve controls the share of air stream passing through the tank, ultimately controlling the seeding density in the flame.

A monochrome, 14-bit, 4.2Mpx, Charge-Couple Device (CCD) camera (Cooke PCO.2000), mounted with a 90 mm Tamron $f/2.8$ macro lens, coupled to a mirror captures the light perpendicular to the incident beam sheet. A band-pass filter of 20 nm width centered around 527 nm is also mounted on the camera lens to remove noise from other light sources. The camera is calibrated before an experimental campaign using a dotted target (Thorlabs R2L2S3P3) to obtain the pixel to mm conversion of the domain (C_{CCD}), attaining a resolution of $6.700 \pm 0.003\,\mu$m/px. The images are captured using the camera manufacturer software (PCO.Camware). The exposure of the camera ($20-100$ ms), and the frequency of the laser ($1-20$ kHz), is adapted for each measurement based on the velocity of the flame.

The camera captures the light resulting from the Mie scattering of the laser beam on the surface of the highly reflective alumina particles. The long image exposure coupled to several irradiation events leads to a Lagrangian description of the particles in the flow, as depicted in Fig. II.2b. The streaks, or streamlines, are automatically extracted from the images *via* the use of a Matlab processing code developed by members of the group [3, 8, 15]. Hundreds to thousands of streaks are obtained throughout the entire 2D domain captured by the camera, leading to a 2D description of the tracer particle velocity in the flow. Only streaks around the centerline of the nozzle are used to extract the 1D velocity profile of the particle in the flow, as seen in Fig. II.2c. The velocity of the particle is calculated from a second-order, central finite difference scheme, such that:

$$u_{\mathrm{p}}\left(z_{\mathrm{p},i}, r_{\mathrm{p},i}\right) = \frac{z_{\mathrm{p},i+1} - z_{\mathrm{p},i-1}}{2} \cdot f \cdot C_{\mathrm{CCD}} + E_{u_{\mathrm{p},i}} \tag{II.1}$$

where $z_{\mathrm{p},i}$ and $r_{\mathrm{p},i}$ are the axial and radial, respectively, particle locations, f is the laser frequency, C_{CCD} is the camera calibration coefficient, and $E_{u_{\mathrm{p},i}}$ is the error induced by the finite difference [3].

The processed velocity profile of the particle is then used to measure experimental boundary conditions required for flame modelling. For this purpose, the inlet velocity (u_{in}) and the axial strain rate ($\mathrm{d}u_{\mathrm{in}}/\mathrm{d}z$) are measured in the unburnt region of the flow, at the location of minimal uncertainty, also determining the length of the numerical domain ($\mathcal{L}$) [6]. The reference flame speed ($S_{\mathrm{u,ref}}$) is also extracted from the profile, at the point of minimum velocity of the particle in the flow. This parameter, an important flame characteristic, is used to later compare the accuracy of the thermochemical models in predicting the measured velocity. Finally, the direct comparison of the measured velocity profiles to those obtained *via* modelling is possible once the simulated velocity profiles are transformed in experimental units to account for the effect of the particle in the flow. The simulated flow is thus virtually seeded with a 1 μm particle to model its drag due to thermophoretic force and particle inertia in high-gradient/high-curvature parts of the flow [16].

II.1.2.2 NO-Laser Induced Fluorescence

To measure both temperature and NO concentration profiles, linear Laser Induced Fluorescence (LIF) of the $\mathrm{A}-\mathrm{X}\,(0,0)$ electronic system of NO is performed. The laser is used to excite and energize the NO molecules contained in the measurement volume. Their de-excitation to a lower energy state generates UV light emission that can be correlated to the initial state of the molecule (density, pressure, and temperature) when employing LIF modelling [17, 18]. In this work, two distinct methodologies are used to determine the temperature and NO concentration profiles in the flames by using NO-LIF. The experimental setup is, nevertheless, common to both methods.

As depicted in Fig. II.3, it comprises of a class IV, pulsed ($f = 10$ Hz), low-power ($I \sim 1$ mJ/pulse), ultra-violet ($\lambda = 355$ nm, third harmonic), Nd:YAG laser (Spectra Physics Quanta-Ray Pro-230).

The laser energy is maximised by delaying the Q-Switch using a digital delay generator (SRS DG535). The YAG laser is used to pump organic solutions of a dye laser (Sirah Cobra-Stretch) composed of Coumarin 450 and methanol, leading to a beam at $\lambda \sim 450-452$ nm. A Barium-Borate (BBO) doubling crystal (Sirah SGH-215) is used to obtain the second harmonic of the beam at $\lambda \sim 225-226$ nm. The final wavelength of the laser is controlled through the manufacturer software (Sirah Control) where the gratings can be adjusted. The laser energy can also be maximised by ensuring phase matching inside the crystal by adjusting the angle of the Frequency Conversion Unit (FCU). To ensure that the laser is at the desired wavelength, the fluorescence spectrum of a cold flowing mixture of NO for varying excitation wavelengths is compared to a theoretical one. This procedure, repeated at the start and the end of a day of measurements, ensures that the laser wavelength has not deviated from the desired one, which could cause significant losses of fluorescence and lead to increased uncertainty for the NO-LIF concentration measurements. The laser beam is shaped into an unfocused thin sheet centered on top of the burner, using a series of fused-silica lenses. A microlens array is also used to improve the spatial homogeneity of the laser beam [19]. The final laser sheet is $\sim$9 mm tall and $\sim$1 mm wide across a region of interest of $\sim$15 mm length. The laser energy is measured using two photodiodes (Thorlabs PDA10A), each coupled to a 90:10 beamsplitter, placed at the exit of the dye laser ($\sim$0.7 mJ/pulse) and $\sim$ 30 cm before the flame ($\sim$0.1 mJ/pulse).

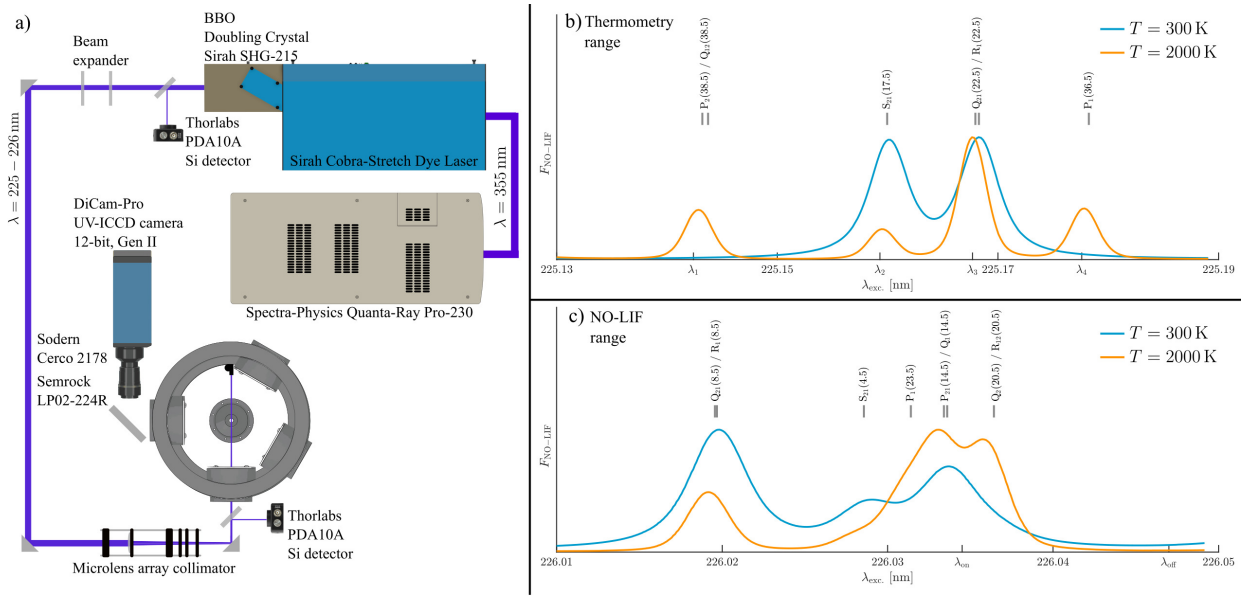

Figure II.3: NO-Laser Induced Fluorescence experimental methodology: a) schematic of the experimental setup; and the NO-LIF signal obtained from LIFSim [20] at two local temperatures for the measurement of: b) the temperature profiles; c) the NO concentration profiles.

A monochrome, 12-bit, 1.3Mpx, UV-Intensified CCD (ICCD) camera (Cook PCO.Dicam Pro with a S20 photocathode), mounted with a 100 mm ultraviolet achromatic $f/2.8$ Sodern lens (Cerco

2178) and a long-pass filter (Semrock LP02-224R), coupled to a mirror captures the light perpendicular to the incident beam sheet, free of Rayleigh scattering and laser reflections. The camera is calibrated using the same technique as for the CCD camera (used for PTV measurements), leading to a conversion of $C_{\text{ICCD}} = 26.3 \pm 0.1$ μm/px. The camera and photodiodes recordings are triggered synchronously with the dye laser gating using the signal of the delay generator, and recorded on a 1 GHz sampling rate oscilloscope (Picoscope 2406B). The images are captured using the manufacturer software. The binning of the images, their exposure ($120-300$ ns), and the hardware accumulation are adjusted to increase the signal-to-noise ratio for each flame.

II.1.2.2.1 Temperature measurements

Temperature measurements are performed using a multi-line NO-LIF thermometry methodology [5, 21, 22]. The NO contained in the domain is energized at varying laser excitation wavelengths. Its fluorescence response, a spectrum specific to the temperature of the location at which it is captured, as seen in Fig. II.3b, is compared to a theoretical spectrum to determine the temperature of the domain. The laser excitation wavelength is varied from 225.13 nm to 225.19 nm using 120 discrete wavelengths. This spectral region includes four rotational lines and has been chosen due to the high sensitivity of the NO line strength to a variation of temperature, and leads to an accuracy of 5% [21].

The flames are seeded with a known, and significant concentration of NO (several hundreds of ppm). Doing so, the temperature can also be measured in regions of the flames that are not producing any, or enough, NO to conduct thermometry, such as in the unburnt region, or in flames producing very low amounts of NO. The captured 2D fluorescence images ($S_{\text{fluo.,nsct+sd}}$) of 80 laser pulses at each excitation wavelength is the result of the de-excitation of NO contained in the flame, comprising of the known seeded amount, and the flame-produced (nascent) NO. To increase the signal-to-noise ratio, the signal of the unseeded flame ($S_{\text{fluo.,nsct}}$), as well as for a flame without laser illumination (S_{dark}) are also captured, removing any noise from flame chemiluminescence, camera dark noise, and ambient light. Both signals are subtracted from $S_{\text{fluo.,nsct+sd}}$, after being corrected by their respective averaged laser energy[1] (E_{L}), as dictated by the linear LIF regime, such that:

$$F_{\text{NO-LIF}} = \frac{(S_{\text{fluo.,nsct+sd}} - S_{\text{dark}}(z))}{E_{\text{L,seeded}}} - \frac{(S_{\text{fluo.,nsct}} - S_{\text{dark}}(z))}{E_{\text{L,unseeded}}}, \tag{II.2}$$

where the processed signal, $F_{\text{NO-LIF}}$, is axially- and spectrally-dependent. To further increase the signal-to-noise ratio, the number of laser pulses per excitation wavelength ($50-80$), the binning of the image, the hardware accumulation, the exposure of the camera ($120-300$ ns), and the concen-

[1] This is done to ensure the capture of any laser energy fluctuation and deviation during the fluorescence measurement of two successive flames.

tration of seeding[2] (200−500 ppm) is adapted for each flame. Examples of images obtained for S_{dark} and $S_{\text{fluo.,nsct+sd}}$ at several wavelengths are displayed in Fig. II.4a-e.

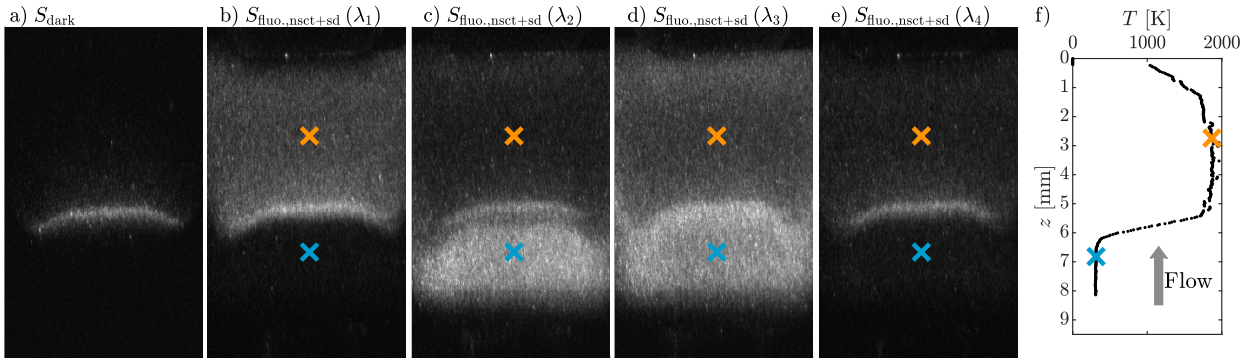

Figure II.4: Images obtained using multi-line NO-LIF thermometry and its resulting temperature profile extracted around the centerline of the nozzle. The intensity scale is kept constant between the images for qualitative comparison.

At each point of the domain, the experimental $F_{\text{NO-LIF}}$ spectrum is compared through a spectra-fitting procedure [21] to theoretical NO-LIF excitation spectra obtained from LIFBase [17] in order to determine the temperature of the NO molecules. This procedure leads to the extraction of the flame temperature profile, as depicted in Fig. II.4f. The experimentally-obtained temperature profile leads to an accuracy of $\pm 5\%$, and is directly compared to simulated profiles.

II.1.2.2.2 NO concentration measurements

NO concentration measurements are conducted using quantitative NO-LIF [23, 24]. The fluorescence signal of the NO produced by the flame is captured by the camera and correlated to the NO concentration using the linear LIF formulation [1, 5, 7, 25]:

$$F_{\text{NO-LIF}}(\lambda) = S_{\text{NO-LIF}}/E_{\text{L}}, \tag{II.3}$$

$$= X_{\text{NO}} \cdot f_{\text{LIF}}\left(\lambda, f_{\text{B}}, p, T, B_{12}, \Delta\nu_L, \Gamma, A_{ul}, Q_{ul}\right) \cdot C_{\text{opt}}\left(\mathcal{E}_{\text{c}}, \mathcal{T}_{\lambda}, \Omega, \ell\right), \tag{II.4}$$

where $S_{\text{NO-LIF}}$ is the fluorescence signal of NO, E_{L} is the averaged laser energy, X_{NO} is the molar fraction of NO in the measurement volume, f_{LIF} is a term encompassing all absorption and emission parameters, and C_{opt} is the optical calibration constant regrouping all optical parameters. The term f_{LIF} is dependent on the laser excitation wavelength (λ), the Boltzmann's fraction (f_{B}), the pressure (p), the local temperature (T), the Einstein absorption coefficient of the transition (B_{12}), the laser spectral linewidth ($\Delta\nu_L$), the overlap fraction (Γ), the Einstein rate constant of sponta-

[2]Note that this technique is insensitive to NO reburn as, for a given point of the domain, only the ratio of the four line-strength is of interest, only dependent on the temperature of the molecule.

neous emission of the transition (A_{ul}), and the rate constant of collisional quenching (Q_{ul}). The term C_{opt} encompasses the quantum efficiency of the camera ($\mathcal{E}_{\text{c}}$), the transmissivity of the optical system ($\mathcal{T}_\lambda$), the collection solid angle (Ω), and the length of the laser path in the measurement volume (ℓ).

The fluorescence signal ($F_{\text{fluo.}}$), however, also contains the LIF signal of interfering species ($F_{\text{interf.-LIF}}$) such as O_2, H_2O, or CO_2, as well as ambient noise caused by the flame or the camera (F_{dark}). Hence, the signal captured needs to be corrected for those background signals, such that:

$$F_{\text{NO-LIF}}(\lambda) = F_{\text{fluo.}}(\lambda) - F_{\text{interf.-LIF}}(\lambda) - F_{\text{dark}}. \tag{II.5}$$

The calculation of $F_{\text{NO-LIF}}$ is performed by measuring the signal at two discrete excitation energies as depicted in Fig. II.3c: an online wavelength corresponding to a peak of NO excitation (λ_{on}), and an offline wavelength corresponding to a minimum excitation state of the NO molecules (λ_{off}). This spectral region was chosen, following the recommendation of Di Rosa [26] and Bessler *et al.* [27, 28], to minimise the impact of interfering LIF signal and to maintain a strong LIF signal with an increasing temperature of the mixture. The subtraction of the signal captured at these two spectral stations removes $F_{\text{interf.-LIF}}$ assuming it to be constant on the spectrum between the online and offline wavelengths.. The signal is also rid of the ambient noise by capturing the signal of the flame without laser illumination and subtracting it from the captured online and offline signal. Finally, the signal is corrected for spatial inhomogeneity in the beam profile by capturing its signal (S_{BP}) in a cold jet flow of constant NO molar fraction. The resulting processed signal is obtained as follows:

$$F_{\text{NO-LIF}} = (F_{\text{fluo.}}(\lambda_{\text{on}}) - F_{\text{dark}}) - (F_{\text{fluo.}}(\lambda_{\text{off}}) - F_{\text{dark}}), \tag{II.6}$$

$$= \left[\frac{(S_{\text{fluo.,on}} - S_{\text{dark}})}{E_{\text{L,on}}} - \frac{(S_{\text{fluo.,off}} - S_{\text{dark}})}{E_{\text{L,off}}}\right] \cdot \frac{1}{S_{\text{BP}}}. \tag{II.7}$$

The signal captured by the camera at several steps of the NO-LIF calculation process are depicted in Fig. II.5, as well as the resulting processed signal. Similarly to other experiments, the NO-LIF profile is extracted at the centerline of the nozzle, as shown in Fig. II.5f, averaging the fluorescence radially on $\sim$0.5 mm. Hence, any absorption of the laser that might occur before reaching the flame does not have an impact on the signal.

The signal obtained from this process leads to $F_{\text{NO-LIF}}$, a qualitative representation of the NO concentration in the domain. In order to obtain a quantitative measurement of NO concentration, calibration is required. Calibration of the signal allows the calculation of X_{NO} from $F_{\text{NO-LIF}}$ by calibrating ($f_{\text{LIF}} \cdot C_{\text{opt}}$) in Eq. II.4. The calibration is required as some terms that are difficult to measure absolutely and accurately (Ω, $\mathcal{T}_\lambda$, $\mathcal{E}_{\text{c}}$, ℓ, ...), and are easier to simply model. In the

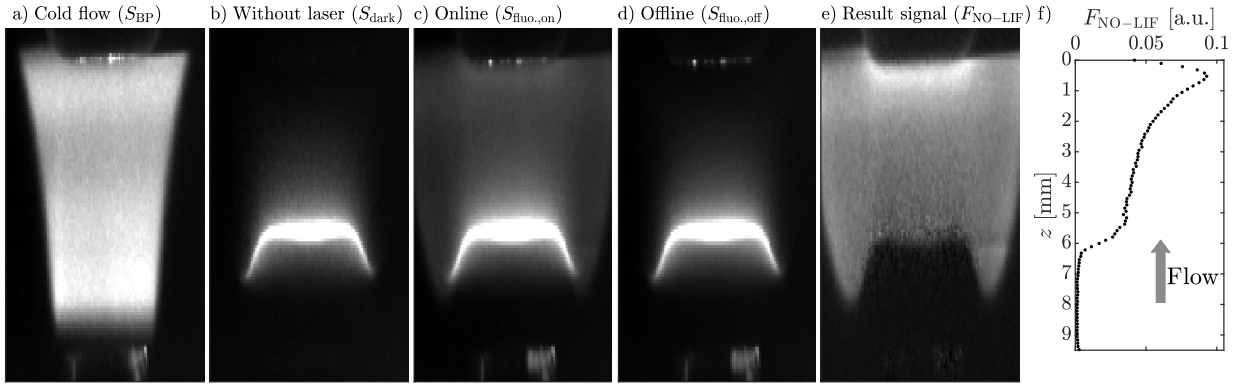

Figure II.5: Images obtained using NO-LIF at different stages of the process, and its resulting LIF signal profile extracted around the centerline of the nozzle. The intensity scale is kept constant between the images for qualitative comparison.

literature, the calibration techniques can be grouped into two categories based on how X_{NO} is determined: experimentally via the signal from several seeded flames, or via modelling of LIF parameters.

In order to obtain quantitative, low-uncertainty, and high-accuracy NO measurements, an extensive study is carried out in Chapter III comparing the different calibration techniques conducted in the literature.

II.2 Flame modelling

Each experimental campaign conducted is compared to state-of-the-art thermochemical models to contextualize the results within the knowledge of the combustion community. The use of a stagnation flame burner produces quasi-1D profiles that are easily comparable with those obtained from 1D simulations. Additionally, the availability of numerical solutions enables the application of various numerical tools to investigate the origins of discrepancies between experimental and simulated results. This provides insights into potential gaps in the current understanding of combustion chemistry

Each experimental flame is simulated using Cantera [29] and the built-in Impinging Jet model. The seven experimental boundary conditions, gathered either during the production of the flames (X_{in}, p, T_{in}, T_{wall}) or through the post-processing of the velocity measurements (u_{in}, $\mathrm{d}u_{in}/\mathrm{d}z$, $\mathcal{L}$), are specified for each flame. Parameters such as the multi-component transport model, the Soret, and radiation effects are included. Simulations are carried out by increasingly constraining the refinement criteria of ratio, curve, and slope until the reference flame speed varies by less than 0.1% between each iteration. It typically leads to solutions containing between 350 to 500 grid points, with a minimum grid size of 1 μm.

Once the simulation is converged, the flame solution containing the specie concentration, velocity, and temperature, at each point of the domain is compared to experimental profiles. Forward (q_{F}), backward (q_{B}), and net (q_{NET}) rate of progress of each reaction, as well as the net production rate of each specie (q_{ROP}) are also obtained for each simulation.

Multiple thermochemical models are used in this work: more or less recent; comprehensive or broad in their description of the chemistry; more or less accurate in predicting previous measurements; etc. This variety allows a more holistic investigation of the current understanding of the combustion chemistry.

References

[1] G. M. G. Watson, P. Versailles, and J. M. Bergthorson. "NO formation in premixed flames of C_1-C_3 alkanes and alcohols". In: *Combustion and Flame* 169 (2016), pp. 242–260.

[2] A. C. A. Lipardi, P. Versailles, G. M. G. Watson, G. Bourque, and J. M. Bergthorson. "Experimental and numerical study on NO_x formation in CH_4–air mixtures diluted with exhaust gas components". In: *Combustion and Flame* 179 (2017), pp. 325–337.

[3] P. Versailles. "CH formation in premixed flames of C_1-C_4 alkanes: assessment of current chemical modelling capability against experiments". PhD. McGill University, 2017.

[4] P. Versailles, A. Durocher, G. Bourque, and J. M. Bergthorson. "Measurements of the reactivity of premixed, stagnation, methane-air flames at gas turbine relevant pressures". In: *Journal of Engineering for Gas Turbines and Power* 141 (2019), p. 011027.

[5] P. Versailles, A. Durocher, G. Bourque, and J. M. Bergthorson. "Effect of high pressures on the formation of nitric oxide in lean, premixed flames". In: *Journal of Engineering for Gas Turbines and Power* 143 (2021), p. 051029.

[6] A. Durocher, M. Meulemans, G. Bourque, and J. M. Bergthorson. "Measurements of the laminar flame speed of premixed, hydrogen-air-argon stagnation flames". In: *Applications in Energy and Combustion Science* 7 (2021), p. 100028.

[7] A. Durocher, M. Meulemans, G. Bourque, and J. M. Bergthorson. "Nitric oxide concentration measurements in low-temperature, premixed hydrogen-air stagnation flames at elevated pressures". In: *Proceedings of the Combustion Institute* 39 (2023), pp. 541–550.

[8] A. Durocher. "Towards robust nitrogen chemistry model development: Uncertainty quantification and prediction capability in atmospheric and elevated-pressure premixed flames". PhD. McGill University, 2021.

[9] R. J. Kee, J. A. Miller, G. H. Evans, and G. Dixon-Lewis. "A computational model of the structure and extinction of strained, opposed flow, premixed methane-air flames". In: *Symposium (International) on Combustion* 22 (1988), pp. 1479–1494.

[10] R. J. Kee, M. E. Coltrin, and P. Glarborg. *Chemically reacting flow: Theory and practice*. John Wiley & Sons, Inc., 2003.

[11] R. W. Schefer, W. D. Kulatilaka, B. D. Patterson, and T. B. Settersten. "Visible emission of hydrogen flames". In: *Combustion and Flame* 156 (2009), pp. 1234–1241.

[12] F. N. Egolfopoulos, H. Zhang, and Z. Zhang. "Wall effects on the propagation and extinction of steady, strained, laminar premixed flames". In: *Combustion and Flame* 109.1-2 (1997), pp. 237–252.

[13] J. M. Bergthorson. "Experiments and Modeling of Impinging Jets and Premixed Hydrogen Stagnation Flames". PhD. California Institute of Technology, 2005.

[14] M. Glass and I. M. Kennedy. "An improved seeding method for high temperature laser doppler velocimetry". In: *Combustion and Flame* 29 (1977), pp. 333–335.

[15] L. J. Benezech, J. M. Bergthorson, and P. E. Dimotakis. "Premixed laminar C_3H_8- and C_3H_6-air stagnation flames: Experiments and simulations with detailed kinetic models". In: *Proceedings of the Combustion Institute* 32 (2009), pp. 1301–1309.

[16] J. M. Bergthorson and P. E. Dimotakis. "Particle velocimetry in high-gradient/high-curvature flows". In: *Experiments in Fluids* 41 (2006), pp. 255–263.

[17] J. Luque and D. R. Crosley. *LIFBASE Version 2.1.1, Database and spectral simulation for diatomic molecules (v1.6)*. 1999.

[18] W. G. Bessler, C. Schulz, T. Lee, J. B. Jeffries, and R. K. Hanson. "Strategies for laser-induced fluorescence detection of nitric oxide in high-pressure flames. III. Comparison of A–X excitation schemes". In: *Applied Optics* 42.24 (2003), pp. 4922–4936.

[19] M. Zimmermann, N. Lindlein, R. Voelkel, and K. J. Weible. "Microlens laser beam homogenizer - from theory to application". In: *Laser Beam Shaping VIII* 6663 (2007), p. 666302.

[20] W. G. Bessler, C. Schulz, S. Volker, and J. W. Daily. "A versatile modeling tool for nitric oxide LIF spectra". In: *Proceedings of the Third Joint Meeting of the U.S. Sections of The Combustion Institute*. Chicago, 2003, P105.

[21] W. G. Bessler and C. Schulz. "Quantitative multi-line NO-LIF temperature imaging". In: *Applied Physics B: Lasers and Optics* 78 (2004), pp. 519–533.

[22] K. K. Foo, N. Lamoureux, A. Cessou, C. Lacour, and P. Desgroux. "The accuracy and precision of multi-line NO-LIF thermometry in a wide range of pressures and temperatures". In: *Journal of Quantitative Spectroscopy and Radiative Transfer* 255 (2020), p. 107257.

[23] P. Versailles, A. Durocher, G. Bourque, and J. M. Bergthorson. "Nitric oxide formation in lean, methane-air stagnation flames at supra-atmospheric pressures". In: *Proceedings of the Combustion Institute* 37 (2019), pp. 711–718.

[24] A. Durocher, M. Meulemans, P. Versailles, G. Bourque, and J. M. Bergthorson. "Back to basics - NO concentration measurements in atmospheric lean-to-rich, low-temperature, premixed hydrogen-air flames diluted with argon". In: *Proceedings of the Combustion Institute* 38 (2021), pp. 2093–2100.

[25] A. C. Eckbreth. *Laser diagnostics for combustion temperature and species*. Ed. by Gordon and Breach Publishers. Second. 1996.

[26] M. D. Di Rosa, K. G. Klavuhn, and R. K. Hanson. "LIF spectroscopy of NO and O_2 in high-pressure flames". In: *Combustion Science and Technology* 118 (1996), pp. 257–283.

[27] W. G. Bessler, C. Schulz, T. Lee, J. B. Jeffries, and R. K. Hanson. "Strategies for laser-induced fluorescence detection of nitric oxide in high-pressure flames. I. A–X(0,0) excitation". In: *Applied Optics* 41.18 (2002), p. 3547.

[28] W. G. Bessler, C. Schulz, T. Lee, J. B. Jeffries, and R. K. Hanson. "Carbon dioxide UV laser-induced fluorescence in high-pressure flames". In: *Chemical Physics Letters* 375.3 (2003), pp. 344–349.

[29] D. G. Goodwin, H. K. Moffat, I. Schoegl, R. L. Speth, and B. W. Weber. *Cantera: An object-oriented software toolkit for chemical kinetics, thermodynamics, and transport processes*. 2021.

Chapter III. Calibration techniques for quantitative NO measurement using Laser-Induced Fluorescence

Publication [1] in *Journal of Quantitative Spectroscopy and Radiative Transfer*, volume 330, 2025, 109221.

M. Meulemans[a], A. Durocher[b], P. Versailles[c], G. Bourque[a], and J. M. Bergthorson[a]

[a] Alternative Fuels Laboratory, McGill University, 817 Sherbrooke St W, Montréal, H3A 0C3, QC, Canada

[b] Gas Turbine Laboratory, National Research Council of Canada, Ottawa, K1K 2E1, ON, Canada

[c] Polytechnique Montréal, 2500 Chemin de Polytechnique, Montréal, H3T 1J4, QC, Canada

III.1 Abstract

Laser-Induced Fluorescence (LIF) is an essential optical diagnostic technique for the high-resolution and low-uncertainty measurement of combustion species concentration in a variety of applications and conditions. Two different calibration techniques are explored in this study to obtain quantitative Nitric Oxide (NO) concentration measurements in flames. The first technique, the most employed in the literature, uses the extrapolation of the fluorescence signal from seeded to nascent NO and is only valid under negligible NO reburn conditions. The second technique uses the optical calibration of the experimental setup to relate it to a modelled LIF signal and can be applied regardless of NO reburn. Both of these techniques are explored under two different assumptions: constant and non-constant interfering LIF signal on the NO absorption spectrum. While the former is most often used in the literature, the latter is necessary when the LIF signal from interfering species cannot be distinguished from the NO-LIF signal, especially in high pressure conditions. Hence, a total of four techniques are presented in this work and are found to be in excellent agreement when performed in different flame conditions. The calibration techniques are applied to three lean, atmospheric, laminar, premixed, methane-air flames to explore their field of applicability. Specifically, the study explores the relevance of the techniques in reburn conditions, which

occur mostly in high pressure, rich, highly-seeded, or NH_3-containing flames. This study aims to offer the reader a portfolio of calibration techniques to use according to the conditions in which they need to be applied. While this study was carried out measuring NO concentration in a stagnation flame burner, the concepts and equations presented can be transposed to the measurement of other species and to other experimental configurations.

Nomenclature

Acronyms

BC	Boundary Condition
CRDS	Cavity Ring-Down Spectroscopy
CRECK	Chemical Reaction Engineering and Chemical Kinetics thermochemical model
DC	Dry-piston Calibrator
EET	Electronic Energy Transfer
GRI	Gas Research Institute thermochemical model
HWHM	Half-Width at Half-Maximum
LIF	Laser-Induced Fluorescence
LS	Logarithmic Sensitivity
MC	Monte-Carlo
MFC	Mass Flow Controller
PTV	Particle Tracking Velocimetry
RET	Rotational Energy Transfer
RMSE	Root Mean Square Error
RPA	Reaction Pathway Analysis
RSS	Root Square Sum
SD	San Diego thermochemical model
VET	Vibrational Energy Transfer

Greek Symbols

Γ	Overlap fraction	[-]
$\Delta\nu_{\mathrm{L}}$	Laser spectral linewidth	[cm^{-1}]
$\delta(\cdot)$	Total absolute uncertainty of quantity $(\cdot)$	[n/a]
$\delta_{\mathrm{rand}}(\cdot)$	Absolute random uncertainty of quantity $(\cdot)$	[n/a]
$\delta_{\mathrm{sys}}(\cdot)$	Absolute systematic uncertainty of quantity $(\cdot)$	[n/a]
$\epsilon(\cdot)$	Total relative uncertainty of quantity $(\cdot)$	[%]
$\epsilon_{\mathrm{rand}}(\cdot)$	Relative random uncertainty of quantity $(\cdot)$	[%]
$\epsilon_{\mathrm{sys}}(\cdot)$	Relative systematic uncertainty of quantity $(\cdot)$	[%]
λ	Wavelength	[nm]
ν	Frequency of light	[s^{-1}]
ν''	Vibrational level in the ground state	[-]
ν'	Vibrational level in the excited state	[-]
ρ_{in}	Density of the inlet mixture	[$\mathrm{kg{\cdot}m}^{-3}$]
τ_2	Average lifetime of the excited molecule in state 2	[s]
τ_{pulse}	Duration of the laser pulse	[s]
ϕ	Equivalence ratio	[-]
Ω	Collection solid angle	[sr]

Roman Symbols

A	Cross-section of the laser beam	[m^2]
A_{nozzle}	Cross-section of the burner nozzle	[m^2]
A_{ul}	Einstein rate constant of spontaneous emission from an upper state u to a lower state l	[s^{-1}]
B_{lu}	Einstein absorption coefficient from a lower state l to an upper state u	[$\mathrm{m}^2{\cdot}\mathrm{J}^{-1}{\cdot}\mathrm{s}^{-1}$]
c	Speed of light	[$\mathrm{m{\cdot}s}^{-1}$]
C_{bckgd}	Background coefficient	[-]
C_{lin}	Linear calibration coefficient	[$\mathrm{J}^{-1}{\cdot}\mathrm{ppm}^{-1}$]
C_{opt}	Optical calibration coefficient	[m]
$\mathrm{d}u_{\mathrm{in}}/\mathrm{d}z$	Inlet axial strain rate of the mixture	[s^{-1}]

E_{L}	Incident laser energy per pulse	[J]
$\mathcal{E}_{\mathrm{c}}$	Quantum efficiency of the camera	[count·photon^{-1}]
f_{B}	Boltzmann fraction	[-]
F_{bckgd}	Background LIF signal encompassing interfering LIF and laser-related noise, normalised by the laser energy	[J^{-1}]
F_{dark}	Signal from the camera dark noise, flame chemiluminescence, and ambient light, normalised by the laser energy	[J^{-1}]
$F_{\mathrm{fluo.}}$	Total fluorescence signal captured by the camera, normalised by the laser energy	[J^{-1}]
$F_{\mathrm{interf.\text{-}LIF}}$	Interfering LIF signal that does not originate from the excitation of the NO molecule, normalised by the laser energy	[J^{-1}]
f_{LIF}	LIF modelling parameter	[J·s^{-1}·m^{-1}]
$F_{\mathrm{NO\text{-}LIF}}$	Fluorescence signal of the laser-excited NO molecule, normalised by the laser energy	[J^{-1}]
$F_{\mathrm{NO\text{-}LIF,nsct}}$	Fluorescence signal of the laser-excited NO molecule, normalised by the laser energy, of an unseeded flame representative of the nascent (nsct) NO	[J^{-1}]
$F_{\mathrm{NO\text{-}LIF,nsct+sd}}$	Fluorescence signal of the laser-excited NO molecule, normalised by the laser energy, of a seeded flame representative of the nascent (nsct) and seeded (sd) NO	[J^{-1}]
$F_{\mathrm{NO\text{-}LIF,sd}}$	Fluorescence signal of the laser-excited NO molecule, normalised by the laser energy, of an unseeded flame subtracted off the signal of a seeded flame, representative of the seeded (sd) NO	[J^{-1}]
$g(\nu)$	Spectral lineshape function of the absorption transition	[s]
g_i	Degeneracy of state i	[-]
h	Planck's constant	[J·s]
I	Incident laser irradiance	[W·m^{-2}]
J''	Rotational number of the ground state	[-]
J'	Rotational number of the excited state	[-]
$L(\nu)$	Laser spectral distribution	[-]
$\mathcal{L}$	Length of the flame domain used for simulations	[mm]
ℓ	Length of laser path in the measurement volume	[m]
M	Target molecule in the ground state and in the excited state (superscript *)	[-]

$\dot{m}_g$	Mass flow rate of a gas g	[g·s^{-1}]
MW_g	Molar weight of gas g	[g·mol^{-1}]
$\mathcal{N}_\mathrm{A}$	Avogadro's number	[mol^{-1}]
n_i°	Number density of the molecule in each state i before laser excitation	[m^{-3}]
n_i	Number density of the molecule in each state i following laser excitation	[m^{-3}]
n_T°	Total number density of the molecule *M* in the measurement volume, prior to laser excitation	[m^{-3}]
$\dot{N}_s$	Molar flow rate of species s	[mol·s^{-1}]
p	Pressure	[Pa]
Q_{ul}	Rate constant of collisional quenching from an upper state u to a lower state l	[s^{-1}]
$\mathcal{R}_\mathrm{u}$	Universal gas constant	[J·mol^{-1}·K^{-1}]
R_{ul}	Rate of rotational energy transfer from a state u to a state l (reversible)	[s^{-1}]
S_BP	Fluorescence signal of a cold flow of NO captured by the camera at a given laser excitation wavelength	[count]
S_dark	Fluorescence signal of a flame captured by the camera without laser excitation	[count]
$S_\mathrm{fluo.}$	Fluorescence signal of a flame captured by the camera at a given laser excitation wavelength	[count]
$S_{M-\mathrm{LIF}}$	Fluorescence signal of the laser-excited molecule *M*	[count]
$\mathcal{S}_\mathrm{NO\text{-}LIF}$	Fluorescence signal of the laser-excited NO, modelled by LIFSim	[W]
$\mathcal{T}_\lambda$	Transmissivity of the optical system	[-]
T	Temperature	[K]
T_ad	Adiabatic flame temperature	[K]
T_in	Inlet temperature of the mixture	[K]
T_wall	Wall temperature of the stagnation plate	[K]
t	Student's distribution score	[-]
u_in	Inlet velocity of the mixture	[m·s^{-1}]
V_{ul}	Rate of vibrational energy transfer from a state u to a state l (reversible)	[s^{-1}]
W_{lu}	Rate constant of laser-induced stimulated absorption from a lower state l to an upper state u	[s^{-1}]
W_sat	Rate constant of the de-excitation of *M**	[s^{-1}]

W_{ul}	Rate constant of laser-induced stimulated emission from an upper state u to a lower state l	[s^{-1}]
$X_{\text{NO,nsct}}$	Molar fraction of nascent (nsct) NO in the flame	[ppm]
$X_{\text{NO,nsct+sd}}$	Total molar fraction of nascent (nsct) and seeded (sd) NO in the flame	[ppm]
$X_{\text{NO,sd}}$	Molar fraction of seeded (sd) NO in the flame	[ppm]
X_s	Molar fraction of species s	[-]
Y_s	Mass fraction of species s	[-]
$Y_{\text{NO,nsct}}$	Mass fraction of nascent (nsct) NO in the flame	[-]
$Y_{\text{NO,nsct+sd}}$	Total mass fraction of nascent (nsct) and seeded (sd) NO in the flame	[-]
$Y_{\text{NO,sd}}$	Mass fraction of seeded (sd) NO in the flame	[-]
z	Axial location in the flame domain	[mm]
z_{f}	Flame front position	[mm]
z_{in}	Inlet position of the unburnt mixture	[mm]

III.2 Introduction

At the heart of the current energy transition is the significant reduction in pollutant emissions, for which Nitric Oxide (NO) plays an important role [2]. Highly resolved and low uncertainty NO measurements are needed to develop state-of-the-art models to design energy systems that meet regulatory limits. Measurements have been performed for over a century and have greatly aided the development of combustion models for accurate NO predictions in practical conditions [3–5]. Many techniques have been employed to measure NO in a variety of combusting systems to meet the desired levels of accuracy and resolution, including probe measurements coupled to a gas analyser [6–9] or to a spectrometer [10, 11], broadband absorption spectroscopy [12–15], and, more recently and commonly, laser spectroscopy [16–23].

NO-Laser-Induced Fluorescence (NO-LIF) is a spectroscopy technique that offers *in-situ*, non-intrusive NO measurements with low uncertainty and high resolution down to sub-ppm levels [24]. It is performed by capturing the fluorescence emitted by the NO molecules as they transition from a laser-excited state to a lower-energy state. The light emitted is a function of the state of the molecules (density, temperature, pressure) in the given measurement volume. Thanks to this property, LIF can either be qualitative, *e.g.* the signal of a flame can be directly compared to another; or quantitative. The latter can be achieved through calibration [24–26], where prior knowledge

of quantum spectroscopy of the excited molecule may, or may not, be required depending on the selected technique. This work focuses on the quantitative measurement of NO using LIF.

Calibration techniques employed in the literature are revolving around two main strategies: the linear extrapolation from seeded to nascent (*i.e.* naturally produced) NO concentrations, and the calibration of the experimental optical setup using modelled LIF parameters. Their application differs in each study according to the flame conditions in which it is performed and the set of assumptions chosen by the authors. Nevertheless, a review of their span of applicability and the assessment of their accuracy is lacking. This study aims to compare both techniques on a sample set of data. Furthermore, both calibration techniques are usually applied by assuming a spectrally constant interfering LIF signal by species other than NO (O_2, CO_2, H_2O, etc), which is only valid at low-pressure conditions. A comparison of both calibration techniques is then performed accounting for the variation of the interfering LIF with the absorption wavelength, as used at high-pressure conditions. Hence, this study compares four techniques to obtain quantitative NO measurements. The intent of this work is not to provide an exhaustive list of NO-LIF calibration techniques, but rather to provide guidance on the applicability of the two main techniques for different experimental conditions and assumptions. The chosen calibration techniques consist of the most commonly used in the literature to obtain quantitative, highly-resolved, low-uncertainty NO measurements.

First, the LIF theory is presented to give context to the assumptions and equations developed in this work. This provides a basis for comparing different calibration techniques used in the literature for quantitative measurements. The experimental configurations and methods are then detailed to be used as a vehicle for the comparison of the calibration techniques presented in subsequent sections. These techniques are introduced by laying out their assumptions and equations. They are then compared using a comprehensive uncertainty analysis. Finally, the advantages and disadvantages of using each technique are summarised, such that this manuscript can be used as a guide for future measurements of NO, or other species concentration, using LIF for various experimental conditions.

III.3 Fundamentals of Laser-Induced Fluorescence

III.3.1 LIF theory

This section aims to provide a summary of LIF theory sufficient to support the assumptions and equations used in the calibration techniques described later in this manuscript. The reader is invited to consult several comprehensive reviews of LIF for a deeper understanding of the theory and the fundamentals: Daily [27], Kohse-Höinghaus [25], Eckbreth [24], Laurendeau [28], Hanson *et al.* [29], and Steinberg and Roy [26].

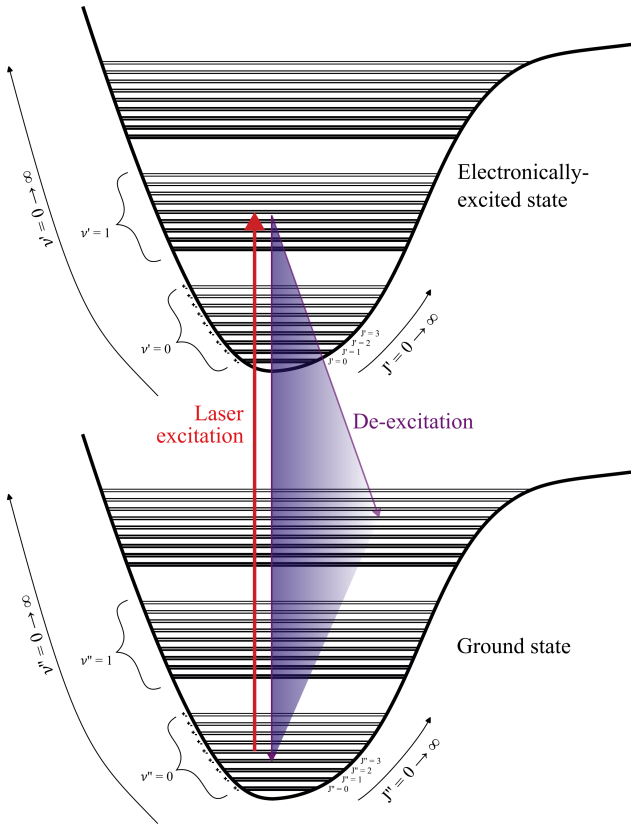

Figure III.1: Illustration of LIF process through the representation of two electronical systems, the ground state (superscript $''$) and the excited state (superscript $'$). For each electronical system, several vibrational bands (ν) represent the possible vibrational levels of the excited molecule. Each band is composed of multiple pairs of rotational lines (J). Each pair of rotational line holds a positive (+) and negative (-) parity representing the spin state of the molecule. While laser excitation targets a very specific transition, represented by the red upward arrow, de-excitation can occur to any allowed de-excited state. It is thus represented by a fan-shaped downward arrow.

LIF is a non-intrusive diagnostic technique capturing the fluorescence emitted by laser-excited molecules as they revert back to a lower-energy state, as illustrated in Fig. III.1. The fluorescence intensity of the molecules is directly correlated to the state of the target molecule in the measurement volume: density, temperature, and pressure. It also depends on other variables, such as the state of other species present in the measurement volume, the laser energy and efficiency to excite the molecule, and the detection system transmissivity and quantum efficiency, amongst others. Therefore, to translate a fluorescence signal into information about the state of the target molecule, LIF modelling is required. It predicts the rate at which different processes occur, responsible for populating and de-populating the different energy levels and, ultimately, how much fluorescence is generated. Two main processes are considered in this study: collisions and radiative transitions (W). The first process includes Rotational Energy Transfer (RET), Vibrational Energy Transfer (VET), and Electronic Energy Transfer (EET). The second encompasses the laser-

induced stimulated transitions and spontaneous emission. Note that in this study, pre-dissociation and photo-ionisation are neglected as typical energies used for NO-LIF are insufficient to trigger these processes [24, 26, 30–32]. Pre-dissociation refers to the phenomenon wherein the absorption of energy by a multi-atomic molecule results in its dissociation before photon emission occurs. Photo-ionisation denotes a process in which a change in the electronic configuration of a molecule (through the gain or loss of an electron) leads to a molecular ion with an emission spectrum distinct from the neutral molecule.

III.3.1.1 LIF signal modelling

LIF modelling can predict the transitions between different energy levels, where an energy level represents a possible state of the molecule. The simplest is the 2-level LIF model [24], often employed due to its simple and computationally-efficient description. In this approach, only transitions between the ground-state and a single electronically-excited energy level are considered. More complex models, such as a 3-level NO and O_2-LIF model developed by Bessler *et al.* [33], a 4-level CH-LIF model developed by Versailles [34], a 5-level NO-LIF model developed by Naik and Laurendeau [35], or a 6-level OH-LIF model developed by Verreycken *et al.* [36], consider additional ro-vibrational levels in the ground and electronically excited states, accessible through RET and VET, as well as spontaneous emission and quenching. These models allow more detailed and comprehensive descriptions of the technique with reduced assumptions as compared to the common 2-level LIF model, which is sufficient for most linear LIF configurations [26].

Figure III.2 represents the process that the laser-excited molecule undergoes within a 3-level LIF model. For simplicity, RET and VET have been depicted together ($R + V$), although they can occur independently. RET is generally the fastest of the possible energy transfers, and VET is often slower than RET, especially in the ground state [35, 37]. Both RET and VET processes force the molecular population towards a statistical Boltzmann distribution, also called thermalisation. RET, however, is generally negligible when using low laser energies (linear LIF) [35], even in high pressure conditions. Yet, RET has still been included in the following model to correspond to the assumptions made in the LIF modelling software, LIFSim [33], used later in the study.

The process under which LIF occurs in Fig. III.2 can be described as follows:

1. A narrow wavelength-tuned laser beam is used to excite a target molecule in the ground state (state 1) known to have a transition at the excitation wavelength. The target molecule, *M*, absorbs energy to the excited state 2. From state 1 to state 2, *M* gets excited through radiative transfer, changing its electronic state. The rate at which it occurs is noted W_{12}, the laser-induced stimulated absorption rate constant. The excited molecule, denoted by *M**, will remain in this state for a lifetime τ_2, on average.

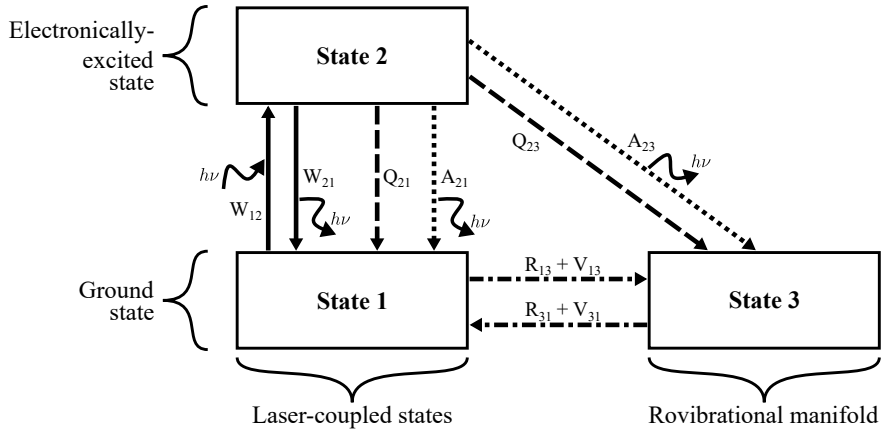

Figure III.2: Schematic of a 3-level LIF model. Arrows represent the possible changes of state of the molecule through: laser-induced stimulated absorption (W_{12}) and emission (W_{21}) represented by the solid arrows, collisional quenching (Q_{ul}) represented by the dashed arrows, spontaneous emission (A_{ul}) represented by the dotted arrows, and through ro-vibrational relaxation ($R_{ul} + V_{ul}$) represented by the dot-dashed arrows. RET, VET, and EET in the electronically-excited state are neglected.

2. Once in state 2, *M** either:
    - returns to its initial ground state 1 through:
        - radiative transfer driven by the rate constant of laser-induced stimulated emission (W_{21}), and by the rate constant of spontaneous emission (A_{21}); or
        - through collisions with other species at the rate constant of collisional quenching (Q_{21}); or
    - goes to a manifold ground state 3 through spontaneous emission (A_{23}) or collisional quenching (Q_{23}).
3. From state 3, the molecule can undergo ro-vibrational relaxation back to its initial ground state (R_{31}+V_{31}).

Any change of state must conform to the allowed transitions. Determining the allowed transitions requires a complex description and understanding of the different quantum numbers of the excited molecule at each state. This is usually done through the use of a LIF modelling software. Ultimately, the description of the population through the different levels, as discussed in this section, elucidates the different sources of fluorescence induced by the laser.

The total fluorescence emitted by the excited molecules is a summation of all fluorescence-emitting transfers (W_{21}, A_{21}, and A_{23}), weighted by the population density of each state (n_i). The latter is calculated according to the rates at which they are either populated or depopulated by the various processes (W, A, and Q). Each of these terms can be calculated independently in

order to correlate the total emitted fluorescence with the state of the pre-excited molecule in the measurement volume.

The population density of each state can be obtained through conservation equations:

$$\frac{\mathrm{d}n_1}{\mathrm{d}t} = -n_1\left(W_{12}+R_{13}+V_{13}\right)+n_2\left(W_{21}+Q_{21}+A_{21}\right)+n_3\left(R_{31}+V_{31}\right); \tag{III.1}$$

$$\frac{\mathrm{d}n_2}{\mathrm{d}t} = n_1 W_{12}-n_2\left(W_{21}+Q_{21}+A_{21}+Q_{23}+A_{23}\right); \tag{III.2}$$

$$\frac{\mathrm{d}n_3}{\mathrm{d}t} = n_1\left(R_{13}+V_{13}\right)+n_2\left(Q_{23}+A_{23}\right)-n_3\left(R_{31}+V_{31}\right). \tag{III.3}$$

The sum of these terms results in:

$$\frac{\mathrm{d}n_1}{\mathrm{d}t}+\frac{\mathrm{d}n_2}{\mathrm{d}t}+\frac{\mathrm{d}n_3}{\mathrm{d}t}=0; \tag{III.4}$$

hence,

$$n_1+n_2+n_3=n_{\mathrm{T}}^{\circ}=\text{constant}, \tag{III.5}$$

where n_{T}° is the total available population of the species of interest, ***M***, in the measurement volume prior to laser excitation (states 1 and 3).

The rate constant at which the molecule absorbs energy through laser-induced stimulated absorption (W_{12}) is described as follows:

$$W_{12}=\frac{B_{12}}{c}\cdot\frac{I}{\Delta\nu_{\mathrm{L}}}\cdot\Gamma, \tag{III.6}$$

where B_{12} is the Einstein absorption coefficient of the transition [$\mathrm{m^2{\cdot}J^{-1}{\cdot}s^{-1}}$], c is the speed of light [$\mathrm{m{\cdot}s^{-1}}$], I is the incident laser irradiance [$\mathrm{W{\cdot}m^{-2}}$], $\Delta\nu_{\mathrm{L}}$ is the laser spectral linewidth [$\mathrm{cm^{-1}}$], and Γ is the dimensionless overlap fraction. The incident laser irradiance is defined as:

$$I=\frac{E_{\mathrm{L}}}{A\cdot\tau_{\text{pulse}}}, \tag{III.7}$$

where E_{L} is the average laser energy per pulse [J], A is the laser sheet cross-section [$\mathrm{m^2}$], and τ_{pulse} is the laser pulse duration [s]. The dimensionless overlap fraction is defined following the formulation of Partridge and Laurendeau [38]:

$$\Gamma=\int_{\nu}L(\nu)\cdot g(\nu)d\nu, \tag{III.8}$$

where $L(\nu)$ is the dimensionless laser spectral distribution normalised such that $\int L d\nu = c \cdot \Delta\nu_{\mathrm{L}}$, and $g(\nu)$ is the spectral lineshape function of the absorption transition normalised such that $\int g d\nu = 1$. The overlap fraction is, therefore, a parameter dependent on the laser linewidth and the flame condition through p and T, which influence $g(\nu)$ through Doppler and collisional broadening.

The rate constant at which the excited molecule returns to the ground state through laser-induced stimulated emission (W_{21}) is directly proportional to W_{12} through the degeneracies (*i.e.* the number of states with the same energy level noted g_i) of their respective energy levels:

$$W_{21} = \frac{g_1}{g_2} \cdot W_{12} = \frac{2J'' + 1}{2J' + 1} \cdot W_{12}, \tag{III.9}$$

where J is the rotational number of the ground (superscript $''$) and excited (superscript $'$) energy level.

The Einstein rate constant of spontaneous emission (A_{ul}) of the molecule transitioning from an upper state (u) to a lower state (l) [s^{-1}] is obtained for each transition [33, 39]. Similarly, the collisional quenching rate constant (Q_{ul}) is obtained empirically for each species contained in the measurement volume.

III.3.1.2 Linear steady-state LIF model assuming extremely fast RET and VET

For NO-LIF measurements, linear LIF is typically employed as less energy is available to excite interfering species that could lead to background signal in the captured NO fluorescence [40]. It is also more difficult to reach complete saturation of the NO population, either spatially, temporally, or spectrally, especially in high pressure conditions [24]. For these reasons, the remaining of the study is conducted assuming the linear LIF regime.

In the linear LIF regime, the population in state 2 linearly increases with an increase of the laser irradiance, and is balanced by collisional quenching, the main driver of the lifetime of excited NO in state 2. When the de-excitation mechanisms are much faster ($\tau_2 \sim \frac{1}{\sum Q_{ul}}$) than the duration of the laser pulse (τ_{pulse}), steady-state can be assumed among the population densities [24, 41]. Thus, the rate of change in the population density n_i is nil ($\frac{\mathrm{d}n_i}{\mathrm{d}t} = 0$), and using Eq. (III.1−III.2) and Eq. (III.5), it leads to:

$$n_2 = n_{\mathrm{T}}^{\circ} \cdot \frac{\left[\frac{R_{31}+V_{31}}{W_{12}+R_{13}+V_{13}}\right]}{\left[1 + \frac{R_{31}+V_{31}}{W_{12}+R_{13}+V_{13}}\right] \cdot \left[\frac{W_{21}+Q_{21}+A_{21}+Q_{23}+A_{23}}{W_{12}}\right] - \left[\frac{W_{21}+Q_{21}+A_{21}-(R_{31}+V_{31})}{W_{12}+R_{13}+V_{13}}\right]}. \tag{III.10}$$

Additionally, prior to laser excitation, the population density in state 2 is assumed negligible ($n_2^\circ \sim 0$), such that Eq. (III.1) transforms to:

$$n_1^\circ \left(R_{13} + V_{13}\right) = n_3^\circ \left(R_{31} + V_{31}\right), \tag{III.11}$$

where n_1° and n_3° are calculated using the Boltzmann fraction (f_B) such that $n_1^\circ = f_\mathrm{B} \cdot n_\mathrm{T}^\circ$, and $n_3^\circ = (1 - f_\mathrm{B}) \cdot n_\mathrm{T}^\circ$:

$$\frac{n_1^\circ}{n_3^\circ} = \frac{R_{31} + V_{31}}{R_{13} + V_{13}} = \frac{f_\mathrm{B}}{1 - f_\mathrm{B}}. \tag{III.12}$$

Assuming extremely fast RET and VET between state 1 and 3, consistent with the modelling software LIFSim [33], R_{13}, V_{13}, R_{31}, and V_{31} are outweighing the other terms in Eq. (III.10), such that:

$$n_2 = f_\mathrm{B} \cdot n_\mathrm{T}^\circ \cdot \frac{W_{12}}{f_\mathrm{B} \cdot W_{12} + W_{21} + W_\mathrm{sat}}, \tag{III.13}$$

where $W_\mathrm{sat} = Q_{21} + A_{21} + Q_{23} + A_{23}$ represents the rate constant at which *M** gets de-excited, independently of the incident laser energy. Thus, the population density of state 2 is dependent on the rate of energy absorbed (W_{12}) by the target molecule at the initial laser-excitation state, and also on the rate at which the state is depleted to fill the other states.

Under the linear regime assumption, $W_\mathrm{sat} \gg (f_\mathrm{B} \cdot W_{12} + W_{21})$, simplifying Eq. (III.13) to:

$$n_2 = f_\mathrm{B} \cdot n_\mathrm{T}^\circ \cdot \frac{W_{12}}{W_\mathrm{sat}}. \tag{III.14}$$

As seen in Fig. III.2, the total fluorescence emitted, and possibly captured by the camera, results from the transitions from state 2 to state 1 (A_{21}) or to state 3 (A_{23}). For a 3-level LIF model, involving the steady-state assumption, the total LIF signal ($S_{M-\mathrm{LIF}}$), per pulse, results from the following equation:

$$S_{M-\mathrm{LIF}} = n_2 \left(A_{21} + A_{23}\right) \cdot \mathcal{E}_\mathrm{c} \mathcal{T}_\lambda \frac{\Omega}{4\pi} \ell A \cdot \tau_\mathrm{pulse}, \tag{III.15}$$

where three factors are distinguished: $n_2 \left(A_{21} + A_{23}\right)$ is the rate of photon emission per unit volume [photon·m^{-3}·s^{-1}], $\mathcal{E}_\mathrm{c} \mathcal{T}_\lambda \frac{\Omega}{4\pi} \ell A$ relates to the collection efficiency over the measurement volume [count·photon^{-1}·m^3], and τ_pulse is the laser pulse length [s] over which the camera integrates the signal. $\mathcal{E}_\mathrm{c}$ is the quantum efficiency of the camera [count·photon^{-1}], $\mathcal{T}_\lambda$ is the transmissivity of the optical system [-], Ω is the collection solid angle over which the fluorescence of *M** is captured by the detection system [sr], and ℓ is the length of the laser path through the measurement volume [m].

Thus, the total population density in the measurement volume prior to laser excitation (n_{T}°) can be recovered by measuring $S_{M-\mathrm{LIF}}$ [count] and re-arranging Eq. (III.14) and Eq. (III.15):

$$S_{M-\mathrm{LIF}} = f_{\mathrm{B}} \cdot n_{\mathrm{T}}^{\circ} \cdot \frac{W_{12}\left(A_{21}+A_{23}\right)}{W_{\mathrm{sat}}} \cdot \mathcal{E}_{\mathrm{c}} \mathcal{T}_{\lambda} \frac{\Omega}{4\pi} \ell A \cdot \tau_{\mathrm{pulse}}. \tag{III.16}$$

The concentration is used to calculate the molar fraction of the molecule in the volume through the ideal gas law:

$$n_{\mathrm{T}}^{\circ} = X_M \cdot \frac{p}{T \cdot \mathcal{R}_{\mathrm{u}}} \cdot \mathcal{N}_{\mathrm{A}}, \tag{III.17}$$

where n_{T}° is the total number density of *M* [m^{-3}], X_M is the molar fraction of *M* [-], p is the pressure [Pa], T is the temperature [K] in the measurement volume, $\mathcal{R}_{\mathrm{u}}$ is the universal gas constant [$\mathrm{J{\cdot}mol^{-1}{\cdot}K^{-1}}$], and $\mathcal{N}_{\mathrm{A}}$ is Avogadro's number [mol^{-1}].

III.3.1.3 Obtaining NO concentration from a 3-level linear steady-state LIF signal

For this study, NO concentration measurements are obtained by conducting NO-LIF in the linear regime and assuming steady-state, thus Eq. (III.16) develops to:

$$S_{\text{NO-LIF}} = X_{\mathrm{NO}} \cdot f_{\mathrm{B}} \cdot \frac{p}{T \cdot \mathcal{R}_{\mathrm{u}}} \cdot \mathcal{N}_{\mathrm{A}} \cdot \frac{B_{12}}{c} \cdot \frac{I}{\Delta\nu_{\mathrm{L}}} \cdot \Gamma \cdot \frac{\sum A_{ul}}{\sum Q_{ul} + \sum A_{ul}} \cdot \mathcal{E}_{\mathrm{c}} \mathcal{T}_{\lambda} \frac{\Omega}{4\pi} \ell A \cdot \tau_{\mathrm{pulse}}, \tag{III.18}$$

with $\sum A_{ul} = A_{21} + A_{23}$ and $\sum Q_{ul} = Q_{21} + Q_{23}$. Normalising $S_{\text{NO-LIF}}$ by the laser energy (linear LIF regime), the total fluorescence emitted per pulse by excited NO and captured by the detection system resolves to:

$$F_{\text{NO-LIF}} = S_{\text{NO-LIF}}/E_{\mathrm{L}}, \tag{III.19}$$

$$= X_{\mathrm{NO}} \cdot f_{\mathrm{B}} \cdot \frac{p}{T \cdot \mathcal{R}_{\mathrm{u}}} \cdot \mathcal{N}_{\mathrm{A}} \cdot \frac{B_{12}}{c} \cdot \frac{\Gamma}{\Delta\nu_{\mathrm{L}}} \cdot \frac{\sum A_{ul}}{\sum Q_{ul} + \sum A_{ul}} \cdot \mathcal{E}_{\mathrm{c}} \mathcal{T}_{\lambda} \frac{\Omega}{4\pi} \ell, \tag{III.20}$$

where $F_{\text{NO-LIF}}$ has the unit of [$\mathrm{count{\cdot}J^{-1}}$] or [$\mathrm{J}^{-1}$].

Ultimately, the total fluorescence measured by the detection system and normalised by the laser energy can be expressed as:

$$F_{\text{NO-LIF}} = X_{\mathrm{NO}} \cdot f_{\mathrm{LIF}}\left(\lambda, f_{\mathrm{B}}, p, T, B_{12}, \Delta\nu_L, \Gamma, A_{ul}, Q_{ul}\right) \cdot C_{\mathrm{opt}}\left(\mathcal{E}_{\mathrm{c}}, \mathcal{T}_{\lambda}, \Omega, \ell\right), \tag{III.21}$$

where X_{NO} is the molar fraction of NO in the measurement volume, f_{LIF} is a factor encompassing all absorption and emission parameters, and C_{opt} is the optical calibration constant regrouping all optical parameters [$\mathrm{count{\cdot}photon^{-1}{\cdot}m}$] or [m].

f_{LIF} can also be re-arranged according to the type of terms composing it:

$$f_{\text{LIF}} = \overbrace{\frac{p f_{\text{B}}}{T} \cdot \frac{1}{\sum Q_{ul}}}^{\text{flame-dependent}} \cdot \overbrace{\frac{\mathcal{N}_{\text{A}}}{c\mathcal{R}_{\text{u}}}}^{\text{constants}} \cdot \overbrace{\frac{1}{\Delta\nu_{\text{L}}}}^{\text{laser-dependent}} \cdot \overbrace{B_{12}\sum A_{ul}}^{\text{line-dependent}} \cdot \overbrace{\Gamma}^{\substack{\text{flame-}\\\text{laser-}\\\text{dependent}}}, \tag{III.22}$$

where $(\sum Q_{ul} + \sum A_{ul}) \sim \sum Q_{ul}$ as, generally, $\sum A_{ul} \ll \sum Q_{ul}$. Thus, for a setup that is kept untouched during an experimental campaign, only few parameters related to the flame condition impact $F_{\text{NO-LIF}}$.

In this study, for a given condition, X_{NO} is determined through the measurement of $F_{\text{NO-LIF}}$, and through the inference of $(f_{\text{LIF}} \cdot C_{\text{opt}})$ obtained *via* calibration. This forms the core of quantitative NO-LIF to which different techniques of calibration vary in the application of Eq. (III.21).

III.3.2 LIF calibration techniques and assumptions

In practical settings, LIF measurements must be performed by taking into consideration two experimental effects: background subtraction and reburn. Both of these effects are tackled in this work by employing different calibration techniques and assumptions, ultimately extending the applicability of LIF for quantitative NO measurement.

III.3.2.1 Background subtraction

In flames, the LIF fluorescence is the result of the excitation of, not only the NO molecules, but also other species present in the volume, typically O_2, CO_2, and H_2O. Thus, the captured fluorescence, $F_{\text{fluo.}}(\lambda)$, integrates the light emitted by NO-LIF ($F_{\text{NO-LIF}}(\lambda)$), the LIF interfering signal ($F_{\text{interf.-LIF}}(\lambda)$), and signal related to other light sources (F_{dark}), such as flame chemiluminescence, ambient light, and camera dark noise:

$$F_{\text{fluo.}}(\lambda) = F_{\text{NO-LIF}}(\lambda) + F_{\text{bckgd}}(\lambda), \tag{III.23}$$

$$= F_{\text{NO-LIF}}(\lambda) + F_{\text{interf.-LIF}}(\lambda) + F_{\text{dark}}. \tag{III.24}$$

To obtain the signal that is only dependent on NO excitation and, therefore, solely proportional to the NO concentration at the measurement location, the total fluorescence signal needs to be rid of any background signal ($F_{\text{bckgd}}(\lambda)$). While F_{dark} can easily be measured, $F_{\text{interf.-LIF}}(\lambda)$ usually needs to be inferred as its direct measurement is practically impossible.

Assumption of constant $F_{\text{interf.-LIF}}(\lambda)$ on the spectrum

Typically, $F_{\text{interf.-LIF}}(\lambda)$ is assumed constant for small changes in the excitation wavelength. This is generally valid at atmospheric conditions where NO lines can be easily isolated from O_2-LIF

or H_2O-LIF systems and where CO_2-LIF is a broadband faint background signal [42]. Thus, $F_{\text{interf.-LIF}}(\lambda)$ can be deducted using the measured fluorescence signal of the flame at two excitation wavelengths. These are chosen to correspond to an on-resonance peak of NO absorption (λ_{on}), and an off-resonance wavelength (λ_{off}). The subtraction of the signal $F_{\text{fluo.}}(\lambda)$ obtained at both wavelengths leads to $F_{\text{NO-LIF}}$ free from $F_{\text{bckgd}}(\lambda)$, as it is assumed that $F_{\text{interf.-LIF}}(\lambda_{\text{on}}) = F_{\text{interf.-LIF}}(\lambda_{\text{off}})$:

$$F_{\text{NO-LIF}} = F_{\text{fluo.}}(\lambda_{\text{on}}) - F_{\text{fluo.}}(\lambda_{\text{off}}) = F_{\text{NO-LIF}}(\lambda_{\text{on}}) - F_{\text{NO-LIF}}(\lambda_{\text{off}}), \tag{III.25}$$

where $F_{\text{NO-LIF}}(\lambda_{\text{off}}) \sim 0$.

Assumption of non-constant $F_{\text{interf.-LIF}}(\lambda)$ on the spectrum

When constant interfering LIF cannot be assumed, an alternative solution was proposed by Versailles *et al.* [23, 43]. They developed a strategy to calculate $F_{\text{interf.-LIF}}(\lambda)$ at high pressure conditions using the signal of a seeded (subscript 'nsct+sd') and unseeded (subscript 'nsct') flames[1]. By recognising that $F_{\text{interf.-LIF}}(\lambda)$ is the same in seeded and unseeded flames:

$$F_{\text{interf.-LIF}}(\lambda) = F_{\text{fluo.,nsct}}(\lambda) - F_{\text{dark}} - F_{\text{NO-LIF,nsct}}(\lambda), \text{ and} \tag{III.26}$$

$$= F_{\text{fluo.,nsct+sd}}(\lambda) - F_{\text{dark}} - F_{\text{NO-LIF,nsct+sd}}(\lambda), \tag{III.27}$$

where $F_{\text{NO-LIF,nsct}}(\lambda)$ and $F_{\text{NO-LIF,nsct+sd}}(\lambda)$ are *a priori* unknown, and defining $F_{\text{NO-LIF,sd}}(\lambda)$ as the difference of signal between seeded and unseeded flames, only proportional to the seeded concentration of NO:

$$F_{\text{NO-LIF,sd}}(\lambda) = F_{\text{NO-LIF,nsct+sd}}(\lambda) - F_{\text{NO-LIF,nsct}}(\lambda), \tag{III.28}$$

$$= F_{\text{fluo.,nsct+sd}}(\lambda) - F_{\text{fluo.,nsct}}(\lambda), \tag{III.29}$$

then, $F_{\text{interf.-LIF}}(\lambda)$ can be calculated:

$$F_{\text{interf.-LIF}}(\lambda) = F_{\text{fluo.,nsct+sd}}(\lambda) - F_{\text{dark}} - F_{\text{NO-LIF,sd}}(\lambda) \cdot C_{\text{bckgd}}, \tag{III.30}$$

where C_{bckgd}, the dimensionless background coefficient, is obtained by removing the NO spectral features from $F_{\text{interf.-LIF}}(\lambda)$ through a fitting procedure. Using this technique, $F_{\text{interf.-LIF}}(\lambda)$ is obtained assuming a spectrally non-constant interfering LIF signal, enabling the calculation of $F_{\text{NO-LIF}}$, free from $F_{\text{bckgd}}(\lambda)$:

$$F_{\text{NO-LIF}}(\lambda) = F_{\text{fluo.}}(\lambda) - F_{\text{dark}} - F_{\text{interf.-LIF}}(\lambda). \tag{III.31}$$

[1] These notations were defined to be representative of the source of NO in the flame, see nomenclature.

This method was used to obtain NO-LIF measurements at high pressure conditions [23, 43, 44].

III.3.2.2 Reburn

Both calibration techniques that are presented in the following section rely on seeding the flame with NO in order to obtain $(f_{\text{LIF}} \cdot C_{\text{opt}})$, or some terms of it, from Eq. (III.21). In this work, seeding is possible because NO is a stable molecule at ambient conditions. Despite its initially-stable state, NO can react through the flame, so called reburn, leading to a lower fluorescence signal than expected from what should be a constant concentration. This occurs when seeding is performed in large quantity [45], at rich and/or high pressure conditions, and in N-containing fuels such as NH_3. Conditions for NO reburn are explored in Appendix A.3.1.

As such, two calibration techniques are presented in this work: the linear extrapolation from seeded to nascent NO concentrations that cannot be applied in case of non-negligible reburn, and the optical calibration using experimental and modelled LIF parameters that can be applied in conditions of reburn or when the molecule cannot be seeded (such as CH, NH, or OH).

Assumption of negligible NO reburn

Under the assumption of negligible reburn, a calibration technique can be employed to avoid calculating $(f_{\text{LIF}} \cdot C_{\text{opt}})$ explicitly in order to obtain X_{NO} from $F_{\text{NO-LIF}}$ in Eq. (III.21).

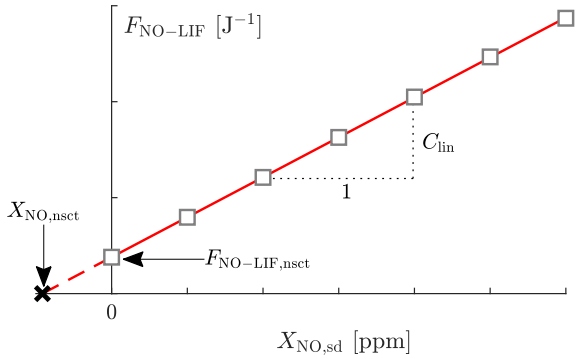

Figure III.3: Illustration of the linear extrapolation from seeded to nascent NO concentrations calibration technique. The extrapolation of the measured $F_{\text{NO-LIF}}$ with the different levels of NO seeding leads to the determination of C_{lin}, valid for a given flame condition and axial location in the domain.

The calibration technique *via* the linear extrapolation involves the seeding of the measurement volume with one, or several, levels of NO concentration, as demonstrated in Fig. III.3. This is possible by assuming that every term of Eq. (III.22) as well as C_{opt}, remain constant between the unseeded and seeded flames, at a given location, such that:

$$F_{\text{NO-LIF,nsct}} = X_{\text{NO,nsct}} \cdot f_{\text{LIF}} \cdot C_{\text{opt}}, \tag{III.32}$$

and,

$$F_{\text{NO-LIF,nsct+sd}} = X_{\text{NO,nsct+sd}} \cdot f_{\text{LIF}} \cdot C_{\text{opt}}, \tag{III.33}$$

where $X_{\text{NO,nsct}}$ is the nascent concentration of NO, *i.e.* the measurement of interest, and $X_{\text{NO,nsct+sd}}$ is the concentration of NO contained in flame after seeding, composed of the seeded NO in the initial mixture ($X_{\text{NO,sd}}$) and the nascent NO ($X_{\text{NO,nsct}}$). As such, the following applies:

$$F_{\text{NO-LIF,nsct}} = X_{\text{NO,nsct}} \cdot C_{\text{lin}}, \tag{III.34}$$

where C_{lin} is the linear coefficient between the LIF signal and the seeded NO level [$\text{J}^{-1}\cdot\text{ppm}^{-1}$]:

$$C_{\text{lin}} = f_{\text{LIF}} \cdot C_{\text{opt}} = \frac{F_{\text{NO-LIF,nsct+sd}} - F_{\text{NO-LIF,nsct}}}{X_{\text{NO,sd}}}, \tag{III.35}$$

and, ultimately, allows the calculation of $X_{\text{NO,nsct}}$.

If this technique was applied under NO reburn conditions, the actual $X_{\text{NO,sd}}$ would be lower than expected (see Fig. A.2 in Appendix), leading to a lower $F_{\text{NO-LIF,nsct+sd}}$ and C_{lin}. This would invalidate the linear extrapolation of $X_{\text{NO,nsct}}$.

This technique is valid in the three LIF regimes (linear, intermediate, saturated) and is one of the most commonly employed calibration techniques since it does not require any LIF modelling [17, 19, 21, 22, 46–49]. Nonetheless, care must be employed when performing such calculations as it is valid only if the composition and condition (pressure and temperature) are assumed constant between the seeded and unseeded flames; thus, it is only applicable in flames that are temporally-stable and at a single given location of the flame. To apply the calibration to other conditions, corrections must be applied between the calibration flame and the measured flame, accounting for the difference in the temperature, the Boltzmann fraction, and the collisional quenching rate, as seen through the flame-dependent terms of Eq. (III.22), and described by Watson *et al.* [48], Sahu and Ravikrishna [49], and Brackmann *et al.* [22]. By employing such corrections, this technique is ultimately similar to the one presented next, where f_{LIF} is modelled and C_{opt} calibrated.

Assumption of non-negligible NO reburn

Under the assumption of non-negligible NO reburn, or in cases where seeding of the target molecule is not possible, a technique is used to model the terms of f_{LIF} in Eq. (III.22) and to calibrate C_{opt} as its terms are difficult to model and measure. With this calibration technique, the experimental LIF signal is compared to a modelled one such that:

$$F^{\text{exp}}_{\text{NO-LIF}} = X^{\text{exp}}_{\text{NO}} \cdot f^{\text{exp}}_{\text{LIF}} \cdot C_{\text{opt}}, \tag{III.36}$$

and,

$$F^{\text{num}}_{\text{NO-LIF}} = X^{\text{num}}_{\text{NO}} \cdot f^{\text{num}}_{\text{LIF}}, \tag{III.37}$$

where a distinction is made between the terms obtained numerically (superscript 'num') and experimentally (superscript 'exp'). The determination of C_{opt} is done by fitting the experimental to the modelled LIF signal of a calibration flame with a known and finite concentration of seeded NO, under which assumptions of negligible NO reburn apply, such that:

$$F^{\text{num}}_{\text{NO-LIF,sd}} = \frac{F^{\text{exp}}_{\text{NO-LIF,sd}}}{C_{\text{opt}}}, \tag{III.38}$$

or,

$$C_{\text{opt}} = \frac{(F_{\text{NO-LIF,nsct+sd}} - F_{\text{NO-LIF,nsct}})^{\text{exp}}}{(F_{\text{NO-LIF,nsct+sd}} - F_{\text{NO-LIF,nsct}})^{\text{num}}} = \mathcal{E}_{\text{c}} \mathcal{T}_{\lambda} \frac{\Omega}{4\pi} \ell. \tag{III.39}$$

C_{opt} is independent of the calibration flame chosen as it only represents the experimental optical constants (see Appendix A.3.4). Once obtained, quantitative measurement of NO can be achieved by normalising the signal of the unseeded flame by C_{opt}, $F_{\text{NO-LIF,nsct}}/C_{\text{opt}}$, or by calculating $X_{\text{NO,nsct}}$ through the modelling of $f^{\text{exp}}_{\text{LIF}}$.

This calibration technique is, therefore, applicable to any other flame conditions, even if there is reburn of NO or if they are temporally-unstable, as long as the optical calibration coefficient is obtained in a flame without reburn, or in a flow that can be accurately modelled chemically. This considerably extends the applicability of LIF for quantitative NO measurements. It relies on the assumption that the parameters of $f^{\text{num}}_{\text{LIF}}$ are accurately captured by the numerical model in the calibration flame. This technique is also valid in the three LIF regimes as long as $f^{\text{num}}_{\text{LIF}}$ is modelled accordingly. While not always used under the same terminology, several studies use this exact technique [50–52], or a variant [22, 48, 49, 53].

The C_{opt} calibration technique is also applicable in conditions where the target molecule cannot be seeded. In this case, a surrogate molecule can be excited in place of the target molecule [54, 55], or the LIF measurement can be combined with another measurement technique, such as Rayleigh [34, 56–58] or Raman scattering [59, 60], to ultimately obtain C_{opt}. The Rayleigh and Raman calibration techniques rely on measuring the scattered signal of a stable molecule, such as N_2, He, or H_2, using the same experimental and optical setup than for the LIF signal measurement. The measured scattered signal is a function of the molecule cross-section and its number density, the laser parameters, and the calibration coefficient of the optical system (C_{opt}). Hence, C_{opt} can be obtained by modelling the other parameters and can then be integrated in the LIF model to obtain the absolute measurement of the short-lived species. An alternative consists of calculating the ratio of the LIF and scattering signals, leading to a fluorescence signal free of the optical calibration

coefficient [34]. The measurement of the Rayleigh or Raman scattering signals can, however, lead to experimental difficulties, specifically in handling laser reflections [26].

These techniques are important for the quantitative measurement of short-lived species, though they are less commonly employed. The specifics of these techniques are beyond the scope of this work, but can readily be applied from the general principles outlined in this study.

III.3.2.3 Scope of the study

This work specifically focuses on the two pairs of calibration techniques and background subtraction methods aforementioned as, combined, they represent the largest span of applicability for quantitative NO measurements. Therefore, this study aims to compare four techniques by presenting their experimental strategies, mathematics, and uncertainties: the extrapolation of seeded to nascent NO concentrations assuming constant and non-constant interfering LIF, and the optical calibration using experimental and modelled LIF parameters assuming constant and non-constant interfering LIF.

III.4 Experimental setup and methods

The comparison of the NO quantification techniques is conducted by collecting the LIF signal of several flames at varying experimental conditions, and processed using different methodologies to obtain the measurement of NO produced by the flames. This work presents measurements from flames obtained in a stagnation flame burner, however, LIF diagnostics are applicable to a variety of different flame setups thanks to its non-intrusive *in situ* nature, such as in porous burners [17, 19, 47], Bunsen burners [60], diffusion and premixed counter-flow burners [21, 35, 49, 61], shock tubes [62], jet flames [63], and Direct-Injection engines [46].

III.4.1 Stagnation flame burner

Premixed, laminar, quasi-1D, methane-air flames are produced using a water-cooled stagnation plate burner, as depicted by Fig. III.4a. It is placed inside a high-pressure enclosure with four windows for optical diagnostics. It is designed for gas turbine operating pressures, and has been used up to 16 atm [23, 43]. The fuel/oxidiser blend flows through a mixing tank to ensure homogeneity of the mixture. A co-flowing stream of inert gas is used to shield the flame from the surrounding gas. The flat, lifted, stagnation flame is stabilised between the nozzle and the plate, separated by a distance of ~ 9.5 mm. The stagnation plate is maintained at a constant temperature during the experiments using cooling water.

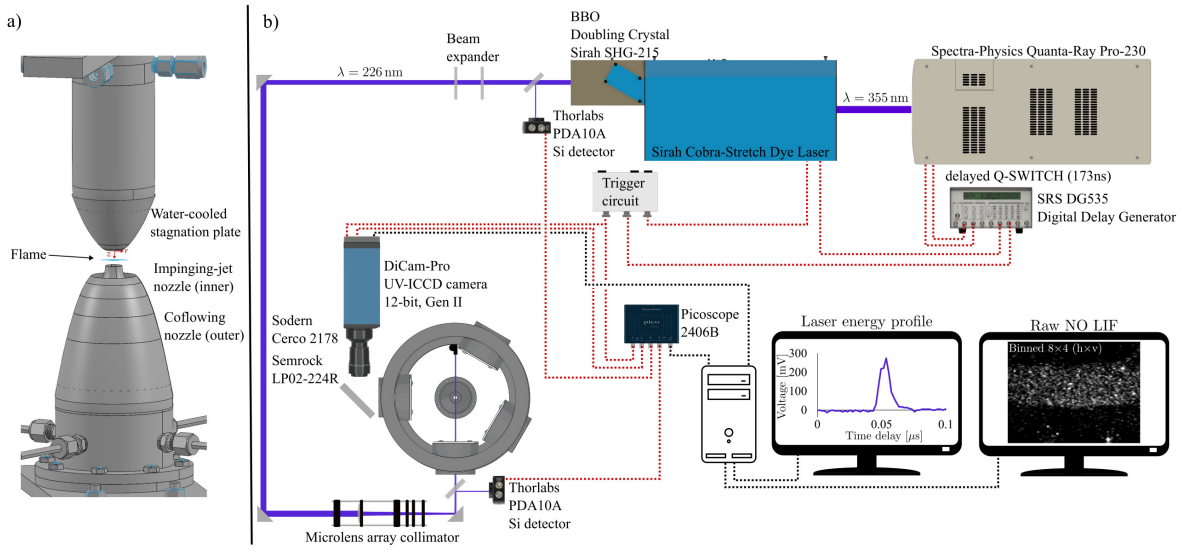

Figure III.4: Side view of the stagnation flame burner (a), top view of the laser and detection system setup for NO-LIF diagnostic (b).

In this study, three flames are produced, covering a variety of conditions described in Tab. III.1. They have been chosen to demonstrate the applicability of the calibration techniques at varying equivalence ratios and through a wide range of adiabatic flame temperatures. To reach a high adiabatic flame temperature (Phi0.9_Tad2500K_O40), oxygen-enriched air is used in combination with argon dilution in the oxidiser stream for improved flame stability. To perform NO-LIF calibration, each flame is also seeded with NO at several concentrations. The notation presented in Tab. III.1 is defined as:

$$X_{\mathrm{O_2}} = \frac{\dot{N}_{\mathrm{O_2}}}{\dot{N}_{\mathrm{O_2}} + \dot{N}_{\mathrm{N_2}}}, \tag{III.40}$$

$$X_{\mathrm{Ar}} = \frac{\dot{N}_{\mathrm{Ar}}}{\dot{N}_{\mathrm{O_2}} + \dot{N}_{\mathrm{N_2}} + \dot{N}_{\mathrm{Ar}}}, \tag{III.41}$$

$$X_{\mathrm{NO,sd}} = \frac{\dot{N}_{\mathrm{NO,sd}}}{\dot{N}_{\mathrm{total}}} = \frac{\dot{N}_{\mathrm{NO,sd}}}{\dot{N}_{\mathrm{CH_4}} + \dot{N}_{\mathrm{O_2}} + \dot{N}_{\mathrm{N_2}} + \dot{N}_{\mathrm{Ar}} + \dot{N}_{\mathrm{NO,sd}}}, \tag{III.42}$$

where $\dot{N}_s$ is the molar flow rate of species s [mol·s^{-1}], $X_{\mathrm{O_2}}$ is the oxygen molar fraction of the oxidiser mixture, X_{Ar} is the argon dilution in the diluted-oxidising mixture, and $X_{\mathrm{NO,sd}}$ is the NO mole fraction of seeded NO in the premixed flow.

The different gas flow rates are controlled using a series of thermal Mass Flow Controllers (MFCs, Bronkhorst El-Select). They are calibrated before the measurement campaign using their respective gas with a dry-piston calibrator (DryCal ML-500), yielding an uncertainty of $\pm 0.4\%$ on the flow rate of each MFC. NO is seeded in the mixture from gas cylinders containing 247 ppm $\pm$ 2%

Table III.1: Flame conditions used in this study.

Flame nomenclature	Fuel species	ϕ [-]	T_{ad} [K]	p [atm]	$X_{\mathrm{O_2}}$ [-]	X_{Ar} [-]	$X_{\mathrm{NO,sd}}$ [ppm]	Experimental samples Constant $F_{\text{interf.-LIF}}$	Non-constant $F_{\text{interf.-LIF}}$
Phi0.9_Tad2130K_O21	CH_4	0.9	2130	1	0.21	0.0000	0	6	4
							25	3	2
							50	4	2
							75	5	2
Phi0.7_Tad1830K_O21	CH_4	0.7	1830	1	0.21	0.0000	0	2	-
							50	2	-
Phi0.9_Tad2500K_O40	CH_4	0.9	2500	1	0.40	0.3085	0	2	-
							150	2	-

of NO in N_2 for the undiluted flames, and 2965 ppm $\pm$ 2% of NO in Ar for the Ar-diluted flames. The NO gas mixture is further diluted to the desired seeding concentration using additional bath gas. In the case of non-diluted flames (Phi0.9_Tad2130K_O21 and Phi0.7_Tad1830K_O21), enriched oxygen is used to compensate for the extra dilution of N_2 due to the seeding of NO, ensuring a final 3.76:1 ratio of N_2 to O_2 in the oxidiser stream.

Boundary conditions needed to perform simulations are acquired during the experiments with Particle Tracking Velocimetry (PTV) [34, 41, 64, 65]. Type-K thermocouples are used to measure the inlet temperature of the mixture (T_{in}) and the stagnation plate temperature (T_{wall}) within $\pm$ 2 K and $\pm$ 5 K, respectively. The length of the domain used for the simulations $(\mathcal{L})$ is determined at the location of minimum uncertainty of the velocity, in the unburnt region, which is where the inlet velocity (u_{in}) and the axial strain rate $(\mathrm{d}u_{\text{in}}/\mathrm{d}z)$ are extracted. The boundary conditions for each flame and their respective uncertainties are presented in Appendix A.1.

III.4.2 Laser and detection system

Figure III.4b presents the hardware setup to obtain NO-LIF data. Light is emitted by a pulsed Nd:YAG laser (Spectra-Physics Quanta-Ray Pro-230) using the third harmonic at 355 nm. Short and energetic pulses are achieved by delaying the Q-switch by 173 ns using a delay generator (SRS DG535). The laser beam passes through a wavelength-tunable dye laser (Sirah Cobra-Stretch) containing a Coumarin 450/methanol dye solution, and through a frequency-doubling crystal (Sirah BBO SGH-215). The resulting laser beam can be tuned to a wavelength of $\sim$ 226 nm with a pulse duration of $\sim$10.5 ns at a repetition rate of 10 Hz. A series of lenses shape the beam into a thin sheet ($\sim$ 9 mm tall and $\sim$ 1 mm wide) focused above the centre of the burner. A micro-lens array system is also used to ensure beam homogeneity [66]. The laser beam is used to excite the A$-$X $(0,0)$ electronic system of NO at different wavelengths around 226 nm (see theoretical excitation spectrum in Fig. III.5). This spectral region was chosen, following the recommendation of

Di Rosa [67] and Bessler *et al.* [42, 68], to minimise the impact of interfering LIF signal and to maintain a strong LIF signal with an increasing temperature of the mixture.

The wavelength of the laser is monitored several times per day to ensure that the laser beam is produced at the desired wavelength. This is done by comparing a theoretical excitation spectrum to one obtained experimentally. The experimental spectrum is obtained by varying the wavelength of the dye laser from ~ 226.00 nm to ~ 226.06 nm and capturing the LIF signal of a cold flow of constant NO concentration. The resulting comparison is presented in Fig. III.5.

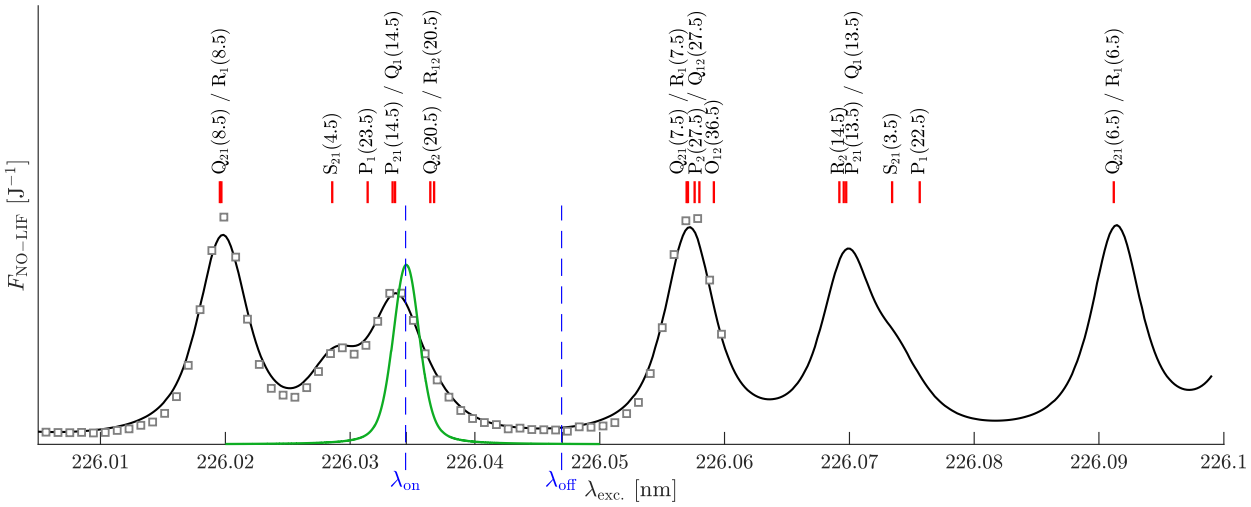

Figure III.5: NO excitation spectrum obtained experimentally (squares) and with LIFSim (black curve) at a temperature of 300 K. The NO transition lines positions and labels are also specified. The nomenclature of each NO transition is specific to the quantum features of the transition. The position of the online (λ_{on}) and offline (λ_{off}) excitation wavelengths, used experimentally, is also shown (blue dashed lines). The laser lineshape, inferred experimentally, is displayed *via* the green curve, centred around λ_{on}.

This routine procedure also permits to obtain the laser beam profile, often not perfectly homogeneous when resulting from a dye laser, to correct the signal for any spatial fluctuation. An example of such inhomogenity is depicted later in this paper (see Fig. III.6).

The emitted fluorescence from excited NO molecules is captured by a UV-Intensified CCD camera (DiCam-Pro 12-bit, Gen II). The ICCD camera records the LIF signal at 90° from the laser sheet. It is equipped with extension tubes and an UV achromatic lens (Sodern Cerco 2178), yielding a resolution of 26.3 ± 0.1 μm/pix. The camera is also equipped with a 235 nm long-pass filter to remove Rayleigh scattering and reflections. The image is binned 4×8 (vertically and horizontally, respectively) to enhance the signal-to-noise ratio. Finally, a gating of 300 ns is used to capture the entirety of the fluorescence emitted and reduce the contribution from the flame chemiluminescence.

Two photo-diodes (Thorlabs PDA10A), each coupled to a 90:10 beamsplitter, monitor the laser energy and pulse duration along the optical path and allow the assessment of the shot-to-shot

change in laser energy used for the normalisation of the experimental LIF signal. As it is impossible to measure the absolute laser energy at the location of the flame, a measurement of the laser energy is obtained $\sim$30 cm upstream of the flame and is assumed proportional to the energy irradiating the NO molecules. An absolute measurement of the laser energy prior to each measurement is performed at the exit of the dye laser ($\sim$300 cm upstream of the flame) and leads to $\sim$0.7 mJ/pulse spread on an unfocused sheet of $\sim$1 mm width by $\sim$9 mm height. Additionally, linearity was verified by comparing experimentally-obtained spectra with theoretical linear spectra obtained from LIFSim [33], as seen in Fig. III.5. It was also confirmed that the response of the signal for a given concentration of NO in a cold flow is linear with a change in the laser energy. The camera and photo-diodes are triggered synchronously with the dye laser gating with each signal collected using a 1 GHz sampling rate oscilloscope (Picoscope 2406B).

The acquired data results in a set of 2D fluorescence images ($S_{\text{fluo.}}(\lambda)$) with their associated shot-to-shot laser energy ($E_{\text{L}}(\lambda)$). The signal of each image is averaged along the centre-line of the burner and is normalised by the average laser energy leading to a signal, $F_{\text{fluo.}}(\lambda)$, composed of $F_{\text{NO-LIF}}(\lambda)$, $F_{\text{interf.-LIF}}(\lambda)$, and F_{dark}, as seen in Eq. (III.24).

For each calibration technique presented, strategies must be employed to: 1) rid the signal $F_{\text{fluo.}}(\lambda)$ from any background signal $F_{\text{bckgd}}(\lambda)$ to obtain $F_{\text{NO-LIF}}(\lambda)$; and 2) relate $F_{\text{NO-LIF}}(\lambda)$ to the concentration or molar fraction of NO to solve Eq. (III.21).

III.5 NO-LIF calibration techniques

This section presents four techniques to transform $F_{\text{fluo.}}(\lambda)$ into quantitative NO measurements. Two calibration methodologies are employed: the linear extrapolation from seeded to nascent NO concentration (C_{lin}) and the optical calibration using experimental and modelled LIF parameters (C_{opt}). Both techniques are used under two background subtraction methods, assuming spectrally constant and non-constant interfering LIF signal. They differ in the way that $F_{\text{NO-LIF}}(\lambda)$ is calculated. The four techniques are presented and compared using the sample data obtained as described in the previous section.

III.5.1 Calculation of $F_{\text{NO-LIF}}(\lambda)$ using $F_{\text{fluo.}}(\lambda)$

The experimental methodology to measure $F_{\text{fluo.}}(\lambda)$ differs according to the assumption formulated about $F_{\text{interf.-LIF}}(\lambda)$. This leads to a different calculation of $F_{\text{NO-LIF}}(\lambda)$.

III.5.1.1 Assumption of constant $F_{\text{interf.-LIF}}(\lambda)$ on the spectrum

As presented in Section III.3.2.1, the interfering LIF signal can be assumed constant under low pressure conditions, up to 4 atm [23]. In such conditions, the contribution of $F_{\text{interf.-LIF}}(\lambda)$ can be removed from $F_{\text{fluo.}}(\lambda)$ by subtracting the signal of an off-resonance absorption from an on-resonance absorption signal, as recalled from Eq. (III.25).

The axially-resolved signal produced within the measurement volume ($F_{\text{fluo.}}(\lambda)$) is obtained by averaging the LIF signal of 5,000 images at two wavelengths, indicated in Fig. III.5. An online signal ($S_{\text{fluo.,on}}$) is captured at a wavelength $\lambda_{\text{on}} = 226.0345$ nm corresponding to a peak in absorption of the NO molecules comprising the $P_1(23.5)$, Q_1+$P_{21}(14.5)$, and Q_2+$P_{12}(20.5)$ lines. Additionally, an offline signal ($S_{\text{fluo.,off}}$) is captured at a wavelength $\lambda_{\text{off}} = 226.0470$ nm corresponding to a minimum in absorption. The signal of the flame without laser illumination (S_{dark}) is also captured (1,000 images) to obtain the flame chemiluminescence, ambient light, and camera dark noise signals. Finally, the laser beam profile is obtained (S_{BP}) in a cold flow of NO (1,600 images) and is used to correct the signal for spatial inhomogeneity in the laser sheet.

The background signal is subtracted from the online and offline signals, and these are normalised by their corresponding laser energies ($E_{\text{L,on}}$ and $E_{\text{L,off}}$). The offline fluorescence is used to remove the contribution from any interfering LIF signals from the online fluorescence. The subtraction of the two signals is normalised by the laser beam profile (S_{BP}, normalised such that $\int S_{\text{BP}} \mathrm{d}z = 1$), and results in a signal ($F_{\text{NO-LIF}}$) that is only proportional to the NO concentration in the measurement volume. These operations are conducted as follows:

$$F_{\text{NO-LIF}} = (F_{\text{fluo.}}(\lambda_{\text{on}}) - F_{\text{dark}}) - (F_{\text{fluo.}}(\lambda_{\text{off}}) - F_{\text{dark}}), \tag{III.43}$$

$$= \left[\frac{(S_{\text{fluo.,on}} - S_{\text{dark}})}{E_{\text{L,on}}} - \frac{(S_{\text{fluo.,off}} - S_{\text{dark}})}{E_{\text{L,off}}} \right] \cdot \frac{1}{S_{\text{BP}}}. \tag{III.44}$$

Each step of the LIF processing is presented in Fig. III.6. A sample image is presented on the left-hand side of the figure, along with its extracted signal profile on the right-hand side. Each profile is extracted at the centre line of the nozzle (r_0) and averaged radially from $r_0 - \Delta r$ to $r_0 + \Delta r$, representing a band of $\sim$4.2 mm. Figure III.6a presents the laser beam profile in a cold flow of NO. In the profile, the laser inhomogeneity can clearly be distinguished. Despite the use of a micro-lens array [66], fluctuations in the laser energy occur throughout the domain. Slight laser reflections on the stagnation plate ($z = 0$ mm) and on the nozzle ($z = 9.5$ mm) can also be seen in the image and on the profile. Figure III.6b presents the LIF signal obtained at the online wavelength in an unseeded flame. The signal is nil in the cold unburnt region of the flow as the flow is not seeded with NO, and naturally, does not produce NO. In the flame front, the signal is stronger due to flame chemiluminescence. This leads to background in the signal that needs to be accounted for. The

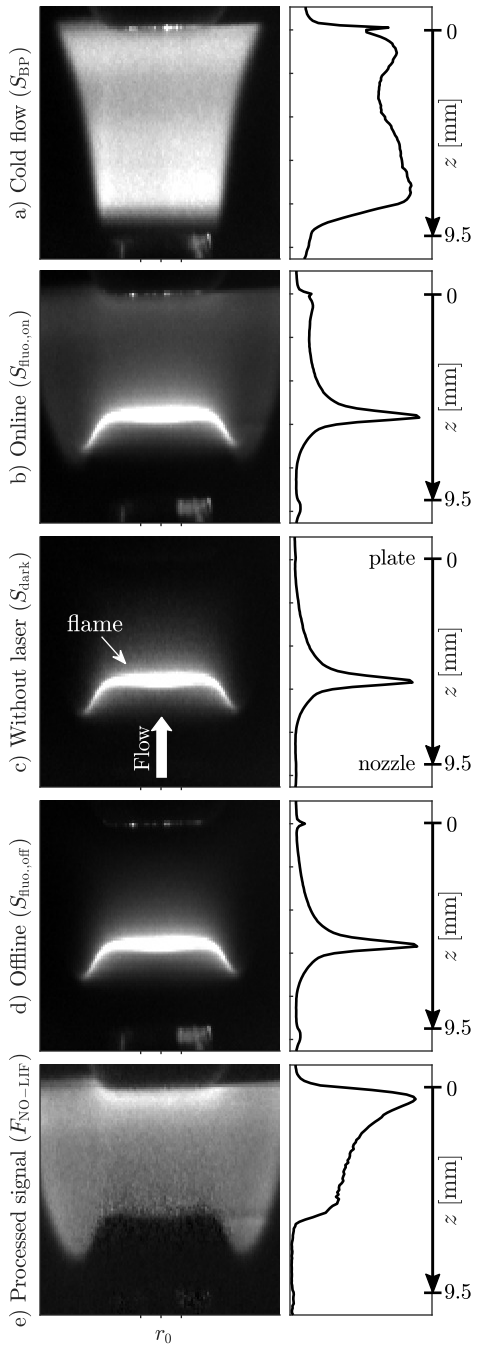

Figure III.6: LIF signal obtained at several steps of the experimental process: a) in a cold flow of NO; and b-e) in the unseeded Phi0.9_Tad2130K_O21 flame.

signal in the post-flame region is mostly produced by the NO naturally formed by the flame. The signal seems to decrease in the post-flame region, opposite to what is expected from the formation of NO in the post-flame region through the thermal-NO pathway. This artificial effect is due to the laser spatial inhomogeneity and background signal discussed previously, and hence, requires the signal to be corrected for it. Figure III.6c depicts the image obtained without laser illumination to

obtain the dark signal, encompassing the flame chemiluminescence, camera dark noise, and ambient light. This signal is later removed from the online and offline profiles. Figure III.6d shows the image obtained at the offline wavelength. Despite production of NO in the post-flame region, the signal cannot be clearly distinguished because the offline excitation wavelength represents a minimal absorption of the NO molecules, as seen in Fig. III.5. The flame chemiluminescence, and the laser reflections on the plate and nozzle can still be seen in the image and profile. Finally, Fig. III.6e presents the processed signal following the methodology described below and in Eq. III.44. The resulting signal is rid of laser inhomogeneity, flame chemiluminescence, camera dark noise, reflections, and ambient light. The signal sharply increases through the flame front, followed by a slower increase through the post-flame region. The increase of the signal near the plate is due to the thermal boundary layer of the cold plate, increasing the LIF signal despite no production of NO in this region.

III.5.1.2 Assumption of non-constant $F_{\text{interf.-LIF}}(\lambda)$ on the spectrum

In conditions where the interfering LIF signal cannot be assumed constant, as discussed in Section III.3.2.1, another experimental methodology needs to be employed to infer $F_{\text{interf.-LIF}}(\lambda)$ without its direct measurement. In such conditions, $F_{\text{interf.-LIF}}(\lambda)$ is determined by measuring the signal of a seeded and an unseeded flame at varying excitation wavelengths.

The signal produced within the measurement volume ($F_{\text{fluo.}}(\lambda)$) is calculated using the average of the captured signals of 120 laser pulses at 80 different excitation wavelengths from ~ 226.006 nm to ~ 226.116 nm, in steps of 1.4 pm. The resulting signal is axially- and spectrally-resolved. Similar to the previous experimental technique, S_{dark} and S_{BP} are captured to rid the signal of flame chemiluminescence, camera dark noise, ambient light, and the laser sheet spatial inhomogeneity, as per the subsequent equations:

$$F_{\text{NO-LIF}}(\lambda) = (F_{\text{fluo.}}(\lambda) - F_{\text{dark}}) - F_{\text{interf.-LIF}}(\lambda), \tag{III.45}$$

$$= \left[\frac{(S_{\text{fluo.}}(\lambda) - S_{\text{dark}})}{E_{\text{L}}(\lambda)}\right] \cdot \frac{1}{S_{\text{BP}}} - F_{\text{interf.-LIF}}(\lambda). \tag{III.46}$$

Following Eq. (III.46), $F_{\text{interf.-LIF}}(\lambda)$ needs to be inferred in order to obtain $F_{\text{NO-LIF}}(\lambda)$.

The measurements are carried out in a seeded and unseeded flame, and examples of images captured during the process are shown in Fig. III.7. Selected images of the excitation spectrum in a flame seeded with 50 ppm of NO are displayed on the top row of Fig. III.7. They represent either an on-resonance (Fig. III.7a, b, and d), or an off-resonance excitation (Fig. III.7c and e). The associated excitation spectrum, $S_{\text{fluo.,nsct+sd}}(\lambda)$ extracted at $z = 3$ mm, is plotted in red in the middle of the figure. Similarly, images captured in the unseeded flame are displayed on the bottom

row of the figure. Its associated excitation spectrum, $S_{\text{fluo.,nsct}}(\lambda)$ also extracted at $z = 3\,\text{mm}$, is plotted in blue in the middle of the figure. The wavelengths at which the images were extracted are indicated by the dashed lines. The brightness of the images was kept constant with wavelength for qualitative comparison. Naturally, the signal is stronger in the cold seeded region of the flame on an on-resonance wavelength due to the increased number density and the reduced quenching rate. For a given wavelength, on or off-resonance, the signal is also stronger in the seeded flame than it is in the unseeded flame due to the increased concentration of NO. The signal remains to be corrected for the background signal (especially flame chemiluminescence) and the laser inhomogeneity, as described in Eq. (III.46).

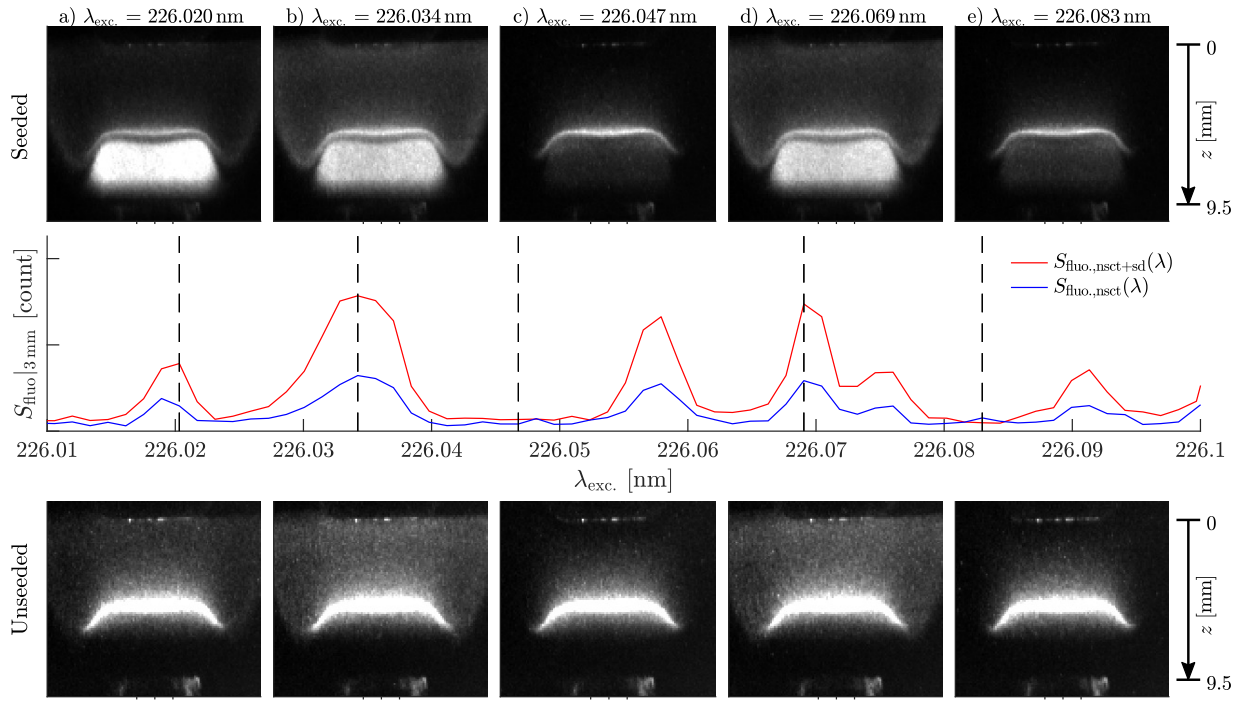

Figure III.7: LIF signal obtained at several excitation wavelengths during the experimental process in the seeded (top) and unseeded (bottom) Phi0.9_Tad2130K_O21 flame. The fluorescence signal ($S_{\text{fluo.}}(\lambda)$), extracted at $z = 3\,\text{mm}$, is plotted for both flames in the centre of the figure. The dashed lines represent the excitation wavelength at which each image was extracted. Note that the brightness of the images from the unseeded flame are enhanced compared to those from the seeded flame.

The interfering LIF signal is determined by eliminating any contribution from the NO lines on a seeded NO-LIF spectrum. Following the previous logic described in Eq. (III.24), the fluorescence signal of the flame is rid of its dark signal, such that for a seeded flame, the following equation is obtained:

$$F_{\text{fluo.,nsct+sd}}(\lambda) - F_{\text{dark}} = F_{\text{NO-LIF,nsct+sd}}(\lambda) + F_{\text{interf.-LIF}}(\lambda), \tag{III.47}$$

and by defining:

$$F_{\text{NO-LIF,sd}}(\lambda) = F_{\text{NO-LIF,nsct+sd}}(\lambda) - F_{\text{NO-LIF,nsct}}(\lambda), \tag{III.48}$$

the following relationships apply:

$$F_{\text{fluo.,nsct+sd}}(\lambda) - F_{\text{dark}} = F_{\text{NO-LIF,sd}}(\lambda) + F_{\text{NO-LIF,nsct}}(\lambda) + F_{\text{interf.-LIF}}(\lambda), \tag{III.49}$$

$$= F_{\text{NO-LIF,sd}}(\lambda) \cdot \left[1 + \frac{F_{\text{NO-LIF,nsct}}(\lambda)}{F_{\text{NO-LIF,sd}}(\lambda)}\right] + F_{\text{interf.-LIF}}(\lambda), \tag{III.50}$$

$$= F_{\text{NO-LIF,sd}}(\lambda) \cdot C_{\text{bckgd}} + F_{\text{interf.-LIF}}(\lambda), \tag{III.51}$$

where C_{bckgd} represents a scaling coefficient between the interfering LIF signal and the signal of a known concentration of NO, necessary for the calculation of the total seeded fluorescence signal, with:

$$C_{\text{bckgd}} = 1 + \frac{F_{\text{NO-LIF,nsct}}(\lambda)}{F_{\text{NO-LIF,sd}}(\lambda)}. \tag{III.52}$$

The coefficient is not wavelength-dependent due to the division of the two wavelength-dependent signals, that spectrally scale uniformly with NO concentration.

To obtain C_{bckgd}, Eq. (III.52) cannot be used as $F_{\text{NO-LIF,nsct}}(\lambda)$ is unknown without the prior knowledge of $F_{\text{interf.-LIF}}(\lambda)$. Instead, C_{bckgd} is obtained through Eq. (III.51) by fitting $F_{\text{interf.-LIF}}(\lambda)$ on measured profiles as follows:

$$F_{\text{interf.-LIF}}(\lambda) = (F_{\text{fluo.,nsct+sd}}(\lambda) - F_{\text{dark}}) - F_{\text{NO-LIF,sd}}(\lambda) \cdot C_{\text{bckgd}}, \tag{III.53}$$

where $F_{\text{NO-LIF,sd}}(\lambda)$ is obtained by subtracting the signal of an unseeded flame from a seeded flame. This applies if the NO seeding is assumed to not change the concentration of interfering species and therefore remains constant for a given wavelength (see Appendix A.3.2). The determination of C_{bckgd} is performed by iterative least-squares minimisation of the difference between the calculated $F_{\text{interf.-LIF}}(\lambda)$ and a filtered (smoothed) version of itself, using Eq. (III.53) to remove any NO spectral features from $F_{\text{interf.-LIF}}(\lambda)$. The filtering of $F_{\text{interf.-LIF}}(\lambda)$ removes the effect of experimental noise.

This process is demonstrated in Fig. III.8 for a given axial location of a flame. In Fig. III.8a, each term of Eq. (III.53) is presented, including the final calculated interfering LIF spectrum, obtained after the iteration process of C_{bckgd}. Figure III.8b-d presents the iteration process of C_{bckgd}, where $F_{\text{interf.-LIF}}(\lambda)$ is plotted with its smoothed counterpart for different values of C_{bckgd}.

The iteration of C_{bckgd} is performed to obtain $F_{\text{interf.-LIF}}(\lambda)$ under three constraints:

1. $F_{\text{interf.-LIF}}(\lambda)$ must not contain NO features;

2. $F_{\text{interf.-LIF}}(\lambda)|_{\text{smoothed}}$ must be non-negative, as a negative signal is non-physical; and

3. C_{bckgd} must minimise the least-square difference between $F_{\text{interf.-LIF}}(\lambda)$ and $F_{\text{interf.-LIF}}(\lambda)|_{\text{smoothed}}$.

In the event that C_{bckgd} is too small (Fig. III.8b), $F_{\text{interf.-LIF}}(\lambda)$ still displays contributions of the NO-lines captured in the peaks of the grey curve aligning with the peaks present in the red, blue, and black curves of Fig. III.8a. In the event that C_{bckgd} is too large (Fig. III.8c), $F_{\text{interf.-LIF}}(\lambda)|_{\text{smoothed}}$ becomes negative and is, thus, a non-physical solution showing negative NO-LIF features. The appropriately fitted $F_{\text{interf.-LIF}}(\lambda)$ is displayed in Fig. III.8d where negative values in the grey curve are limited to experimental noise, and where NO features cannot be clearly distinguished.

As the sample data was collected at atmospheric conditions, Fig. III.8a validates the assumption of a nearly constant interfering LIF signal between the online (λ_{on}) and offline (λ_{off}) wavelengths. Hence, the previous experimental methodology assuming constant interfering LIF signal is demonstrated valid in these conditions, as per [23].

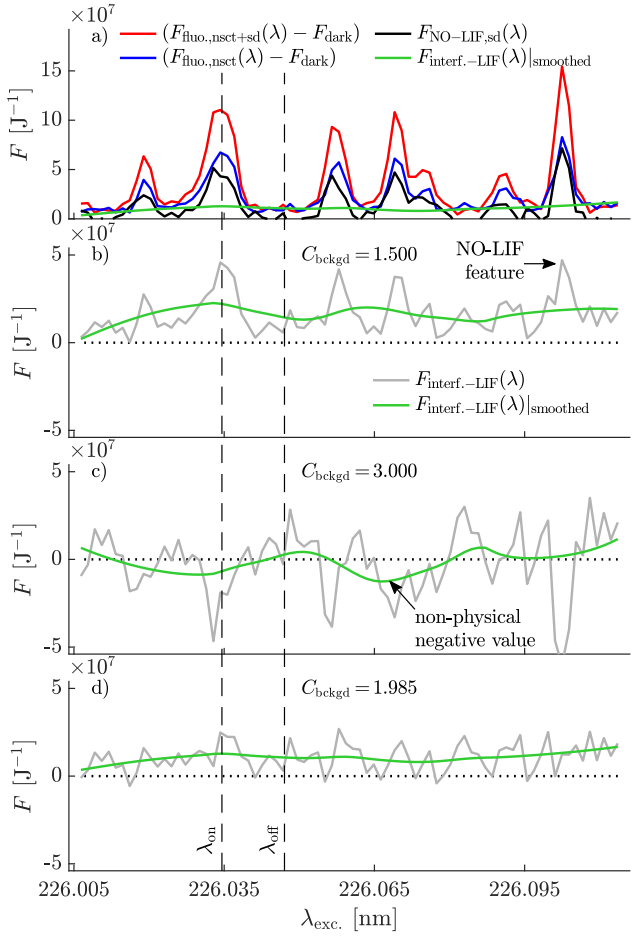

Figure III.8: Determination process of C_{bckgd} *via* iteration, at a given position of the post-flame region of the Phi0.9_Tad2130K_O21 flame ($p = 1$ atm): a) signals composing the terms of Eq. (III.53); b-d) inference of $F_{\text{interf.-LIF}}(\lambda)$ using different values of C_{bckgd} (b - too small, c - too large, d - optimal).

It is important to note that C_{bckgd} can be determined in flames with significant reburn, as long as the flame can be seeded and that the NO-LIF features of $F_{\text{fluo.,nsct+sd}}(\lambda)$ and $F_{\text{fluo.,nsct}}(\lambda)$ can be distinguished from the interfering LIF profile.

Finally, C_{bckgd} is computed for each axial location, and the profile is approximated by a sextic Bézier curve to reduce noise [43]. Once $F_{\text{interf.-LIF}}(\lambda)$ is obtained, $F_{\text{NO-LIF}}(\lambda)$ is calculated following Eq. (III.46) for a given wavelength. For the remaining of this work, the $F_{\text{NO-LIF}}$ profile is calculated using the signal at λ_{on} as it possesses the best signal-to-noise ratio, as well as the least temperature dependency.

III.5.1.3 Comparison of $F_{\text{NO-LIF}}$ profiles considering both assumptions on $F_{\text{interf.-LIF}}(\lambda)$

The calculated $F_{\text{NO-LIF}}$ profiles are compared for the Phi0.9_Tad2130K_O21 flames in Fig. III.9. Only the unseeded and one seeding level ($X_{\text{NO,sd}} = 50$ ppm) are displayed for clarity. They are presented with their respective uncertainty quantification through the error-bar at $z = 3$ mm. Profiles are normalised by the optical calibration coefficient (C_{opt}) for a quantitative comparison as they have been measured using a different experimental configuration. The methodology to do so is presented in Section III.5.2.2.

Profiles obtained using constant and non-constant $F_{\text{interf.-LIF}}(\lambda)$ assumptions show a perfect agreement for each level of seeding along the entire domain. Discrepancies can be observed in the region near the plate ($z \sim 0 - 1$ mm) due to larger scatter and a smaller data set for the technique assuming non-constant $F_{\text{interf.-LIF}}(\lambda)$, but is, usually, not the region of interest in the measurement of NO. These results demonstrate the effectiveness of both assumptions in the calculation of $F_{\text{NO-LIF}}$, as expected for atmospheric conditions.

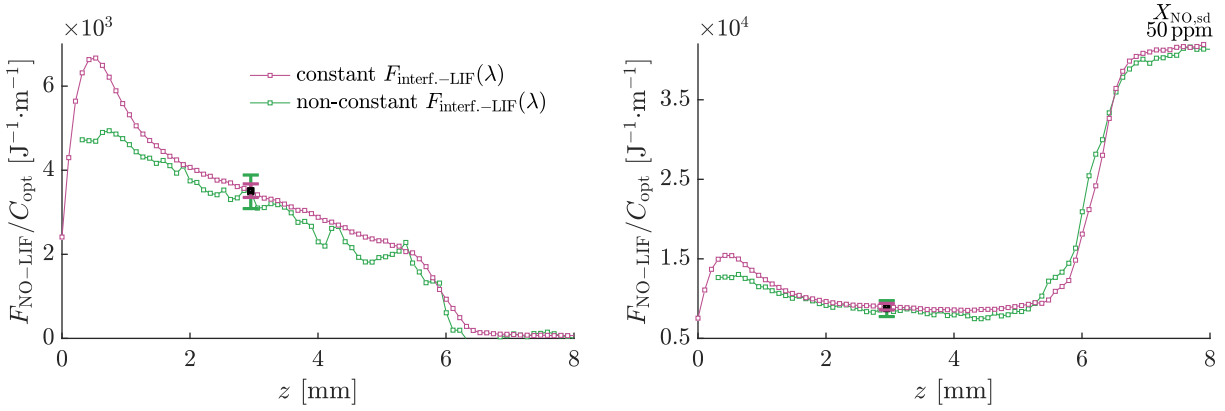

Figure III.9: Comparison of the $F_{\text{NO-LIF}}/C_{\text{opt}}$ profiles of the unseeded (left) and seeded (right) Phi0.9_Tad2130K_O21 flames using the assumptions of constant (purple) and non-constant (green) $F_{\text{interf.-LIF}}(\lambda)$. Note the different scales of the vertical axis between both figures.

III.5.2 Calculation of $X_{\text{NO,nsct}}$ using $F_{\text{NO-LIF}}(\lambda)$

Once $F_{\text{NO-LIF}}(\lambda)$ is rid of $F_{\text{bckgd}}(\lambda)$, it can be used to calculate the amount of NO in the volume, as per Eq. (III.21). The application of this equation differs according to the assumption of NO reburn that is formulated. This translates into a different post-processing of the experimental results through two distinct calibration techniques.

III.5.2.1 C_{lin}: Linear extrapolation from seeded to nascent NO concentrations - Assumption of negligible NO reburn

This calibration technique relies on the determination of a coefficient, C_{lin}, representing the linear proportionality of a signal for a given molar fraction of NO. As discussed in Section III.3.2.2, C_{lin} replaces ($f_{\text{LIF}} \cdot C_{\text{opt}}$) in Eq. (III.21), and is found by assuming that:

1. there is negligible reburn of the NO molecules through the flame front (see Appendix A.3.1);
2. the temperature and species composition (except NO molar fraction) is identical in the unseeded and seeded flames (see Appendix A.3.2); and
3. the LIF signal scales linearly with NO concentration (see Fig. III.10b).

To obtain C_{lin}, the signal of several flames, unseeded and seeded, are needed to calculate the proportionality of the captured fluorescence signal with NO molar fraction. The NO molar fraction produced by the unseeded flame can later be inferred from the proportionality coefficient, such that:

$$X_{\text{NO,nsct}} = \frac{F_{\text{NO-LIF,nsct}}}{C_{\text{lin}}}, \tag{III.54}$$

where C_{lin} represents the slope of a linear fit between $F_{\text{NO-LIF}}$ (seeded and unseeded) and $X_{\text{NO,sd}}$, and $F_{\text{NO-LIF,nsct}}$ is the intercept of the fit at $X_{\text{NO,sd}} = 0$. Thus, the accuracy of $X_{\text{NO,nsct}}$ results from the confidence interval of the fit[2] (see Appendix A.4).

Interestingly, C_{bckgd} can also be used directly to derive $X_{\text{NO,nsct}}$ without the explicit calculation of C_{lin}. This is shown using Eq. (III.35) to develop Eq. (III.54) into the following:

$$X_{\text{NO,nsct}} = \frac{F_{\text{NO-LIF,nsct}}}{F_{\text{NO-LIF,nsct+sd}} - F_{\text{NO-LIF,nsct}}} \cdot X_{\text{NO,sd}}. \tag{III.55}$$

Similarly, Eq. (III.52) can be derived to:

$$X_{\text{NO,nsct}} = (C_{\text{bckgd}} - 1) \cdot X_{\text{NO,sd}}, \tag{III.56}$$

[2]Note that the fit is not forced to have a positive intercept.

which is directly equivalent to Eq. (III.55). Hence, when C_{bckgd} is obtained under the assumption of non-constant $F_{\text{interf.-LIF}}(\lambda)$, the calculation of C_{lin} can be avoided as it is already contained in C_{bckgd}. Such methodology, however, leads to an extrapolation of $X_{\text{NO,nsct}}$ from $F_{\text{NO-LIF}}$ using only one seeding level[3], while several seeding levels can be used in the derivation of C_{lin}. Similar to C_{lin}, however, the transformation from C_{bckgd} to $X_{\text{NO,nsct}}$ must be performed under negligible NO reburn.

This leads to an important point when using this calibration technique under reburn conditions. When seeding the flame with several NO levels, reburn can be observed through a non-linearity of the LIF signal with seeding, assuming a non-linearity of the reburn fraction as seen in Fig. A.2 in Appendix. Instead, if only one seeding level is performed, it is impossible to determine if reburn is affecting the flames. Hence, it is preferable to ensure that there is no reburn in the flames (through a numerical or experimental analysis), and to proceed with at least two seeding levels, when possible.

Both techniques are compared later, in Fig. III.10 and Fig. III.11, where $F_{\text{NO-LIF}}(\lambda)$ is obtained using constant and non-constant $F_{\text{interf.-LIF}}(\lambda)$, respectively.

III.5.2.1.1 Assuming constant interfering LIF signal

The C_{lin} calibration methodology using the assumption of constant $F_{\text{interf.-LIF}}(\lambda)$ is presented in Fig. III.10. Figure III.10a presents the LIF profiles of flames with varying levels of NO seeding from 0 to 75 ppm as defined by Eq. (III.42). The measurements were repeated at least twice for each seeding level to ensure repeatability of the results, but only the averaged profiles are displayed for clarity. The $F_{\text{NO-LIF}}$ profiles demonstrate the scaling of the signal with the several levels of seeding.

[3]Nevertheless, the calculation could be performed several times using several seeding levels.

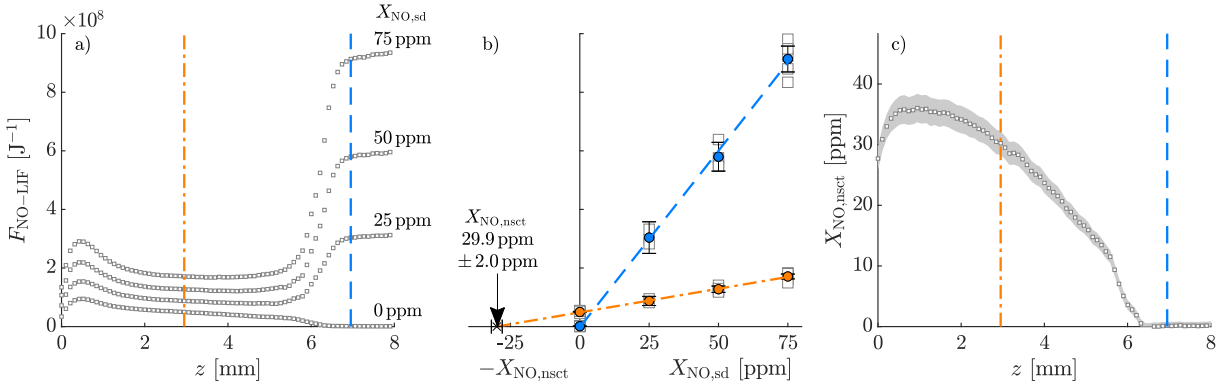

Figure III.10: Linear fit calibration technique applied on the Phi0.9_Tad2130K_O21 flame assuming constant $F_{\text{interf.-LIF}}(\lambda)$: a) Experimental NO-LIF profiles obtained for an unseeded and three NO-seeding levels; b) Linear fit applied on the NO-LIF signal versus the known NO molar fraction at two axial locations (blue at $z = 7$ mm and orange at $z = 3$ mm) allowing the extrapolation of NO produced by the unseeded flame; c) Post-calibration NO molar fraction profile in ppm.

Additionally, it is clear that the temperature is the main driver of the signal through the change in NO number density, as shown through the strong signal in the unburnt region ($T \sim 300$ K) compared to the post-flame region ($T \sim 2000$ K). This highlights that the calibration coefficient is dependent on the local thermodynamic conditions and is, therefore, not applicable at other conditions unless correction for temperature, Boltzmann fraction, and quenching coefficient rates are applied [22]. This is also shown in Fig. III.10b where the linear fit is performed in the unburnt and post-flame regions. For both positions, the extrapolation of the fit to a zero LIF signal leads to the produced NO molar fraction. Results of the extrapolation at each point of the axial domain are reported in Fig. III.10c where the complete NO molar fraction profile of the flame is presented in ppm along with its uncertainty (shaded grey area). It presents the expected characteristics of a NO profile of a methane-air flame at moderate temperatures: first, a rapid production of NO through the flame front mostly attributable to the prompt-NO pathway and, second, a slower increase of NO in the post-flame region mostly driven by the thermal-NO pathway [64]. The determination of $X_{\text{NO,nsct}}$ through this technique leads to an uncertainty of $\epsilon_{X_{\text{NO,nsct}}|C_{\text{lin,constant interf.-LIF}}} \sim 3-8\%$, for which calculations are detailed in Appendix A.4.

III.5.2.1.2 Assuming non-constant interfering LIF signal

The linear extrapolation from seeded to nascent NO concentrations calibration methodology using the assumption of non-constant $F_{\text{interf.-LIF}}(\lambda)$ is presented in Fig. III.11. The iterative process to determine C_{bckgd} is applied to each axial location of the domain for a given seeding level, as shown in Fig. III.11a, along with its sextic Bézier curve. The higher is the seeding, the lower is the value of C_{bckgd}, as expected from Eq. (III.52). With the knowledge of C_{bckgd}, $F_{\text{NO-LIF,nsct}}(\lambda_{\text{on}})$

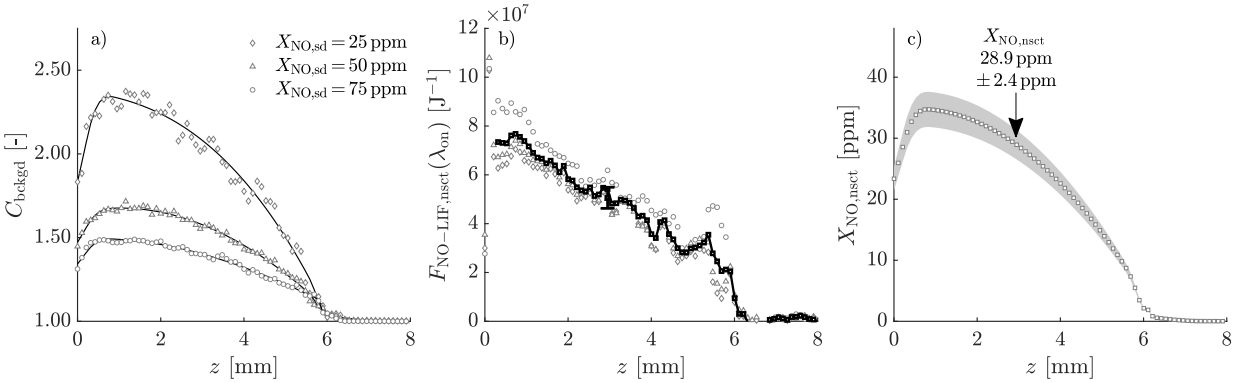

Figure III.11: Transformation of the NO-LIF signal obtained for the Phi0.9_Tad2130K_O21 flame using C_{bckgd} to calculate $X_{\text{NO,nsct}}$: a) C_{bckgd} profiles (symbols) obtained for a single flame using three seeding levels and its fitted sextic Bézier curve (lines); b) $F_{\text{NO-LIF,nsct}}(\lambda_{\text{on}})$ calculated for an unseeded flame at every point of the domain using the three C_{bckgd} profiles (diamonds, triangles, and circles) and its average (black line and squares); c) $X_{\text{NO,nsct}}$ profile calculated using Eq. (III.56), resulting from an averaging of profiles.

can be calculated as shown in Fig. III.11b. Fig. III.11a-b demonstrates that $F_{\text{NO-LIF,nsct}}(\lambda)$ can be calculated independently of the seeding value used. This is seen through the consistency of the calculated $F_{\text{NO-LIF,nsct}}(\lambda_{\text{on}})$ profiles from the three different C_{bckgd} profiles in Fig. III.11b. Note that, for clarity, only the averaged profile for each seeding was presented, despite several measurements being performed to ensure repeatability.

As mentioned previously, the profile obtained in Fig. III.11b is not directly comparable to the one obtained in Fig. III.10a because the experimental configuration has been modified between the measurements. Specifically, the number of laser pulses and, therefore, images accumulated on the ICCD camera, per wavelength, is different, changing the signal-to-noise ratio. Additionally, the subtraction of $F_{\text{NO-LIF,nsct}}(\lambda_{\text{off}})$ from $F_{\text{NO-LIF,nsct}}(\lambda_{\text{on}})$ performed assuming constant $F_{\text{interf.-LIF}}(\lambda)$ can lead to an underestimated signal if some NO-LIF signal is present at the offline wavelength (through broadening for example), whereas the technique performed assuming non-constant $F_{\text{interf.-LIF}}(\lambda)$ ensures that $F_{\text{interf.-LIF}}(\lambda)$ is free of any unduly subtracted NO-LIF contribution. Hence, in order to be comparable to one another, the flame data need to be normalised by C_{opt} obtained in each experimental configuration, as seen in Fig. III.9, and explained later in this work, see Section III.5.2.2.

Finally, the calculation of $X_{\text{NO,nsct}}$ using Eq. (III.56) is shown in Fig. III.11c. The NO molar fraction profile of the flame is presented in ppm along with its uncertainty. The determination of $X_{\text{NO,nsct}}$ through this technique leads to an uncertainty of $\epsilon_{X_{\text{NO,nsct}}}|_{C_{\text{lin,non-constant interf.-LIF}}} \sim 8.5\%$, and its calculation is detailed in Appendix A.4. The profile presents similar characteristics to the one presented in Fig. III.10c. The direct comparison of both profiles is performed later in this study, see Section III.6.

III.5.2.1.3 Applicability of the technique

This calibration technique yields a quantitative measurement of the NO contained in the flame regardless of the assumption formulated on $F_{\text{interf.-LIF}}(\lambda)$. The resulting NO molar fraction profiles obtained experimentally are directly comparable to numerical results obtained from a thermochemical model through the use of a combustion modelling software.

To measure the NO produced by a flame, this calibration technique requires the seeding of the flame by at least one seeding level in order to obtain C_{lin} or C_{bckgd} depending on the assumption on $F_{\text{interf.-LIF}}(\lambda)$. Naturally, the higher the number of seeded flames, the more certain is the fit, and the more constrained the confidence interval, see Appendix A.4. Additionally, it is crucial that the experimental setup remains undisturbed between the unseeded and seeded flame measurements to ensure the consistency of $(f_{\text{LIF}} \cdot C_{\text{opt}})$.

This technique is often used in the literature, see Section III.3.2.2, as it is simple to post-process, does not require any LIF modelling, is based on assumptions that are easy to verify and fulfil, and

is valid for the entire flame domain. It can, however, be challenging to use if many flames have to be studied, as it requires at least twice the experimental time and cost to obtain quantitative NO measurements of a single flame. Furthermore, an *a priori* estimation of the NO produced in the flame is required in order to seed the flame with NO levels of the same order of magnitude as the NO produced by the unseeded flame. Seeding levels that are too far from the produced NO would lead to a more uncertain extrapolation. Additionally, seeding levels that are too large would lead to significant reburn throughout the flame domain. This is demonstrated in Appendix A.3.1 where, for some flame conditions, significant reburn is present with even low levels of seeding, especially in rich flames. This leads to a calibration technique whose applicability is limited mostly to lean to stoichiometric and low to moderate pressure premixed flames. This technique is also inapplicable in the case of flames containing molecules that are known to favour reburn, such as NH_3, regardless of the pressure or stoichiometry of the flame. Finally, this technique can only be performed in flames that are time-averaged due to the requirement to seed the flame. Hence, it can be applied in temporally-stable flows, such as bunsen or flat flames, leading to an accurate quantification of the NO produced. It can also be applied in temporally-unstable flows, such as turbulent flames, but this will result in a less resolved and accurate measurement of NO due to the time-averaging of the signal.

To avoid significant experimental time, the calibration can also be done on a single flame and at a single point of the domain. This is done by accounting for the quenching effects and temperature differences between the calibration point and the points on which the transformation is applied. Therefore, this technique requires an assumption of the flame composition to extract the quenching coefficients, as well as the temperature, at each point of the domain [22, 48]. This variant of the calibration technique is effectively equivalent to the methodology presented next, using C_{opt}, where f_{LIF} is modelled.

III.5.2.2 C_{opt}: Optical calibration using experimental and modelled LIF parameters - Assumption of non negligible NO reburn

As discussed in the previous section, the calculation of $X_{\text{NO,nsct}}$ using C_{lin} or C_{bckgd} is only valid for a given axial position of the flame domain as the changes in temperature and composition throughout the domain affect f_{LIF}. This can be resolved by modelling the signal using its local flame-dependent parameters: the temperature and pressure, the quenching rate, the overlap fraction, and the Boltzmann fraction, as seen in Eq. (III.21). While, in theory, these parameters could be obtained experimentally, it is easier to get them numerically. Therefore, this technique depends on obtaining the LIF parameters through modelling.

This calibration technique relies on the determination of C_{opt}, a flame- and axially-independent coefficient that represents the optical parameters of the experimental setup[4]. As discussed in Section III.3.2.2, C_{opt} is obtained by fitting experimental and modelled $F_{\text{NO-LIF}}$ profiles, as seen in Eq. (III.38). The comparison is performed on net profiles obtained through the difference of $F_{\text{NO-LIF}}(\lambda)$ of seeded and unseeded flames, such that the resulting signal, $F_{\text{NO-LIF,sd}}(\lambda)$, is only proportional to the known seeded molar fraction of NO ($X_{\text{NO,sd}}$), removing the contribution of the flame-produced NO (unknown *a priori*):

$$F^{\text{exp}}_{\text{NO-LIF,sd}}(\lambda) = F^{\text{exp}}_{\text{NO-LIF,nsct+sd}}(\lambda) - F^{\text{exp}}_{\text{NO-LIF,nsct}}(\lambda), \tag{III.57}$$

$$= \left[X^{\text{exp}}_{\text{NO,nsct+sd}} \cdot f^{\text{exp}}_{\text{LIF}} - X^{\text{exp}}_{\text{NO,nsct}} \cdot f^{\text{exp}}_{\text{LIF}}\right] \cdot C_{\text{opt}}, \tag{III.58}$$

$$\approx X^{\text{exp}}_{\text{NO,sd}} \cdot f^{\text{exp}}_{\text{LIF}} \cdot C_{\text{opt}}, \tag{III.59}$$

and similarly,

$$F^{\text{num}}_{\text{NO-LIF,sd}}(\lambda) = F^{\text{num}}_{\text{NO-LIF,nsct+sd}}(\lambda) - F^{\text{num}}_{\text{NO-LIF,nsct}}(\lambda), \tag{III.60}$$

$$= \left[X^{\text{num}}_{\text{NO,nsct+sd}} \cdot f^{\text{num}}_{\text{LIF}} - X^{\text{num}}_{\text{NO,nsct}} \cdot f^{\text{num}}_{\text{LIF}}\right], \tag{III.61}$$

$$\approx X^{\text{num}}_{\text{NO,sd}} \cdot f^{\text{num}}_{\text{LIF}}. \tag{III.62}$$

This relationship is particularly useful for this calibration technique where thermochemical models are used to obtain a calibration coefficient through LIF modelling. By using the net signal, $F_{\text{NO-LIF,sd}}(\lambda)$ is only dependent on $X_{\text{NO,sd}}$[5] and not on $X_{\text{NO,nsct}}$ for which thermochemical models can vary significantly. This is valid assuming that f_{LIF} is independent from the thermochemical model employed, as demonstrated in Appendix A.3.3. This requires that all thermochemical models predict the temperature and main quenching species (CO_2, H_2O, N_2, O_2, and OH) profiles accurately.

The experimental net signal, $F^{\text{exp}}_{\text{NO-LIF,sd}}(\lambda)$, is obtained by subtracting the LIF signal of an unseeded flame from the seeded one. $F^{\text{exp}}_{\text{NO-LIF,nsct+sd}}(\lambda)$ and $F^{\text{exp}}_{\text{NO-LIF,nsct}}(\lambda)$ are calculated using either methodologies described in Section III.5.1.

The numerical net signal, $F^{\text{num}}_{\text{NO-LIF,sd}}(\lambda)$, is also obtained by subtracting the LIF signal of an unseeded flame from the seeded one. $F^{\text{num}(\lambda)}_{\text{NO-LIF,nsct+sd}}$ and $F^{\text{num}}_{\text{NO-LIF,nsct}}(\lambda)$ are obtained using flame simulation and LIF modelling. Similarly to the experiments, simulations are performed by virtually seeding the flame with $X_{\text{NO,sd}}$. The Impinging Jet model in Cantera 3.0 [69] is used to simulate the experimental flames using the measured boundary conditions presented in Tab. III.1 and Appendix A.1. Three thermochemical models are used: CRECK (v.2003) [70, 71], GRI (v.3.0) [72],

[4]Conveniently, the determination of C_{opt} could also be grouped with any other linear effects that cannot be easily measured in Eq. (III.21), such as an absolute energy measurement of the laser beam.

[5]This is valid assuming negligible reburn.

and SD (v.2016-12+v.2018-07) [73]. They have been chosen due to their span of accuracy in predicting NO measurements in a previous methane-air flame campaign [64]. The CRECK and GRI thermochemical models have shown the best agreement with the measured NO, while SD displayed the worst. Additionally, CRECK is one of the most comprehensive thermochemical models available to the community, while GRI and SD are simpler models validated for a limited set of fuels [52]. The choice of these models was made to demonstrate that the C_{opt} calibration technique is minimally dependent on the accuracy of the thermochemical model in predicting $X_{\text{NO,nsct}}$ (see Appendix A.3.3 for demonstration).

The numerical flame results are fed to LIFSim [33], a linear 3-level NO-LIF model, to transform a numerically-obtained NO molar fraction profile ($X_{\text{NO}}^{\text{num}}$) to a numerical LIF profile ($F_{\text{NO-LIF}}^{\text{num}}(\lambda)$) by modelling $f_{\text{LIF}}^{\text{num}}$. Calculations are made assuming a linear regime, consistent with the experimental conditions used in this study. Extremely fast Rotational Energy Transfer (RET) is assumed leading to an equilibrium population in the ground states. The fluorescence modelled by the software is a summation of A_{21} and A_{23}, neglecting pre-dissociation and photo-ionisation. In the case of several transitions being excited by the laser, the total LIF signal is a summation of the fluorescence calculated for each individual transition. The output is a spectrally-resolved LIF signal, per pulse, $\mathcal{S}_{\text{NO-LIF}}$ [10^{-17} W], for a given set of flame condition, and laser and detection parameters. To appropriately model the experimental configuration that comprises a filter and a camera with their own transmissivity and quantum efficiency, the LIF signal obtained from LIFSim is integrated from 220 nm to 340 nm (corresponding to the 8$^{\text{th}}$ vibrational band) at each location of the domain. Finally, the integrated signal is multiplied by the NO number density from the flame simulation, such that:

$$F_{\text{NO-LIF}}^{\text{num}}(\lambda) = \int_{\lambda_{\text{collection}}} \mathcal{S}_{\text{NO-LIF}} \cdot n_{\text{NO}}^{\circ} \cdot \mathrm{d}\lambda_{\text{collection}}. \tag{III.63}$$

Additional parameters used in LIFSim to obtain $F_{\text{NO-LIF}}^{\text{num}}(\lambda)$ are detailed in Appendix A.2.

III.5.2.2.1 Assuming constant interfering LIF signal

Similar to the experiments, the numerical-LIF signal of each flame is obtained by calculating the difference between the online and offline signals:

$$F_{\text{NO-LIF}}^{\text{num}} = F_{\text{NO-LIF}}^{\text{num}}(\lambda_{\text{on}}) - F_{\text{NO-LIF}}^{\text{num}}(\lambda_{\text{off}}). \tag{III.64}$$

The direct comparison of $F_{\text{NO-LIF,sd}}^{\text{num}}$ and $F_{\text{NO-LIF,sd}}^{\text{exp}}$ allows the optical calibration coefficient (C_{opt}) to be determined, as depicted in Fig. III.12. C_{opt} is found by fitting the experimental profile to the

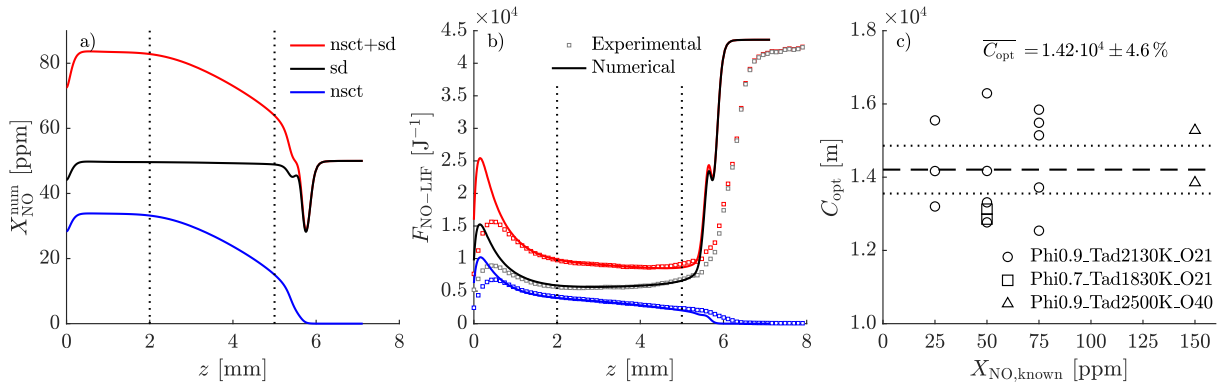

Figure III.12: C_{opt} calibration technique: a) Numerical NO profiles for the flame Phi0.9_Tad2130K_O21 unseeded (blue line), seeded with 50 ppm of NO (red), and the resulting net profile (black) using the GRI thermochemical model, along with the axial bounds within which X_{NO}^{num} remains constant (dotted lines); b) LIF numerical profiles (solid lines) and C_{opt}-normalised experimental LIF profiles (squares) of the flame unseeded (blue), seeded (red), and net (black), along with the axial bounds within which C_{opt} was fitted (dotted lines); c) Calibration coefficient C_{opt} obtained for 16 flames at varying levels of seeding and flame conditions, along with its average (dashed line) and its 95% confidence interval (dotted lines).

numerical one using a least-square fit, leading to:

$$F_{\text{NO-LIF}} = \frac{F_{\text{NO-LIF,sd}}^{\text{exp}}}{C_{opt}} = F_{\text{NO-LIF,sd}}^{\text{num}}, \tag{III.65}$$

within the selected axial locations where there is negligible reburn, as discussed in Appendix A.3.1.

Once the LIF experimental signal of a flame is normalised by C_{opt}, the signal becomes independent of the optical parameters. Therefore, the C_{opt}-normalised signal obtained from several flames using different optical setups can be compared quantitatively relative to each other. On the contrary to the C_{lin} extrapolation technique, C_{opt} can be obtained once, and applied to any flame produced using the same optical configuration; it relies on the assumption that the optical parameters remain constant between the calibration and measurement flames. Hence, the technique can be applied regardless of NO reburn; if the coefficient is obtained under conditions of negligible reburn, it can then be applied to measured flames experiencing reburn or not. If the coefficient is obtained under non-negligible reburn, the C_{opt} calibration technique can still be applied provided that the thermochemical model correctly predicts the reburn chemistry[6].

Figure III.12 displays the process for determining C_{opt}. Figure III.12a presents the NO molar fraction profiles of a numerical flame without, and with, NO seeding. The difference of these two signals, $X_{NO,sd}^{num}$, is also plotted. This curve shows that the NO molar fraction remains constant within the axial bounds chosen in the post-flame region to determine C_{opt} (dotted lines). These axial bounds were chosen as they represent the post-flame region where NO reburn is negligible, as

[6]This is necessary to assume $X_{NO,sd}^{num} = X_{NO,sd}^{exp}$ in the demonstration performed in Appendix A.3.4.

shown in Appendix A.3.1, and where composition of the main species, specifically the quenchers, have reached equilibrium.

The numerical profiles are processed through LIFSim and subtracted from one another to obtain the net NO-LIF numerical profile $F^{\text{num}}_{\text{NO-LIF,sd}}$ as shown in Fig. III.12b. Following Eq. (III.65), $F^{\text{exp}}_{\text{NO-LIF,sd}}$ is fitted to $F^{\text{num}}_{\text{NO-LIF,sd}}$ within the axial bounds by adjusting C_{opt} through a least-square minimisation. The resulting C_{opt}-normalised experimental profiles ($F^{\text{exp}}_{\text{NO-LIF}}/C_{\text{opt}}$) are also shown on Fig. III.12b. Within the axial bounds, the numerical and experimental profiles match almost perfectly using the GRI thermochemical model. Using another thermochemical model whose accuracy in the prediction of the NO formation is worse than GRI would, however, lead to discrepancies between the numerical and experimental seeded and unseeded profiles. Nevertheless, it is demonstrated that despite these mispredictions, the net profiles remain almost perfectly predicted regardless of the model and the amount of seeding (see Appendix A.3.3). This demonstrates the effectiveness of using the net profile to determine the calibration coefficient since it is independent of the thermochemical model prediction accuracy.

This technique is valid with greater accuracy in the post-flame region where the net NO molar fraction remains constant. Potential mispredictions in the flame kinetics by thermochemical models can also lead to displacement of the profile in the axial direction, as seen with the unseeded flame in Fig. III.12b. Furthermore, misprediction of temperature-dependent parameters seem to lead to the disagreement observed in the unburnt region, between the net experimental and modelled LIF signal. Due to the incapacity to prove that experimentally, the authors believe that this disagreement stems from an inaccurate prediction of the temperature-dependent quenching cross-section of the species involved in the cold and hot regions of the flame by LIFSim. Indeed, the calculation of the quenching cross-section in LIFSim is performed using the experimental results of Paul *et al.* [74, 75], while more recent results, published by Tamura *et al.* [76] and Settersten *et al.* [77, 78] indicate different temperature-dependencies for several of the most important quenchers. An inaccurate description of the laser linewidth (experimentally inferred) could also lead to the observed temperature-dependent mispredictions in the unburnt region. As NO is not produced at very low temperatures, the fit of C_{opt} is better performed in the hot flow, a region representative of the conditions for NO formation. The fit would therefore be biased if the cold region was included. Despite this, the determination of the profile ($F^{\text{exp}}_{\text{NO-LIF}}/C_{\text{opt}}$) is still valid outside of the axial bounds, as C_{opt} is independent of the flame.

As discussed, the obtained C_{opt} is minimally dependent of the thermochemical model employed for simulations, it is also independent of the amount of NO seeded in the unburnt mixture, and to the flame condition used (under the assumption of negligible reburn), as shown in Fig. III.12c. For the three flames presented in Tab. III.1, several levels of NO seeding were used to calculate C_{opt}. Measurements were performed several times to ensure repeatability and to reduce random uncer-

tainty. The calculated C_{opt} for all these conditions demonstrate the independence of the technique with the flame condition and is presented in Appendix A.3.4. Therefore, only one calibration flame is needed for flames going from lean to rich conditions, although several flames would be recommended for higher confidence in the calculation of C_{opt}. In cases where reburn is not avoidable, this technique remains valid but needs to be employed with a thermochemical model that accurately predicts the reburn chemistry for at least one condition targeted by the experimental study.

III.5.2.2.2 Assuming non-constant interfering LIF signal

The calculation process was repeated assuming non-negligible interfering LIF. For consistency with the experimental profiles, $F^{\text{num}}_{\text{NO-LIF}}$ is obtained by calculating the signal at the online wavelength:

$$F^{\text{num}}_{\text{NO-LIF}} = F^{\text{num}}_{\text{NO-LIF}}(\lambda_{\text{on}}), \tag{III.66}$$

as LIFSim only outputs the fluorescence of the NO molecules and does not contain the fluorescence of interfering species[7]. Hence, $F^{\text{num}}_{\text{NO-LIF}}$ slightly differs between both assumptions, $\sim$9%, proportional to the signal produced at the offline wavelength due to line broadening, see Fig. III.5.

A new C_{opt} is required as the experimental configuration is slightly different for both background subtraction methods, as discussed in Section III.5.1, namely the number of images captured on the camera per pulse and the calculation of $F^{\text{num}}_{\text{NO-LIF}}$. The process to obtain C_{opt}, however, does not differ between both assumptions. Results are not presented for the sake of conciseness. The newly obtained averaged C_{opt} ($1.55{\cdot}10^4$ m) is of the same order of magnitude, and, unsurprisingly, $\sim$9% higher than the one obtained previously ($1.42{\cdot}10^4$ m). Nevertheless, once normalised by C_{opt}, the profiles obtained using both assumptions on $F_{\text{interf.-LIF}}(\lambda)$ are directly comparable. These are presented in Fig. III.9, and thus, prove the effectiveness of C_{opt} in yielding experimental LIF profiles independent from their configurations.

The C_{opt}-normalisation of the $F^{\text{exp}}_{\text{NO-LIF}}$ profiles renders this calibration technique quantitative. The profiles are directly proportional to n°_{NO}. In contrast to the extrapolation technique, however, the profiles are not readily comparable to simulation profiles. In order to do so, two comparison methodologies can be employed: transforming numerical NO molar fraction profiles into NO-LIF profiles, or transforming experimental NO-LIF profiles into NO molar fraction profiles.

III.5.2.2.3 Transforming numerical NO molar fraction profiles into NO-LIF profiles

The advantage of comparing the numerical to experimental results in experimental units, *i.e.* transforming the numerical molar fraction profiles into predicted NO-LIF signals through Eq. (III.21), is to separate the propagation of numerical and experimental uncertainties and, therefore, perform

[7] LIFSim has the possibility to generate O_2-LIF signals, but it was not used in this study.

a more accurate comparison of the results [79]. As per Eq. (III.22), the accurate measurement of some terms, such as the temperature or quencher concentrations, would be required to accurately obtain $f_{\text{LIF}}^{\text{exp}}$. With the availability of the complete simulation solution, however, it is easier and more accurate to transform the numerical NO molar fraction profile using its own prediction of temperature and quencher concentrations to obtain $f_{\text{LIF}}^{\text{num}}$.

To do so, the numerical NO molar fraction profiles are transformed into NO-LIF profiles using the methodology discussed previously to obtain $F_{\text{NO-LIF}}^{\text{num}}$. Thus, the uncertainties in the simulated NO-LIF profiles are limited to numerical ones: in the thermochemical model, Cantera, and LIF-Sim; while the experimental uncertainties are limited to the measurement of $F_{\text{NO-LIF}}$ and C_{opt}. The experimental uncertainty of $F_{\text{NO-LIF}}/C_{\text{opt}}$ is estimated at $\epsilon_{F_{\text{NO-LIF,nsct}}/C_{\text{opt}}}|_{\text{constant interf.-LIF}} \sim 6\%$ under the assumption of constant $F_{\text{interf.-LIF}}(\lambda)$ and $\epsilon_{F_{\text{NO-LIF,nsct}}/C_{\text{opt}}}|_{\text{non-constant interf.-LIF}} \sim 12\%$ under the assumption of non-constant $F_{\text{interf.-LIF}}(\lambda)$.

While this transformation leads to a more accurate comparison of the numerical to experimental results, an absolute NO molar fraction, or concentration may, in certain instances, be required.

III.5.2.2.4 Transforming experimental NO-LIF profiles into NO molar fraction profiles

As discussed, the transformation of experimental NO-LIF profiles into NO molar fraction profiles is feasible if $f_{\text{LIF}}^{\text{exp}}$ can be measured or calculated. In this work, the direct measurement of the quencher concentration is not performed and, thus, $f_{\text{LIF}}^{\text{exp}}$ cannot be estimated directly. Under the assumptions of negligible NO reburn, and that thermochemical models can reproduce the general kinetics of the flame accurately, *i.e.* the flame temperature and main species concentrations, the experimental and numerical f_{LIF} can be assumed constant, such that:

$$X_{\text{NO,nsct}}^{\text{exp}} = \frac{F_{\text{NO-LIF,nsct}}^{\text{exp}}}{C_{\text{opt}}} \cdot \frac{X_{\text{NO,nsct}}^{\text{num}}}{F_{\text{NO-LIF,nsct}}^{\text{num}}}, \tag{III.67}$$

obtained by re-arranging Eq. (III.36−III.37), and Eq. (III.65).

With this technique, any numerical uncertainty will be propagated to the experimental NO molar fraction profile. It is, however, relatively difficult to obtain a quantification of the numerical uncertainties at play in such a scenario, either within the thermochemical model, the combustion simulation software, or the LIF modelling software. This is why, to apply Eq. (III.67) with minimal uncertainty, it is crucial to select the thermochemical model with the best agreement in terms of flame kinetics, through the measurement of the flame speed and temperature profiles, and through the direct comparison of the NO-LIF profiles aforementioned. Such methodology and its limitation are demonstrated in Fig. III.13.

In Fig. III.13a, the C_{opt}-normalised experimental NO-LIF profile ($F_{\text{NO-LIF}}^{\text{exp}}/C_{\text{opt}}$) is compared to numerical NO-LIF profiles ($F_{\text{NO-LIF}}^{\text{num}}$), using three thermochemical models of varying degrees of ac-

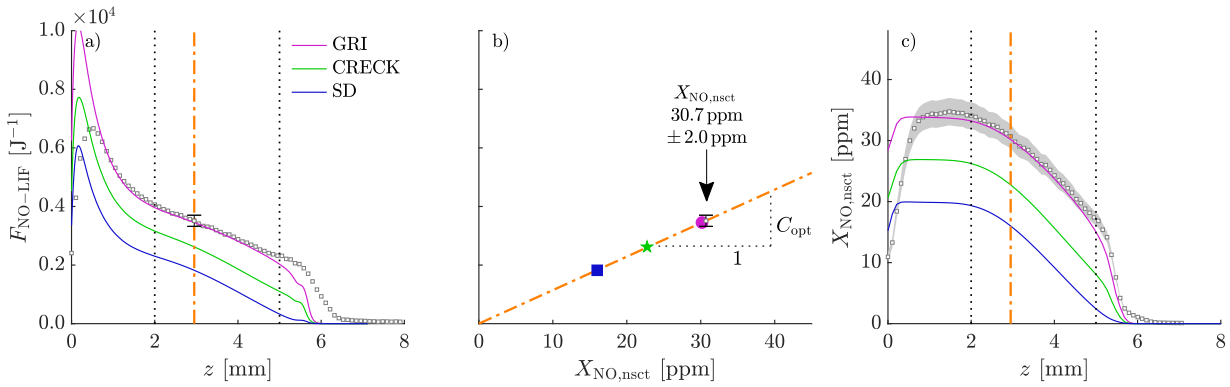

Figure III.13: Transformation of the NO-LIF signal obtained using C_{opt} to $X^{\mathrm{exp}}_{\mathrm{NO,nsct}}$ on the Phi0.9_Tad2130K_O21 flame: a) Comparison of the experimental (squares) to the numerical (coloured lines) NO-LIF profiles using different thermochemical models (GRI - magenta, CRECK - green, SD - blue), b) Linear fit of the NO-LIF signal to NO concentration at a given location, c) Post-transformation NO concentration profile in ppm compared to the numerical predictions using the GRI thermochemical model.

curacy in predicting NO concentration. This comparison is in itself enough to compare numerical to experimental NO-LIF profiles, as discussed above. In this figure, GRI leads to the best agreement in predicting the NO-LIF profile of the flame, while CRECK and SD show worse agreement. Importantly, none of the three models can accurately predict the flame front position as seen at $z \sim 6$ mm, showing a misprediction of the flame kinetics.

Following the observations made on the comparison of the NO-LIF profiles, the transformation of the experimental NO-LIF profile was performed using the GRI thermochemical model in Eq. (III.67)[8]. The calculation is performed at each axial location of the domain and is demonstrated at $z = 3$ mm in Fig. III.13b. The calculation of $X^{\mathrm{exp}}_{\mathrm{NO,nsct}}$ follows closely the prediction made by GRI, as it is also the case for the NO-LIF profiles in Fig. III.13a. It is interesting to note that all three thermochemical models fall on the same line whose slope is C_{opt}, further demonstrating the minimal dependence of C_{opt} (or $F^{\mathrm{num}}_{\mathrm{NO\text{-}LIF,sd}}$) on the thermochemical models under all assumptions mentioned before. Hence, due to a similar misprediction of the flame kinetics by all three models, the transformation of $F^{\mathrm{exp}}_{\mathrm{NO,nsct}}$ to $X^{\mathrm{exp}}_{\mathrm{NO,nsct}}$ could have been performed with any of the three models.

The resulting $X^{\mathrm{exp}}_{\mathrm{NO,nsct}}$ profile is plotted in Fig. III.13c along with its uncertainty (shaded grey area). The numerical molar fraction are also plotted using coloured lines, similar to Fig. III.13a. It is evident that the calculated NO molar fraction profile follows the trend seen in the NO-LIF profiles, it is best predicted by GRI and underestimated by CRECK and SD. With this methodology, the transformation is only valid in the region where C_{opt} is extracted due to the errors present in the thermochemical models predictions in the flame kinetics, seen through the delta in the flame front position. This is demonstrated in the flame-front region ($z \sim 6.5 - 5$ mm) where the experi-

[8]The transformation is performed, despite mispredictions in the flame kinetics by GRI, for the sake of explanation and demonstration of its limit.

mental profile sits upstream of the numerical profiles in Fig. III.13a, but is shifted downstream in Fig. III.13c due to the model misprediction of the flame front position. A similar phenomenon is also occurring near the stagnation plate. This effect supports the use of a comparison based on the NO-LIF profiles rather than a transformation in molar fraction. Despite that, the NO concentration profile follows the expected trend of a methane-air flame at moderate temperatures, and leads to an uncertainty of $\epsilon_{X_{\text{NO,nsct}}}|_{C_{\text{opt}},\text{constant interf.-LIF}} \sim 6-12\%$ on $X^{\text{exp}}_{\text{NO,nsct}}$ depending on the flame condition, in the post-flame region. A larger uncertainty is present for the flame with a larger misprediction of the flame front position by the thermochemical model (Phi0.9_Tad2500K_O40).

III.5.2.2.5 Applicability of the technique

This calibration technique leads to a quantitative measurement of the NO contained in the domain, regardless of the assumption formulated on $F_{\text{interf.-LIF}}(\lambda)$. The experimentally obtained profiles can be compared to numerical results either through raw experimental units, or through molar fraction, leading to different uncertainties as described before.

To limit the propagation of numerical uncertainties (thermochemical model, Cantera, or LIF-Sim inaccuracies), the experimental and numerical results should be compared in experimental units [79]. In cases where an absolute NO measurement is needed, however, the experimental results can be transformed using numerical results of a thermochemical model that best reproduces the flame kinetics. In such instances, numerical inaccuracies are necessarily propagated to the NO molar fraction profile.

This calibration technique requires less experimental time and resources than the one employing seeding of the flame at several concentration levels. When employed with a LIF modelling software, it avoids the explicit calculation of each term of f_{LIF}. This technique has been employed in the literature, either through the denotation of C_{opt} [41, 44, 50–52, 64], or not [22, 35, 48, 49, 53, 80] where the parameters of f_{LIF} were individually determined. In conditions where modelling cannot be employed or where seeding cannot be performed, C_{opt} can be obtained experimentally, such as in another flow or flame that can be modelled, or using Rayleigh or Raman scattering signals [41, 59, 60], as long as the optical system of the experimental setup is kept the same. Finally, with C_{opt} being independent of the calibration flame (see Appendix A.3.4), the calibration can be performed once, on any flame, or flow, in which the previously-cited assumptions hold, and can then be applied to flames at any other condition. Therefore, in contrast to the C_{lin} calibration technique, C_{opt} could be obtained in lean, laminar, and low-pressure calibration flames, and then be applied to rich turbulent and non-premixed flames where NO reburn might be present.

The C_{opt} calibration technique, combined with the calculation of $F_{\text{NO-LIF}}(\lambda)$ under the assumption of non-constant interfering LIF signal, represents the largest span of applicability of the four techniques explored in this work. Hence, quantitative NO measurements can be obtained in flames

with non-negligible NO reburn and non-constant interfering LIF signal, such as in high-pressure rich flames.

III.6 Comparison of the calibration techniques

Two calibration techniques for quantitative NO-LIF measurements have been presented in this article. Both techniques have been applied under two sets of assumptions regarding the calculation of $F_{\text{interf.-LIF}}(\lambda)$. The set of assumptions and hypotheses on which the four techniques rely must be carefully considered when comparing the obtained results in either $X_{\text{NO,nsct}}$ or $F_{\text{NO-LIF}}/C_{\text{opt}}$ form. Hence, the comparison of the techniques is performed in Fig. III.14 through NO molar fraction profiles applied on a set of three flames, and in Tab. III.2 where they are summarised in terms of their assumptions and experimental complexity.

Figure III.14 presents the NO concentration profiles obtained for three flames, using the four quantitative techniques, as indicated in Tab. III.1. For each technique and each flame, the NO concentration throughout the flame domain is plotted along with its individual uncertainty. Figure III.14a presents the results of the four techniques for the flame Phi0.9_Tad2130K_O21. The results show a very good agreement, especially in the post-flame region where the prediction of $X_{\text{NO,nsct}}$, and its uncertainty, overlap almost perfectly. In this region, the uncertainty of each technique is in between $\sim$6 and $\sim$13%. Some discrepancies can, however, be observed in the flame-front region, and close to the stagnation plate. This is mostly due to transformation of the $F_{\text{NO-LIF,nsct}}/C_{\text{opt}}$ profiles into $X_{\text{NO,nsct}}$ using a thermochemical model that inaccurately predicts the flame front position. Therefore, a larger uncertainty in these two regions is expected[9]. These results demonstrate the applicability of the four techniques on lean flames and moderate adiabatic temperatures.

Figure III.14b presents the results of the C_{lin} and the C_{opt} calibration techniques on the low temperature flame Phi0.7_Tad1830K_O21 under the assumption of constant $F_{\text{interf.-LIF}}(\lambda)$. The results show a relatively good agreement between the two calibration techniques, within their uncertainty ranges of $\sim 6-8\%$.

Finally, Fig. III.14c presents the results of the C_{lin} and the C_{opt} calibration techniques for the high temperature flame Phi0.9_Tad2500K_O40 under the assumption of constant $F_{\text{interf.-LIF}}(\lambda)$. For this flame, both techniques lead to a perfect overlap of $X_{\text{NO,nsct}}$, especially in the post flame region. As explained previously, discrepancies in the prediction of the flame front position by the thermochemical model underpredicts $X_{\text{NO,nsct}}$ in the flame front region for the C_{opt} technique.

These results demonstrate the applicability of each of the four techniques in the flame conditions performed in this work to obtain quantitative NO measurements through $X_{\text{NO,nsct}}$ or $F_{\text{NO-LIF}}/C_{\text{opt}}$,

[9]The uncertainty analysis has been performed at $z = 3$ mm and applied to the rest of the profile, see Appendix A.4.

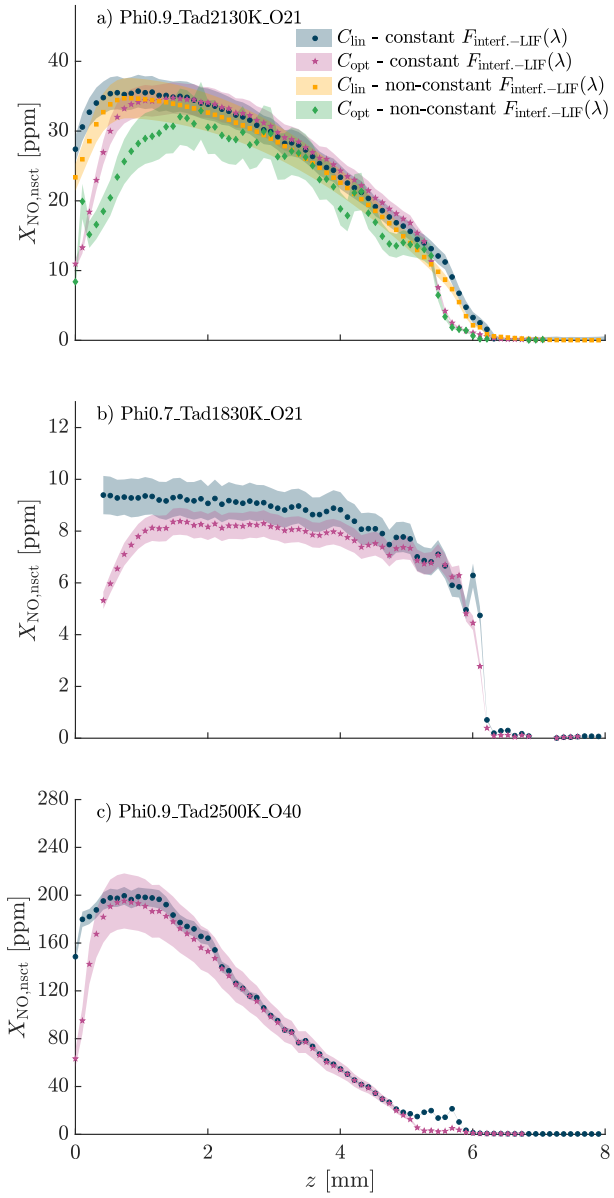

Figure III.14: Comparison of the four quantitative techniques yielding $X_{\text{NO,nsct}}$ applied on three atmospheric, lean, methane flames.

seen through Fig. III.14 and Fig. III.9, respectively. Furthermore, the assumptions, flame conditions, and experimental difficulty of each technique in the determination of $X_{\text{NO,nsct}}$ or $F_{\text{NO-LIF}}/C_{\text{opt}}$ are summarised in Tab. III.2.

Table III.2: Calibration techniques assumptions, applicability, and uncertainty.

Calibration technique	C_{lin}		C_{opt}			
Experimental results	$X_{\text{NO,nsct}}$		$X_{\text{NO,nsct}}$		$F_{\text{NO-LIF,nsct}}/C_{\text{opt}}$	
Assumption on $F_{\text{interf.-LIF}}(\lambda)$	**Constant between** λ_{on} **and** λ_{off}	**Non-constant**	**Constant between** λ_{on} **and** λ_{off}	**Non-constant**	**Constant between** λ_{on} **and** λ_{off}	**Non-constant**
Assumption on reburn	Negligible NO reburn in all flames.		Negligible NO reburn only in the calibration flame to obtain C_{opt} unless the reference thermochemical model can accurately predict it.			
Assumption on the thermochemical model	N/A		The reference thermochemical model must predict the flame kinetics and reburn accurately.		The reference thermochemical model must predict the flame kinetics accurately or another experimental methodology can be used to extract C_{opt} experimentally without numerical profiles.	
Assumption on the calibration flame	The temperature and concentration of the main species remain constant between the unseeded and seeded flames.					
LIF regimes	Can be applied regardless of the LIF regime.		Can be applied regardless of the LIF regime as long as the LIF modelling software is used in the same regime as the experimental one.			
Preferred calibration flame conditions	Lean to stoichiometric flames. Low to moderate pressures. Low level of NO seeding.	Lean to stoichiometric flames. Low to high pressures. Low level of NO seeding.	Lean to stoichiometric flames. Low to moderate pressures. Low level of NO seeding.	Lean to stoichiometric flames. Low to high pressures. Low level of NO seeding.	Lean to stoichiometric flames. Low to moderate pressures. Low level of NO seeding.	Lean to stoichiometric flames. Low to high pressures. Low level of NO seeding.
Measured flame conditions	The calibration and measured flames must be the same.		C_{opt} can be applied to any flame condition under low to moderate pressures if the measured flame kinetics properties are accurately predicted by the reference model.	C_{opt} can be applied to any flame condition under low to moderate pressures if the measured flame kinetics properties are accurately predicted by the reference model. C_{bckgd} must be calculated for each measured flame.	C_{opt} can be applied to any flame condition under low to moderate pressures.	C_{opt} can be applied to any flame condition. C_{bckgd} must be calculated for each measured flame.
Experimental and post-processing time and difficulty	Significant experimental time, as one to several seeding levels are required per flame to obtain C_{lin}. Relatively simple post-processing as LIF modelling is not required.	Extensive experimental time, as one seeding level is required per flame to obtain C_{lin}, as well as an excitation spectrum to obtain C_{bckgd}. Relatively simple post-processing as LIF modelling is not required.	Limited experimental time, only one C_{opt} is required per experimental configuration. Significant post-processing time through LIF modelling.	Moderate experimental time, only one C_{opt} is required per experimental configuration, but one to several C_{bckgd} might be required. Significant post-processing time through LIF modelling.	Limited experimental time, only one C_{opt} is required per experimental configuration. Significant post-processing time through LIF modelling.	Moderate experimental time, only one C_{opt} is required per experimental configuration, but one to several C_{bckgd} might be required. Significant post-processing time through LIF modelling.
Total uncertainty (see Appendix A.4 for details on random and systematic sources)	$\sim 3-15\%$ for one seeding level and depending on the flame condition. Decreases with the number of seeding levels.	$\sim 8\%$ for one seeding level and a given flame condition.	$\sim 6-12\%$ depending on the flame condition.	$\sim 13\%$ for a given flame condition.	$\sim 6\%$ for a given flame condition.	$\sim 12\%$ for a given flame condition.

III.7 Conclusion

Four techniques to obtain quantitative NO-LIF measurements are compared in this work. The different experimental and post-processing approaches have been presented in detail, including uncertainty analysis, to collect available methods used in the community and provide an exhaustive guide for researchers to decide on an appropriate method of calibration in the context of their own experiments. The demonstration of the techniques is performed on three atmospheric, methane-air, stagnation flames with different adiabatic flame temperatures and equivalence ratios to study the applicability of the calibration techniques under varying experimental conditions. The four quantitative techniques result from the application of two calibration methodologies under which two background subtraction methods are applied. They all address two main difficulties in LIF measurement: background subtraction under the assumption of spectrally constant or non-constant interfering LIF signal, and seeding stability of the NO molecules through reburn. The comparison of the techniques, in atmospheric and lean conditions, has shown excellent agreement, highlighting their accuracy.

The first calibration methodology (C_{lin}) uses the linear extrapolation of the LIF signal from seeded to nascent NO concentrations. Used in combination with the assumption of spectrally constant interfering LIF signal from species other than NO, this technique is the most often used in the literature, but it is also the one whose applicability is the most limited. It can only be applied under the condition of negligible reburn and constant flame conditions between the calibration seeded flames and the measured flame. This limits its application to flames from low to moderate pressures, at lean to stoichiometric equivalence ratios, and whose seeding must be performed carefully to avoid reburn. Whilst the technique does not require LIF modelling and post-processing of the signal, it requires significant experimental time and samples to obtain the proportionality coefficient for each individual flame measured. The same calibration technique can be used under the assumption of non-constant interfering LIF signal. In this case, the technique could be applied to high pressures under the assumption of negligible reburn. This technique requires extensive experimental time, since the excitation spectrum of seeded and unseeded flames is required to obtain the quantification of NO produced by the flame.

The second calibration technique (C_{opt}) uses modelled LIF parameters to obtain the optical collection system coefficient. The calibration is performed on a single calibration flame (unseeded and seeded) and applicable to any other flame using the same experimental setup. This is possible through the independence of C_{opt} from the thermochemical model employed to generate numerical LIF profiles. This calibration technique, when used under the assumption of constant interfering LIF signal, can be applied to any low to moderate pressure flames, even if there is reburn. This is possible if C_{opt} is obtained in a flame without reburn, or in cases where reburn is not avoidable, the

thermochemical model used to determine C_{opt} must accurately predict the main thermodynamic and kinetic properties of the flame (temperature, main species concentrations, reburn) at least for one experimental condition. This methodology reduces the experimental time compared to the first calibration technique, but increases the time of post-processing because LIF modelling is required. Under the assumption of non-constant interfering LIF, the calibration technique can be extended to high pressure flames. Similarly to the previous approach, C_{opt} can be obtained once and applied to any flame. The interfering LIF signal, however, must be measured for all flames, increasing the experimental time required for this technique. The C_{opt} calibration technique, combined to the assumption of non-constant interfering LIF signal, has the largest span of applicability of the four techniques presented. This calibration technique bears less uncertainty when experimental and numerical results are compared in raw experimental units [79]. In this instance, quantitative measurement of the NO contained in the flame can be performed once the LIF signal profiles are normalised by C_{opt}. In cases where an absolute molar fraction of NO is required, however, the signal can be transformed using the numerical solution, at the expense of propagating the uncertainty of the numerical model, whose quantification is challenging, onto experimental results. Hence, this calibration technique and its uncertainty was presented under both approaches.

This study presents a comprehensive demonstration of employing two calibration techniques for quantitative NO concentration measurements using LIF. While the LIF diagnostic techniques are performed on stagnation flames, their applicability also extends to other flames, provided that they can be seeded under similar conditions to the unseeded flame. Moreover, each approach, while demonstrated using NO, could be transposed to the concentration measurement of other species, as long as they are stable and can be seeded. When not possible, as for short-lived species such as CH or OH, the optical calibration methodology could still be employed, combined with another measurement, such as Rayleigh scattering [34], to determine the C_{opt} of the experimental setup.

Ultimately, all techniques were proven to yield the same response, within uncertainty, either in molar fraction or in C_{opt}-normalised LIF profiles. Therefore, the choice of the calibration technique should be based on the test conditions and the resolution of the test matrix employed by the researcher. To support this choice, this work provides the theoretical models and underlying assumptions necessary to guide the use of each technique in future quantitative speciation measurements using Laser-Induced Fluorescence.

Acknowledgements

The authors would like to acknowledge the support of the Natural Sciences and Engineering Research Council of Canada (NSERC), Siemens Energy Canada Limited, Climicals, and the Fonds de Recherche du Québec - Nature et Technologies (FRQNT).

References

[1] M. Meulemans, A. Durocher, P. Versailles, G. Bourque, and J. M. Bergthorson. “Calibration techniques for quantitative NO measurement using Laser-Induced Fluorescence”. In: *Journal of Quantitative Spectroscopy and Radiative Transfer* 330 (2025), p. 109221.

[2] P. Singh, D. Yadav, and E. S. Pandian. “Link between air pollution and global climate change”. In: *Global Climate Change*. Elsevier Inc., 2021, pp. 79–108.

[3] J. A. Miller and C. T. Bowman. “Mechanism and modeling of nitrogen chemistry in combustion”. In: *Progress in Energy and Combustion Science* 15 (1989), pp. 287–338.

[4] P. Glarborg, J. A. Miller, B. Ruscic, and S. J. Klippenstein. “Modeling nitrogen chemistry in combustion”. In: *Progress in Energy and Combustion Science* 67 (2018), pp. 31–68.

[5] H. J. Curran. “Developing detailed chemical kinetic mechanisms for fuel combustion”. In: *Proceedings of the Combustion Institute* 37 (2019), pp. 57–81.

[6] M. C. Drake, J. W. Ratcliffe, R. J. Blint, C. D. Carter, and N. M. Laurendeau. “Measurements and modeling of flamefront NO formation and superequilibrium radical concentrations in laminar high-pressure premixed flames”. In: *Symposium (International) on Combustion* 23.1 (1990), pp. 387–395.

[7] A. A. Konnov, I. V. Dyakov, and J. De Ruyck. “Probe sampling measurements and modeling of nitric oxide formation in methane-air flames”. In: *Combustion Science and Technology* 169.1 (2001), pp. 127–153.

[8] I. V. Dyakov, J. De Ruyck, and A. A. Konnov. “Probe sampling measurements and modeling of nitric oxide formation in ethane + air flames”. In: *Fuel* 86.1-2 (2007), pp. 98–105.

[9] W. Kim, H. Do, M. G. Mungal, and M. A. Cappelli. “Investigation of NO production and flame structure in plasma enhanced premixed combustion”. In: *Proceedings of the Combustion Institute* 31 (2007), pp. 3319–3326.

[10] J. Blauwens, B. Smets, and J. Peeters. “Mechanism of “prompt" NO formation in hydrocarbon flames”. In: *Symposium (International) on Combustion* 16.1 (1977), pp. 1055–1064.

[11] N. Lamoureux and P. Desgroux. “*In situ* laser-induced fluorescence and *Ex situ* cavity ring-down spectroscopy applied to NO measurement in flames: Microprobe perturbation and absolute quantification”. In: *Energy and Fuels* 35.9 (2021), pp. 7107–7120.

[12] H. K. Newhall and E. S. Starkman. “Direct spectroscopic determination of Nitric Oxide in reciprocating engine cylinders”. In: *SAE Technical Papers* 76 (1968), pp. 743–762.

[13] M. D. Di Rosa, A. Y. Chang, and R. K. Hanson. “Continuous wave dye-laser technique for simultaneous, spatially resolved measurements of temperature, pressure, and velocity of NO in an underexpanded free jet”. In: *Applied Optics* 32.21 (1993), p. 4074.

[14] D. S. Liscinsky and M. F. Zabielski. "*In situ* resonant ultraviolet absorption of nitric oxide at high pressure". In: *Measurement Science and Technology* 11.7 (2000), pp. 912–919.

[15] H. Trad, P. Higelin, and C. Mounaim-Rousselle. "Nitric oxide detection inside the cylinder of an SI engine by direct UV absorption spectroscopy". In: *Optics and Lasers in Engineering* 43.1 (2005), pp. 1–18.

[16] R. S. Barlow and C. D. Carter. "Raman/Rayleigh/LIF measurements of Nitric Oxide formation in turbulent hydrogen jet flames". In: *Combustion and Flame* 97.3-4 (1994), pp. 261–280.

[17] J. R. Reisel, C. D. Cartel, and N. M. Laurendeau. "Measurements and modeling of OH and NO in premixed $C_2H_6/O_2/N_2$ flames at atmospheric pressure". In: *Energy and Fuels* 11 (1997), pp. 1092–1100.

[18] C. S. Cooper, R. V. Ravikrishna, and N. M. Laurendeau. "Comparisons of laser-saturated, laser-induced, and planar laser-induced fluorescence measurements of nitric oxide in a lean direct-injection spray flame". In: *Applied Optics* 37.21 (1998), p. 4823.

[19] W. G. Bessler, C. Schulz, T. Lee, D. I. Shin, M. Hofmann, J. B. Jeffries, J. Wolfrum, and R. K. Hanson. "Quantitative NO-LIF imaging in high-pressure flames". In: *Applied Physics B: Lasers and Optics* 75.1 (2002), pp. 97–102.

[20] N. Chai, W. D. Kulatilaka, S. V. Naik, N. M. Laurendeau, R. P. Lucht, J. P. Kuehner, S. Roy, V. R. Katta, and J. R. Gord. "Nitric Oxide concentration measurements in atmospheric pressure flames using electronic-resonance-enhanced coherent anti-Stokes Raman scattering". In: *Applied Physics B: Lasers and Optics* 88.1 (2007), pp. 141–150.

[21] L. Pillier, M. Idir, J. Molet, A. Matynia, and S. De Persis. "Experimental study and modelling of NO_x formation in high pressure counter-flow premixed CH_4/air flames". In: *Fuel* 150 (2015), pp. 394–407.

[22] C. Brackmann, T. Methling, M. Lubrano Lavadera, G. Capriolo, and A. A. Konnov. "Experimental and modeling study of nitric oxide formation in premixed methanol + air flames". In: *Combustion and Flame* 213 (2020), pp. 322–330.

[23] P. Versailles, A. Durocher, G. Bourque, and J. M. Bergthorson. "Effect of high pressures on the formation of nitric oxide in lean, premixed flames". In: *Journal of Engineering for Gas Turbines and Power* 143 (2021), p. 051029.

[24] A. C. Eckbreth. *Laser diagnostics for combustion temperature and species*. Ed. by Gordon and Breach Publishers. Second. 1996.

[25] K. Kohse-Höinghaus. "Laser techniques for the quantitative detection of reactive intermediates in combustion systems". In: *Progress in Energy and Combustion Science* 20 (1994), pp. 203–279.

[26] A. Steinberg and S. Roy. *Optical diagnostics for reacting and non-reacting flows: Theory and Practice*. Ed. by T. C. Lieuwen. Vol. 264. 2023.

[27] J. W. Daily. "Laser induced fluorescence spectroscopy in flames". In: *Progress in Energy and Combustion Science* 23 (1997), pp. 133–199.

[28] N. M. Laurendeau. *Statistical thermodynamics: Fundamentals and applications*. 2005, pp. 1–466.

[29] R. K. Hanson, R. M. Spearrin, and C. S. Goldenstein. *Spectroscopy and optical diagnostics for gases*. 2016, pp. 1–279.

[30] J. Brzozowski, P. Erman, and M. Lyyra. "Predissociation rates and perturbations of the A, B, B', C, D and F states in NO studied using time resolved spectroscopy". In: *Physica Scripta* 14 (1976), pp. 290–297.

[31] J. Luque and D. R. Crosley. "Radiative and predissociative rates for NO $A^2\Sigma^+\nu' = 0 - 5$ and $D^2\Sigma^+\nu' = 0 - 3$". In: *Journal of Chemical Physics* 112 (2000), pp. 9411–9416.

[32] J. B. Simeonsson, S. A. Elwood, M. Niebes, R. Carter, and A. Peck. "Trace detection of NO and NO_2 by photoionization and laser induced fluorescence techniques". In: *Analytica Chimica Acta* 397 (1999), pp. 33–41.

[33] W. G. Bessler, C. Schulz, S. Volker, and J. W. Daily. "A versatile modeling tool for nitric oxide LIF spectra". In: *Proceedings of the Third Joint Meeting of the U.S. Sections of The Combustion Institute*. Chicago, 2003, P105.

[34] P. Versailles, G. M. G. Watson, A. C. A. Lipardi, and J. M. Bergthorson. "Quantitative CH measurements in atmospheric-pressure, premixed flames of C_1-C_4 alkanes". In: *Combustion and Flame* 165 (2016), pp. 109–124.

[35] S. V. Naik and N. M. Laurendeau. "Spectroscopic, calibration and RET issues for linear laser-induced fluorescence measurements of nitric oxide in high-pressure diffusion flames". In: *Applied Physics B: Lasers and Optics* 79 (2004), pp. 641–651.

[36] T. Verreycken, R. M. Van Der Horst, N. Sadeghi, and P. J. Bruggeman. "Absolute calibration of OH density in a nanosecond pulsed plasma filament in atmospheric pressure He-H_2O: Comparison of independent calibration methods". In: *Journal of Physics D: Applied Physics* 46 (2013).

[37] J. W. Daily, W. G. Bessler, C. Schulz, V. Sick, and T. B. Settersten. "Role of nonstationary collisional dynamics in determining nitric oxide LIF spectra". In: *42nd AIAA Aerospace Sciences Meeting and Exhibit*. January. 2004.

[38] W. P. Partridge and N. M. Laurendeau. "Formulation of a dimensionless overlap fraction to account for spectrally distributed interactions in fluorescence studies". In: *Applied Optics* 34.15 (1995), p. 2645.

[39] J. Luque and D. R. Crosley. *LIFBASE Version 2.1.1, Database and spectral simulation for diatomic molecules (v1.6)*. 1999.

[40] J. R. Reisel, C. D. Carter, N. M. Laurendeau, and M. C. Drake. "Laser-saturated fluorescence measurements of nitric oxide in laminar, flat, $C_2H_{16}/O_2/N_2$ flames at atmospheric pressure". In: *Combustion Science and Technology* 91 (1993), pp. 271–295.

[41] P. Versailles. "CH formation in premixed flames of C_1-C_4 alkanes: assessment of current chemical modelling capability against experiments". PhD. McGill University, 2017.

[42] W. G. Bessler, C. Schulz, T. Lee, J. B. Jeffries, and R. K. Hanson. "Carbon dioxide UV laser-induced fluorescence in high-pressure flames". In: *Chemical Physics Letters* 375.3 (2003), pp. 344–349.

[43] P. Versailles, A. Durocher, G. Bourque, and J. M. Bergthorson. "Nitric oxide formation in lean, methane-air stagnation flames at supra-atmospheric pressures". In: *Proceedings of the Combustion Institute* 37 (2019), pp. 711–718.

[44] A. Durocher, M. Meulemans, G. Bourque, and J. M. Bergthorson. "Nitric oxide concentration measurements in low-temperature, premixed hydrogen-air stagnation flames at elevated pressures". In: *Proceedings of the Combustion Institute* 39 (2023), pp. 541–550.

[45] P. A. Berg, G. P. Smith, J. B. Jeffries, and D. R. Crosley. "Nitric oxide formation and reburn in low-pressure methane flames". In: *Symposium (International) on Combustion* 27 (1998), pp. 1377–1384.

[46] G. Suck, J. Jakobs, S. Nicklitzsch, T. Lee, W. G. Bessler, M. Hofmann, F. Zimmermann, and C Schulz. "NO Laser-Induced Fluorescence Imaging in the Combustion Chamber of a Spray-Guided Direct-Injection Gasoline Engine". In: *SAE International* 113 (2004), pp. 1043–1056.

[47] T. Lee, J. B. Jeffries, and R. K. Hanson. "Experimental evaluation of strategies for quantitative laser-induced- fluorescence imaging of nitric oxide in high-pressure flames (1-60 bar)". In: *Proceedings of the Combustion Institute* 31 (2007), pp. 757–764.

[48] G. M. Watson, J. D. Munzar, and J. M. Bergthorson. "NO formation in model syngas and biogas blends". In: *Fuel* 124 (2014), pp. 113–124.

[49] A. B. Sahu and R. V. Ravikrishna. "Quantitative LIF measurements and kinetics assessment of NO formation in H_2/CO syngas–air counterflow diffusion flames". In: *Combustion and Flame* 173 (2016), pp. 208–228.

[50] G. M. G. Watson, P. Versailles, and J. M. Bergthorson. "NO formation in premixed flames of C_1-C_3 alkanes and alcohols". In: *Combustion and Flame* 169 (2016), pp. 242–260.

[51] A. Durocher, M. Meulemans, P. Versailles, G. Bourque, and J. M. Bergthorson. "Back to basics - NO concentration measurements in atmospheric lean-to-rich, low-temperature, premixed hydrogen-air flames diluted with argon". In: *Proceedings of the Combustion Institute* 38 (2021), pp. 2093–2100.

[52] M. Meulemans, A. Durocher, G. Bourque, and J. M. Bergthorson. "NO measurements in high temperature hydrogen flames : The crucial role of the hydrogen oxidation chemistry for accurate NO predictions". In: *Combustion and Flame* 261 (2024), p. 113279.

[53] M. Uddi, N. Jiang, I. V. Adamovich, and W. R. Lempert. “Nitric oxide density measurements in air and air/fuel nanosecond pulse discharges by laser induced fluorescence”. In: *Journal of Physics D: Applied Physics* 42 (2009), p. 075205.

[54] G. Cunge, J. P. Booth, and J. Derouard. “Absolute concentration measurements by pulsed laser-induced fluorescence in low-pressure gases: Allowing for saturation effects”. In: *Chemical Physics Letters* 263 (1996), pp. 645–650.

[55] M. Engelhard, W. Jacob, W. Möller, and A. W. Koch. “New calibration method for the determination of the absolute density of CH radicals through laser-induced fluorescence”. In: *Applied Optics* 34.21 (1995), p. 4542.

[56] P. A. Berg, D. A. Hill, A. R. Noble, G. P. Smith, J. B. Jeffries, and D. R. Crosley. “Absolute CH concentration measurements in low-pressure methane flames: Comparisons with model results”. In: *Combustion and Flame* 121.1-2 (2000), pp. 223–235.

[57] K. T. Walsh, M. B. Long, M. A. Tanoff, and M. D. Smooke. “Experimental and computational study of CH, CH*, and OH* in an axisymmetric laminar diffusion flame”. In: *Symposium (International) on Combustion* 27.1 (1998), pp. 615–623.

[58] J. T. Salmon and N. M. Laurendeau. “Calibration of laser-saturated fluorescence measurements using Rayleigh scattering”. In: *Applied Optics* 24.1 (1985), p. 65.

[59] J. Luque and D. R. Crosley. “Absolute CH concentrations in low-pressure flames measured with laser-induced fluorescence”. In: *Applied Physics B: Lasers and Optics* 63.1 (1996), pp. 91–98.

[60] J. Luque, R. J. Klein-Douwel, J. B. Jeffries, G. P. Smith, and D. R. Crosley. “Quantitative laser-induced fluorescence of CH in atmospheric pressure flames”. In: *Applied Physics B: Lasers and Optics* 75 (2002), pp. 779–790.

[61] D. E. Thomas, K. P. Shrestha, F. Mauss, and W. F. Northrop. “Extinction and NO formation of ammonia-hydrogen and air non-premixed counterflow flames”. In: *Proceedings of the Combustion Institute* 39 (2023), pp. 1803–1812.

[62] P. C. Palma, P. M. Danehy, and A. F. Houwing. “Fluorescence imaging of rotational and vibrational temperature in shock-tunnel nozzle flow”. In: *AIAA Journal* 41.9 (2003), pp. 1722–1732.

[63] I. A. Mulla, G. Godard, G. Cabot, F. Grisch, and B. Renou. “Quantitative imaging of nitric oxide concentration in a turbulent *n*-heptane spray flame”. In: *Combustion and Flame* 203 (2019), pp. 217–229.

[64] M. Meulemans, A. Durocher, P. Versailles, G. Bourque, and J. M. Bergthorson. “How well do we know thermal-NO? An investigation of NO formation in flames over a wide temperature range”. In: *Proceedings of the Combustion Institute* 39 (2023), pp. 521–529.

[65] A. Durocher, M. Meulemans, G. Bourque, and J. M. Bergthorson. "Measurements of the laminar flame speed of premixed, hydrogen-air-argon stagnation flames". In: *Applications in Energy and Combustion Science* 7 (2021), p. 100028.

[66] M. Zimmermann, N. Lindlein, R. Voelkel, and K. J. Weible. "Microlens laser beam homogenizer - from theory to application". In: *Laser Beam Shaping VIII* 6663 (2007), p. 666302.

[67] M. D. Di Rosa, K. G. Klavuhn, and R. K. Hanson. "LIF spectroscopy of NO and O_2 in high-pressure flames". In: *Combustion Science and Technology* 118 (1996), pp. 257–283.

[68] W. G. Bessler, C. Schulz, T. Lee, J. B. Jeffries, and R. K. Hanson. "Strategies for laser-induced fluorescence detection of nitric oxide in high-pressure flames. I. A–X(0,0) excitation". In: *Applied Optics* 41.18 (2002), p. 3547.

[69] D. G. Goodwin, H. K. Moffat, I. Schoegl, R. L. Speth, and B. W. Weber. *Cantera: An object-oriented software toolkit for chemical kinetics, thermodynamics, and transport processes (v.3.0.0)*. 2023.

[70] G. Bagheri, E. Ranzi, M. Pelucchi, A. Parente, A. Frassoldati, and T. Faravelli. "Comprehensive kinetic study of combustion technologies for low environmental impact: MILD and OXY-fuel combustion of methane". In: *Combustion and Flame* 212 (2020), pp. 142–155.

[71] Y. Song et al. "The sensitizing effects of NO_2 and NO on methane low temperature oxidation in a jet stirred reactor". In: *Proceedings of the Combustion Institute* 37 (2019), pp. 667–675.

[72] G. P. Smith et al. "GRI-Mech 3.0". In: (1999).

[73] University of California at San Diego. *Chemical-Kinetic Mechanisms for Combusiton Applications*. 2016.

[74] P. H. Paul, C. Carter, J. A. Gray, J. L. Durant, J. Thomson, and M. Furlanetto. *Correlations for the NO $A^2\Sigma^+$ (ν'=0) electronic quenching cross-section*. Tech. rep. Sandia National Lab. (SNL-CA), Livermore, CA (United States), 1995.

[75] P. H. Paul, J. A. Gray, J. L. Durant, and J. W. Thoman. "A model for temperature-dependent collisional quenching of NO $A^2\ \Sigma^+$". In: *Applied Physics B Photophysics and Laser Chemistry* 57.4 (1993), pp. 249–259.

[76] M. Tamura, P. A. Berg, J. E. Harrington, J. Luque, J. B. Jeffries, G. P. Smith, and D. R. Crosley. "Collisional quenching of CH(A), OH(A), and NO(A) in low pressure hydrocarbon flames". In: *Combustion and Flame* 114 (1998), pp. 502–514.

[77] T. B. Settersten, B. D. Patterson, and J. A. Gray. "Temperature- and species-dependent quenching of NO $A^2\Sigma^+$ (ν'=0) probed by two-photon laser-induced fluorescence using a picosecond laser". In: *Journal of Chemical Physics* 124 (2006).

[78] T. B. Settersten, B. D. Patterson, and C. D. Carter. "Collisional quenching of NO $A^2\Sigma^+$ (ν'=0) between 125 and 294 K". In: *Journal of Chemical Physics* 130 (2009), p. 204302.

[79] B. C. Connelly, B. A. V. Bennett, M. D. Smooke, and M. B. Long. “A paradigm shift in the interaction of experiments and computations in combustion research”. In: *Proceedings of the Combustion Institute* 32 (2009), pp. 879–886.

[80] R. V. Ravikrishna, S. V. Naik, C. S. Cooper, and N. M. Laurendeau. “Quantitative laser-induced fluorescence measurements and modeling of nitric oxide in high-pressure (6-15 atm) counterflow diffusion flames”. In: *Combustion Science and Technology* 176 (2004), pp. 1–21.

Bridging the use of a low-uncertainty NO-LIF calibration technique to the investigation of thermal NO in methane flames

To fulfill the objectives of this thesis, *i.e.* studying the NO modelling chemistry by promoting thermal NO and providing the modelling community with a full set of data of high confidence levels, a review of several NO-LIF calibration methodologies was performed in the previous chapter to obtain low-uncertainty and high-resolution NO measurements.

Among the several calibration techniques presented, it was shown that, for high temperature, atmospheric, lean flames, the measurement of NO can be performed using the C_{opt} calibration technique combined with the assumption of constant interfering LIF signal. This technique allows to quantitatively compare the experimental results to numerical predictions under low uncertainty as well as to provide a molar fraction calculation of the NO produced by the flames. This is particularly suited to study the current state of understanding of the NO chemistry by comparing numerical predictions to experimental results, and to provide a high resolution and low uncertainty NO concentration dataset to the modelling community. Hence, this calibration technique was employed to obtain NO measurements for the remainder of the thesis.

The investigation of the NO chemistry is first studied under current gas turbine representative conditions, in high-temperature methane-air flames, promoting the thermal NO pathway over the contribution of the prompt, N_2O, and NNH pathways. To permit the assessment of current NO models, three measurements are carried out: velocity, temperature, and NO concentrations. While the later permits the direct study of the NO formation chemistry, the velocity and temperature measurements are necessary to ensure that the basic thermodynamic and kinetic properties of the flames are accurately predicted. Velocity and temperature measurements are directly representative of the modelling of the core H_2/O_2 chemistry and major species involved in the methane-air flames. Any disagreements in such measurements would be indicative of major errors in the combustion modelling of, not only the NO chemistry, but also the core chemistry on which it is highly dependent. Hence, these measurements are compared to the predictive capabilities of several thermochemical models, assumed to be representative of the current state of understanding of the modelling chemistry of NO of methane-air flames.

Chapter IV. How well do we know thermal-NO? An investigation of NO formation in flames over a wide temperature range

Publication [1] in *Proceeding of the Combustion Institute*, volume 39, Issue 1, 2023, pages 521−529.

M. Meulemans[a], A. Durocher[a], P. Versailles[b], G. Bourque[a,b], and J. M. Bergthorson[a]

[a] Alternative Fuels Laboratory, McGill University, 817 Sherbrooke St W, Montréal, H3A 0C3, QC, Canada

[b] Siemens Energy Canada Limited, 9545 Chemin de la côte de Liesse, Dorval, H9P 1A5, QC, Canada

IV.1 Abstract

This study investigates the large variability and uncertainty in the thermal-initiation reaction rates found in the literature. An experimental study is conducted at atmospheric pressure in lean, premixed, laminar methane-air stagnation flames. Flame temperatures ranging from 1900 K to 2500 K are achieved by varying the argon concentration, in 21% and 40% oxygen mixtures balanced with nitrogen. The conditions are selected to promote the thermal route in the overall post-flame NO formation. One-dimensional velocity, temperature, and NO concentration profiles are measured with Particle Tracking Velocimetry (PTV), NO multi-line thermometry, and NO Laser-Induced Fluorescence (NO-LIF), respectively. While velocity and temperature measurements are accurately predicted by different thermochemical models, the simulated NO-LIF signal profiles show significant disagreement and large variability, relative to the measurements. Results show that, across all conditions, none of the studied mechanisms are able to capture accurately both the NO concentration, and formation rate in the post-flame region, suggesting that the fundamental chemistry remains inaccurate. The discrepancy in the predictions appears to be linked to the chosen parameters of the Arrhenius rate, specifically the pre-exponential factor, and the activation energy. Sensitivity and Reaction Pathway Analyses suggest that the differences in the Arrhenius parameters could originate from different consideration of the base radical chemistry, as well as different relative contributions of the four NO-formation routes. As a result, some models can predict sim-

ilar NO concentrations but using significantly different underlying base and NO_x chemistry. This implies that the models could diverge significantly in conditions where other non-thermal routes are more important. This study demonstrates the need for spatially-resolved experimental data across a broad range of experimental conditions, promoting and considering a variety of routes, in order to optimise NO_x chemistry models with reduced uncertainty.

IV.2 Introduction

Nitric oxide (NO) is highly regulated to limit its harmful impact on the environment and human health. The understanding of its formation is of interest to meet these regulations in practical systems. Many studies have been performed using a variety of experimental configurations and conditions to promote specific NO formation pathways, or routes, namely the prompt-NO, the NNH, the N_2O, and the thermal routes [2–7].

The main pathway to NO formation in traditional combustion applications is generally the thermal route, which scales with temperature and residence time. It has been extensively studied, experimentally and numerically, via its limiting reaction:

$$N_2 + O \underset{k_r}{\overset{k_f}{\rightleftharpoons}} NO + N \tag{R1}$$

Despite its importance and the large amount of experimental data available, wide uncertainty and variability remains in the rate of the reaction, as shown for the reverse direction of R1 in Fig. IV.1.

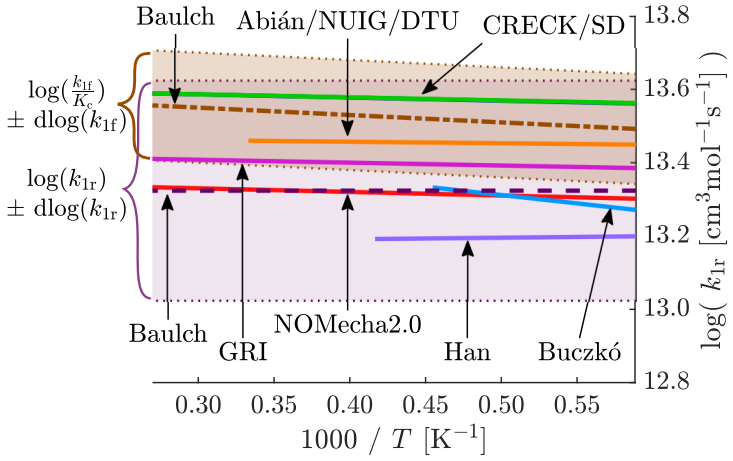

Figure IV.1: Comparison of the reverse kinetic rate (k_{1r}) for the reaction $N_2 + O \rightleftharpoons NO + N$, of the mechanisms and references used in this study (–). k_{1r} as provided (- -) and calculated from k_{1f} and K_c (-.-) in Baulch *et al.* [8].

In the compilation work of Baulch *et al.* [8], a recommended reaction rate for both, the forward ($k_{1\mathrm{f}}$) and reverse ($k_{1\mathrm{r}}$), directions are provided independently. However, when the reverse rate is derived from the recommended forward rate ($k_{1\mathrm{f}}$) and the equilibrium constant (K_{c}), its value and uncertainty do not overlap the recommended reverse rate ($k_{1\mathrm{r}}$) at high temperatures, see Fig. IV.1. This also shows the scatter of more recently determined rates, which suggests that the understanding of thermal-NO route, and thus the post-flame NO chemistry, remains uncertain.

Abián *et al.* [4] proposed a thermal-initiation rate ($k_{1\mathrm{f}}$) using flow reactor measurements performed at temperatures ranging from 1700 K to 1800 K. However, lacking data to accurately derive Arrhenius rate coefficients, they used literature data to extrapolate a rate covering temperatures from $250-3000$ K, a more practical range of conditions. Buczkó *et al.* [9] characterized the uncertainty of this rate and provided corrected values, by considering the interaction of the N_2O pathway on the thermal rate. Similarly targeting the thermal rate, Han *et al.* [10] performed NO measurements on a heat flux burner using a wide range of conditions, and observed the interaction of the prompt and the thermal routes. As demonstrated, these studies account for different interactions of the NO formation pathways and thus infer different thermal-initiation rates. Therefore, it is still unclear how all the routes interact together, particularly in the post-flame region.

The objective of this study addresses this ambiguity by measuring NO over extreme temperature conditions, to promote the thermal NO pathway. The focus of this study is the post-flame region where the thermal pathway is dominant and NO is most affected by the four routes. Additionally, the use of extreme conditions challenges six thermochemical models across a wide range of temperatures. These experiments are conducted in atmospheric, lean, premixed, methane-air stagnation flames, at flame temperatures ranging from 1900 K to 2500 K. Flame temperatures are reached by varying argon concentration, in 21% and 40% oxygen balanced in nitrogen. Spatially-resolved measurements are used, inline with current trends in the literature that increasingly recommend the use of time-resolved measurements to improve the predictions of thermochemical mechanisms, particularly those which involve complex formation pathways [11–13].

IV.3 Experimental Methods

An atmospheric jet-wall stagnation burner is used to conduct experiments in premixed flames. This provides accurate boundary conditions necessary for 1D simulations [14]. This setup, along with the diagnostic methods, have been detailed in [3, 5, 15–17].

The gas mixture is premixed before exiting the nozzle and impinging on a water-cooled stagnation plate located at a distance of ~ 9 mm. This provides a flat, lifted flame, minimally affected by the burner, as shown in Fig. IV.2. The flame is shielded from ambient air by a nitrogen coflow, improving stability and preventing chemical interference. Flame temperatures from 1900 K to

2500 K are used to promote the thermal pathway. These temperatures are reached by producing lean methane-air-argon flames at a constant equivalence ratio ($\phi = 0.9$) with two oxygen to nitrogen ratios: 21% and 40%. Argon dilution, up to 65% in the oxidizer stream, allows different flame temperatures to be obtained while maintaining the same stoichiometry. Mixture concentrations are defined as:

$$\mathrm{O_2\text{-}to\text{-}N_2} = \frac{N_{\mathrm{O_2}}}{N_{\mathrm{O_2}} + N_{\mathrm{N_2}}}, \text{ and} \tag{IV.1}$$

$$X_{\mathrm{Ar}} = \frac{N_{\mathrm{Ar}}}{N_{\mathrm{O_2}} + N_{\mathrm{N_2}} + N_{\mathrm{Ar}}}, \tag{IV.2}$$

where N_i is the number of moles of species i.

The boundary conditions for the simulations are given in the Supplementary Materials, see Appendix B. The inlet velocity (u_{in}) and the strain rate $(\mathrm{d}u_{\mathrm{in}}/\mathrm{d}z)$ are determined in the unburnt region of the axial velocity profile. The inlet temperature (T_{in}) and the stagnation plate temperature (T_{wall}) are measured during the experiments using thermocouples.

Axial velocity profiles are obtained by Particle Tracking Velocimetry (PTV) [16, 18, 19]. The laser beam illuminates the flow seeded with alumina (Al_2O_3 at 1 μm avg. diameter) tracer particles, to track their instantaneous position. Camera exposures from 20 to 100 ms and laser pulse frequencies from 4 to 10 kHz are used (fixed for a given experiment). The acquisition of over 500 images allows the extraction of a 1D velocity profile of the tracer particle, u_{p}, along the central axis of the burner using a second-order central finite difference scheme, such that:

$$u_{\mathrm{p}}\left(z_{\mathrm{p},i}, r_{\mathrm{p},i}\right) \approx \frac{z_{\mathrm{p},i+1} - z_{\mathrm{p},i-1}}{2} \cdot f \cdot C \tag{IV.3}$$

at the particle location $z_{\mathrm{p},i}$ and $r_{\mathrm{p},i}$, and with f defined as the laser frequency in Hz, and C the camera calibration coefficient in mm/pixel. The direct comparison to simulated velocity profiles is possible through the modeling of the particle motion in the flow. The modeling accounts for drag due to thermophoretic force and particle inertia in high-gradient/high-curvature parts of the flow [20].

The NO concentration profiles are obtained using 2D Planar Laser Induced Fluorescence (PLIF) [5, 6]. NO molecules are excited in the A−X (0,0) electronic system, using an Nd:YAG-pumped

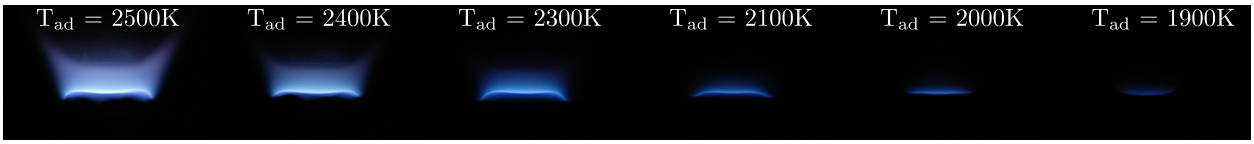

Figure IV.2: Methane stagnation flames from T_{ad} = 2500 K to 1900 K obtained by argon dilution and enriched oxygen.

wavelength-tunable dye laser at a wavelength of ~ 226 nm. The NO fluorescence is collected using an image intensified CCD camera at an exposure of 300 ns and binned 4×8 (vertically and horizontally, respectively) to enhance signal-to-noise ratio. Signals of 2,000 images are captured at an online (S_{on}) and offline (S_{off}) wavelength of $\lambda_{\text{on}}\sim$226.03nm and $\lambda_{\text{off}} \sim 226.05$ nm, respectively, allowing the subtraction of interfering LIF and scattering signals. Signals are corrected for background noise (S_{bckg}) by capturing 200 images without laser irradiation and subtracting them from the samples to remove the effect of flame chemiluminescence, camera dark noise, and ambient luminosity. The resulting signal is normalised by the mean of the time-integrated laser pulse power of the online and offline signals, $E_{\text{L,on}}$ and $E_{\text{L,off}}$ respectively. Spatial fluctuations in the laser sheet are corrected by obtaining the LIF signal in an inert cold flow seeded with NO. For low laser irradiance, the signal F_{NO} is linearly proportional to NO number density as follows:

$$F_{\text{NO}} = \frac{(S_{\text{on}} - S_{\text{bckg}})}{E_{\text{L,on}}} - \frac{(S_{\text{off}} - S_{\text{bckg}})}{E_{\text{L,off}}}, \tag{IV.4}$$

$$= f_{\text{LIF}} \cdot C_{\text{opt}} \cdot n^{\circ}_{\text{NO}}, \tag{IV.5}$$

where f_{LIF} is the number of photons emitted per unit molecule of NO, per unit volume, and per laser energy, C_{opt} is the optical calibration coefficient accounting for optic transmitivity and camera sensitivity, and $\text{n}^{\circ}_{\text{NO}}$ is the number density of NO molecules. f_{LIF} is obtained using a two-level LIF model, allowing C_{opt} to be determined by calibration [3, 6]. These are further explained in the Supplementary Materials, see Appendix B. Based on the *paradigm shift* presented by Connelly *et al.* [21], species concentration and temperature from the numerical solutions are used to derive numerical NO-LIF profiles, directly comparable to the measured NO-LIF profiles. This prevents the introduction of uncertainty through unit transformations of the experimental profiles, which require assumptions of temperature and quenching-species concentration (H_2O, O_2, ...) that are not measured.

The NO-LIF profiles presented in this paper result from an average of several profiles obtained for each flame, from 2 to 7 measurements per condition, leading to a total of 48 flames used to determine C_{opt}. The experimental uncertainty associated with this measurement is calculated at $z = 3.5$mm, and is reported on the NO-LIF profiles and on the subsequent figures. The large number of flames used for calibration leads to an uncertainty of less than 3% across all conditions, in the post-flame region. Details of the calculations are given in the Supplementary Materials, see Appendix B. The resulting NO-LIF profiles, while having a relatively high accuracy in the post-flame region, might still experience experimental uncertainty in the flame front due to the imaging system (image binning and point spread function), the chemiluminescence of the flame, as well as the sharp change of density, NO concentration, and temperature of the flow.

Temperature profiles are measured using a multi-line NO-LIF thermometry approach [15, 22]. The flames are seeded with a known concentration of NO (500 ppm) to track the emitted fluorescence from the nozzle to the plate while varying the laser over 120 discrete wavelengths between $\lambda = 225.13$ nm and $\lambda = 225.19$ nm. The raw NO signal intensity and laser energy are measured similarly to the NO-LIF methodology. The unseeded and background signals are subtracted in order to maximise signal-to-noise ratio. For each wavelength, the NO signal is averaged over 50 laser pulses. An NO excitation spectrum is obtained for each pixel of the domain and is directly compared to LIFBase [23] NO-excitation spectra, which vary with temperature, to determine the temperature field of the domain. A 1D temperature profile is extracted at the centerline of the nozzle and is directly compared to simulation results. This temperature measurement methodology leads to an uncertainty of $\pm 5\%$ at 2000 K [22]. While this methodology has proven successful in previous works, the excitation spectra are less sensitive for temperatures greater than 2300 K, leading to increased uncertainty (see Fig. IV.3d).

IV.4 Results and discussion

Three flames are stabilized at 21% oxygen-to-nitrogen ratio (O_2-to-$N_2 = 21\%$, or $21\%O_2$) with different levels of argon dilution to reach adiabatic flame temperatures of 1900 K, 2000 K, and 2130 K, and six flames at O_2-to-$N_2 = 40\%$ ($40\%O_2$) to obtain adiabatic flame temperatures from 2000 K to 2500 K. An overlap at 2000 K is used for both oxygen ratios to assess the role of the oxygen content on NO formation.

The predictive capabilities of several thermochemical models are evaluated by comparison to the measured profiles. In this paper, the following thermochemical models are evaluated: GRI-Mech3.0 (GRI) [24]; the San Diego 2016 mechanism (SD) with the 2018 NO_x chemistry [25]; the Chemical Reaction Engineering and Chemical Kinetics mechanism C1C3HT version 1412 (CRECK) [26]; the National University of Ireland, Galway mechanism NUIGMech1.1 (NUIG) [27] reduced to 206 species [28]; the Technical University of Denmark 2016 mechanism (DTU) [29]; and the Konnov 0.6 mechanism [30] with the NO_x chemistry of NOMecha2.0 [7] (KON). While the NOMecha2.0 sub-mechanism has been optimised with the GDF-Kin3.0 base chemistry [31], the latter has shown large discrepancies in predicting velocity profiles of previous experiments [19]. Instead, NOMecha2.0 has been paired to Konnov 0.6 base chemistry, showing better agreement. Furthermore, both NUIG and DTU mechanisms have developed their NO_x chemistry based on the recent review paper by Glarborg *et al.* [32].

These simulations are performed using Cantera's *Impinging Jet* model [33], including multicomponent modeling of the transport coefficients, as well as radiative heat losses. The grids are

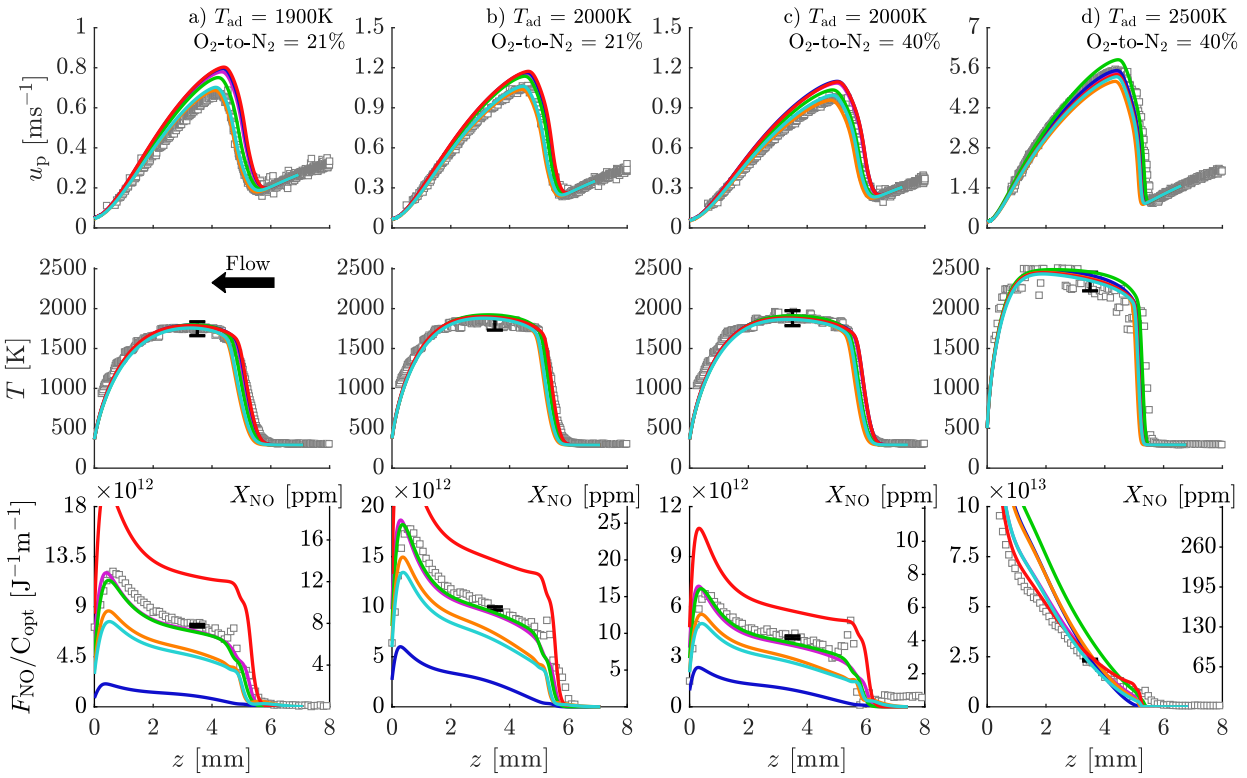

Figure IV.3: Profiles of velocity (top), temperature (middle), and NO-LIF signal (bottom). Measured (▫) and simulated (—) profiles are illustrated. Different thermochemical models are shown: GRI (—), SD (—), CRECK (—), NUIG (—), DTU (—) and KON (—). Note the different scales of the velocity and NO-LIF profiles. The vertical axes to the right of the NO-LIF signal profiles represent the estimate of NO concentration in ppm.

refined to achieve criteria of 2, 0.05, and 0.05, for ratio, curve, and slope, respectively, with a 1μm minimum grid size, leading to solutions with $\sim$ 350 gridpoints.

Velocity, temperature, and NO-LIF signals are presented in Fig. IV.3a−d, for the lowest (1900 K), the two overlapping (2000 K), and the highest (2500 K) temperatures, respectively. The results of all nine flames are presented in the Supplementary Materials, see Appendix B. The flow exits the nozzle at $z \sim 9$ mm and impinges on the wall at $z = 0$ mm. Estimates of the NO concentration in ppm, valid for the post-flame region only, are extracted from the comparison to a reference mechanism, in this case GRI. These are presented on the right-hand vertical axis of the NO-LIF signal graphs. However, conclusions are drawn from F_{NO}/C_{opt} as this carries less uncertainty.

The general behaviour of the measured velocity profiles is correctly described by the models. The particles decelerate gradually from the inlet to the flame front, reaching the reference flame speed $S_{u,ref}$, and then accelerate through the flame front due to thermal expansion of the flow. They decelerate again as the flow impinges on the stagnation plate. As expected from flame theory, $S_{u,ref}$ increases with T_{ad}. Additionally, there is little difference in velocity for the two oxygen contents at

2000 K. Despite overall good agreement between the mechanisms in predicting the axial velocity of the particles, a slight difference in flame position and flame speed can be observed between the models and measurements. This discrepancy is amplified in the high-curvature and -velocity region downstream of the flame front, leading to an underprediction of the velocity by DTU and NUIG and an over-estimation of the velocity by most other mechanisms considered.

For all cases, there is also good agreement between the measured and simulated temperature profiles. The temperature rises through the flame front to reach a maximum temperature of the order of the adiabatic temperature in the post-flame region. It then decreases through the wall thermal boundary layer to reach T_{wall}. Temperature predictions are within the uncertainty of the measurement technique.

The NO-LIF profiles have the characteristic sharp increase from flame-front NO (at $z \sim 6\,\mathrm{mm}$), and slow increase from the post-flame NO (from $z \sim 5\,\mathrm{mm}$ to $z \sim 1.5\,\mathrm{mm}$). The signal increases near the plate (from $z \sim 1\,\mathrm{mm}$ to $z = 0\,\mathrm{mm}$) from the change in NO density due to the thermal boundary layer. Additionally, at a spatial location, the NO signal increases with the increase in T_{ad}, as expected. As T_{ad} increases, the contribution of post-flame NO increases relative to the flame-front NO. Finally, at the overlap T_{ad}, a smaller NO concentration is produced at higher oxygen content as a larger dilution of Ar is needed. This leads to lower initial O- and N-atom availability, producing less NO.

In contrast to the temperature and velocity profiles, the measured NO-LIF profiles are only well described by a few thermochemical models, and a large variability of predictions can be observed over the entire range of temperatures. Discrepancies in both the flame-front and post-flame NO are present. The signal increase through the flame front is generally only properly captured by GRI and CRECK across all conditions, unlike KON which largely overpredicts it, and other mechanisms which underpredict it. These results support previous findings [2, 3], where an important discrepancy was found in the prediction of CH concentration in these mechanisms for various fuels, leading to a misprediction of the prompt-NO produced through the flame front. In addition, the absence of the prompt initiation reaction in the SD model leads to a greater underprediction of the NO produced in the entire profile. For low temperatures, the misprediction in the post-flame NO appears to be consistent with the discrepancies in the flame-front region. This shows that a correct description of the post-flame NO requires an accurate description of the flame-front NO.

Furthermore, some mechanisms achieve good agreement with the measurements at specific points, despite having a strong disagreement throughout the rest of the profile. This can be seen on the NO-LIF profile for 2500 K (Fig. IV.3d), where most mechanisms intersect the experimental profile at $z \sim 4\,\mathrm{mm}$. This demonstrates the necessity of including spatially- or time-resolved measurements to understand the origin of discrepancy in complex formation pathways.

To specifically target the post-flame region, comparisons between measurements and simulations of the NO-LIF signal are performed at $z = 3.5$ mm. This location is far enough from the thermal boundary layer of the plate and allows enough time for the post-flame NO to develop. The analysis, at this location, of the absolute NO signal ($F_{\mathrm{NO}}/C_{\mathrm{opt}}$) is presented on Fig. IV.4a−c, and the analysis of the NO signal rate of change ($\mathrm{d}F_{\mathrm{NO}}/(C_{\mathrm{opt}} \cdot \mathrm{d}z)$) on Fig. IV.4d−f.

The ratio of the absolute NO signal is presented in Fig. IV.4b−c for 21%O_2 and 40%O_2, respectively. A perfect agreement between the models and measurements would be described by a ratio equal to unity. The shaded area represents the root-sum square of both the experimental and the numerical uncertainties, the latter emanating from uncertainty in the estimated boundary conditions. A larger uncertainty ($\sim 20\%$) is present for low temperature measurements as they produce less NO, leading to smaller LIF signal-to-noise ratio. Conversely, there is lower uncertainty ($\sim 6\%$) at high temperature due to higher signal-to-noise ratio from increased NO production. These uncertainties make these experimental datasets valuable additions to model optimisation.

The figures show that the difference between the measurements and simulations, for both oxygen contents, changes with temperature. The large variability of predictions is mostly present at low temperatures, and appears to stem mostly from the flame-front NO prediction, as observed

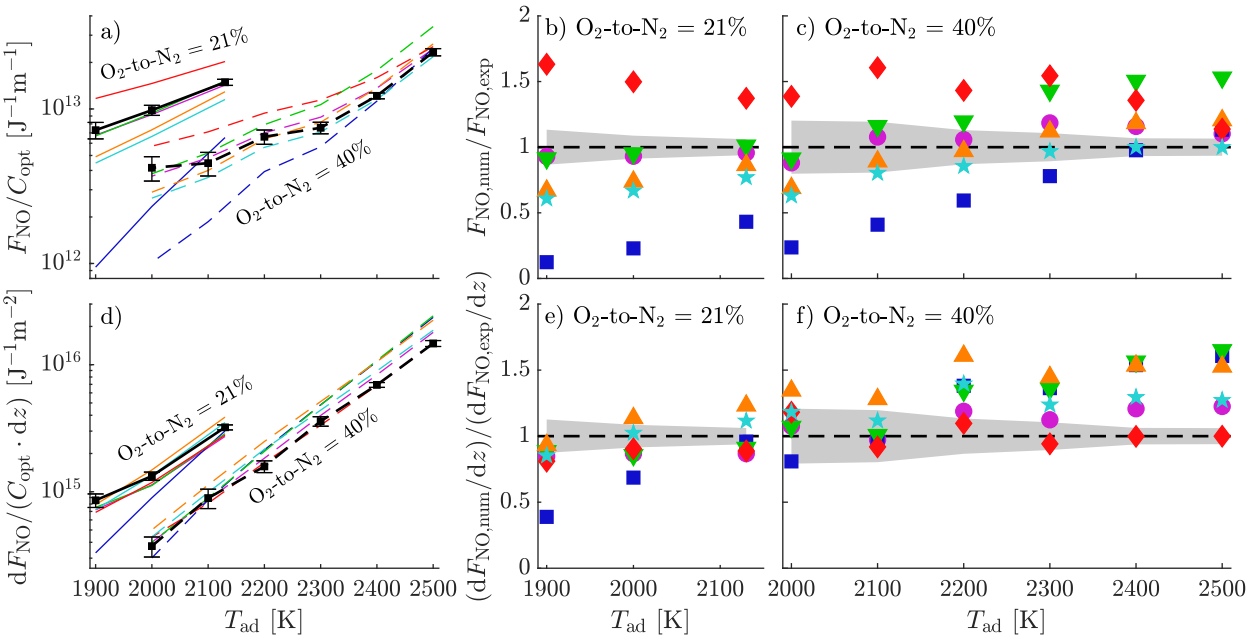

Figure IV.4: Comparison of experimental (black lines and symbols) and numerical (coloured lines and symbols), at $z = 3.5$ mm for: a) Absolute NO-LIF signal, b−c) Ratio of numerical to experimental absolute NO-LIF signals, d) NO-LIF signal slope, e−f) Ratio of numerical to experimental NO-LIF signal slopes. Different thermochemical models represented by the following colours and lines: GRI (●), SD (■), CRECK (▼), NUIG (▲), DTU (★) and KON (◆). Shaded areas represent the root-sum square of both the experimental and numerical uncertainties.

in Fig. IV.3. This again indicates that the flame-front NO is not accurately captured, and its mis-prediction impacts mostly conditions where thermal NO is not dominant. Similar to previous observations, only CRECK and GRI capture the absolute NO signals at 3.5 mm, up to 2200 K.

To better understand the prediction of post-flame NO by the mechanisms, the rate of change of the signal $(\mathrm{d}F_{\mathrm{NO}}/(C_{\mathrm{opt}} \cdot \mathrm{d}z))$, or slope of $F_{\mathrm{NO}}/C_{\mathrm{opt}}$, is calculated for the measured and simulated profiles. It is determined by a linear regression of the signals between 2 and 4.5 mm. The values are presented in Fig. IV.4d and ratios of numerical to experimental values in Fig. IV.4e−f for 21%O_2 and 40%O_2, respectively. Overall, all mechanisms tend to be in reasonable agreement with the measured NO rate of formation at temperatures below 2200 K. From 2200 K, all mechanisms, except for KON, exhibit significant discrepancies. In contrast, KON reasonably predicts the post-flame NO rate of formation, across the entire range of temperatures, despite the significant overprediction of the flame-front NO.

Interestingly, it is at the highest temperature, where the mechanisms are most challenged, that the widest spread of predictions can be observed in between the different models. At this condition, despite the small experimental and numerical uncertainty, KON precisely predicts $\mathrm{d}F_{\mathrm{NO}}/(C_{\mathrm{opt}} \cdot \mathrm{d}z)$. In contrast, CRECK overpredicts the rate of formation by 65%. These results can directly be correlated with the Arrhenius rates illustrated in Fig. IV.1. KON (NOMecha2.0) possesses the best agreement with the slope measurements at 2500 K and it uses a rate with the lowest pre-exponential factor (A), and is inline with the recommended $k_{1\mathrm{r}}$ from Baulch *et al.* [8]. Furthermore, GRI, DTU & NUIG, and CRECK & SD, in this order, possess an increasing pre-exponential factor, and Fig. IV.4f shows that their overprediction is also in the same order. This demonstrates that the error in prediction of $\mathrm{d}F_{\mathrm{NO}}/(C_{\mathrm{opt}} \cdot \mathrm{d}z)$ grows with A. Additionally, KON seems to accurately predict the correlation of the slope with temperature, indicating an accurate definition of the activation energy (E_{a}). These nuances in the reaction rates of each model could cause the differences in predictions in Fig. IV.4.

The sources of the differences in the models is explored in Fig. IV.5 with a Sensitivity Analysis performed on the NO rate of formation at $z = 3.5$ mm, on the reactions of the KON and GRI mechanisms. This analysis demonstrates that the slope is most sensitive to the thermal-initiation reaction (N_2 + O), across the studied temperatures. As expected, the influence of this reaction on the slope increases with temperature. In contrast, the reaction H + O_2, driving O-atom production, is inversely correlated with the slope, and its impact reduces with temperature. This illustrates the importance of an accurate base radical chemistry to precisely predict NO production as it controls the radical pool size, for the entire range of temperatures, and especially at low temperatures. The set of reactions involved in defining the slope of NO though the N_2O pathway, has a reduced impact with increasing temperature. However, its influence at low temperatures is of similar order to the thermal. This shows that the N_2O pathway is particularly important in defining the thermal rate

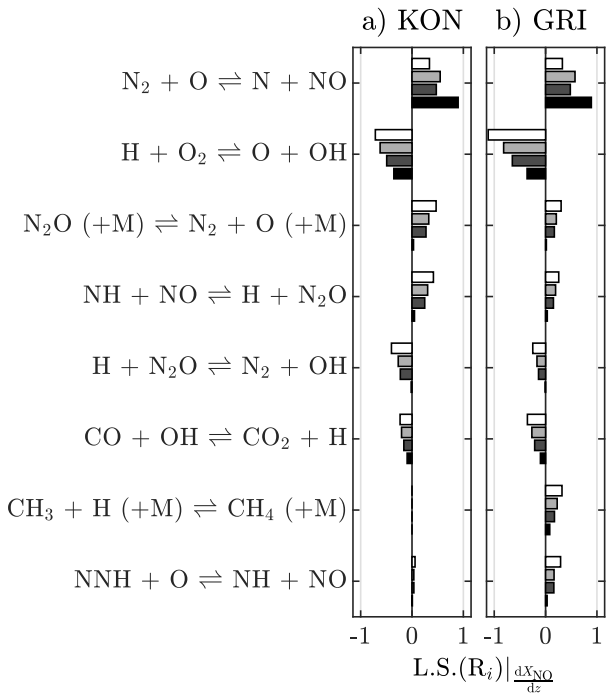

Figure IV.5: Sensitivity Analysis performed on $\mathrm{d}X_{\mathrm{NO}}/\mathrm{d}z$, for the KON (a) and GRI (b) mechanisms, using $\mathrm{d}k = 1\%$ on each reaction. Bars represent the four flames of Fig. IV.3, 1900 K – 21%O_2 (white), 2000 K – 21%O_2 (light grey), 2000 K – 40%O_2 (dark grey), 2500 K – 40%O_2 (black).

at lower temperatures. A similar observation can be made with the NNH reaction that is of more significant importance for GRI compared to KON.

These results demonstrate the importance of accurately predicting the N_2O and NNH pathways, and the base radical chemistry, as they have a significant influence on the post-flame NO. Therefore, if models would recommend an accurate thermal-initiation rate, they would require accurate modeling of each of the NO-producing pathways and the base radical chemistry. This could aid in resolving the variability of the thermal-initiation rate, shown in Fig. IV.1, via the A and E_{a} parameters.

As the Sensitivity Analysis showed the importance of the N_2O pathway, a Reaction Pathway Analysis (RPA) is performed to determine the contribution of all four routes to the overall NO production. This is conducted on the 2500 K flame, following the methodology established by Grcar *et al.* [34] and Versailles *et al.* [18]. The analysis is performed using the KON and GRI mechanisms, which offer the best agreement at 2500 K regarding the absolute NO concentration and formation rate in the post-flame region. Fig. IV.6 presents the relative share of the four routes (prompt, NNH, N_2O, and thermal) to the overall NO formation. Individual absolute contributions to NO formation of the thermal, N_2O, and NNH routes are also provided in the sub-figures. As expected from the analysis of the thermal-initiation rate, KON predicts lower absolute contribution

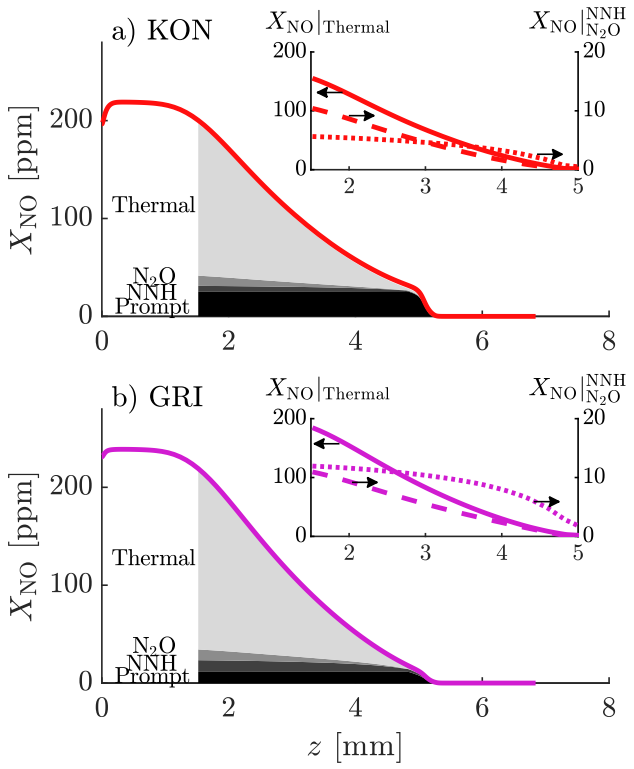

Figure IV.6: Reaction Pathway Analysis performed on the flame at 2500 K, using the KON (a) and GRI (b) mechanisms. Estimates of the NO produced by each route in the post-flame region are illustrated in each sub-figure: thermal (—), N_2O (– –), and NNH (···).

of the thermal-NO compared to GRI. Furthermore, the prompt overprediction of KON shown in Fig. IV.3, is also observed.

While the two mechanisms predict a similar total NO production, they display significant differences in the relative contributions of the four pathways, for both the flame-front NO and the post-flame NO production. As a result, despite similar absolute NO predictions, the thermal-initiation rate that would be inferred by the models, could stem from differences in the importance placed upon, not only the N_2O pathway, but also the NNH and prompt pathways. This suggests that the fundamental chemistry governing NO production remains not well understood.

IV.5 Conclusion

In this study, a stagnation flame burner under controlled boundary conditions is used to measure the velocity, temperature, and NO concentration profiles, using Particle Tracking Velocimetry (PTV), NO multi-line thermometry, and NO laser-induced fluorescence (NO-LIF), respectively. The measurements are performed on nine flames using two levels of oxygen concentration, 21 and 40%O_2,

as well as argon dilution to reach adiabatic flame temperatures ranging from 1900 K to 2500 K. 1D simulated profiles are compared to the results using six thermochemical models.

Measurements are performed in conditions to promote the thermal-NO pathway. Large variability in predictions of the NO-LIF profiles show that none of the considered mechanisms are able to predict accurately the produced NO concentration and the NO rate of formation in the post-flame region, revealing that the fundamental chemistry of NO formation remains inaccurate. Analysis of the discrepancy between measurements and simulations demonstrate that the prediction of post-flame NO by the models, is directly related to their definition of the thermal-initiation rate, specifically the pre-exponential factor A, and the activation energy E_{a}.

Sensitivity and Reaction Pathway Analyses indicate that the discrepancy in the definition of the thermal-initiation reaction could result from different consideration of the base radical chemistry, and the contribution of other NO formation routes. This paper shows that it is possible to predict NO concentrations and NO formation rates that are in reasonable agreement with experiments, but with different underlying chemistry. This suggests that the model predictions would significantly diverge under conditions where non-thermal routes become increasingly important.

To address this, future efforts in optimizing NO_x chemistry should employ measured NO profiles across a broad range of experimental conditions, which promote a variety of NO formation pathways. This would allow the development of models with reduced uncertainty and increased predictive capability to further improve the emissions of state-of-the-art combustion technologies.

Acknowledgments

The authors would like to acknowledge the contribution of Siemens Energy Canada, the National Research Council Canada (NRC), and the Réseau Québécois sur l'Énergie Intelligente (RQEI).

References

[1] M. Meulemans, A. Durocher, P. Versailles, G. Bourque, and J. M. Bergthorson. "How well do we know thermal-NO? An investigation of NO formation in flames over a wide temperature range". In: *Proceedings of the Combustion Institute* 39 (2023), pp. 521–529.

[2] P. Versailles, G. M. G. Watson, A. C. A. Lipardi, and J. M. Bergthorson. "Quantitative CH measurements in atmospheric-pressure, premixed flames of C_1-C_4 alkanes". In: *Combustion and Flame* 165 (2016), pp. 109–124.

[3] G. M. G. Watson, P. Versailles, and J. M. Bergthorson. "NO formation in premixed flames of C_1-C_3 alkanes and alcohols". In: *Combustion and Flame* 169 (2016), pp. 242–260.

[4] M. Abián, M. U. Alzueta, and P. Glarborg. "Formation of NO from N_2/O_2 mixtures in a flow reactor: Toward an accurate prediction of thermal NO". In: *International Journal of Chemical Kinetics* 47 (2015), pp. 518–532.

[5] P. Versailles, A. Durocher, G. Bourque, and J. M. Bergthorson. "Nitric oxide formation in lean, methane-air stagnation flames at supra-atmospheric pressures". In: *Proceedings of the Combustion Institute* 37 (2019), pp. 711–718.

[6] A. Durocher, M. Meulemans, P. Versailles, G. Bourque, and J. M. Bergthorson. "Back to basics - NO concentration measurements in atmospheric lean-to-rich, low-temperature, premixed hydrogen-air flames diluted with argon". In: *Proceedings of the Combustion Institute* 38 (2021), pp. 2093–2100.

[7] N. Lamoureux, H. E. Merhubi, L. Pillier, S. de Persis, and P. Desgroux. "Modeling of NO formation in low pressure premixed flames". In: *Combustion and Flame* 163 (2016), pp. 557–575.

[8] D. L. Baulch et al. "Evaluated Kinetic Data for Combustion Modeling: Supplement II". In: *Journal of Physical and Chemical Reference Data* 34 (2005), pp. 757–1397.

[9] N. A. Buczkó, T. Varga, I. G. Zsély, and T. Turányi. "Formation of NO in high-temperature $N_2/O_2/H_2O$ mixtures: re-evaluation of rate coefficients". In: *Energy and Fuels* 32 (2018), pp. 10114–10120.

[10] X. Han, M. Lubrano Lavadera, C. Brackmann, Z. Wang, Y. He, and A. A. Konnov. "Experimental and kinetic modeling study of NO formation in premixed CH_4+O_2+N_2 flames". In: *Combustion and Flame* 223 (2021), pp. 349–360.

[11] O. Mathieu, C. R. Mulvihill, and E. L. Petersen. "Assessment of modern detailed kinetics mechanisms to predict CO formation from methane combustion using shock-tube laser-absorption measurements". In: *Fuel* 236 (2019), pp. 1164–1180.

[12] Y. Zhang, O. Mathieu, E. L. Petersen, G. Bourque, and H. J. Curran. "Assessing the predictions of a NO_x kinetic mechanism on recent hydrogen and syngas experimental data". In: *Combustion and Flame* 182 (2017), pp. 122–141.

[13] R. K. Hanson and D. F. Davidson. "Recent advances in laser absorption and shock tube methods for studies of combustion chemistry". In: *Progress in Energy and Combustion Science* 44 (2014), pp. 103–114.

[14] R. J. Kee, J. A. Miller, G. H. Evans, and G. Dixon-Lewis. "A computational model of the structure and extinction of strained, opposed flow, premixed methane-air flames". In: *Symposium (International) on Combustion* 22 (1988), pp. 1479–1494.

[15] P. Versailles, A. Durocher, G. Bourque, and J. M. Bergthorson. "Effect of high pressures on the formation of nitric oxide in lean, premixed flames". In: *Journal of Engineering for Gas Turbines and Power* 143 (2021), p. 051029.

[16] A. Durocher, M. Meulemans, G. Bourque, and J. M. Bergthorson. "Measurements of the laminar flame speed of premixed, hydrogen-air-argon stagnation flames". In: *Applications in Energy and Combustion Science* 7 (2021), p. 100028.

[17] A. C. A. Lipardi, P. Versailles, G. M. G. Watson, G. Bourque, and J. M. Bergthorson. "Experimental and numerical study on NO_x formation in CH_4–air mixtures diluted with exhaust gas components". In: *Combustion and Flame* 179 (2017), pp. 325–337.

[18] P. Versailles. "CH formation in premixed flames of C_1-C_4 alkanes: assessment of current chemical modelling capability against experiments". PhD. McGill University, 2017.

[19] P. Versailles, A. Durocher, G. Bourque, and J. M. Bergthorson. "Measurements of the reactivity of premixed, stagnation, methane-air flames at gas turbine relevant pressures". In: *Journal of Engineering for Gas Turbines and Power* 141 (2019), p. 011027.

[20] J. M. Bergthorson and P. E. Dimotakis. "Particle velocimetry in high-gradient/high-curvature flows". In: *Experiments in Fluids* 41 (2006), pp. 255–263.

[21] B. C. Connelly, B. A. V. Bennett, M. D. Smooke, and M. B. Long. "A paradigm shift in the interaction of experiments and computations in combustion research". In: *Proceedings of the Combustion Institute* 32 (2009), pp. 879–886.

[22] W. G. Bessler and C. Schulz. "Quantitative multi-line NO-LIF temperature imaging". In: *Applied Physics B: Lasers and Optics* 78 (2004), pp. 519–533.

[23] J. Luque and D. R. Crosley. *LIFBASE Version 2.1.1, Database and spectral simulation for diatomic molecules (v1.6)*. 1999.

[24] G. P. Smith et al. "GRI-Mech 3.0". In: (1999).

[25] University of California at San Diego. *Chemical-Kinetic Mechanisms for Combusiton Applications*. 2016.

[26] E. Ranzi, A. Frassoldati, R. Grana, A. Cuoci, T. Faravelli, A. P. Kelley, and C. K. Law. "Hierarchical and comparative kinetic modeling of laminar flame speeds of hydrocarbon and oxygenated fuels". In: *Progress in Energy and Combustion Science* 38 (2012), pp. 468–501.

[27] Y. Wu et al. "Understanding the antagonistic effect of methanol as a component in surrogate fuel models: A case study of methanol/*n*-heptane mixtures". In: *Combustion and Flame* 226 (2021), pp. 229–242.

[28] M. Kelly, S. Dooley, and G. Bourque. "Toward machine learned highly reduced kinetic models for methane/air combustion". In: *ASME Turbo Expo* (2021), V03AT04A005.

[29] H. Hashemi, J. M. Christensen, S. Gersen, H. Levinsky, S. J. Klippenstein, and P. Glarborg. "High-pressure oxidation of methane". In: *Combustion and Flame* 172 (2016), pp. 349–364.

[30] A. A. Konnov. "Implementation of the NCN pathway of prompt-NO formation in the detailed reaction mechanism". In: *Combustion and Flame* 156 (2009), pp. 2093–2105.

[31] A. El Bakali, L. Pillier, P. Desgroux, B. Lefort, L. Gasnot, J. F. Pauwels, and I. da Costa. "NO prediction in natural gas flames using GDF-Kin3.0 mechanism NCN and HCN contribution to prompt-NO formation". In: *Fuel* 85 (2006), pp. 896–909.

[32] P. Glarborg, J. A. Miller, B. Ruscic, and S. J. Klippenstein. "Modeling nitrogen chemistry in combustion". In: *Progress in Energy and Combustion Science* 67 (2018), pp. 31–68.

[33] D. G. Goodwin, H. K. Moffat, I. Schoegl, R. L. Speth, and B. W. Weber. *Cantera: An object-oriented software toolkit for chemical kinetics, thermodynamics, and transport processes*. 2021.

[34] J. F. Grcar, M. S. Day, and J. B. Bell. "A taxonomy of integral reaction path analysis". In: *Combustion Theory and Modelling* 10.4 (2006), pp. 559–579.

Deepening the investigation of thermal NO using hydrogen flames

Through the investigation of the thermal NO chemistry using high-temperature methane-air flames, conducted in the previous chapter, a wide variability was found in the predictive capabilities of various thermochemical models in modelling NO formation.

While most thermochemical models are capable of reproducing the velocity and temperature measurements, none can predict accurately NO concentrations for the entire flame domain and for the entire range of conditions studied. These results are indicative of modelling errors in the NO formation mechanisms, particularly, but not limited to, the thermal NO pathway, dominant in these conditions. Interestingly, an analysis of the two best performing predictive models show that to obtain a similar prediction of the NO produced in a flame, the underlying chemistry (number of species, reactions, and their rates) used in both models is widely different. This indicates that these models were optimised by adjusting the reaction rates of key reactions very differently, hence, demonstrating that the confidence of the community in these rates is low. Further analyses of the models seem to point at an inaccurate description of the thermal-initiation rate, the base chemistry, as well as a misprediction of the pathway interactions, as all of these have an impact on the prediction of NO concentration in the flames. These findings give a first insight into the current understanding of the NO modelling chemistry.

To deepen the investigation of the thermal pathway, the NO chemistry is studied in high-temperature hydrogen flames. The use of hydrogen eliminates NO produced through the prompt pathway, improving the focus on the thermal route. Additionally, the study of the H_2/O_2 core chemistry is simplified through the elimination of the carbon-based reactions. Similar to the previous chapter, the experimental velocity, temperature, and NO concentration profiles are compared to the predictions of a variety of thermochemical models. With a simpler chemistry involved in hydrogen flames, sources of misprediction between the models and measurements can be tracked more easily. This ensures a complete understanding of the current NO modelling chemistry, as well as obtaining measurements relevant to the next generation of gas turbines running using hydrogen fuel.

Chapter V. NO measurements in high temperature hydrogen flames: The crucial role of the hydrogen oxidation chemistry for accurate NO predictions

Publication [1] in *Combustion and Flame*, volume 261, 2024, 113279.

M. Meulemans[a], A. Durocher[a,b], G. Bourque[a,c], and J. M. Bergthorson[a]

[a] Alternative Fuels Laboratory, McGill University, 817 Sherbrooke St W, Montréal, H3A 0C3, QC, Canada

[b] Gas Turbine Laboratory, National Research Council of Canada, Ottawa, K1K 2E1, ON, Canada

[c] Siemens Energy Canada Limited, 9545 Chemin de la côte de Liesse, Dorval, H9P 1A5, QC, Canada

V.1 Abstract

The current work investigates the formation of Nitric Oxide (NO) in hydrogen-air flames, over a wide range of flame temperatures. The use of hydrogen allows improved focus on the thermal-NO pathway by removing the complexity introduced by the prompt-NO pathway, which has been shown to be an important contributor to inaccurate predictions of absolute post-flame NO concentrations in hydrocarbon flames. This experimental study is conducted at atmospheric pressure using stoichiometric, premixed, laminar stagnation flames. Adiabatic flame temperatures ranging from 1600 K to 2300 K are achieved by varying the argon concentration in air. One-dimensional velocity, temperature, and NO concentration profiles are measured using non-intrusive laser diagnostics: Particle Tracking Velocimetry (PTV), NO multiline thermometry, and NO Laser Induced Fluorescence (NO-LIF), respectively. Results show that the experimental velocity profiles are incorrectly captured by the studied mechanisms, especially at low and high temperatures. This suggests that major inaccuracies are present in the hydrogen oxidation chemistry of the thermochemical models, regardless of their optimisation methodology. Furthermore, NO-LIF profiles show major discrepancies between all the studied mechanisms and the experiments, especially at

elevated temperatures. The disagreement stems from an inaccurate description of the base chemistry of the models. These inaccuracies arise specifically from the description of the radical pool driving the flame behaviour and NO formation. This study demonstrates the need for model optimisation on experimental measurements using pure hydrogen 1D flames to obtain an accurate description of the hydrogen oxidation chemistry at play. This would lead to an improved description of the NO_x sub-chemistry of any hydrogen, or hydrocarbon, combustion system.

V.2 Introduction

As industries are transitioning from fossil fuels to more sustainable, carbon-free fuels, such as hydrogen, the interest in Nitric Oxide (NO) formation is growing, and accurate modelling is required as a design tool. Constant efforts have been spent over the last few decades to accurately model NO_x chemistry through the different NO-formation pathways.

Glarborg *et al.* [2] formalised these efforts to validate a new comprehensive nitrogen chemistry model. They not only reviewed the two most important pathways of NO formation in flame conditions, prompt-NO and thermal-NO, they also emphasised the less dominant pathways, N_2O and NNH, and their inter-dependencies to one another. The importance of these two minor pathways is increasing as industries target operating conditions that mitigate the prompt-NO and thermal-NO pathway contributions [3, 4].

Extensive work has been conducted to precisely model these four pathways. The prompt-NO pathway, one of the most important sources of NO in hydrocarbon combustion, occurs through the reaction of CH with N_2 to form NCN+H [5, 6]. The further reaction of NCN leads to NO formation through reactions with the radical pool. Efforts to model each reaction of the prompt-NO subset are still underway [7–10].

The thermal-NO pathway, another important source of NO formation, occurs through the reaction of N_2 with O to form NO+N [11]. This reaction is the rate limiting step due to its high activation energy. Thermal-NO pathway is highly dependent on temperature and residence time and is, generally, the main source of NO formation in practical systems, such as gas turbines. Therefore, this pathway is extensively studied, as it is generally limited to the study of a single reaction instead of a subset of reactions [12–15].

The N_2O pathway consists of the oxidation of N_2 with O to form N_2O [16]. The further reaction of N_2O with the radical pool leads to NO formation. The formation conditions of this pathway, in lean flames at moderate temperatures and high pressures, makes it relevant to practical combustion systems, such as Dry Low Emission (DLE). Yet, this subset of reactions still has limited data as it is not as dominant as the previous two pathways. This is in part due to the fact that this pathway is predicted to be dominant only at high pressures, and thus presents experimental

challenges to perform laser-based diagnostics to characterise it. Nevertheless, the interest in this pathway is growing as its contribution increases with the use of emission-reduction strategies and the reduction of the contribution of previously dominant pathways [17–20].

Similar to the N_2O pathway, the NNH pathway is the reaction of N_2 with H to form NNH [21]. NO is formed through the reaction of NNH with the radical pool. This subset of reactions is the least studied in the literature as it is rarely dominant in combustion systems [22–24]. With the advent of sustainable fuels, especially hydrogen, this pathway could see its contribution growing with a greater availability of H-atoms through H_2 breakdown and the absence of the prompt-NO pathway.

Recently, Lee *et al.* [25] and Meng *et al.* [26] have presented a new potential formation channel through the HNNO intermediate. This pathway appears to be active at low temperatures and moderate to elevated pressures. This discovery implies that some models would not accurately describe NO formation as they have, so far, been optimised accounting for only 4 pathways.

Despite all these efforts to precisely model each pathway involved in NO formation over a wide range of flame conditions, inaccuracies remain in the understanding of its chemistry [15, 18, 27–30]. In several experimental and numerical studies targeting the prompt-NO pathway in short-chain hydrocarbon flames [27, 29, 31], it was demonstrated that an inaccurate description of the radical species, especially CH, O, and H, leads to misprediction of the NO chemistry in the flames. Similarly, experiments in high-pressure hydrogen flames [30], targeting the N_2O and the NNH pathways, have shown large variability in the prediction capability of different models. The dependence of these pathways with the co-reacting radicals O, H, and OH, could lead to mispredictions of NO concentration if they are not modelled adequately. Furthermore, Meulemans *et al.* [15] have shown that models are not able to accurately capture the NO chemistry in methane-air flames, particularly at high temperatures where thermal-NO is most active. They concluded that the discrepancies observed are likely due to an inaccurate description of the base chemistry of the thermochemical models employed, as well as an inaccurate description of the NO formation pathways, specifically their reaction rates and the pathway inter-dependencies.

These studies suggest that a significant gap remains in the understanding of NO formation pathway description and their interaction with one another, independently of the fuel used. A strong dependency is also demonstrated between the pathway prediction accuracy and the adequate modelling of the radical pool concentration by the models. These modelling inaccuracies in the formation pathway rates or in the radical pool formation would hinder the accurate prediction of NO formation in conditions that approach practical applications.

Recent measurements in atmospheric, lean-to-rich, hydrogen flames [32] interrogates the accuracy of the radical pool modelling by thermochemical models. They found that large discrepancies are observed between measurements and predictions of the laminar flame speed of 8 lean-to-rich

hydrogen flames. This study demonstrates that inaccuracies in the kinetic performance of existing models for hydrogen oxidation. This finding is concerning as it suggests that the hydrogen oxidation modelling remains inaccurate. Indeed, the hydrogen oxidation chemistry is the first, and most important, building block of any combustion model [33]. It is only composed of a limited set of reactions and species (generally around 30 and 10, respectively), but its description is paramount to an accurate description of any combustion property (kinetics, thermodynamics, speciation).

Thermochemical models, especially those built in a hierarchical manner, are expected to perform well in this first building block, as they individually optimise the hydrogen oxidation chemistry on relevant dataset (directly, indirectly, or *ab initio*). Nevertheless, this review of recent experimental studies indicate that this assumption may not hold true, the description of the NO chemistry remains mispredicted in most conditions presented. This could be explained by the fact that most models, when optimising their NO_x sub-chemistry, generally include data from non-flame setup (shock tube, flow reactor), as well as a range of dataset from both hydrogen and hydrocarbon combustion. Therefore, a misunderstanding of the radical pool description in such contexts could lead to a mis-optimisation of the NO_x chemistry subset. An improvement in modelling accuracy could be gained by including more hydrogen experimental datasets generated from relevant flame conditions. Unfortunately, relatively few experiments have been performed using pure hydrogen flames, especially those that measure NO formation [4, 18, 30, 34–37]. Therefore, the use of pure hydrogen fuel stretches these models into conditions where they have little validation data, possibly propagating the existing errors in NO predictions of hydrocarbon flames when employed to predict NO formation in hydrogen flames. As a consequence, hydrogen flames should be employed to validate any hierarchical models regarding NO measurements, as well as velocity measurements.

To address the lack of hydrogen flame data, this study provides a dataset of velocity, temperature, and NO concentration measurements in pure hydrogen flames. Nine atmospheric, premixed, laminar, stoichiometric, hydrogen-air flames are studied using a stagnation flame burner. Adiabatic temperatures ranging from 1600 K to 2300 K are achieved using argon dilution to emphasise the thermal-NO pathway. The resulting dataset is compared to the modelling capability of several recent and commonly-used thermochemical models. These conditions have been chosen to provide a robust set of data fit for model optimisation and validation. The use of hydrogen focuses on the first building block of any hierarchical thermochemical model. In addition, it allows the removal of the contribution of the prompt-NO formation pathway, a source of misprediction in previous studies. Furthermore, the use of elevated temperatures challenges the models in extreme conditions, outside of their traditional validation range. Models that perform well in these conditions are more likely to have been built in a robust manner, as they capture the fundamental behaviour of the relevant reactions.

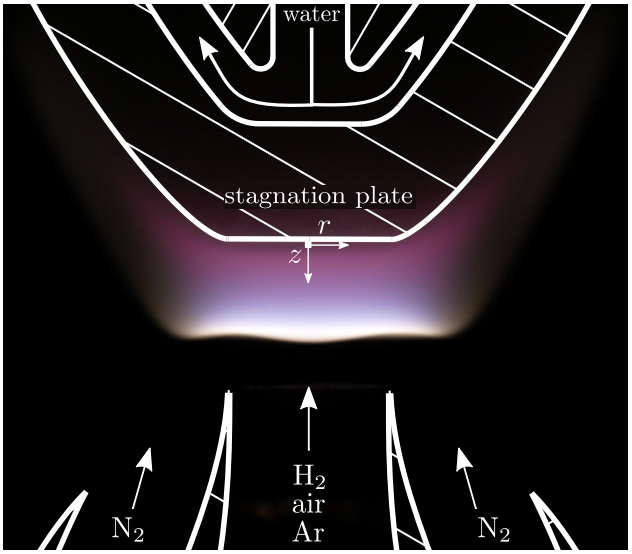

Figure V.1: Stagnation flame burner displaying a stoichiometric hydrogen-air-argon flame at $T_{\text{ad}} = 2100\,\text{K}$ using an exposure time of 4 s. The red and white hues result from H_2O and OH emissions respectively [40].

V.3 Experimental methods

V.3.1 Stagnation burner

Atmospheric, stoichiometric, premixed hydrogen-air-argon flames are obtained using the jet-wall stagnation flame burner shown in Fig. V.1. This setup provides accurate boundary conditions allowing the performance of 1D simulations [38]. The premixed laminar flow exits the nozzle and impinges on a water-cooled stagnation plate maintained at a constant temperature during the experiment. The nozzle-to-plate distance is $\sim 9\,\text{mm}$, and the flame is stabilised approximately at a third of the domain for each experiment in order to maximise the post-flame region, while retaining accurate velocity boundary conditions. The use of nitrogen as a coflow shields the flame from reacting with ambient oxygen. This setup provides flat, lifted, quasi-1D, stretched flames that are minimally affected by the burner. It is ideal for performing optical diagnostics, similar to previous work [15, 19, 28–30, 32, 39].

Adiabatic flame temperatures ranging from 1600 K to 2300 K are used to span a large range of temperatures used in practical systems and promote the formation of thermal-NO at higher temperatures. These temperatures are achieved by producing nine stoichiometric hydrogen-air flames diluted with different levels of argon, such that argon concentration defined by Eq. (V.1) varies between 62.81% at 1600 K and 12.05% at 2300 K in the oxidizer stream with:

$$X_{\text{Ar}} = \frac{N_{\text{Ar}}}{N_{\text{O}_2} + N_{\text{N}_2} + N_{\text{Ar}}}\,, \tag{V.1}$$

where N_i is the number of moles of species i. Non-diluted flat flames with temperatures beyond 2300 K could not be stabilised due to intrinsic flame instabilities. The use of argon as a diluent to control the flame temperature is intentional. This enables the equivalence ratio and the oxygen-to-nitrogen ratio to remain constant while the adiabatic flame temperature varies. It is also a common bath gas in shock tubes studies and, therefore, its use in this study reduces the impact of third body reaction uncertainty due to the familiarity of its behaviour to common thermochemical models.

The different gas flow rates are controlled using thermal mass flow controllers. They are calibrated before the experiments using their respective gases with a DryCal ML-500 dry-piston calibrator, leading to an uncertainty of $\pm 0.7\%$ on the equivalence ratio and $\pm 0.85\%$ on the argon concentration.

Boundary conditions, necessary to perform simulations, are acquired during the experiments through post-processing of the velocity measurements. Type-k thermocouples are used to measure the inlet temperature of the mixture (T_{in}) and the stagnation plate temperature (T_{wall}) within ± 2 K and ± 5 K, respectively. The length of the domain used for simulations $(\mathcal{L})$ is determined at the location of minimum uncertainty in the unburnt region of the velocity profiles, and is also where the inlet velocity (u_{in}) and the axial strain rate $(\mathrm{d}u_{\text{in}}/\mathrm{d}z)$ are extracted [41]. This dataset can be found in the Supplementary Materials, see Appendix C.

V.3.2 Velocity measurements

Velocity profiles are obtained using Particle Tracking Velocimetry (PTV). The flow is seeded upstream of the nozzle with $\sim 1\ \mu$m inert alumina particles illuminated by a 527 nm laser beam. The beam is focused on the center of the nozzle and is stretched to cover almost the entirety of the nozzle-to-plate region. The laser is triggered at a frequency varying from 5 kHz to 10 kHz according to the velocity of the flow. The laser light scattered on the alumina particles is captured using a Charge-Coupled Device (CCD) camera set on a long exposure from 120 ms to 20 ms according to the frequency of the laser. A set of 1,200 images is obtained for each flame on which the tracer particle positions are tracked using an automated streak detection algorithm [42]. The processing of the images allows the extraction of the particle velocity profile along the center-line of the nozzle using a second-order central finite difference scheme:

$$u_{\text{p}}\left(z_{\text{p},i}, r_{\text{p},i}\right) \approx \frac{z_{\text{p},i+1} - z_{\text{p},i-1}}{2} \cdot f \cdot C, \tag{V.2}$$

at the particle location $z_{\text{p},i}$ and $r_{\text{p},i}$, and with f defined as the laser frequency in Hz, and C the camera calibration coefficient in mm/pixel. The particle velocity measurements are performed twice for each flame to ensure repeatability and reach low uncertainty. The direct comparison of the simulated and measured velocity profiles are performed in the measurement unit as suggested by

Connelly *et al.* [43]. Therefore, the simulated gas velocity profiles are converted to particle velocity profiles through the estimation of the particle drag and motion in the flow through the modelling of thermophoretic forces, particle inertia, and the finite particle-track interval effects [44].

V.3.3 NO concentration measurements

NO concentration profiles are obtained using two dimensional NO Laser Induced Fluorescence (NO-LIF). A wavelength-tunable dye laser, using a solution of Coumarin 450, is pumped by a Nd:YAG laser to excite NO molecules in the A−X $(0,0)$ electronic system at a wavelength of ~ 226 nm, comprising of the $P_1(23.5)$, Q_1+$P_{21}(14.5)$, and Q_2+$P_{12}(20.5)$ transitions. The fluorescence of the NO molecules going from the excited state to the ground state is captured using an Intensified-CCD (ICCD) camera equipped with a 235 nm long-pass filter to remove Rayleigh scattering and reflections. To enhance the signal-to-noise ratio, a 120 ns gate is used to reduce the noise contribution from the flame chemiluminescence. The image is binned 4×8 (vertically and horizontally, respectively) to enhance the signal while only minimally compromising the spatial resolution. Finally, 50 individual illumination events are aggregated by the camera, before readout, to enhance the fluorescence signal on single images. The axially-resolved signal of NO produced by the flame (F_{NO}) is captured using 10,000 laser pulses at two different wavelengths: at $\lambda_{\text{on}} = 226.0345$ nm, to capture the online signal (S_{on}) corresponding to a maximum excitation state of the molecules, and at $\lambda_{\text{off}} = 226.0470$ nm, to capture the offline signal (S_{off}), corresponding to a minimum excitation state of the NO molecules. The subtraction of the two signals results in a signal free of interfering LIF and scattering signals. The signal of the flame without laser illumination (S_{bckg}) is also captured using 100 images. The subtraction of the latter to S_{off} and S_{on}, removes the effect of the remaining flame chemiluminescence, camera dark noise, and ambient luminosity. The laser energy is measured close to the flame using a photo-detector, and ensures that the measurements are performed in the LIF linear regime. The signal obtained from fluorescence is normalised by the measured laser energy $E_{\text{L,on}}$ and $E_{\text{L,off}}$, such that the signal is proportional to the NO density only. Finally, the signal is corrected for spatial inhomogeneity in the laser sheet, obtained in a cold jet flow of NO. Under linear LIF, the normalised NO signal can be expressed by Eq. (V.4):

$$F_{\text{NO}} = \frac{(S_{\text{on}} - S_{\text{bckg}})}{E_{\text{L,on}}} - \frac{(S_{\text{off}} - S_{\text{bckg}})}{E_{\text{L,off}}}, \tag{V.3}$$

$$= f_{\text{LIF}}\left(f_{\text{B}}, \lambda, \Delta\nu_{\text{L}}, \Gamma, B_{12}, A_{21}, Q_{21}\right) \cdot C_{\text{opt}} \cdot n^{\circ}_{\text{NO}}\left(T, p, X_{\text{NO}}\right), \tag{V.4}$$

where f_{LIF}, obtained using LIFSim [45], is the number of photons emitted per unit molecule of NO, per unit volume, and per laser energy,and is a function of; $f_{\text{B}}(T)$ the Boltzmann fraction of NO molecules in the excited state, λ the laser wavelength, $\Delta\nu_{\text{L}}$ the spectral width of the laser,

$\Gamma\left(\Delta\nu_{\mathrm{L}}, T, p, X_i\right)$ the dimensionless overlap fraction, A_{21} and B_{12} the Einstein coefficients for spontaneous emission and photon absorption, respectively, and $Q_{21}\left(T, p, X_i\right)$ the rate constant of non-radiative collisional quenching. C_{opt}, obtained experimentally, is the optical calibration coefficient accounting for optic transmissivity and camera sensitivity, and n°_{NO} is the number density of NO molecules, directly proportional to the concentration of NO in the flame.

C_{opt} is obtained through calibration by measuring the signals of both an NO-seeded and unseeded flame. The difference in signals is only proportional to the NO seeded in the flame, and is independent of the NO produced by the flame. Therefore, C_{opt} can be applied on all flames of the experimental campaign, despite individually producing different levels of NO. This method is valid as long as there is negligible NO reburn or recombination within the flame, and that the seeded molecules do not significantly affect the flame properties. The methodology is further detailed in Supplementary Materials, see Appendix C.

In order to model f_{LIF}, the knowledge of instantaneous quenching species concentrations and temperature throughout the domain is required. Thus, transforming experimental NO-LIF signals to NO concentrations relies on assumed profiles which might induce further uncertainty in the reported measurements if the assumptions and models used are proven inaccurate [43]. Therefore, to improve the comparison between measurements and simulations, simulated NO concentration profiles are transformed through LIFSim [45], a three-level LIF model, to obtain simulated NO-LIF profiles, which are directly comparable to C_{opt}-normalised experimental NO-LIF profiles. Consequently, the NO concentration profiles presented in this study are reported through $F_{\mathrm{NO}}/C_{\mathrm{opt}}$ in arbitrary units [a.u.], a combination of power and length units. The measurements of NO-LIF profiles are conducted twice, and the measurement of C_{opt} is performed 8 times. This ensures repeatability in the measurements and leads to low experimental uncertainty. Further details of the uncertainty calculation is given in the Supplementary Materials, see Appendix C.

To accurately transform the NO-LIF signals into ppm, an uncertainty calculation of the LIF modelling parameters would be required. Despite this, for improved context, an estimate of the NO concentration is also given on the NO-LIF profiles. This estimate is obtained by comparing the modelled NO-LIF signal of a reference mechanism to its NO concentration prediction in ppm, achieving a conversion [a.u. $\rightarrow$ ppm]. This conversion is applied to the other simulated NO-LIF profiles, as well as on the experimental NO-LIF profiles, and is mainly valid in the post-flame region of the profiles presented.

V.3.4 Temperature measurements

Temperature profiles are obtained using multi-line NO-LIF thermometry [46–48]. The technique uses a similar methodology as for NO concentration measurement. The flames are seeded with

200 ppm to 500 ppm (high temperature to low temperature flames, respectively, to enhance signal-to-noise ratio) of NO to track the emitted fluorescence across the entire domain. The laser wavelength is varied from 225.13 nm to 225.19 nm over 120 discrete wavelengths. The NO fluorescence is captured at each wavelength by the ICCD camera for a hardware accumulation of 80 images at 300 ns exposure, using the same technique as in a previous study [15]. However, this technique proved not adapted for high temperatures hydrogen flames due to a low signal-to-noise ratio and temperature sensitivity. Therefore, for flames with $T_{\text{ad}} > 2000\,\text{K}$, the image is binned 4×8 (vertically and horizontally, respectively). This allows the reduction of the exposure time to 120 ns, limiting the noise from flame chemiluminescence and improving the signal-to-noise ratio of high temperature flames. In order to avoid over-exposure of the photo-detectors, the image accumulation on the camera is limited to 40 images. The signal is also obtained for an unseeded flame and a flame without laser illumination. These signals are subtracted from the signal of the seeded flame, to maximise the signal-to-noise ratio. The resulting signal is representative of the fluorescence spectra of NO at each point of the domain, and is compared through a spectra-fitting procedure [46] to NO-LIF excitation spectra obtained from LIFBase [49] in order to determine the temperature of the NO-fluorescing molecule. A 1D temperature profile, with an uncertainty of $\pm\,5\%$, is extracted at the centre-line of the nozzle and is directly compared to the simulated profiles.

V.3.5 Flame simulation and thermochemical models

Simulations of the experimental flames are performed using the Impinging Jet model in Cantera 2.5.1 [50]. The multi-component transport model is used, and the radiation and Soret effects are included. Simulations are converged to reach refinement criteria of 2, 0.03, and 0.03, for ratio, curve, and slope respectively, and until the reference flame speed varies by less than 0.1% between each iteration of the refinement criteria. This leads to solutions containing ~ 400 grid points, with a 1 μm minimum grid size. Eleven thermochemicals models are used to simulate the flames, and are presented in Tab. V.1.

Three of these mechanisms; ELTE, KON, and TUM; do not possess a NO_x chemistry as they are optimised solely for hydrogen oxidation. Therefore, their simulations will only be used for the velocity analysis. The remaining eight mechanisms have been developed for fuels heavier than hydrogen. In order to simplify and minimise simulation time, they have been stripped of their carbon chemistry.

Other than stripping the thermochemical models of their carbon chemistry (or as detailed later in this paper, stripped of their NO_x chemistry), the mechanisms are not modified. Therefore,

Table V.1: Thermochemical models used in this study.

Ref.	Mech. (version)	Colour and symbol	Modelled chemistry	Original version		Hydrogen sub-mechanism					
				Entire chemistry		Entire chemistry		H_2/O_2 chemistry		NO_x chemistry	
				Reactions	Species	Reactions	Species	Reactions	Species	Reactions	Species
[51]	**BUT**	— +	H_2, C_1-C_4, NH_3, NO_x	1089	125	252	33	30	11	222	22
[52, 53]	**CRECK** (2003)	— ▼	H_2, C_1-C_6, NH_3, NO_x	2459	159	222	33	23	11	199	22
[2, 54]	**DTU**	— ★	H_2, C_1-C_2, NH_3, NO_x	1397	151	211	33	27	13	184	21
[55]	**ELTE**	— *	H_2	30	12	30	12	30	12	/	/
[56, 57]	**GDF** (3.0)	— *	H_2, C_1-C_6, NH_3, NO_x	934	123	123	22	21	10	102	12
[58]	**GRI** (3.0)	— ●	C_1-C_3, NO_x	325	53	70	19	29	11	41	8
[59]	**KON**	— ♦	H_2	75	15	75	15	75	15	/	/
[60]	**NUIG** (1.1)	— ▲	H_2, C_1-C_{10}, NH_3, NO_x	5966	923	236	34	37	12	199	12
[61]	**SD** (2016-12+2018-07)	— ■	C_1-C_4, NO_x	311	68	64	21	23	11	41	10
[62]	**TUM**	— ×	H_2	19	11	19	11	19	11	/	/
[63]	**XJTUNO**	— ·	H_2, NH_3, NO_x	266	44	243	37	35	12	208	15

the third-body collision factors remained as they have been specified in the mechanisms. If not specified, a default value of 1 is used.

It is worth mentioning that none of the mechanisms used in this study have implemented the potential new HNNO formation pathway. This pathway is also excluded from the analysis performed later in the paper, regarding the formation of NO through the different pathways active in these conditions. This pathway would have minimal impact on the overall NO predictions of the flames presented in this study as the conditions are outside of the pathway active region, moderate pressures and low temperatures, [25, 26]. Similarly, the fuel-NO and the prompt-NO pathways are not considered in this study due to the lack of N- and C-species in hydrogen.

The paper by Curran [33] gives a good insight on how thermochemical models are usually developed. Models are built either following a hierarchical or global approach. Those built in a hierarchical manner will optimise their model according to different subsets, with the first one being the hydrogen oxidation chemistry, followed by C_1 chemistry (CO, CH_4), and then heavier hydrocarbons (C_{2+}). Pollutant formation (NO_x, soot...) is generally optimised last and is added to the combustion model on top of the other subsets. On the contrary to the hierarchical approach, models built in a global manner have been optimised considering all reactions at play as a whole, and have adjusted their reaction rates on data containing any part of the combustion subsets.

Regardless of the construction approach chosen by the models, the optimisation process can be performed following various strategies. One commonly used approach is to adjust the kinetic rates of the reactions “by hand", as detailed by Curran [33]. In this approach, each reaction is adjusted individually to fit a validation target. This is conducted using direct and indirect measurements. Direct measurements are where kinetic rates are measured directly: *ab initio*, shock tubes, flow reactors. Indirect measurements derive kinetic rates by fitting velocity, species concentrations, and ignition delay data, generally obtained experimentally in flow or jet-stirred reactors, or in burners. To remove the potential for human error introduced during manual adjustment, formal optimisation tools have been developed. This first led to the introduction of globally optimised mechanisms with ignition delay times, flame speeds, speciations, etc. used as targets [58]. More

robust approaches have since been used to perform optimisation under uncertainty (statistical, Bayesian inference, etc.) [55, 64, 65], where, not only the nominal measurements (direct and indirect), but also the measurement uncertainty is used to optimise the mechanisms and, in some cases, provide confidence intervals on the predictions.

Despite this understanding, it still remains unclear how most models are optimised. Some models are developed using other models as a base, that they will append to and adjust rates based on new experimental dataset, such as BUT [51]. It therefore renders their categorisation very complex. In this study, the authors have attempted to classify, to the best of their understanding, the 11 thermochemical models into the aforementioned categories.

Only two mechanisms used in this study follow a global optimisation approach, rather than a hierarchical one:

- GRI [58] is a small mechanism, containing few species and reactions, and has been developed to model natural gas combustion with NO_x formation. This mechanism is widely used in the community due to its limited numerical processing time. It is one of the first examples of mathematical optimisation.

- GDF [56, 57] mechanism was also developed to model natural gas combustion and its NO_x formation. In contrast to GRI, it possess many more reactions and species, and the model kinetic rates have been adjusted by hand.

Many mechanisms, and most in this study, base their modelling on a hierarchical approach. They all have optimised the H_2/O_2 core chemistry individually:

- ELTE [55] and TUM [62], use a formal algorithm-based approach to optimise their model. They use uncertainty quantification and probabilistic techniques to adjust the kinetic rates of the H_2/O_2 system. These two mechanisms do not possess a NO_x chemistry, nor any other combustion-chemistry subset, and have been solely developed to model hydrogen combustion.

- BUT [51], CRECK [52, 53], DTU [2, 54], KON [59], NUIG [60], XJTUNO [63], employ the “by hand" optimisation process as described by Curran [33]. Most of them use a similar core chemistry in which the rates of the reactions vary from model to model based on their individual validation targets. NUIG and CRECK are generally recognised as the most comprehensive mechanisms as they include the combustion modelling of many fuels (light to heavy) and for many combustion conditions. BUT and DTU have been developed to model small-chain hydrocarbon combustion, with a detailed core chemistry, and the modelling of a NO_x chemistry. XJTUNO was developed to model $H_2/CO/NO_x$ with no other combustion-

chemistry subset. Finally, KON has been developed for the single modelling of hydrogen combustion and does not possess a NO_x chemistry.

It is unclear to the authors how SD [61] has been optimised as no publications accompany the mechanism; however, it is likely that the latter has been optimised using a hierarchical “by hand" method. It is important to note that this NO_x-containing mechanism has been released without any flame-front NO reactions such as for the NNH or the prompt-NO pathway.

Although this classification may not fully describe the model optimisation process, it is important to understand that the specifics of these optimisation processes are still relatively opaque in most instances.

V.4 Results

Velocity, temperature, and NO concentration measurements are presented in the following subsections for all nine flames. Each experimental profile is extracted at the center-line of the nozzle and is presented as a function of the axial distance between the nozzle ($z \sim 9$ mm) and the stagnation plate ($z = 0$).

V.4.1 Velocity measurements

Figure V.2 presents the measured particle velocity profiles, u_p, obtained for all nine flames. Experimental results are compared to the particle velocity profiles from each thermochemical model considered in this study.

The particle velocity profiles show the expected trend in the stagnation flow configuration: the flow exits the nozzle at $z \sim 9$ mm and then decelerates towards the flame-front ($z \sim 6$ mm) reaching the reference flame speed ($S_\mathrm{u,ref}$), measured at the velocity minimum, it accelerates through the flame-front, and finally decelerates as it impinges on the plate ($z = 0$). Overall, the technique leads to profiles of high spatial resolution and low uncertainty on the reference flame speed ($\pm\, 2 - 10\%$). Equipment limitations lead to a few absent data points in the high-velocity gradient of the flame-front for the flame at $T_\mathrm{ad} = 2300$ K; however, this does not limit the analysis or the extraction of the boundary conditions in the low-velocity, unburnt region.

All thermochemical models reproduce the general behaviour of the particle motion in the flow field. Despite this, significant discrepancies between the measured and simulated profiles can be observed in the flame position (z_f) defined by the axial location of $S_\mathrm{u,ref}$.

$S_\mathrm{u,ref}$ is measured for each flame condition and is presented in Fig. V.3a. The ratio of the experimental to the numerical $S_\mathrm{u,ref}$ is also calculated to determine the level of disagreement between the models and the experiments. Results are presented in Fig. V.3b, where a perfect agreement is

defined by a ratio of unity. Uncertainties are reported using the shaded area and account for the experimental uncertainty as well as for the uncertainty of the experimentally-measured boundary conditions propagated through the simulations. Discrepancies between the measurements and the simulations outside the shaded region should then arise from model inaccuracies. The calculation methodology of the uncertainties is given in the Supplementary Materials, see Appendix C.

As expected, the reference flame speed increases with the adiabatic flame temperature, as dictated by flame theory. While this general trend is correctly captured by the models, disagreements between the experimental and numerical $S_{\text{u,ref}}$ are apparent, particularly at low temperatures, where models unanimously underpredict the reference flame speed by 10% to 20%. Furthermore, the non-linearity of $S_{\text{u,ref,num}}/S_{\text{u,ref,exp}}$ indicates that the dependence of the thermochemical models with temperature and/or with argon concentration is not correctly predicted. Overall, GDF is the model that performs the best, relative to the measurements, across the entire temperature range.

These results are consistent with the findings of Durocher *et al.* [32] who found that mechanisms tend to underestimate the reference flame speed in lean-to-rich, atmospheric, low-temperature, hydrogen-argon-air stagnation flames. These discrepancies lead to the observed disagreement in

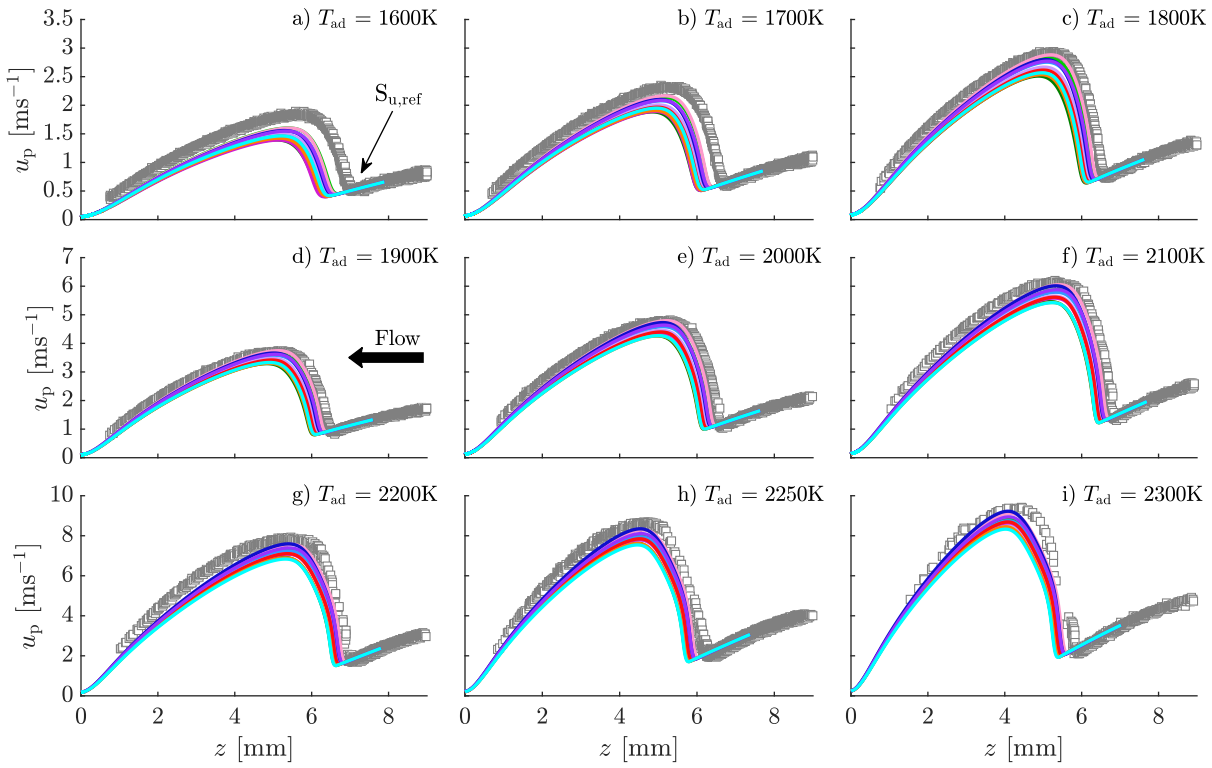

Figure V.2: Particle velocity profiles, measured (▫) and simulated (—) using different thermochemical models. The legend follows the colour-scale presented in Tab. V.1. Note the different scale of the velocity profiles between the top, middle, and bottom rows. Note the same velocity scale for a single row of 3 sub-figures.

the flame position. With a lower predicted flame speed, the numerical flame stabilises in the region of lower flow velocity, further away from the nozzle.

Such disagreements in the velocity profiles prove the presence of inaccuracies in the base chemistry driving hydrogen oxidation, especially at the low- and high-end temperatures. Further investigation is performed in this study (see Section V.5 to V.8) to identify the origin of the disagreement.

V.4.2 Temperature measurements

The measured and simulated temperature profiles are presented in Fig. V.4. The temperature of the flow remains at ambient conditions in the unburnt region, it then sharply increases in the flame-front, follows a more gentle increase in the post-flame region, and then, finally, decreases as it reaches the stagnation plate. All thermochemical models capture the profiles accurately, for all conditions tested, within experimental uncertainty. This is expected as the thermodynamic parameters of the species involved in these flames are well known. Only a discrepancy in the flame position can be observed on the profiles, as discussed for the velocity profiles. Finally, these temperature profiles confirm that the target adiabatic flame temperature is reached by each flame.

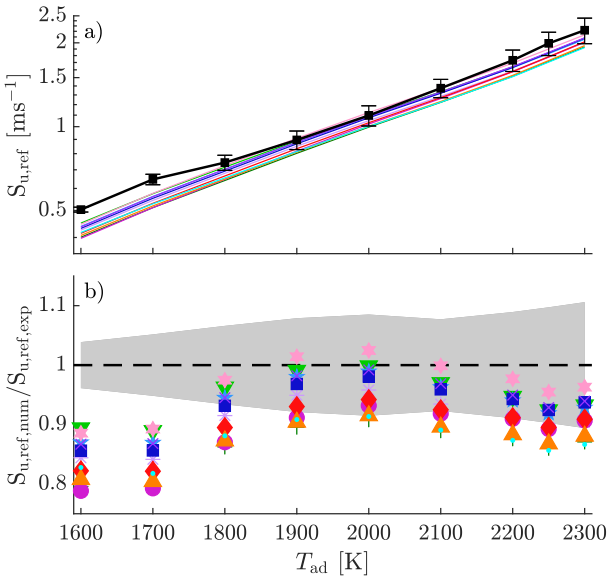

Figure V.3: Comparison of the experimental (black) and numerical (coloured) of: a) the absolute reference flame speed $S_{u,ref}$, and b) the ratio of the numerical to experimental reference flame speed $S_{u,ref,num}/S_{u,ref,exp}$. Shaded area represent the uncertainties. The legend follows the colour-scale presented in Tab. V.1. Note the logarithmic scale used in sub-figure a.

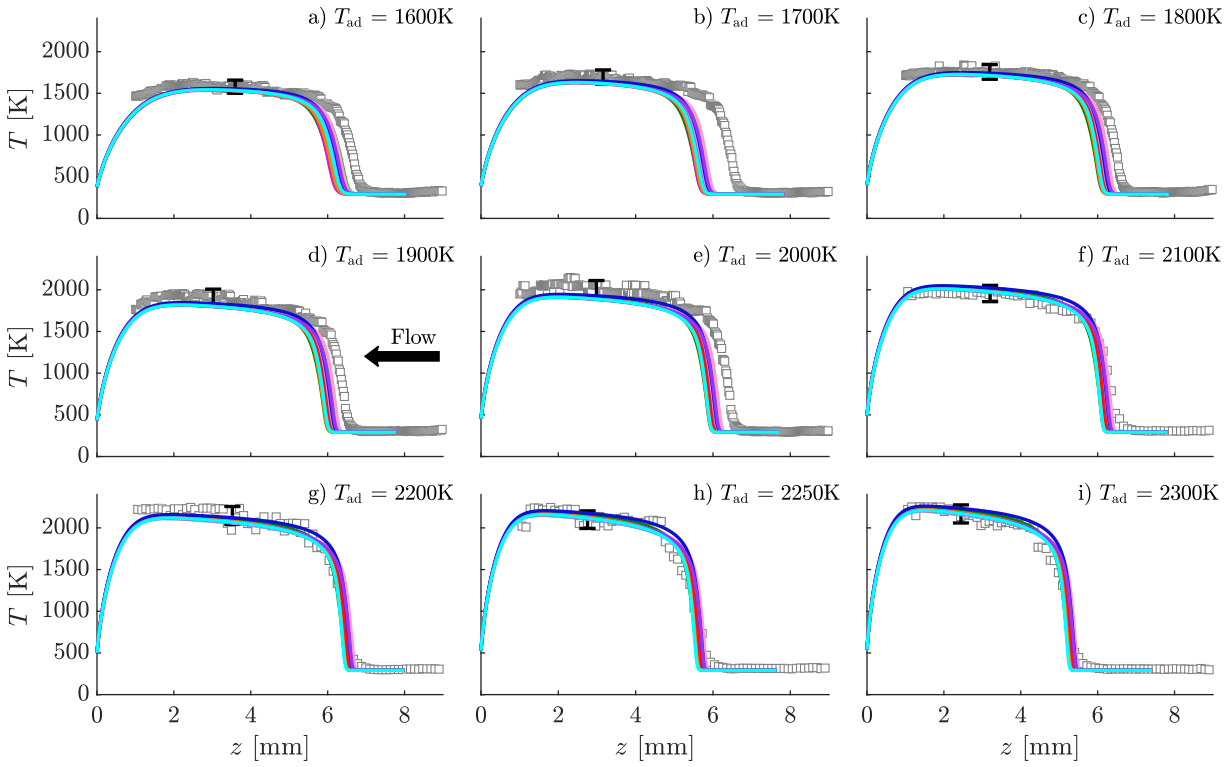

Figure V.4: Temperature profiles, measured (▫) and simulated (—) using different thermochemical models. The legend follows the colour-scale presented in Tab. V.1. The signal close to the stagnation plate, at $z < 1$ mm, is not plotted due to a low signal-to-noise ratio. Note the same temperature scale for a single row of 3 sub-figures.

V.4.3 NO concentration measurements

Figure V.5 displays the NO-LIF signal profiles obtained experimentally and numerically for all conditions. Estimates of the NO concentration in ppm is given on the right-hand vertical axis of each graph. This estimation is valid in the post-flame region only, except within the plate thermal boundary layer ($z \lesssim 1.0$ mm). Further details of the calculation is given in the Supplementary Materials, see Appendix C. The profiles presented are the result of an average of profiles measured twice for each condition.

The measured NO-LIF profiles follow the expected trend: an absence of signal in the unburnt region followed by a sharp increase through the flame, defining the flame-front ($z \sim 6$ mm), and a transient increase in the post-flame region ($z \sim 5.5$ mm to $z \sim 1$ mm). Note that the NO-LIF signal increases as it approaches the stagnation plate due to the thermal effect of the cold boundary layer, increasing the NO number density even at constant NO mole fraction. For a given axial position throughout all nine flames, the signal increases with the increase of the adiabatic flame temperature, as expected from the dependence of the thermal-NO pathway with temperature.

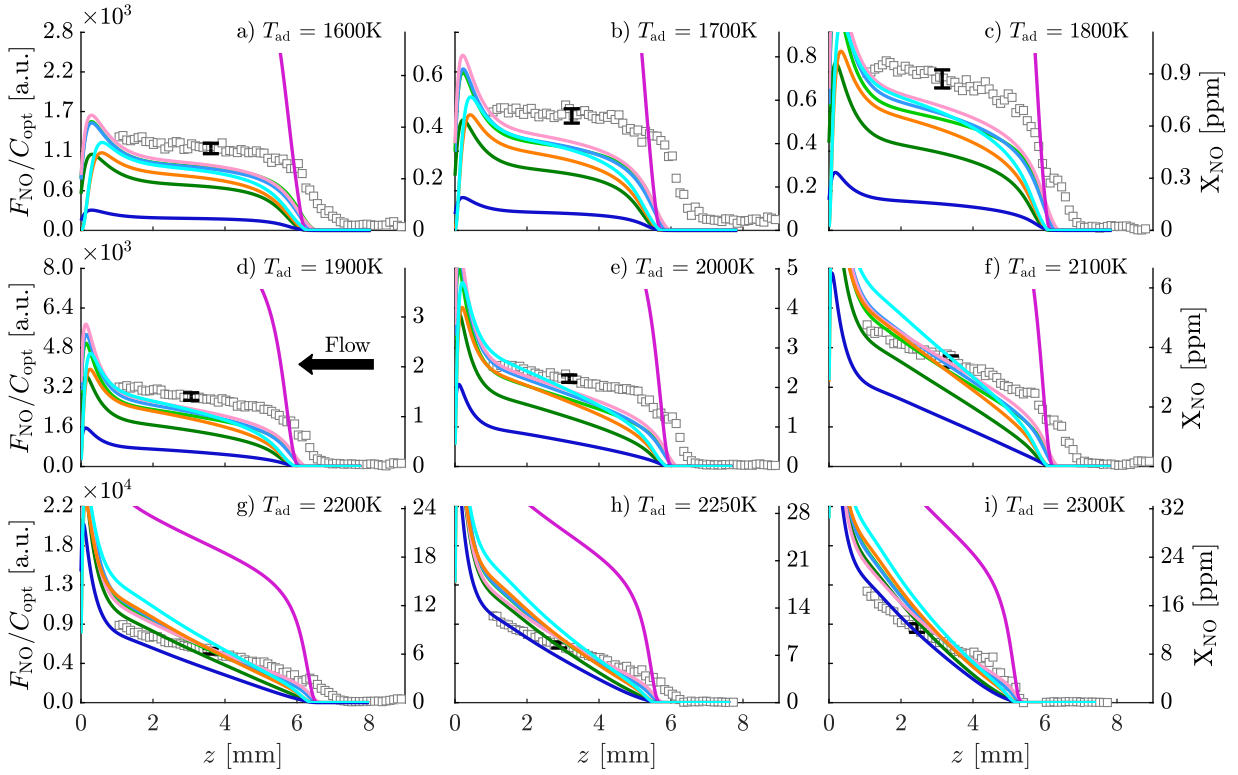

Figure V.5: NO-LIF signal profiles, measured (▫) and simulated (—) using different thermochemical models. The legend follows the colour-scale presented in Tab. V.1. Note the same NO-LIF signal scale for a single row of 3 sub-figures. Estimates of NO production in ppm is provided on the right-hand vertical axis of each sub-figure. The signal close to the stagnation plate, at $z < 1$ mm, is not plotted due to a low signal-to-noise ratio.

While the measured profiles are of high resolution and relatively low uncertainty ($\sim \pm 6\%$ on average for all flames), no thermochemical models are able to accurately capture the measured profiles. Models tend to underestimate the contribution of the flame-front NO while they overestimate the rate of NO formation in the post-flame region. None of the models appear to precisely capture either the flame-front or the post-flame NO for more than a few axial points, and none are able to capture both regions at the same time. These observations apply to all flames considered in this study.

These discrepancies can be better observed in Fig. V.6, where the absolute signals and the ratios are presented for a location in the flame-front, in the post-flame, and for the slope of the profile. Details of the extraction of these parameters from the measured and simulated NO-LIF profiles are given in the Supplementary Materials, see Appendix C. Note that large uncertainties are present at low temperatures due to the very low signal (sub-ppm NO concentrations) at these flame temperatures. Additionally, the extraction of the absolute flame-front NO and the slope of the NO signal in the post-flame region is performed in such a way to be independent from upstream

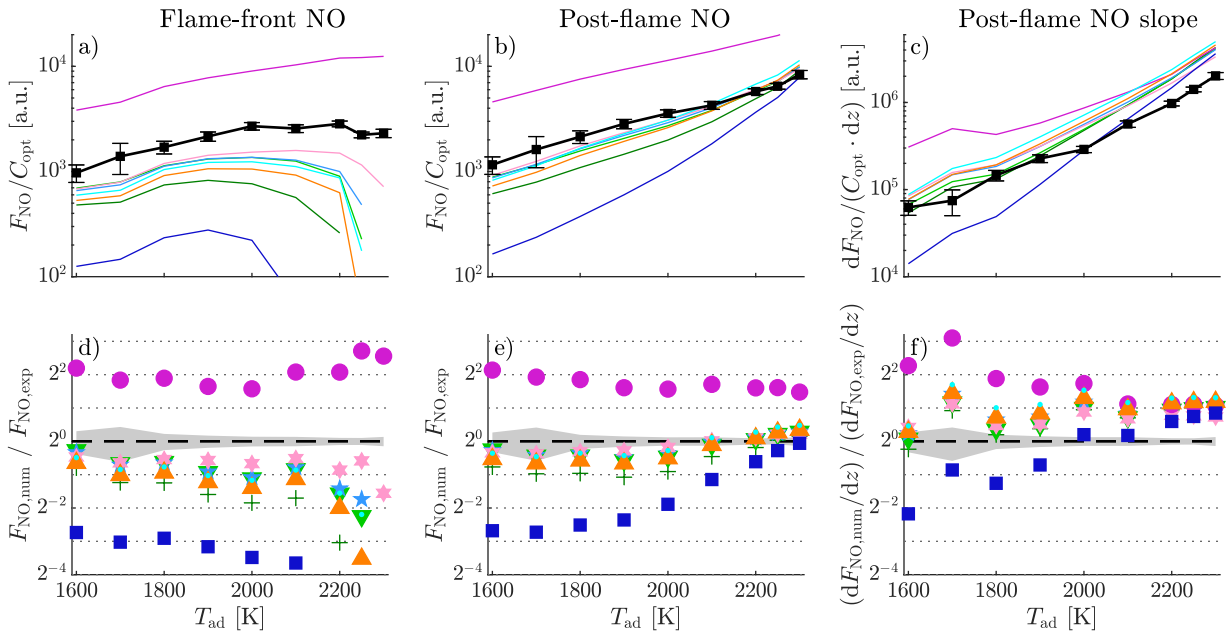

Figure V.6: Comparison of experimental (black) and numerical (coloured): a) the absolute NO-LIF signal in the flame-front, b) the absolute NO-LIF signal in the post-flame region at $z_f - 3.5$ mm, c) the slope of the post-flame NO-LIF signal, and their respective numerical to experimental ratios (d−f). The legend follows the colour-scale presented in Tab. V.1. Shaded areas represent the root-sum square of both the experimental and numerical uncertainties. Note the logarithmic scale used in sub-figures a−c (base 10) and d−f (base 2).

velocity mispredictions. In contrast, the absolute post-flame NO signal is extracted such that it is dependent on any mispredictions upstream to the extraction location.

Figure V.6a shows that the measured flame-front NO increases with the increase in the adiabatic temperature, and appears to plateau (note the logarithmic scale used in the figure) at temperatures around 2200 K. Correspondingly, Fig. V.6d shows that the simulations generally follow the temperature dependence of the measurement (flat trend) up to 2200 K. However, it is apparent from Fig. V.6a and d that large discrepancies are present between the simulation and experimental results, across the entire temperature range, especially at high temperatures. The ratio of the numerical to the experimental absolute flame-front NO signal demonstrates the notable overprediction of GRI stemming from a known overestimation of the NNH pathway in the flame-front region [15], most likely due to the fact that GRI was solely optimised to model natural gas and not hydrogen. Inversely, SD significantly underpredicts the flame-front NO due to the absence of any reaction contributing to flame-front NO formation. All other models also consistently underpredict the flame-front NO signal, especially at high temperatures. Nevertheless, the flat trends of the mechanisms up to $\sim$2100 K, observed in Fig. V.6d, indicates that the dependence with temperature of the reaction(s) (through either the activation energy or the temperature coefficient of the Arrhenius equation) involved in the formation of flame-front NO is well described. There-

fore, the observed discrepancies are potentially due to an inaccurate description of the Arrhenius pre-exponential factor of the reaction(s) responsible for NO production in this region.

As indicated in Fig. V.6b, the measured NO-LIF signal in the post-flame region increases exponentially (note the logarithmic scale in Fig. V.6) with the increase of the adiabatic flame temperature. This behaviour is expected, as the flame-front and post-flame NO are intrinsically linked, such that an increase of the absolute signal in the flame-front region will lead to an increase of the signal in the post-flame region, assuming that NO-reburn does not occur. It is, therefore, expected to find that GRI and SD have similar inaccuracies than what is observed for the flame-front NO. In Fig. V.6e, it can be seen that mechanisms all have the same flat trend up to $\sim 2000\,\mathrm{K}$, underpredicting the measurement (except GRI). Beyond this temperature, there is a shift in the prediction trends, and models tend to overpredict the measurement from $\sim 2100\,\mathrm{K}$. The trend in the model predictions suggests an inaccurate dependence on temperature of the reactions controlling post-flame NO formation, through either the activation energy or the temperature coefficient.

Finally, it is apparent in Fig. V.6c that the spatial rate of change of NO (slope) in the post-flame region is also increasing with temperature. This indicates that some, if not all, of the NO-producing pathways active in the post-flame region are spatially- and temperature- dependent for these flames. Fig. V.6f shows the significant disagreements observed between the experiments and the simulations for the post-flame rate of change of the NO-LIF signal. At low temperatures, few models are within uncertainty, while GRI overestimates the value and SD underestimates it. At temperatures above 1900 K, all models unanimously overpredict the rate of change of NO. This trend in predictions proves that there is an overprediction of the spatial and temperature dependence of the reactions controlling post-flame NO. This leads to overpredictions of the rate of formation of NO around 225% for all the models studied at $T_{\mathrm{ad}} \geqslant 2200\,\mathrm{K}$. This discrepancy is much larger than the measured uncertainty ($\sim 6\%$) for the rate of formation of NO for these conditions with steep slopes.

This discrepancy in NO prediction worsens if the residence time of typical gas turbines is taken into account. Indeed, the residence times of the flames measured in this study vary from $\sim 2.5\,\mathrm{ms}$ at 1600 K to $\sim 0.5\,\mathrm{ms}$ at 2300 K (at the location of the uncertainty calculation), which is much lower than the residence time in traditional hydrocarbon combustion systems.

To explore this effect, Fig. V.7 presents an extrapolation of the measured signals of Fig. V.5a, e, and f, to longer residence times. A residence time of 10 ms is selected to represent a practical combustion chamber. It is apparent that the models significantly diverge with increasing residence time. Extrapolated model predictions of absolute NO concentration, at 10 ms, vary from -90% to $+270\%$ relative to the extrapolated measured profile. This is of significant concern for any practical application when these models are used to identify promising designs within sub-ppm targets.

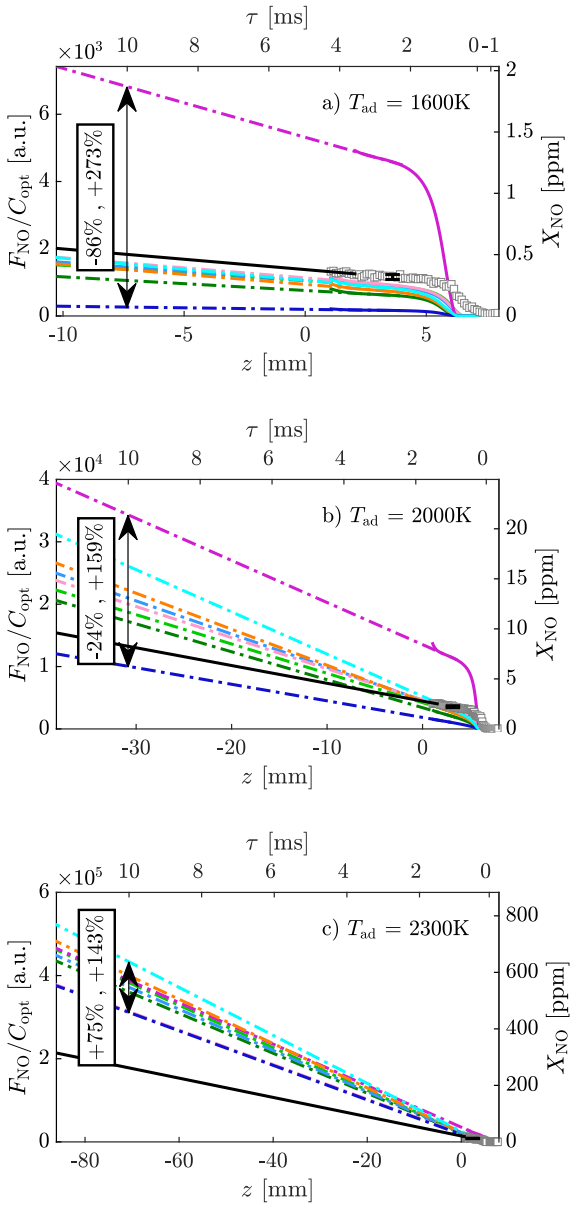

Figure V.7: Extrapolated numerical (- -) and experimental (–) profiles of NO-LIF signal results of the flame at T_{ad} = a) 1600 K, b) 2000 K, and c) 2300 K, to 10 ms residence time. Residence time is calculated the experimental velocity profiles. The origin (0 ms) is determined at the location of the reference flame speed, z_f. The legend follows the colour-scale presented in Tab. V.1.

The findings of this section are consistent with Meulemans *et al.* [15] who found that no thermochemical models could correctly reproduce the NO-LIF signals measured in methane flames at adiabatic temperatures from 1900 K to 2500 K. They attributed the disagreements to an imprecise description of the models' chemistry, principally due to mispredicting the interaction between the four NO-producing pathways, with some minor contribution to the base radical chemistry. They found that the NO_x sub-chemistry NOMecha2.0 (attached to KON v.0.6) was the best in predicting

the NO rate of change in the post-flame region across the entire range of temperature. Despite this, in the current study, this specific sub-chemistry (attached to GDF) significantly overpredicts the NO rate of change in the post-flame region at high temperatures. Thus, despite the agreement of NOMecha2.0 for the methane study, the contributions of the change in fuel has changed its prediction behaviour relative to measurements. This suggests that the base chemistry may have a larger contribution to NO slope misprediction than previously hypothesised.

It is worth noting that the optimisation method used by the models, hierarchical or global, and mathematical or “by hand", does not appear to have an impact on the accuracy of the model predictions, either for the velocity or NO concentration measurements.

V.5 Sensitivity analysis

A sensitivity analysis is performed using the GDF mechanism to identify the reactions that have the greatest influence on flame speed and NO concentrations. This mechanism is used as a reference in this study because it shows the closest agreement with the velocity and NO-LIF measurements.

A brute-force method is used by applying a perturbation of 1% sequentially on the reaction rate constants of the reference mechanism. Duplicate reactions are only perturbed once by applying the perturbation on all duplicates simultaneously, resulting in only one sensitivity value for the set. The 15 most sensitive reactions to four chosen parameters are extracted in order of importance following the decreasing value of the root sum square of the four Logarithmic Sensitivity (L.S.) for each reaction (R_i). The four parameters are: $S_{u,ref}$, the absolute flame-front NO, and the post-flame NO absolute concentration and slope. While all reactions are reversible, the reaction labels display the directionality determined using the net rate of progress of the reactions, for example $R_I : NNH + O \rightarrow NH + NO$ has a net production of NH and NO species. Logarithmic sensitivities are obtained by normalising the solution by the perturbation, such that a L.S. presents a relative change in the quantity of interest with respect to the change in the reaction rate constant. A positive sensitivity on a reaction indicates that an increase of its rate would lead to an increase of this parameter value, *e.g.* $\text{L.S.}(R_I)|_{X_{NO,PF}} = 0.5$ implies that an increase of the reaction rate of R_I of 1% would lead to an increase of the post-flame NO concentration by 0.5%. Therefore, results of the sensitivity analysis can be directly compared to the discrepancies observed between the measurements and the models in Fig. V.3 and Fig. V.6.

Figure V.8 presents the results of the analysis performed on all nine flames, for the four parameters cited previously.

V.5.1 Reference flame speed

Unsurprisingly, the reference flame speed is not sensitive to any of the NO forming reactions. Instead, $S_{\text{u,ref}}$ is highly sensitive to the hydrogen oxidation elementary reactions [66], namely the hydrogen-oxygen shuffle reactions:

$$H_2 + OH \rightarrow H + H_2O \quad (R_{II})$$

$$H + O_2 \rightarrow O + OH \quad (R_{III})$$

$$H_2 + O \rightarrow H + OH \quad (R_{XI})$$

the hydroperoxyl reactions:

$$H + O_2\ (+M) \rightarrow HO_2\ (+M) \quad (R_V)$$

$$H + HO_2 \rightarrow 2OH \quad (R_X)$$

$$H + HO_2 \rightarrow H_2 + O_2 \quad (R_{XII})$$

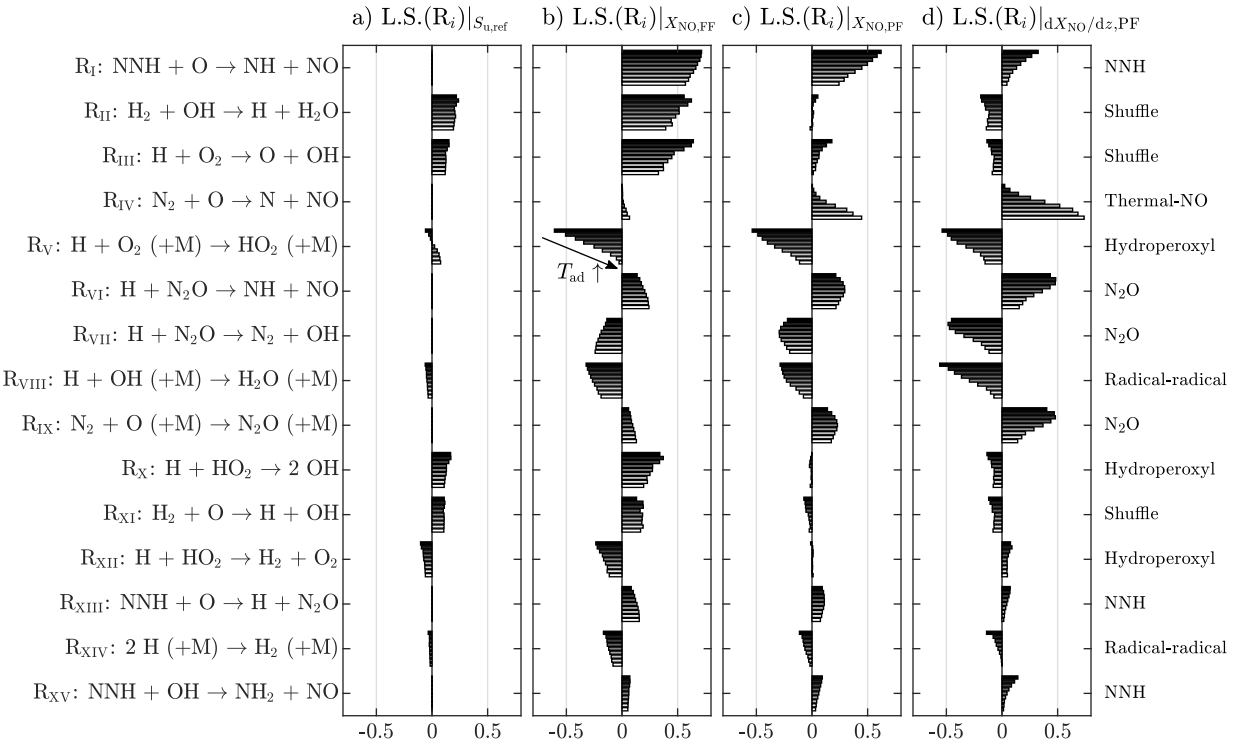

Figure V.8: Brute-force sensitivity analysis performed using GDF on four parameters: a) the reference flame speed $S_{\text{u,ref}}$, b) the concentration of NO in the flame-front $X_{\text{NO,FF}}$ c) the concentration of NO in the post-flame $X_{\text{NO,PF}}$ at $z_{\text{f}} - 3.5\,\text{mm}$, and d) the NO rate of change $\text{d}X_{\text{NO}}/\text{d}z$. Results for the nine flame conditions are presented using a gradient in grey from $T_{\text{ad}} = 1600\,\text{K}$ (black) to $T_{\text{ad}} = 2300\,\text{K}$ (white).

and the radical-radical recombination reactions:

$$H + OH\ (+M) \rightarrow H_2O\ (+M) \qquad (R_{VIII})$$

$$2H\ (+M) \rightarrow H_2\ (+M) \qquad (R_{XIV})$$

These three groups of hydrogen oxidation elementary reactions fully control the radical pool present in the flame with the hydrogen-oxygen shuffle reactions producing the radicals H, O, and OH; the hydroperoxyl reactions, producing and consuming HO_2 through radicals; and the radical-radical recombination reactions rearranging the radical pool through recombination. These reactions govern the combustion taking place in all hydrogen-containing fuels.

In this study, only 8 reactions control the radical pool of these flames, however, changing the rate of a single one of them would not allow the solving of $S_{\text{u,ref}}$ mispredictions observed in Fig. V.3, as the trend of sensitivity with temperature of each of the 8 reactions does not match the trend of discrepancy with temperature of $S_{\text{u,ref}}$. Reactions with a positive sensitivity (R_{II}, R_{III}, and R_X) seem to have a higher sensitivity at low temperatures, where the observed discrepancies between the measurements and simulations are most significant. It is also interesting to note the temperature dependence of the sensitivity of R_V, with a negative L.S. at low temperatures, an almost zero L.S. at moderate temperatures, and a positive L.S. at high temperatures. Therefore, R_V could potentially help in balancing the high sensitivity at the low-end temperatures of the other reactions (R_{II}, R_{III}, and R_X) in order to improve the flame speed predictions.

As discussed, it is clear that resolving the flame speed mispredictions in Fig. V.3 requires resolving the complex behaviour of several reactions and their interactions. As shown by the sensitivity analysis, the balance of the 3 groups of reactions, and their impact on the radical pool, is of significant importance in attempting to close the velocity prediction gap at low- and high-end temperatures. Designing more experiments targeting these regions specifically could produce better model improvement by challenging the established kinetic models with datasets outside the typical validation ranges.

V.5.2 Flame-front NO

It is expected to find that flame-front NO is highly sensitive to not only NO-formation reactions, but also to some hydrogen oxidation reactions governing the radical pool. For hydrogen flames,

flame-front NO is dominantly sensitive to the NNH pathway:

$$NNH + O \rightarrow NH + NO \quad (R_I)$$

$$NNH + O \rightarrow H + N_2O \quad (R_{XIII})$$

$$NNH + OH \rightarrow NH_2 + NO \quad (R_{XV})$$

and, less significantly, to the N_2O pathway:

$$H + N_2O \rightarrow NH + NO \quad (R_{VI})$$

$$H + N_2O \rightarrow N_2 + OH \quad (R_{VII})$$

$$N_2 + O \ (+M) \rightarrow N_2O \ (+M) \quad (R_{IX})$$

These two pathways are highly dependent on the formation of H, O, and OH radicals through the base chemistry. Therefore, NO formation in the flame-front is favored if these radicals are favored (through R_{II}, R_{III}, R_X, and R_{XI}), and disfavored through the consumption of these radicals (R_V, R_{VIII}, R_{XII}, and R_{XIV}).

Furthermore, it is observed in the NO measurements that the temperature dependency of the reactions appears to be accurately captured by GDF up to 2100 K (Fig. V.6d), despite this model consistently underpredicting the measurement. Changing the reaction rate of the hydrogen oxidation reactions to improve $S_{u,ref}$ would potentially be sufficient to also improve the prediction of the flame-front NO, without having to change the NO-formation reaction rates. Increasing the rates of R_{II}, R_{III}, R_X, and R_{XI} would increase the predictions in $S_{u,ref}$ and in $X_{NO,FF}$ across the entire range of temperature and, therefore, reduce the gap of predictions between GDF and the measurements observed in Fig. V.3b and Fig. V.6d. As a matter of fact, only changing the rate of the NO-formation reactions would not be sufficient to improve the prediction of flame-front NO. It would therefore be ill-advised to optimise the NO_x sub-chemistry without considering changes in the base chemistry, as well. These results indicate that the optimisation of the base chemistry of any combustion model could be performed using, not only the velocity results ($S_{u,ref}$), but also using NO concentration measurements in the flame-front ($X_{NO,FF}$) as they are strongly dependent on the hydrogen oxidation reactions.

V.5.3 Absolute post-flame NO

In contrast to the sensitivity analysis performed on the flame-front NO, the sensitivity analysis performed on NO at a given location of the post-flame region (3.5 mm from the reference flame speed z_f) could be influenced by either the flame-front or post-flame formation mechanisms. Depending

on how far the analysis is performed from z_f, the results will be more or less dependent on the flame-front chemistry. Therefore, the sensitivity analysis performed on the spatial rate of change of NO in the post-flame region is more relevant in this study to understand the role played by the reactions in this region.

Despite this, L.S.$(R_i)|_{X_{NO,PF}}$ shows in Fig. V.8c that, if a model was to be optimised on a sensitivity analysis performed at one given location, disregarding any spatial information, this could lead to an inaccurate model. If one was to refer to L.S.$(R_i)|_{X_{NO,PF}}$ uniquely, the contribution of many reactions playing an important role otherwise in L.S.$(R_i)|_{X_{NO,FF}}$, for example through R_{II}, could be underestimated, or disregarded, in the optimisation process.

V.5.4 Rate of change of post-flame NO

The spatial rate of change of NO in the post-flame region is, unsurprisingly, highly dependent on the thermal-NO initiation reaction:

$$N_2 + O \rightarrow N + NO, \qquad (R_{IV})$$

especially at high temperatures. In fact, as the adiabatic temperature is increased and, consequently, the thermal pathway sensitivity is increased, the sensitivity of the NNH and N_2O pathways is decreased. This is not due to a change of reactivity of the NNH and N_2O reactions with increased temperature, but rather due to the channeling of the O-atoms through the thermal pathway, reducing their availability in the radical pool for R_I and R_{IX}. This suggests that the three NO-forming pathways have a spatial inter-dependency, likely due to the radical pool depletion. This behaviour is considerably different than the behaviour observed in hydrocarbon flames. The strong spatial dependency of the N_2O and NNH pathways, in the post-flame region of hydrogen flames, is almost non-existent in the previous methane flames study [15]. Indeed, in the post-flame region of hydrocarbon flames, the radical pool, especially for H atoms, is less present and is mostly depleted through the flame-front as it is required to breakdown the fuel bond. A comparison of such flames is presented in the Supplementary Materials, see Appendix C, to support this hypothesis. As a result, it is possible that the more significant impact of the radical dependence of NO-formation pathways in hydrogen flames are overlooked due to their relatively weaker effect in hydrocarbon flames.

Interestingly, despite the sensitivity of $\mathrm{d}X_{NO}/\mathrm{d}z$ to the N_2O pathway, the latter is likely not responsible for any NO formation through R_{VI}. This is because the reaction forming N_2O from N_2 (R_{IX}) is almost entirely balanced by the reaction forming N_2 from N_2O (R_{VII}).

Furthermore, the overall negative sensitivity of the hydrogen oxidation reactions indicates that any change in the radical pool, especially the consumption of radicals, would decrease the post-flame NO rate of change, especially at low temperatures through R_V and R_{VIII}.

This, once again, suggests that the base chemistry is one of the biggest drivers in improving the predictions of NO measurements. Nevertheless, in this instance, the change of the reaction rate of the hydrogen oxidation chemistry would not solely suffice to resolve the mispredictions of GDF regarding the NO rate of change in the post-flame region. Indeed, all the base chemistry reactions have a negative sensitivity, stronger at low-end than at high-end temperatures. This would have implied that GDF would be less accurate at low-end temperatures and yet, the opposing trend is shown in Fig. V.6f. Therefore, the adjustment of some NO-formation reactions seems inevitable to compensate for the optimisation of the hydrogen oxidation reactions to target $S_{\text{u,ref}}$ and $X_{\text{NO,FF}}$.

It is clear that a complex combination of reaction rate inaccuracies interact in this study. The three NO-formation pathways are highly dependent on O, H, and OH radical formation. The three pathways are also highly dependent on each other through the competition for these radicals. Therefore, any imbalance in the prediction of the reaction rate of any elementary reaction could lead to significant discrepancy in the prediction of NO formation through any of the three NO-forming pathways in hydrogen flames. This analysis demonstrates that optimisation efforts have to be conducted targeting several spatially-dependent parameters in order to account for all reactions playing a role in the hydrogen combustion-chemistry.

Finally, this analysis introduces NO data as a potentially additional parameter that can be used when optimising and validating the velocity prediction performance of a thermochemical model, and its associated base chemistry. As observed in Fig. V.8, the sensitivity on the hydrogen oxidation reactions is stronger for $X_{\text{NO,FF}}$ than for $S_{\text{u,ref}}$. This would allow improved constraints on the optimisation of the base chemistry reactions, especially in cases where velocity measurements are uncertain and less sensitive than NO measurements [67].

V.6 Reaction kinetic rates

V.6.1 Hydrogen oxidation chemistry

Despite the relatively simple chemistry involved in the oxidation process of hydrogen, many reactions still possess large uncertainties [59, 66, 68–70].

Figure V.9 presents the reaction rates of all mechanisms used in this study for the 8 hydrogen oxidation reactions identified as the most important reactions presented in the sensitivity analysis. The reaction rates are plotted in the direction that corresponds to a positive net rate of progress, and are extracted using Cantera, such that, if a reaction is only specified in the reverse direction,

the forward rate is the same as what would be used within the simulations, with the calculation using the equilibrium constant.

The discrepancy in the reaction rate given by the different mechanisms, $\Delta \log_{10}(k_i)$, is calculated as the average of the span, $\left(\log_{10}(k_i)|_{\max} - \log_{10}(k_i)|_{\min}\right)/2$, at each temperature between 400 K and 2300 K. It is important to note that this measurement is not representative of the current

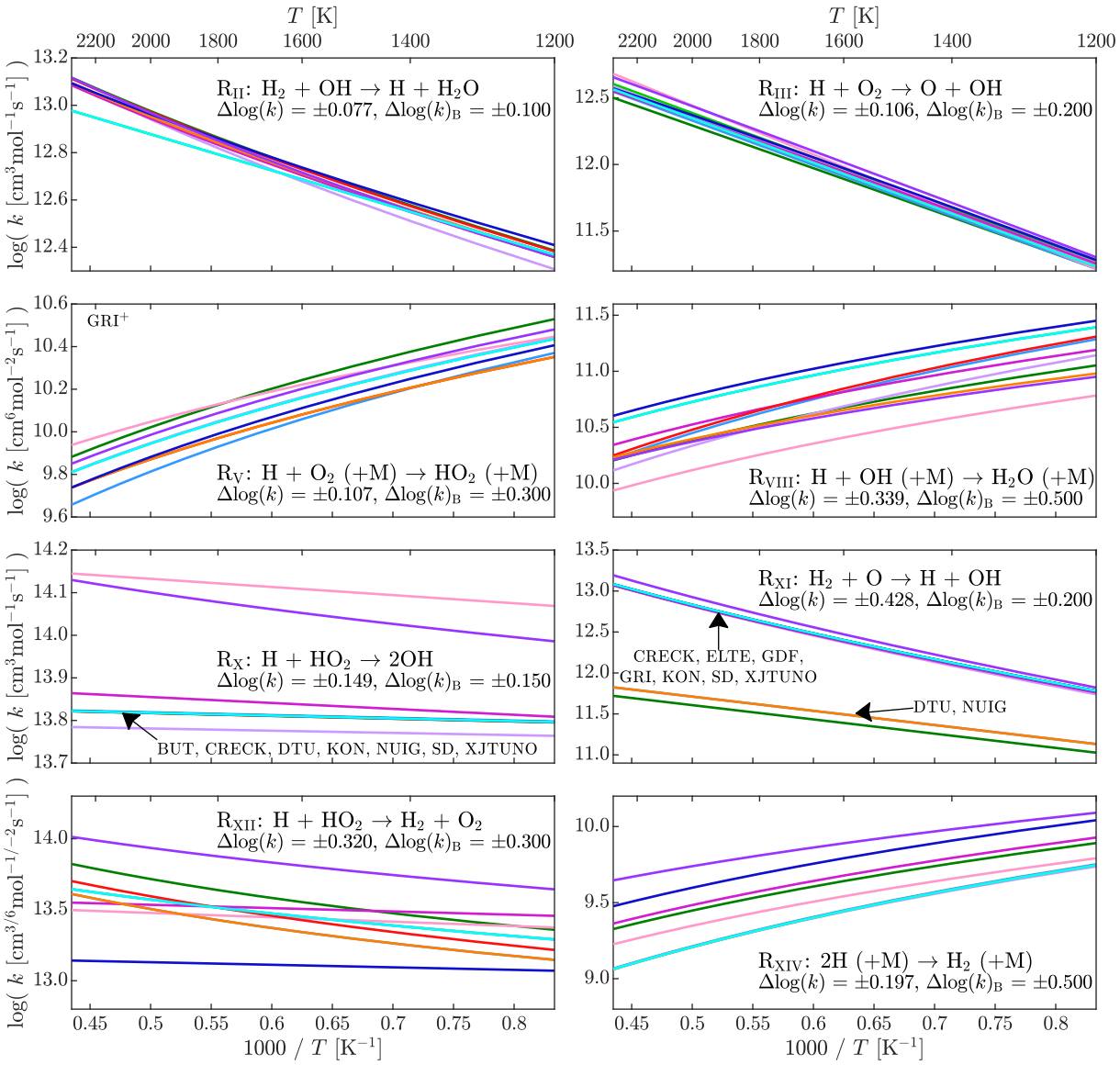

Figure V.9: Arrhenius plot of the 8 base chemistry reactions identified in the sensitivity analysis. The rate is presented according to the directionality of the reaction determined using the net rate of progress of the reactions. Rates are extracted for each mechanism using Cantera at temperatures from 400 K to 2300 K. The spread of the reaction rate within this temperature range is represented by $\Delta \log_{10}(k_i)$. The legend follows the colour-scale presented in Tab. V.1. Please note the difference of units between bimolecular [$cm^3.mol^{-1}.s^{-1}$] and termolecular [$cm^6.mol^{-2}.s^{-1}$] reaction rates. GRI$^+$: this model indicates a collision factor of 0 for O_2, H_2O, N_2, and Ar for R_V, leading to a null rate for these flames.

uncertainty bands of a reaction. Instead, $\Delta \log_{10}(k_i)$ is only indicative of the similarity between the models for a given reaction rate. Therefore, a low $\Delta \log_{10}(k_i)$ could imply that the reaction has been studied extensively and the uncertainty bands are tight and constrained, but it could also mean that this reaction has, conversely, not been studied as much, and mechanisms use a common rate due to the lack of measurements and studies on this reaction. When available, the reliability of the preferred reaction rate given by Baulch *et al.* [68] is displayed as $\Delta \log_{10}(k_i)_{\mathrm{B}}$. This gives an insight of the amount of experimental work used to bound the reaction rate, as these preferred rates are still widely used by the models. Therefore, a tight $\Delta \log_{10}(k_i)$ with a larger $\Delta \log_{10}(k_i)_{\mathrm{B}}$ is indicative of a lack of data on this reaction, at least up until 2005.

Defining $\Delta \log_{10}(k_i) < 0.2$ as being a strong similarity between the models for R_i, several of the base reactions possess a tight agreement:

$$\mathrm{H_2 + OH \rightarrow H + H_2O} \qquad (\mathrm{R_{II}})$$

$$\mathrm{H + O_2 \rightarrow O + OH} \qquad (\mathrm{R_{III}})$$

$$\mathrm{H + O_2\ (+M) \rightarrow HO_2\ (+M)} \qquad (\mathrm{R_V})$$

$$\mathrm{H + HO_2 \rightarrow 2OH} \qquad (\mathrm{R_X})$$

$$\mathrm{2H\ (+M) \rightarrow H_2\ (+M)} \qquad (\mathrm{R_{XIV}})$$

These reactions all have a similar temperature dependence, but vary slightly in the activation energy of their Arrhenius equations. Despite the strong similarity between the models, some of these reactions were identified to contain large uncertainty in their rates [70, 71]. $\mathrm{R_{III}}$ and $\mathrm{R_V}$ are some of the most important reactions due to their role in determining the 2$^{\mathrm{nd}}$ explosion limit in $\mathrm{H_2/O_2}$ systems. Despite many studies dedicated to the measurement of their reaction rates, an uncertainty of up to 20% is still expected in flame speed [59, 69], due to the current understanding of the collisional energy transfer properties involved in $\mathrm{R_V}$. This impacts $\mathrm{R_{III}}$ through the competition for H atoms. In this study, the agreement observed between the models actually hides the large uncertainty linked to these reaction rates, and likely points to mechanisms simply assuming the same reaction rate and focusing on other reactions during their optimisation processes. In contrast,

$$\mathrm{H + OH\ (+M) \rightarrow H_2O\ (+M)} \qquad (\mathrm{R_{VIII}})$$

$$\mathrm{H_2 + O \rightarrow H + OH} \qquad (\mathrm{R_{XI}})$$

$$\mathrm{H + HO_2 \rightarrow H_2 + O_2} \qquad (\mathrm{R_{XII}})$$

display a relatively large spread in their rates ($\Delta \log_{10}(k_i)$ >0.3). For $\mathrm{R_{VIII}}$, it appears that the discrepancy arises from a difference in the activation energies. It was also identified by Burke *et al.* [69] to not be able to accurately describe the flame behaviour over a wide range of pressures

and temperatures, due to the high dependency of the bath gas description. In this study, R_{VIII} is active in both the flame-front and the post-flame region and is responsible for depleting the H and OH radical pool available throughout the domain. Disagreements in the rate of the models lead to differences in the concentration of these radicals and, therefore, would lead to differences in the concentration of NO, in both the flame-front and the post-flame region, as observed in the sensitivity analysis.

R_{XI} and R_{XII} display significant disagreement in the temperature dependency of their rates. It was shown by Burke *et al.* [69] that R_{XII} (along with R_X), participate in the 2nd explosion limit and is not well known at high temperatures. In this study, Fig. V.8 shows that R_{XI} and R_{XII} are mostly active in the flame-front, and are responsible for the consumption and recombination of H_2 through the use of O and H atoms. Disagreements in the rates of these reactions throughout the models would lead to disagreements in the concentration of NO formed through the flame-front, as well as disagreements in the reference flame speed.

As discussed, these 3 reactions, R_{VIII}, R_{XI}, and R_{XII}, appear to be at the origin of the discrepancies between the models in both the velocity and NO concentration predictions of this study. Tightening the uncertainty of these rates would likely contribute to an improved description of the parameters presented in the sensitivity analysis.

V.6.2 NO_x sub-chemistry

Figure V.10 presents the reaction rates of the 7 NO_x reactions identified as the most important reactions presented in the sensitivity analysis. This shows a relatively moderate span of $\Delta \log_{10}(k_i)$ observed for most of the NO-formation reaction rates. The reactions presenting a large span,

$$NNH + O \rightarrow NH + NO \qquad (R_I)$$

$$H + N_2O \rightarrow N_2 + OH \qquad (R_{VII})$$

$$N_2 + O\ (+M) \rightarrow N_2O\ (+M) \qquad (R_{IX})$$

seem to be due to some outlier rates, while most of the other mechanisms agree well.

These outlier rates can easily explain the behaviour observed in the NO measurements for some mechanisms. GRI overestimates the rate of R_I, leading to an overprediction of the flame-front NO. Inversely, SD underestimates R_{IX}, and does not include several NNH reactions (R_I, R_{XIII}, and R_{XV}), leading to a significant underprediction of the flame-front NO. Furthermore, special attention is brought on R_{VII}, where a clear segregation is observed between the models. Several mechanisms (DTU, GRI, NUIG, and XJTUNO) are predicting a greater reaction rate than the rest of the models, and the recent mechanisms (DTU, NUIG, and XJTUNO) are using a rate coming

from *ab initio* calculations performed by Klippenstein *et al.* [22]. This discrepancy in the rate would affect the N_2O transformation to N_2 and, therefore, reduce the N_2O contribution pathway and reduce the concentration of N_2O produced.

The study from Glarborg *et al.* [2] indicates that, while the models have a good agreement on most of the NO_x reactions involved in this study, this could conceal large uncertainties in their ki-

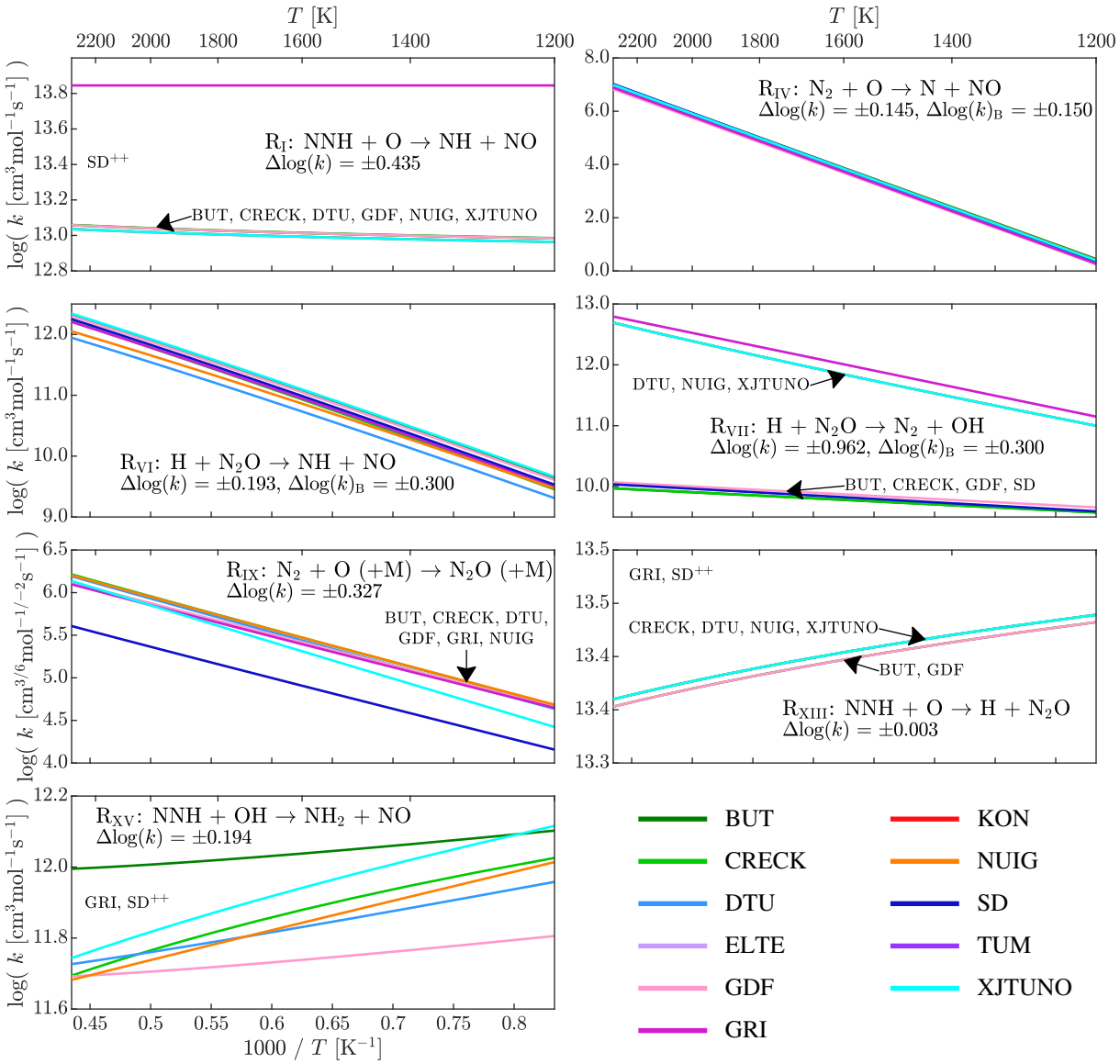

Figure V.10: Arrhenius plot of the 7 NO-forming reactions identified in the sensitivity analysis. The rate is presented according to the directionality of the reaction determined using the net rate of progress of the reactions. Rates are extracted for each mechanism using Cantera at temperature from 400 K to 2300 K. The spread of the reaction rate within this temperature range is represented by $\Delta \log_{10}(k_i)$. The legend follows the colour-scale presented in Tab. V.1. Please note the difference of units between bimolecular [$cm^3.mol^{-1}.s^{-1}$] and termolecular [$cm^6.mol^{-2}.s^{-1}$] reaction rates. GRI, SD^{++}: these mechanisms do not contain the reaction.

netic rates, especially regarding the NNH and N_2O pathways. R_I has never been measured directly and still carries large uncertainty. Similarly, R_{VI} and R_{VII} possess large uncertainty, especially at temperatures above 2200 K. Finally, according to Glarborg *et al.* [2], the dissociation of N_2O *via* the reverse of R_{IX} is studied a lot, but only few measurements have been performed to measure the rate of the forward direction, leading to the observed agreement between the models (except SD) in Fig. V.10 for R_{IX}.

Except for 3 reactions, R_I, R_{IX} and R_{VII}, the rest of the NO_x chemistry seems to be fairly well agreed upon between the mechanisms. Therefore, the disagreements in NO prediction between the models cannot be solely attributed to NO chemistry, and points to its interaction with the base chemistry as a more significant driver. This reinforces the significant observed impact of the hydrogen oxidation chemistry on NO predictions and implies that, without improving this, further work on optimising the NO_x sub-chemistry may yield diminishing returns.

V.7 Base chemistry impact on NO concentration

To fully grasp the contribution of the base chemistry in the discrepancy of the NO measurements and predictions, the mechanisms used in this study have been stripped of their NO_x sub-chemistry (except for ELTE, KON, and TUM which were already without). The NOMecha2.0 sub-chemistry [57], already discussed in the previous sections, is used as a reference in this analysis and is added to each of the base chemistries. Only GDF is not modified as it already includes NOMecha2.0, and is used as the reference in this analysis. Simulations using the 10 modified mechanisms (plus GDF) are performed using different base chemistry, but identical NO_x chemistry, such that any disagreement between the models are solely caused by disagreement within their hydrogen oxidation chemistry. It is important to note that the modification of the mechanisms is only conducted in the context of the analyses performed in the following sections. They are not intended as a direct improvement of the mechanisms, but rather to highlight the importance of the hydrogen base chemistry on the predictions of NO concentration.

Figure V.11 presents the difference of NO-LIF signal predictions for the original 8 mechanisms (left) and the 10 modified mechanisms (right) for $T_{ad} =$ 1600 K, 2000 K, and 2300 K. This shows that the use of a common NO_x sub-chemistry reduced the span of predictions that was observed in the original models. This indicates that some mechanisms have a NO_x sub-chemistry that is notably different from NOMecha2.0. This is specifically true for GRI and SD for which the change in NO_x sub-chemistry leads to significant improvement of the flame-front NO predictions.

Nevertheless, the same NO_x sub-chemistry does not completely remove differences in predictions between the models. In particular, the absolute flame-front NO prediction, and the predicted

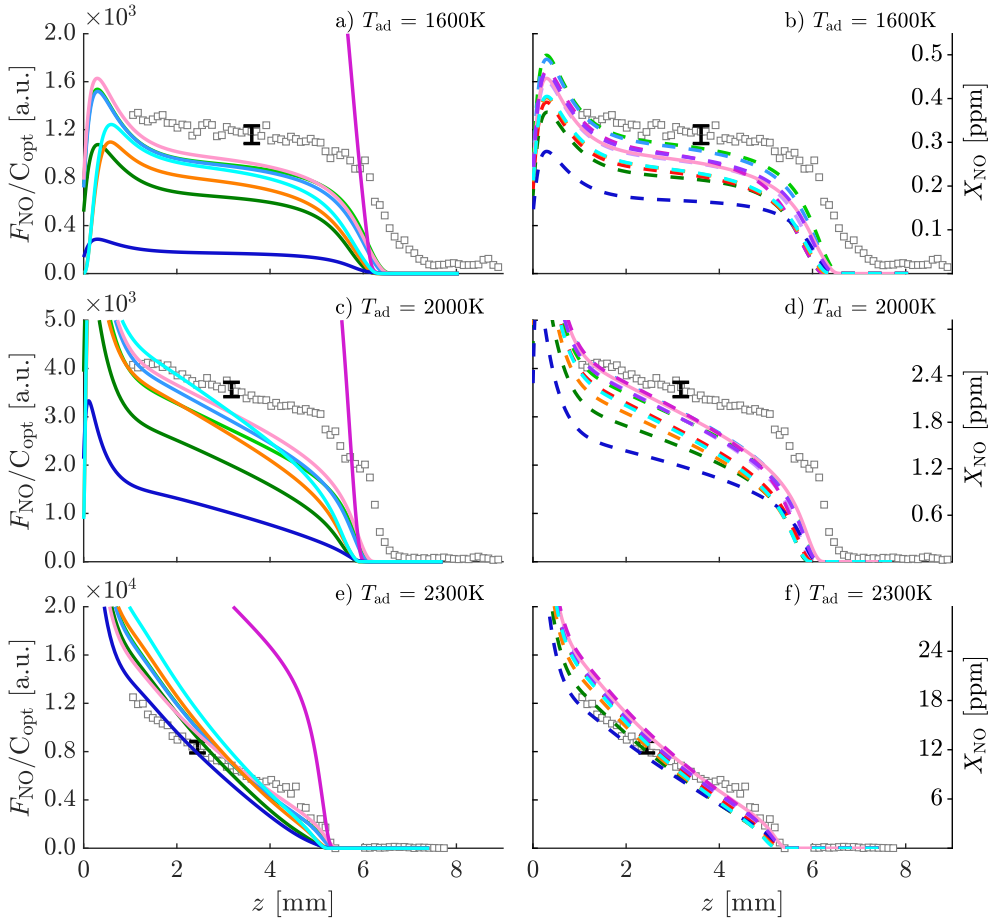

Figure V.11: NO-LIF signal profiles of the flames at $T_{ad} = 1600$ K (top), 2000 K (middle), and 2300 K (bottom) for the experimental results (▫) and simulated results using the non-modified (—, left of the figure) and the modified mechanisms (- -, right of the figure). The legend follows the colour-scale presented in Tab. V.1.

slope of post-flame NO formation, still vary considerably between models. These results demonstrate the impact of the different base chemistries on NO predictions.

V.8 Base chemistry impact on NO pathway contribution

A Reaction Pathway Analysis (RPA), which tracks atomic nitrogen, is performed to understand the impact of using a different hydrogen oxidation chemistry on the prediction of NO, whilst using the same NO_x sub-chemistry. The analysis is performed on the reference mechanism GDF, and the modified SD mechanism, referred to as SD*. These two mechanisms were chosen as they appear to be in significant disagreement regarding NO predictions at 3.5 mm from z_f (see Fig. V.11b, d, and f). Tracking N-atoms describes how N_2 is broken-down to later form NO through the different NO_x pathways.

Figure V.12 presents the results of the RPA performed for the flame condition at $T_{ad} = 2300\,K$. The arrows represent the net fluxes of N-atoms between two species and the arrow widths are scaled with the values of the net fluxes. Coloured arrows depict the species entering (darker colour) and exiting (lighter colour) the domain. Reactive species participating in the transformation of one specie into another, in either forward or backward direction, have been added on each arrow. To simplify the drawing, any fluxes, species, and reactive species participating in less than 5% of the total inlet flux are not depicted. The analysis is performed for a fixed control volume and the fluxes are normalised by the N_2 entering the domain. This allows the analysis to be comparable for both mechanisms. Naturally, as both models possess the same NO_x sub-chemistry, both diagrams have the same appearance. In this comparison, it is the scaling of the arrows that is of interest.

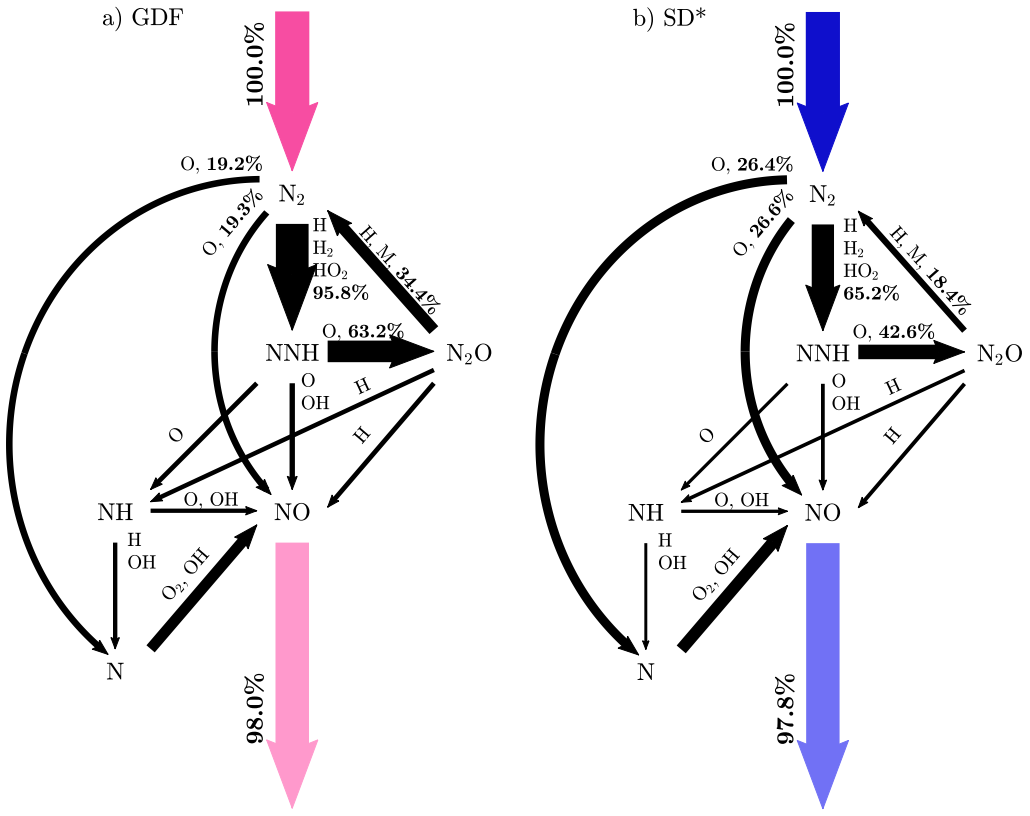

Figure V.12: Reaction pathway analysis performed on atomic nitrogen at 3.5 mm from z_f, for the $T_{ad} = 2300\,K$ flame, using GDF (→) and SD* (→) mechanisms. The arrow sizes are scaled with the flux between two species. Only fluxes greater than 5% are shown. Reactive species participating in the transformation from one specie to another are shown and identified using the net rate of progress of each reaction. Note that the sum of the fluxes originating from N_2 to N, NO, and NNH is greater than 100% due to the recirculation loop $N_2 \rightarrow NNH \rightarrow N_2O \rightarrow N_2$.

Two main streams can be identified in this diagram: N_2 reacting through the thermal pathway and forming N and NO species, and N_2 forming NNH. The stream of N_2 forming NNH is dominant in this flame condition due to the rapid equilibrium of $N_2 + H \rightarrow NNH$ [2]. Some of the NNH species are oxidised into NO (directly or through NH), while a considerable part of NNH transforms into N_2O through R_{XIII}: $NNH + O \rightarrow N_2O + H$. The N_2O species then either transform into NO (directly or through NH), or are reduced back into N_2. This diagram highlights the recirculation channel of $N_2 \rightarrow NNH \rightarrow N_2O \rightarrow N_2$, already identified by Durocher *et al.* [30]. This shows that NO production is dependent on the branching ratios of the mechanism at three points:

- $N_2 \rightarrow NNH$ versus $N_2 \rightarrow N/NO$;
- $NNH \rightarrow N_2O$ versus $NNH \rightarrow NH/NO$; and
- $N_2O \rightarrow N_2$ versus $N_2O \rightarrow NH/NO$.

By comparing this diagram to the sensitivity analysis, it is now obvious why

$$NNH + O \rightarrow NH + NO \quad (R_I)$$

$$N_2 + O \rightarrow N + NO \quad (R_{IV})$$

$$H + N_2O \rightarrow NH + NO \quad (R_{VI})$$

are the most sensitive reactions for NO production (ignoring the base reactions), as they control the 3 branching ratios identified above.

It is evident that NO production is mostly dependent on the presence of O, OH, and H reactive species, as identified in the previous sections of this study. Therefore, it is clear that any difference in the hydrogen oxidation chemistry between mechanisms, will necessarily lead to differences in the predictions of NO formation through differences in the reactive species concentrations.

Comparing the GDF and the SD* analyses, it is obvious that the different base chemistry leads to differences in the contribution of the NO-formation pathways. While the overall NO production is similar for both mechanisms, the fluxes between species is significantly different. Overall, GDF predicts a stronger recirculation of N_2, stronger $NNH \rightarrow NH/NO$ and $N_2O \rightarrow NH/NO$ fluxes, but a weaker $N_2 \rightarrow N/NO$ flux. Conversely, SD* predicts a weaker recirculation of N_2, with a weaker branching ratio of $NNH \rightarrow NH/NO$ and $N_2O \rightarrow NH/NO$, but a stronger flux from $N_2 \rightarrow N/NO$. These differences in branching ratios and fluxes can be quantified by identifying the share of NO produced through the different NO-forming pathways, and is presented in the Supplementary Materials, see Appendix C.

The difference of branching ratios between these two mechanisms appears to be uniquely controlled by the radical availability. The radical profiles for O, H, and OH are presented in Fig. V.13,

as well as the profile of NO concentration, for the 2300 K case. As observed, significant differences between GDF and SD* in the radical concentration profiles persist throughout the domain. These differences are more pronounced in the post-flame region, where a difference in the shape of the profiles can be observed. This observation is true for any mechanism considered in this study, a full comparison is presented in the Supplementary Materials, see Appendix C, for all non-modified mechanisms. At the location of the performed RPA, the discrepancies between the two models for the OH profile reach ~ 2500 ppm, or 14% of the average value at this location. Similarly, deltas of $\sim 30\%$ can be observed in the O and H profiles at the same location. The behaviour of these profiles is indicative of a different rate of consumption/production of the radicals due to differences in the hydrogen oxidation chemistries. This impacts the NO predictions in the post-flame region, as seen in Fig. V.13d.

The measurement of radical profile concentrations, on residence time scales representative of flames, would be paramount to better identify the source of uncertainty in the description of the hydrogen oxidation chemistry. Consequently, this illustrates the importance of using accurate and validated base chemistry before optimising NO_x sub-chemistries to achieve accurate NO predictions of hydrogen flames. Otherwise, prediction errors would be concealed through an over-compensation of NO-formation pathways. This also illustrates the importance of integrating time- or spatially-resolved species data, representative of practical systems residence times, in order to improve the predicting capability of the core H_2/O_2 chemistry.

V.9 Conclusions

In this work, nine atmospheric, stagnation, hydrogen-air flames are studied, over a wide range of adiabatic flame temperatures, to provide a set of spatially-dependent velocity, temperature, and NO concentration measurements. The stoichiometric flames are diluted with argon to reach adiabatic flame temperatures ranging from 1600 K to 2300 K. Experiments conducted using this setup, under well-controlled boundary conditions, lead to measurements with low uncertainty and high repeatability. The results of the velocity, temperature, and NO concentration measurements are compared to the prediction capability of eleven thermochemical models through 1D simulations.

Major discrepancies in the velocity prediction of the eleven models are observed at the low- and high-end temperatures. All models underpredict the reference flame speed, $S_{\text{u,ref}}$, by up to $\sim 20\%$. Better agreement can be seen at moderate temperatures from 1900 K to 2100 K, where most models predict $S_{\text{u,ref}}$ within uncertainty. This effect indicates inaccuracies in the base chemistry driving hydrogen oxidation, especially at the low- and high-end temperatures.

Predictions of NO concentration profiles by the simulations show discrepancies of several times the measured values, for both the flame-front and post-flame regions. NOMecha2.0, despite per-

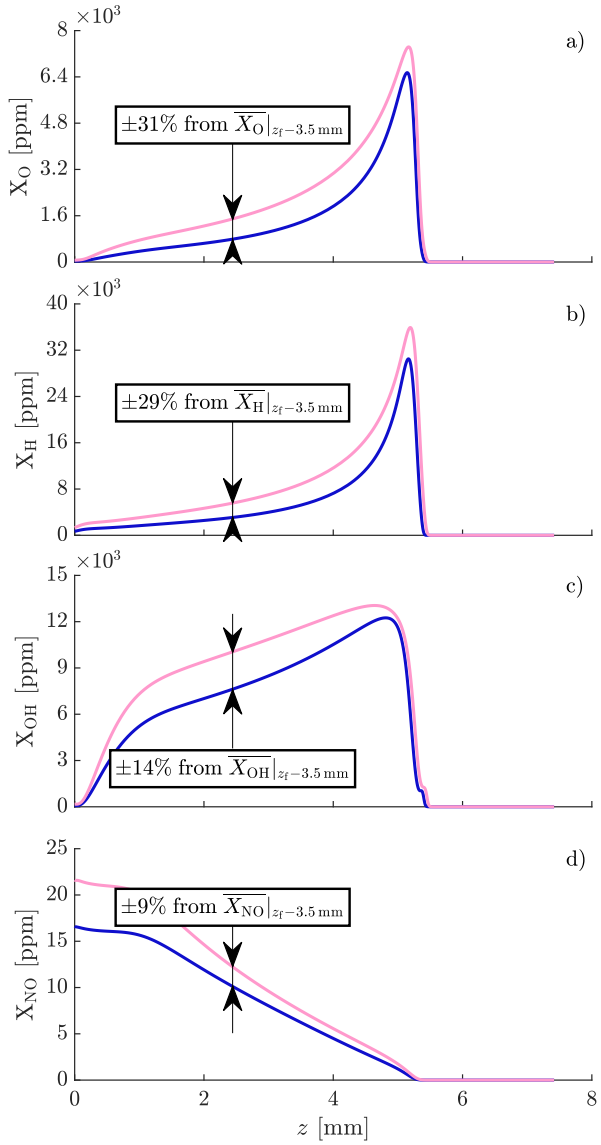

Figure V.13: Numerical profiles of a) O, b) H, c) OH, and d) NO molar fraction for the flame at $T_{ad} = 2300$ K using GDF (—) and SD* (—) mechanisms.

forming well in predicting NO formation in methane flames, shows poor agreement with the measurements in hydrogen flames. This suggests that the hydrogen oxidation chemistry may have a larger contribution to NO misprediction in hydrogen flames than in hydrocarbon flames.

Further analyses revealed that key reaction rates controlling O, H, and OH radicals play a major role on the velocity and NO concentration predictions and are at the origin of disagreements with the measurements. Reaction pathway analyses show that NO predictions are ultimately controlled through three branching ratios. These are uniquely controlled by radical availability, determined almost exclusively by the base chemistry used. This produces different contributions of each of the NO formation pathways, and results in an overall misprediction of NO concentration.

This study demonstrates that, no matter the optimisation process employed by the different models, major inaccuracies remain in the understanding of the H_2/O_2 core chemistry. This could be caused by a lack of hydrogen-based data in the literature, especially including time or spatially-resolved speciation profiles in flames approaching practical conditions. Therefore, this demonstrates the importance of including hydrogen-based data within the development and optimisation of models to improve hydrogen and hydrocarbon combustion modelling. Neglecting to do so will result in inaccurate NO predictions, concealed through incorrect NO formation pathway contributions driven by the radical pool behaviour defined by the base chemistry.

This work provides a robust and high accuracy NO concentration dataset, targeting a wide range of flame temperatures, performed under well controlled conditions, that could be employed for thermochemical model optimisation in order to improve their prediction capabilities in velocity and NO concentration of hydrogen flames. This would facilitate the enhancement of the performance of advanced combustion technologies and further minimise emissions from hydrogen and hydrocarbon fuelled engines.

Acknowledgments

The authors would like to thank the support of the National Research Council of Canada (NRC), Siemens Energy Canada Limited, the Natural Sciences and Engineering Research Council of Canada (NSERC), the Fonds de Recherche du Québec - Nature et Technologies (FRQNT), and Climicals.

References

[1] M. Meulemans, A. Durocher, G. Bourque, and J. M. Bergthorson. “NO measurements in high temperature hydrogen flames : The crucial role of the hydrogen oxidation chemistry for accurate NO predictions”. In: *Combustion and Flame* 261 (2024), p. 113279.

[2] P. Glarborg, J. A. Miller, B. Ruscic, and S. J. Klippenstein. “Modeling nitrogen chemistry in combustion”. In: *Progress in Energy and Combustion Science* 67 (2018), pp. 31–68.

[3] S. Park. “Hydrogen addition effect on NO formation in methane/air lean-premixed flames at elevated pressure”. In: *International Journal of Hydrogen Energy* 46 (2021), pp. 25712–25725.

[4] T. Capurso, D. Laera, E. Riber, and B. Cuenot. “NO_x pathways in lean partially premixed swirling H_2-air turbulent flame”. In: *Combustion and Flame* 248 (2023), p. 112581.

[5] Q. Cui and K. Morokuma. "The spin-forbidden reaction CH($^2\Pi$) + N_2 → HCN + N(^{4}S) revisited I. Ab initio study of the potential energy surfaces". In: *Theoretical Chemistry Accounts* 102 (1999), pp. 127–133.

[6] L. Moskaleva and M. C. Lin. "The spin-conserved reaction CH + N_2 → H + NCN: A major pathway to prompt NO studied by quantum/statistical theory calculations and kinetic modeling of rate constant". In: *Proceedings of the Combustion Institute,* 28 (2000), pp. 2393–2401.

[7] N. Lamoureux, P. Desgroux, A. El Bakali, and J. F. Pauwels. "Experimental and numerical study of the role of NCN in prompt-NO formation in low-pressure CH_4-O_2-N_2 and C_2H_2-O_2-N_2 flames". In: *Combustion and Flame* 157 (2010), pp. 1929–1941.

[8] P. Versailles, G. M. G. Watson, A. C. A. Lipardi, and J. M. Bergthorson. "Quantitative CH measurements in atmospheric-pressure, premixed flames of C_1-C_4 alkanes". In: *Combustion and Flame* 165 (2016), pp. 109–124.

[9] S. J. Klippenstein, M. Pfeifle, A. W. Jasper, and P. Glarborg. "Theory and modeling of relevance to prompt-NO formation at high pressure". In: *Combustion and Flame* 195 (2018), pp. 3–17.

[10] N. Lamoureux, P. Desgroux, M. Olzmann, and G. Friedrichs. "The story of NCN as a key species in prompt-NO formation". In: *Progress in Energy and Combustion Science* 87 (2021), p. 100940.

[11] Y. B. Zeldovich. "The oxidation of nitrogen in combustion and explosions". In: *Acta Physiochimica* 21 (1946), pp. 577–628.

[12] M. Abián, M. U. Alzueta, and P. Glarborg. "Formation of NO from N_2/O_2 mixtures in a flow reactor: Toward an accurate prediction of thermal NO". In: *International Journal of Chemical Kinetics* 47 (2015), pp. 518–532.

[13] N. A. Buczkó, T. Varga, I. G. Zsély, and T. Turányi. "Formation of NO in high-temperature N_2/O_2/H_2O mixtures: re-evaluation of rate coefficients". In: *Energy and Fuels* 32 (2018), pp. 10114–10120.

[14] X. Han, M. Lubrano Lavadera, C. Brackmann, Z. Wang, Y. He, and A. A. Konnov. "Experimental and kinetic modeling study of NO formation in premixed CH_4+O_2+N_2 flames". In: *Combustion and Flame* 223 (2021), pp. 349–360.

[15] M. Meulemans, A. Durocher, P. Versailles, G. Bourque, and J. M. Bergthorson. "How well do we know thermal-NO? An investigation of NO formation in flames over a wide temperature range". In: *Proceedings of the Combustion Institute* 39 (2023), pp. 521–529.

[16] P. C. Malte and D. T. Pratt. "Measurement of atomic oxygen and nitrogen oxides in jet-stirred combustion". In: *Symposium (International) on Combustion* 15 (1975), pp. 1061–1070.

[17] G. M. Watson, J. D. Munzar, and J. M. Bergthorson. "NO formation in model syngas and biogas blends". In: *Fuel* 124 (2014), pp. 113–124.

[18] A. Durocher, M. Meulemans, P. Versailles, G. Bourque, and J. M. Bergthorson. "Back to basics - NO concentration measurements in atmospheric lean-to-rich, low-temperature, premixed hydrogen-air flames diluted with argon". In: *Proceedings of the Combustion Institute* 38 (2021), pp. 2093–2100.

[19] P. Versailles, A. Durocher, G. Bourque, and J. M. Bergthorson. "Effect of high pressures on the formation of nitric oxide in lean, premixed flames". In: *Journal of Engineering for Gas Turbines and Power* 143 (2021), p. 051029.

[20] M. Rieth, A. Gruber, and J. H. Chen. "A direct numerical simulation study on NO and N_2O formation in turbulent premixed ammonia/hydrogen/nitrogen-air flames". In: *Proceedings of the Combustion Institute* 39 (2023).

[21] J. W. Bozzelli and A. M. Dean. "O + NNH: A possible new route for NO_x formation in flames". In: *International Journal of Chemical Kinetics* 27 (1995), pp. 1097–1109.

[22] S. J. Klippenstein, L. B. Harding, P. Glarborg, and J. A. Miller. "The role of NNH in NO formation and control". In: *Combustion and Flame* 158 (2011), pp. 774–789.

[23] M. S. Day, J. B. Bell, X. Gao, and P. Glarborg. "Numerical simulation of nitrogen oxide formation in lean premixed turbulent $H_2/O_2/N_2$ flames". In: *Proceedings of the Combustion Institute* 33 (2011), pp. 1591–1599.

[24] A. B. Sahu and R. V. Ravikrishna. "Quantitative LIF measurements and kinetics assessment of NO formation in H_2/CO syngas–air counterflow diffusion flames". In: *Combustion and Flame* 173 (2016), pp. 208–228.

[25] J. Lee, M. C. Barbet, Q. Meng, R. E. Cornell, and M. P. Burke. "Experimental support for a new NO_x formation route via an HNNO intermediate". In: *Combustion and Flame* (2023).

[26] Q. Meng, L. Lei, J. Lee, and M. P. Burke. "On the role of HNNO in NO_x formation". In: *Proceedings of the Combustion Institute* 39 (2023), pp. 551–560.

[27] G. M. Watson, P. Versailles, and J. M. Bergthorson. "NO formation in rich premixed flames of C_1-C_4 alkanes and alcohols". In: *Proceedings of the Combustion Institute* 36 (2017), pp. 627–635.

[28] G. M. G. Watson, P. Versailles, and J. M. Bergthorson. "NO formation in premixed flames of C_1-C_3 alkanes and alcohols". In: *Combustion and Flame* 169 (2016), pp. 242–260.

[29] P. Versailles, A. Durocher, G. Bourque, and J. M. Bergthorson. "Nitric oxide formation in lean, methane-air stagnation flames at supra-atmospheric pressures". In: *Proceedings of the Combustion Institute* 37 (2019), pp. 711–718.

[30] A. Durocher, M. Meulemans, G. Bourque, and J. M. Bergthorson. "Nitric oxide concentration measurements in low-temperature, premixed hydrogen-air stagnation flames at elevated pressures". In: *Proceedings of the Combustion Institute* 39 (2023), pp. 541–550.

[31] A. Durocher, G. Bourque, and J. M. Bergthorson. "Bayesian calibration of kinetic parameters in the CH chemistry toward accurate prompt-NO modelling". In: *Journal of Engineering for Gas Turbines and Power* 145 (2022), p. 021014.

[32] A. Durocher, M. Meulemans, G. Bourque, and J. M. Bergthorson. "Measurements of the laminar flame speed of premixed, hydrogen-air-argon stagnation flames". In: *Applications in Energy and Combustion Science* 7 (2021), p. 100028.

[33] H. J. Curran. "Developing detailed chemical kinetic mechanisms for fuel combustion". In: *Proceedings of the Combustion Institute* 37 (2019), pp. 57–81.

[34] R. C. Sausa, W. R. Anderson, D. C. Dayton, C. M. Faust, and S. L. Howard. "Detailed structure study of a low pressure, stoichiometric H_2/N_2O/Ar flame". In: *Combustion and Flame* 94 (1993), pp. 407–425.

[35] J. E. Harrington, G. P. Smith, P. A. Berg, A. R. Noble, J. B. Jeffries, and D. R. Crosley. "Evidence for a new NO production mechanism in flames". In: *Symposium (International) on Combustion* 26 (1996), pp. 2133–2138.

[36] G. J. Rørtveit, J. E. Hustad, S.-C. Li, and F. A. Williams. "Effects of diluents on NO_x formation in hydrogen counterflow flames". In: *Combustion and Flame* 130 (2002), pp. 48–61.

[37] M. Skottene and K. E. Rian. "A study of NO_x formation in hydrogen flames". In: *International Journal of Hydrogen Energy* 32 (2007), pp. 3572–3585.

[38] R. J. Kee, J. A. Miller, G. H. Evans, and G. Dixon-Lewis. "A computational model of the structure and extinction of strained, opposed flow, premixed methane-air flames". In: *Symposium (International) on Combustion* 22 (1988), pp. 1479–1494.

[39] A. C. A. Lipardi, P. Versailles, G. M. G. Watson, G. Bourque, and J. M. Bergthorson. "Experimental and numerical study on NO_x formation in CH_4–air mixtures diluted with exhaust gas components". In: *Combustion and Flame* 179 (2017), pp. 325–337.

[40] R. W. Schefer, W. D. Kulatilaka, B. D. Patterson, and T. B. Settersten. "Visible emission of hydrogen flames". In: *Combustion and Flame* 156 (2009), pp. 1234–1241.

[41] P. Versailles. "CH formation in premixed flames of C_1-C_4 alkanes: assessment of current chemical modelling capability against experiments". PhD. McGill University, 2017.

[42] A. Durocher. "Towards robust nitrogen chemistry model development: Uncertainty quantification and prediction capability in atmospheric and elevated-pressure premixed flames". PhD. McGill University, 2021.

[43] B. C. Connelly, B. A. V. Bennett, M. D. Smooke, and M. B. Long. "A paradigm shift in the interaction of experiments and computations in combustion research". In: *Proceedings of the Combustion Institute* 32 (2009), pp. 879–886.

[44] J. M. Bergthorson and P. E. Dimotakis. "Particle velocimetry in high-gradient/high-curvature flows". In: *Experiments in Fluids* 41 (2006), pp. 255–263.

[45] W. G. Bessler, C. Schulz, S. Volker, and J. W. Daily. "A versatile modeling tool for nitric oxide LIF spectra". In: *Proceedings of the Third Joint Meeting of the U.S. Sections of The Combustion Institute*. Chicago, 2003, P105.

[46] W. G. Bessler and C. Schulz. "Quantitative multi-line NO-LIF temperature imaging". In: *Applied Physics B: Lasers and Optics* 78 (2004), pp. 519–533.

[47] G. M. Watson, J. D. Munzar, and J. M. Bergthorson. "Diagnostics and modeling of stagnation flames for the validation of thermochemical combustion models for NO_x predictions". In: *Energy and Fuels* 27 (2013), pp. 7031–7043.

[48] K. K. Foo, N. Lamoureux, A. Cessou, C. Lacour, and P. Desgroux. "The accuracy and precision of multi-line NO-LIF thermometry in a wide range of pressures and temperatures". In: *Journal of Quantitative Spectroscopy and Radiative Transfer* 255 (2020), p. 107257.

[49] J. Luque and D. R. Crosley. *LIFBASE Version 2.1.1, Database and spectral simulation for diatomic molecules (v1.6)*. 1999.

[50] D. G. Goodwin, H. K. Moffat, I. Schoegl, R. L. Speth, and B. W. Weber. *Cantera: An object-oriented software toolkit for chemical kinetics, thermodynamics, and transport processes*. 2021.

[51] K. P. Shrestha, L. Seidel, T. Zeuch, and F. Mauss. "Kinetic modeling of NO_x formation and consumption during methanol and ethanol oxidation". In: *Combustion Science and Technology* 191 (2019), pp. 1627–1659.

[52] G. Bagheri, E. Ranzi, M. Pelucchi, A. Parente, A. Frassoldati, and T. Faravelli. "Comprehensive kinetic study of combustion technologies for low environmental impact: MILD and OXY-fuel combustion of methane". In: *Combustion and Flame* 212 (2020), pp. 142–155.

[53] Y. Song et al. "The sensitizing effects of NO_2 and NO on methane low temperature oxidation in a jet stirred reactor". In: *Proceedings of the Combustion Institute* 37 (2019), pp. 667–675.

[54] H. Hashemi, J. G. Jacobsen, C. T. Rasmussen, J. M. Christensen, P. Glarborg, S. Gersen, M. van Essen, H. B. Levinsky, and S. J. Klippenstein. "High-pressure oxidation of ethane". In: *Combustion and Flame* 182 (2017), pp. 150–166.

[55] T. Varga et al. "Optimization of a hydrogen combustion mechanism using both direct and indirect measurements". In: *Proceedings of the Combustion Institute* 35 (2015), pp. 589–596.

[56] A. El Bakali, L. Pillier, P. Desgroux, B. Lefort, L. Gasnot, J. F. Pauwels, and I. da Costa. "NO prediction in natural gas flames using GDF-Kin3.0 mechanism NCN and HCN contribution to prompt-NO formation". In: *Fuel* 85 (2006), pp. 896–909.

[57] N. Lamoureux, H. E. Merhubi, L. Pillier, S. de Persis, and P. Desgroux. "Modeling of NO formation in low pressure premixed flames". In: *Combustion and Flame* 163 (2016), pp. 557–575.

[58] G. P. Smith et al. “GRI-Mech 3.0”. In: (1999).

[59] A. A. Konnov. “Yet another kinetic mechanism for hydrogen combustion”. In: *Combustion and Flame* 203 (2019), pp. 14–22.

[60] Y. Wu et al. “Understanding the antagonistic effect of methanol as a component in surrogate fuel models: A case study of methanol/*n*-heptane mixtures”. In: *Combustion and Flame* 226 (2021), pp. 229–242.

[61] University of California at San Diego. *Chemical-Kinetic Mechanisms for Combusiton Applications*. 2016.

[62] H. Wang, N. Slavinskaya, and O. Haidn. “A comprehensive kinetic modeling study of hydrogen combustion with uncertainty quantification”. In: *Fuel* 319 (2022), p. 123705.

[63] W. Sun et al. “Further insights into the core mechanism of H_2/CO/NO_x reaction system”. In: *Combustion and Flame* 245 (2022), p. 112308.

[64] H. Wang and D. A. Sheen. “Combustion kinetic model uncertainty quantification, propagation and minimization”. In: *Progress in Energy and Combustion Science* 47 (2015), pp. 1–31.

[65] J. Bell, M. Day, J. Goodman, R. Grout, and M. Morzfeld. “A Bayesian approach to calibrating hydrogen flame kinetics using many experiments and parameters”. In: *Combustion and Flame* 205 (2019), pp. 305–315.

[66] A. L. Sánchez and F. A. Williams. “Recent advances in understanding of flammability characteristics of hydrogen”. In: *Progress in Energy and Combustion Science* 41 (2014), pp. 1–55.

[67] M. P. Burke. “Harnessing the combined power of theoretical and experimental data through multiscale informatics”. In: *International Journal of Chemical Kinetics* 48 (2016), pp. 212–235.

[68] D. L. Baulch et al. “Evaluated Kinetic Data for Combustion Modeling: Supplement II”. In: *Journal of Physical and Chemical Reference Data* 34 (2005), pp. 757–1397.

[69] M. P. Burke, M. Chaos, Y. Ju, F. L. Dryer, and S. J. Klippenstein. “Comprehensive H_2/O_2 kinetic model for high-pressure combustion”. In: *International Journal of Chemical Kinetics* 44 (2012), pp. 444–474.

[70] S. J. Klippenstein. “From theoretical reaction dynamics to chemical modeling of combustion”. In: *Proceedings of the Combustion Institute* 36 (2017), pp. 77–111.

[71] M. P. Burke and S. J. Klippenstein. “Ephemeral collision complexes mediate chemically termolecular transformations that affect system chemistry”. In: *Nature Chemistry* 9 (2017), pp. 1078–1082.

Chapter VI. Conclusion

VI.1 Summary of research

The work presented in this thesis had two objectives: 1) obtain the current understanding of the modelling chemistry of NO in conditions representative of gas-turbine conditions, hence where the thermal NO pathway is promoted; and 2) provide the community with an experimental dataset of high confidence levels to improve current models. These objectives were fulfilled by organising the work in three distinct parts: a comprehensive comparison of several calibration techniques for high-resolution and high-accuracy NO-LIF measurements; the measurements of velocity, temperature, and NO concentration in high temperature methane-air flames; and similarly in hydrogen flames.

Chapter III presents a comparison of four experimental and post-processing calibration methodologies to obtain quantitative NO measurements using NO-Laser-Induced Fluorescence (NO-LIF). This work lays out the methodology, assumptions, and uncertainty analysis of each technique, providing guidance to fellow researchers of which method to choose according to the experimental conditions they plan on studying. This comparison work also guides the choice of a calibration technique for the experimental work presented in the subsequent chapters. For quantitative NO measurements in atmospheric flames producing a wide variability of NO and at high temperatures, potentially experiencing reburn, only one calibration technique is accurate: the calculation of the optical coefficient (C_{opt}) of the experimental setup by modelling the LIF signal of numerical flames, assuming constant interfering LIF signal. Using this methodology leads to a relatively small uncertainty ($\sim$5%) on the measured NO concentration profiles, ideal for the comparison of experimental and numerical results, with limited experimental time, and is applicable in reburn conditions. This work is of major importance to clarify the current state of the literature regarding NO-LIF calibration, especially the conditions in which the techniques are applicable and their uncertainties. Through this work, the aim is to facilitate the publication of speciation measurements using LIF, hence, participating in an overall better understanding of the combustion chemistry.

Chapter IV investigates the formation of NO in high-temperature methane-air flames. These conditions are chosen to be representative of current gas turbine combustors running using natural gas fuel, for which the contribution of the thermal pathway is dominant. The comparison of the measured velocity, temperature, and NO concentration profiles to the predictions of several thermochemical models indicated that the current understanding of NO modelling in combustion was still inaccurate. Results showed that all models predictions could vary from -90% to $+65\%$

from the experimental NO concentration. As a result, the emissions of current gas turbine designs, which depend heavily on accurate thermochemical models, could differ significantly from the initial predictions and designs.

Finally, Chapter V investigates the formation of NO in high-temperature hydrogen-air flames. Similarly to the previous campaign, the thermal pathway is expected to be dominant, representative of future gas turbine combustors running using hydrogen fuel. The prediction of the velocity and NO concentrations are in significant disagreement with the experimental results, indicating inaccuracies in the modelled NO chemistry, as noted in the previous campaign, but also in the core H_2/O_2 chemistry. This leads to a misprediction of -90% to $+275\%$ by the models compared to the measured NO concentrations. Considering the current legislative constraints on the emissions of NO by gas turbines, this could significantly inhibit and delay the use of gas turbines running on hydrogen fuel.

The results from both experimental campaigns investigating the NO chemistry in high temperature flames demonstrate that the current understanding of the NO formation chemistry remain significantly inaccurate. These inaccuracies seem to be consequences of an inaccurate prediction of the thermal initiation reaction rate, but also from deeper modelling issues in the core H_2/O_2 chemistry. While the latter is not directly observable in the velocity results of the methane-air flames, it was easily noticed in the hydrogen flames because they have a simpler chemistry. These results unveiled a bias that currently affect the thermochemical models: there is insufficient experimental data available to the modelling community, specifically those deviating from hydrocarbon fuels, at low to moderate temperatures, and low pressure flames. Hence, the development of models is mainly performed using validation data that is not representative of what is required for the design of gas turbine combustors fit for the energy transition. Ultimately, an overhaul of the predictive models, from the core H_2/O_2 to the NO chemistry is needed, such as in a hierarchical manner [1]. The models need to be fitted on experimental data obtained in well controlled conditions, and for which each modelling subset is validated against data representative of a diversity of combustion conditions. This can be improved by providing high resolution and low uncertainty experimental data to the modelling community in conditions that better represent current and future gas-turbine conditions.

VI.2 Recommendations for future work

This thesis work is part of a larger experimental investigation ongoing at the Alternative Fuels Laboratory, in which each of the four NO formation pathways are studied. Throughout the publications [2–9], several recommended studies emerge:

- An experimental study of hydrogen flames in a variety of conditions. There is a gap in the literature for highly-resolved, low-uncertainty, 1D thermodynamic and speciation profiles obtained in such conditions. Such experimental results are of significance for model improvements.

- An experimental study of the radical pool in hydrogen flames. It is crucial to have a better understanding of the core chemistry in modelling combustion. This can be improved through the measurement of the concentration of O, H, and OH within flames. It is recommended for these measurements to be performed in hydrogen flames to resolve, first, the core chemistry describing the H_2 and O_2 interactions void of any carbon-based reactions. The methodology presented using NO-LIF can be adapted to quantitatively measure short-lived species.

- An experimental study of NO formation in low-temperature, lean, high-pressure hydrogen flames to study the N_2O pathway. Measurements of NO in such conditions would give a better insight of NO formation in relevant gas turbine conditions, as well as the interactions with the thermal NO pathway. Previous work up to 8 atm was unsuccessful in triggering the formation of NO through this pathway alone [7].

- A numerical study for the improvement of predictive thermochemical models by using the current experimental dataset through statistical calibration [10]. Such work could help identify key reactions responsible for the large uncertainties observed between the models and the experiments, and could constrain the numerical uncertainties. This could guide the modelling community to orientate their effort towards these most uncertain and important reactions using *ab initio* calculations, or demanding the experimental community for reaction rate measurements in shock tubes or flow reactors.

These would lead to an overall improved understanding of the combustion chemistry occurring in hydrogen flames. Such efforts would contribute to an accelerated implementation of sustainable solutions in the current energy sector and, hopefully, limit the impacts of the current climate crisis on the human health and the environment.

References

[1] H. J. Curran. “Developing detailed chemical kinetic mechanisms for fuel combustion”. In: *Proceedings of the Combustion Institute* 37 (2019), pp. 57–81.

[2] G. M. G. Watson, P. Versailles, and J. M. Bergthorson. “NO formation in premixed flames of C_1-C_3 alkanes and alcohols”. In: *Combustion and Flame* 169 (2016), pp. 242–260.

[3] P. Versailles, G. M. G. Watson, A. C. A. Lipardi, and J. M. Bergthorson. "Quantitative CH measurements in atmospheric-pressure, premixed flames of C_1-C_4 alkanes". In: *Combustion and Flame* 165 (2016), pp. 109–124.

[4] G. M. Watson, P. Versailles, and J. M. Bergthorson. "NO formation in rich premixed flames of C_1-C_4 alkanes and alcohols". In: *Proceedings of the Combustion Institute* 36 (2017), pp. 627–635.

[5] P. Versailles, A. Durocher, G. Bourque, and J. M. Bergthorson. "Nitric oxide formation in lean, methane-air stagnation flames at supra-atmospheric pressures". In: *Proceedings of the Combustion Institute* 37 (2019), pp. 711–718.

[6] A. Durocher, M. Meulemans, P. Versailles, G. Bourque, and J. M. Bergthorson. "Back to basics - NO concentration measurements in atmospheric lean-to-rich, low-temperature, premixed hydrogen-air flames diluted with argon". In: *Proceedings of the Combustion Institute* 38 (2021), pp. 2093–2100.

[7] A. Durocher, M. Meulemans, G. Bourque, and J. M. Bergthorson. "Nitric oxide concentration measurements in low-temperature, premixed hydrogen-air stagnation flames at elevated pressures". In: *Proceedings of the Combustion Institute* 39 (2023), pp. 541–550.

[8] M. Meulemans, A. Durocher, P. Versailles, G. Bourque, and J. M. Bergthorson. "How well do we know thermal-NO? An investigation of NO formation in flames over a wide temperature range". In: *Proceedings of the Combustion Institute* 39 (2023), pp. 521–529.

[9] M. Meulemans, A. Durocher, G. Bourque, and J. M. Bergthorson. "NO measurements in high temperature hydrogen flames : The crucial role of the hydrogen oxidation chemistry for accurate NO predictions". In: *Combustion and Flame* 261 (2024), p. 113279.

[10] A. Durocher. "Towards robust nitrogen chemistry model development: Uncertainty quantification and prediction capability in atmospheric and elevated-pressure premixed flames". PhD. McGill University, 2021.

Appendix A. Supplementary Materials to Chapter III

A.1 Experimentally measured boundary conditions

Table A.1 reports the experimental boundary conditions used to perform simulations of quasi-1D stagnation flames, along with their respective uncertainty in parentheses.

Table A.1: Boundary conditions and their respective uncertainty (in parentheses) for each flame produced in this study.

	p [atm]	$\mathcal{L}$ [mm]	T_{in} [K]	T_{wall} [K]	u_{in} [m.s^{-1}]	du_{in}/dz [s^{-1}]	$X_{\text{NO,sd}}$ [ppm]	ϕ [-]	X_{O_2} [-]	X_{Ar} [-]
Phi0.9_Tad2130K_O21	1 (0.005)	7.12 (0.01)	291.3 (2)	402.3 (5)	0.545 (0.001)	156.4 (2.58)	0 (0.0)	0.90 (0.005)	0.21 (0.001)	0 (0)
							25 (0.1)	0.90 (0.096)	0.21 (0.023)	0 (0)
							50 (0.1)	0.90 (0.096)	0.21 (0.023)	0 (0)
							75 (0.2)	0.90 (0.096)	0.21 (0.023)	0 (0)
Phi0.7_Tad1830K_O21	1 (0.005)	7.62 (0.01)	293.5 (2)	361.5 (5)	0.266 (0.001)	61 (3.87)	0 (0.0)	0.70 (0.004)	0.21 (0.001)	0 (0)
							50 (0.1)	0.70 (0.167)	0.21 (0.051)	0 (0)
Phi0.9_Tad2500K_O40	1 (0.005)	6.84 (0.01)	291.9 (2)	501.9 (5)	1.575 (0.003)	472.7 (5.38)	0 (0.0)	0.90 (0.005)	0.40 (0.002)	0.3085 (0.00175)
							150 (0.4)	0.90 (0.005)	0.40 (0.002)	0.3085 (0.00840)

A.2 LIFSim parameters

Table A.2 presents the constants used in LIFSim to calculate the numerical NO-LIF signal.

A.3 Assumptions and supporting evidence

A.3.1 Negligible NO reburn conditions

The assumption that negligible reburn occurs through the flame is valid depending on the amount of NO that is seeded in the flame. This is verified experimentally in lean low pressure methane-air flames seeded with up to 30,000 ppm [6]. This is also explored numerically for this study. Figure A.1 presents the simulation results of NO-seeded flames at different levels ($X_{\text{NO,sd}}$). The flames were simulated according to the conditions presented in Tab. III.1, and using three thermochemical models: CRECK [7, 8], GRI [9], and SD [10]. When seeding a flame, the mass flow rate of seeded NO ($\dot{m}_{\text{NO,sd}}$) is expected to remain constant. The calculation is performed on a mass basis as it is

Table A.2: Parameters used to obtain f_{LIF} in Eq. (III.21) using LIFSim

Parameter	Notation	Value	Units	Source
LIFSim version		E 3.17		
Target molecule		NO		
Online excitation wavelength	λ_{on}	226.0345	[nm]	Experimental condition
Offline excitation wavelength	λ_{off}	226.0470	[nm]	Experimental condition
Laser energy density	I	7.8	[mJ·cm^2]	Experimentally measured
Laser pulse duration	τ_{pulse}	10.5	[ns]	Experimentally measured
HWHM of laser instrument Gauss function	$\Delta\nu_{\mathrm{L,Gauss}}$	0.3926 / 2	[cm^{-1}]	Experimentally inferred*
HWHM of laser instrument Lorentz function	$\Delta\nu_{\mathrm{L,Loren}}$	0.1664 / 2	[cm^{-1}]	Experimentally inferred*
Minimum detection wavelength	λ_{min}	220	[nm]	
Maximum detection wavelength	λ_{max}	340	[nm]	
Detection resolution	$\Delta\lambda$	0.01	[cm^{-1}]	
HWHM of detection instrument function	$\Delta\nu_{\mathrm{det,Gauss}}$	100	[cm^{-1}]	LIFSim default value
HWHM of detection instrument function	$\Delta\nu_{\mathrm{det,Loren}}$	10	[cm^{-1}]	LIFSim default value
Detection instrument transmissivity	$\mathcal{T}_\lambda$	λ-dependent	[-]	Long-pass filter manufacturer
Pressure	p	1	[bar]	Experimental condition
Temperature	$T(z)$	z-dependent	[K]	Numerical solution
Composition	$X(z)$	z-dependent	[-]	Numerical solution
Quenching cross-section	σ_{M}	speciesdependent**	[Å^2]	[1, 2]
Collisional coefficient	2γ	speciesdependent***	[cm^{-1}·atm^{-1}]	[3–5]
Collisional shift coefficient	δ	speciesdependent***	[cm^{-1}·atm^{-1}]	[3–5]

* Experimentally inferred by fitting a Voigt profile on an isolated NO transition

** Species included: N_2, O_2, CO_2, CO ,H_2O, CH_4, C_2H_6, C_3H_8, C_2H_4, C_2H_2, NO, NO_2, N_2O, NH_3, NH, H_2, O, H, OH, CH, He, Ne, Ar, Kr, Xe

*** Species included: N_2, O_2, H_2O, Ar, CO_2, CO, CH_4

a conserved quantity, as opposed to a molar basis that changes with the formation or reaction of species other than NO. The mass flow rate of seeded NO can be calculated numerically through the difference of the NO produced in a seeded and unseeded flame. Calculations were performed such that:

$$\dot{m}_{\mathrm{NO,sd}}(z) = \dot{m}_{\mathrm{NO,nsct+sd}}(z) - \dot{m}_{\mathrm{NO,nsct}}(z), \tag{A.1}$$

and with

$$\dot{m}_{\mathrm{NO,nsct+sd}}(z) = Y_{\mathrm{NO,nsct+sd}}(z) \cdot \rho_{in} \cdot u_{in} \cdot A_{\mathrm{nozzle}}, \text{and} \tag{A.2}$$

$$\dot{m}_{\mathrm{NO,nsct}}(z) = Y_{\mathrm{NO,nsct}}(z) \cdot \rho_{in} \cdot u_{in} \cdot A_{\mathrm{nozzle}}. \tag{A.3}$$

Hence, reburn can be defined as any mass flow rate of seeded NO that is lower than the initial seeded mass flow rate:

$$\text{Reburn fraction} = \frac{\dot{m}_{\mathrm{NO,sd}}(z) - \dot{m}_{\mathrm{NO,sd}}(z_{\mathrm{in}})}{\dot{m}_{\mathrm{NO,sd}}(z_{\mathrm{in}})}, \tag{A.4}$$

such that the reburn fraction represents the proportion of the seeded NO that reacted through the flame.

For each flame, the largest reburn occurs in the flame-front and close to the stagnation plate. A Reaction Pathway Analysis (RPA) performed on N from the inlet to the peak of NO reburn in

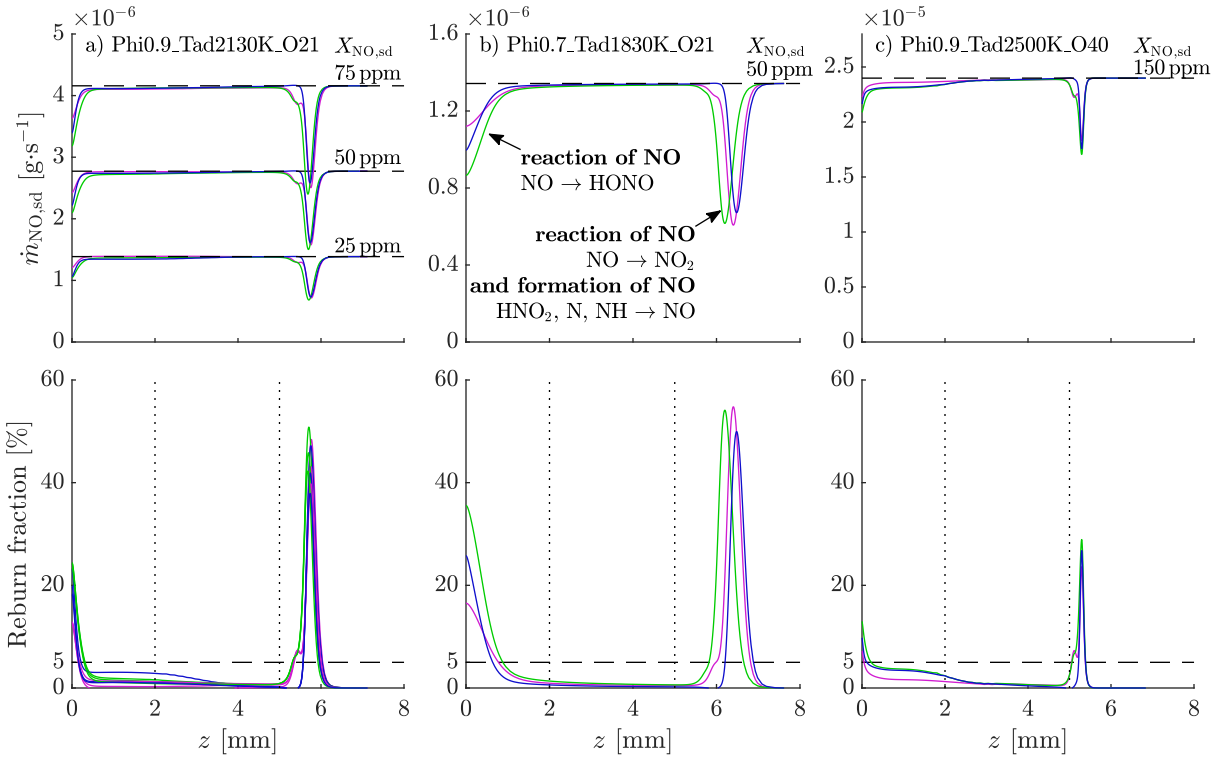

Figure A.1: NO reburn simulations performed for three flames: a) Phi0.9_Tad2130K_O21, b) Phi0.7_Tad1830K_O21, and c) Phi0.9_Tad2500K_O40, using three thermochemical models (CRECK —, GRI —, and SD —).

the flame-front indicates that NO reacts to form mainly NO_2. Near the stagnation plate, a RPA shows that NO reacts to form HONO instead. Most of the mass flow rate of NO is restored after the peak in the flame front thanks to the formation of NO from species such as HNO_2, N, and NH. It demonstrates that calibration techniques assuming negligible NO reburn are only valid in the post-flame region, and should be used with care in the flame-front region of the flames. As seen through the reburn fraction evolution with z, NO reburn remains well under 5% for the three flames and for all seeding levels performed in this study, as well as for the three thermochemical models used.

An investigation is performed as well on which flame condition would lead to significant NO reburn. Figure A.2 presents the NO reburn fraction for a given thermochemical model at a fixed position of the post-flame region, by varying the level of seeded NO ($X_{NO,sd}$) in the initial mixture. The reburn fraction of flames at varying conditions is presented for lean ($\phi = 0.7$) and rich ($\phi = 1.3$) stoichiometries, and at atmospheric ($p = 1$ atm) and elevated pressures ($p = 8$ atm).

In lean and atmospheric conditions, the NO reburn fraction remains under 5% up to large NO seeding levels. In these conditions, the assumption that negligible reburn occurs is valid. With increasing pressure, still in lean conditions, reburn fractions above 5% occur at about 250 ppm of

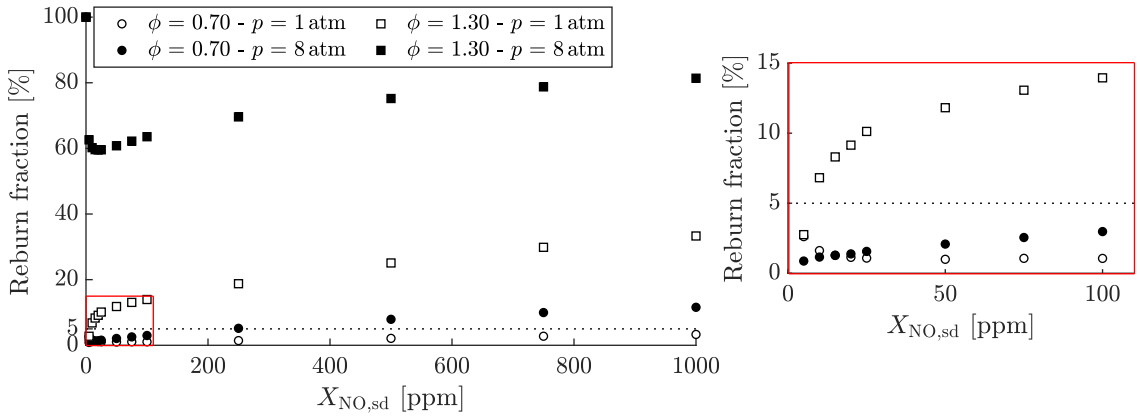

Figure A.2: NO reburn fraction calculated for several seeding levels in the post-flame region of four flame conditions: lean and atmospheric pressure (hollow circle), lean and elevated pressure (solid circle), rich and atmospheric pressure (hollow square), and rich and elevated pressure (solid square).

seeded NO. This indicates that, at elevated pressure conditions, lower seeding should be employed than for atmospheric conditions to avoid significant NO reburn. On the rich side, reburn fractions are consistently above 5%, except for very low seeding at atmospheric pressure (5 ppm), and three to four times more important at elevated pressures. Therefore, the assumption of negligible NO reburn in rich conditions ($\phi = 1.3$) is not valid, as expected.

Ideally, these claims should be verified experimentally in conditions in which the flames will be performed. In conditions where NO reburn is observed, only the calibration technique employing the optical constant C_{opt} is valid. Two scenarios can occur using the C_{opt} calibration technique: 1) There is reburn in the measured flame but a calibration flame can be produced in conditions of negligible reburn. In this case, the determination of C_{opt} is not impacted by reburn, and the coefficient can be applied to any flame. 2) There is reburn in the measured flame and in the calibration flame. In such scenario, it is important to select a thermochemical model that accurately predicts reburn to determine C_{opt}. Once obtained, the coefficient can be applied to any flame condition.

This investigation points at the applicability of the two calibration techniques presented in the main article. In the case of the extrapolation from seeded to nascent NO technique (C_{lin}), its applicability is limited to lean low-pressure flames. In the case of the optical calibration technique (C_{opt}), its applicability is not limited by reburn, as long as the coefficient is obtained in a flame that does not experience any reburn. As such, the coefficient can be obtained in low pressure lean flames and applied to rich or high pressure flames.

A.3.2 Constant temperature and concentration between the unseeded and seeded flames

The assumption of constant temperature and concentration of the main species between unseeded and seeded flames is necessary in order to assume that f_{LIF} remains constant between both flames. This is confirmed by calculating the relative difference of molar fraction of every major specie (defined as $X_s > 0.1$ ppm) of each seeded flame compared to the unseeded flame, as well as for the temperature, at the point of analysis (in the post-flame region). As only the molar fraction of NO is expected to vary significantly, due to the seeding, it is removed from the analysis.

Figure A.3 presents the relative difference calculated for each parameter, at a given location of the post-flame region, between each seeding level and the unseeded condition of the three flames performed in this study. For each flame, the relative difference remains under 1%. This demonstrates that negligible differences in temperature and species concentration occur between the unseeded and seeded flames. Therefore, the assumption that f_{LIF} remains relatively constant between the unseeded and seeded flame is valid for the flame and seeding levels studied.

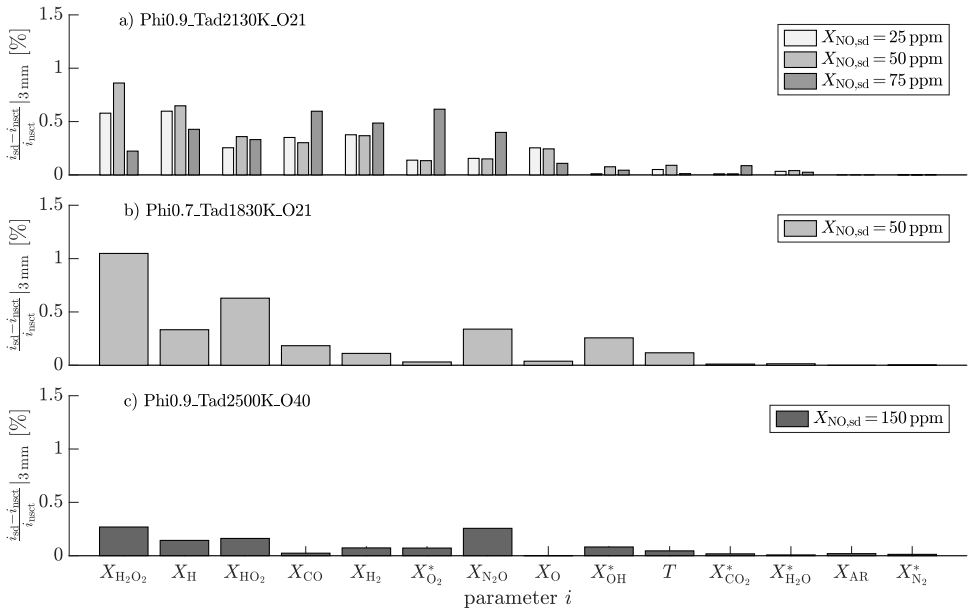

Figure A.3: Relative difference of parameter i between the seeded and unseeded simulation of a given flame: a) Phi0.9_Tad2130K_O21, b) Phi0.7_Tad1830K_O21, and c) Phi0.9_Tad2500K_O40, using the CRECK thermochemical model, at $z = 3$ mm. Molar fractions marked with * identify the main quenchers of these flames, see Section A.3.3.

A.3.3 The C_{opt} calibration technique is minimally dependent on the thermochemical model employed

In order to obtain C_{opt}, the flame is simulated using a thermochemical model and then transformed into a NO-LIF signal that can be compared to the experimental LIF signal. In the article, it is stated that any thermochemical model could be used to calculate C_{opt}, as long as the model captures relatively well the kinetics of the flame. This is possible through the use of the net LIF signal between a seeded and the unseeded flame to calculate C_{opt}.

This can be demonstrated using the 3-level linear LIF equation developed in Section III.3.1.3, see Eq. (III.20-III.22):

$$F_{\text{NO-LIF}} = X_{\text{NO}} \cdot \overbrace{\frac{p f_{\text{B}}}{T} \cdot \frac{1}{\sum Q_{ul}}}^{\text{flame-dependent}} \cdot \overbrace{\frac{\mathcal{N}_{\text{A}}}{c\mathcal{R}_{\text{u}}}}^{\text{constants}} \cdot \overbrace{\frac{1}{\Delta\nu_{\text{L}}}}^{\text{laser-dependent}} \cdot \overbrace{B_{12} \sum A_{ul}}^{\text{line-dependent}} \cdot \overbrace{\Gamma}^{\substack{\text{flame-}\\\text{laser-}\\\text{dependent}}} \cdot \overbrace{\mathcal{E}_{\text{c}} \mathcal{T}_{\lambda} \frac{\Omega}{4\pi} \ell}^{\text{setup-dependent}} , \tag{A.5}$$

Regrouping all experimental constants under the term α, the previous relationship simplifies to:

$$F_{\text{NO-LIF}} = X_{\text{NO}} \cdot \frac{p f_{\text{B}}}{T} \cdot \frac{1}{\sum Q_{ul}\left(X_s, p, T\right)} \cdot \Gamma \cdot \alpha, \tag{A.6}$$

where only X_{NO}, p, T, f_{B}, Q_{ul}, and Γ are flame-dependent. Note that B_{12} and A_{ul} are only line-dependent and are also experimental constants in this case. In LIFSim, most of the setup-dependent parameters are not modelled, bringing their values to 1. Therefore, when determining C_{opt} following Eq. (III.65) by replacing $F^{\text{num}}_{\text{NO-LIF,sd}}$ with Eq. (A.6), it becomes[1]:

$$C_{\text{opt}} = \frac{F^{\text{exp}}_{\text{NO-LIF,sd}}}{\alpha \frac{X_{\text{NO,sd}} \cdot \frac{p f_{\text{B}}}{T} \cdot \Gamma}{\sum Q_{ul}(X_s, p, T)}}, \tag{A.7}$$

where only $X_{\text{NO,sd}}$, p, T, f_{B}, Q_{ul}, and Γ are dependent on the prediction of the thermochemical model employed. As previously discussed, the pressure and temperature is generally properly captured by the thermochemical models, as it relies on the accurate prediction of major species. Thus, C_{opt} becomes only dependent on the thermochemical model through $X_{\text{NO,sd}}$ and X_{s}.

As shown in Fig. A.4, regardless of the level of accuracy of the thermochemical models (see Fig. III.13), the profile of $X_{\text{NO,sd}}$ remains consistent. Therefore, C_{opt} is independent of the choice of the thermochemical model through $X_{\text{NO,sd}}$.

As for X_s, a sensitivity analysis is used to determine the most important species driving Q_{ul} for the three flames of the study. Figure A.5 presents the result of the sensitivity analysis performed

[1] Note that a simplification is done here, the direct measurement of the fluorescence of $X_{\text{NO,sd}}$ is not feasible, instead the difference of the seeded and unseeded fluorescence signal is obtained, following Eq. (III.59) and Eq. (III.62).

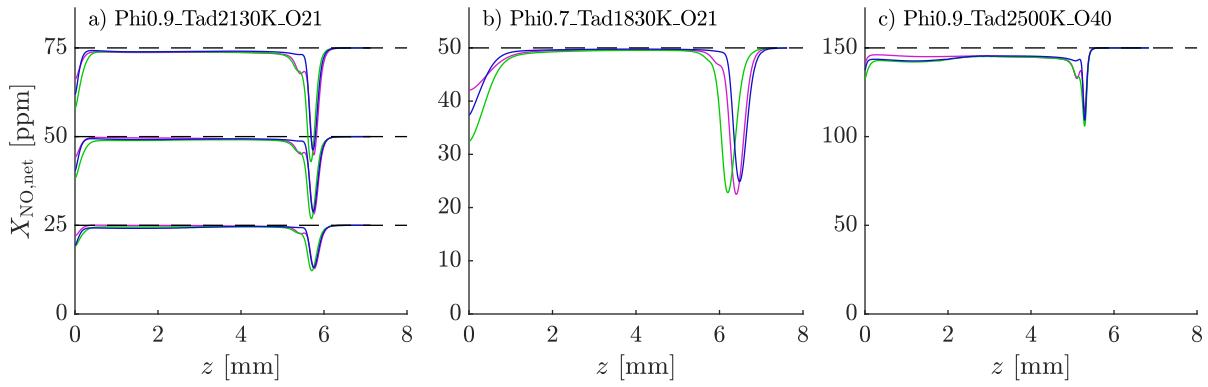

Figure A.4: Predictions of $X_{NO,sd}$ for three flames: a) Phi0.9_Tad2130K_O21, b) Phi0.7_Tad1830K_O21, and c) Phi0.9_Tad2500K_O40, using three thermochemical models (CRECK —, GRI —, and SD —).

on $F^{num}_{NO\text{-}LIF}$ at a given location of the post-flame region of the flames, for which the molar fraction of each quenching species was perturbed by 1%. Results show that, for all three flames, only about five species drive the quenching process: CO_2, H_2O, N_2, O_2, and OH.

Comparing the predictions of the three thermochemical models for the species driving Q_{ul}, it shows that the predictions are relatively consistent between the thermochemical models, as shown in Fig. A.6. Note that, even if the molar fraction of OH shows the largest variation between the models, it is also the species with the least impact on quenching, as seen in Fig. A.5. Thus, C_{opt} is also independent of Q_{ul} as the species driving it are consistently predicted by the different models.

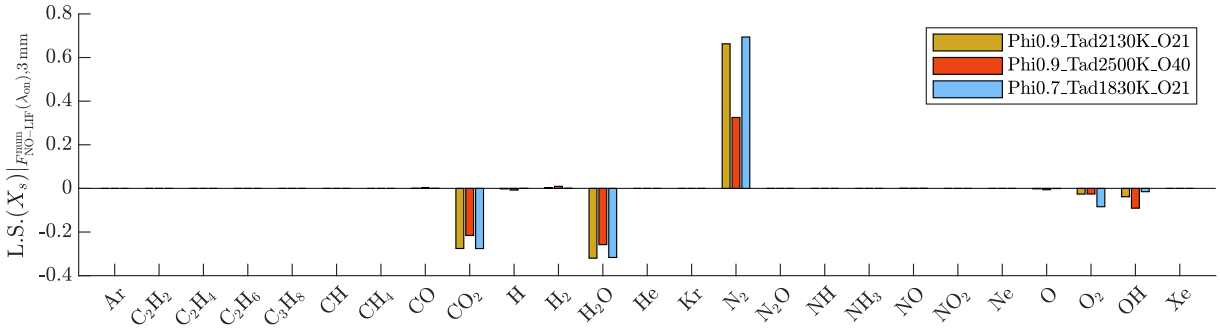

Figure A.5: L.S. of the NO-LIF signal by perturbing the molar fraction of the quenching species for the three flames, at $z = 3$ mm, using the CRECK thermochemical model.

These assumptions are also verified by generating C_{opt} for the three thermochemical models, widely varying in their level of accuracy in predicting NO (see Fig. III.13). Results are shown in Fig. A.7. The values of C_{opt} obtained by averaging the results of the 16 individual flames for each thermochemical model are consistent and within the 95% confidence interval. This can be better understood by looking at individual profiles on which C_{opt} is calculated, as presented in Fig. A.8. For a selected seeding at each flame condition, it is evident that, despite the discrepancies

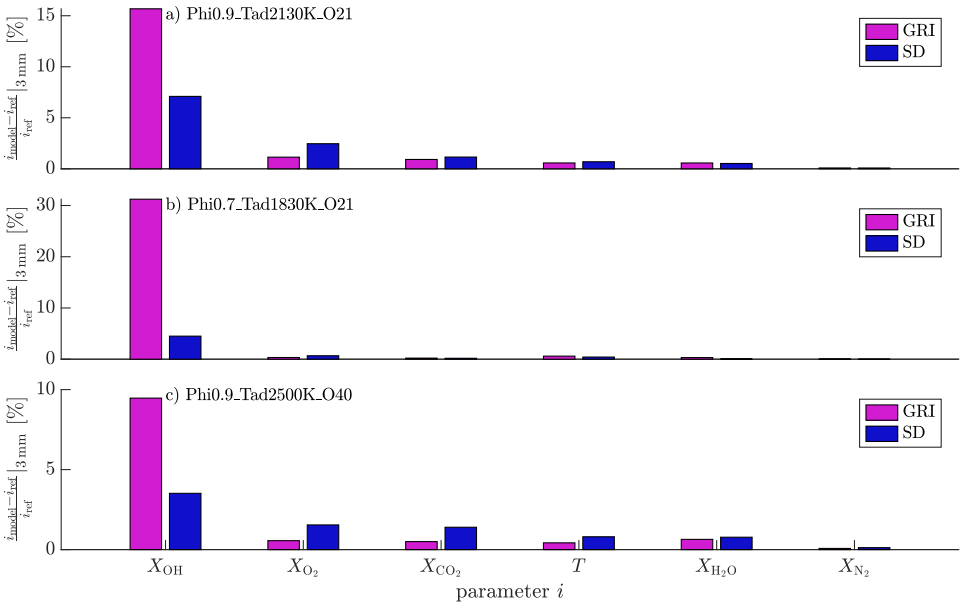

Figure A.6: Relative difference of parameter i between the CRECK model (reference) and the GRI and SD models of a given unseeded flame: a) Phi0.9_Tad2130K_O21, b) Phi0.7_Tad1830K_O21, and c) Phi0.9_Tad2500K_O40, at $z = 3$ mm.

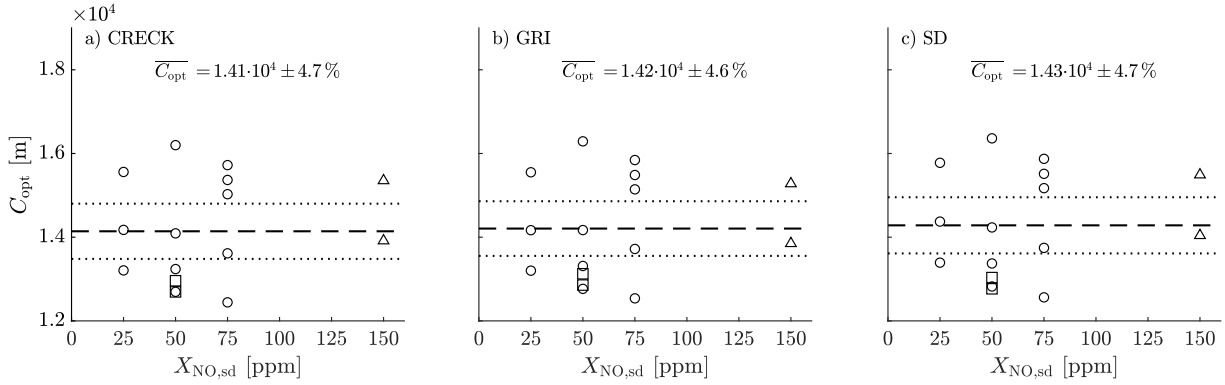

Figure A.7: C_{opt} calculated for all flame conditions (▫ Phi0.9_Tad2130K_O21, ○ Phi0.7_Tad1830K_O21, △ Phi0.9_Tad2500K_O40), using three thermochemical models: a) CRECK, b) GRI, and c) SD. The dashed line represents the average value and the dotted lines represent the 95% confidence interval around the average.

observed in the seeded or unseeded profiles between the thermochemical model prediction and the experimental results, the net profile is in good agreement.

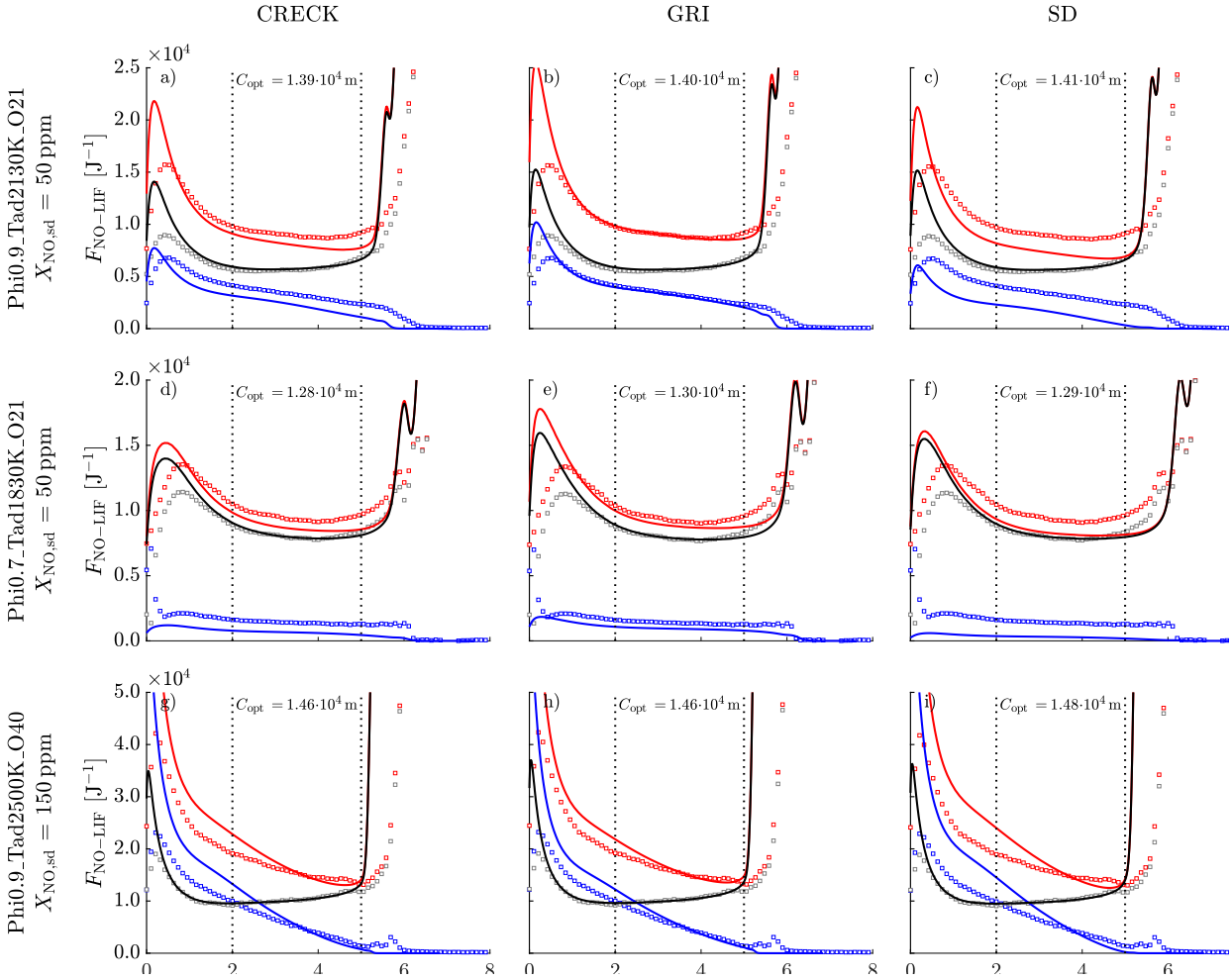

Figure A.8: LIF numerical profiles (solid lines) and LIF C_{opt}-normalised experimental profiles (squares) of the flame unseeded (blue), seeded (red), and net (black) for a selected seeding of each flame condition and for each thermochemical model.

A.3.4 C_{opt} is independent from the calibration flame

Similar to the previous demonstration, C_{opt} is demonstrated to be independent from the calibration flame, as long as the flame is not affected by NO reburn. As recalled from Eq. (III.39), C_{opt} is simply a coefficient regrouping all optical constants of the experimental setup.

In continuity with the previous demonstration, see Eq. (A.5), and assuming negligible NO reburn, C_{opt} is equivalent to:

$$C_{\text{opt}} = \frac{\left[X_{\text{NO,sd}} \cdot \frac{p f_{\text{B}}}{T} \cdot \frac{1}{\sum Q_{ul}} \cdot \frac{\mathcal{N}_{\text{A}}}{c\mathcal{R}_{\text{u}}} \cdot \frac{1}{\Delta\nu_{\text{L}}} \cdot B_{12} \sum A_{ul} \cdot \Gamma \cdot \mathcal{E}_{\text{c}} \mathcal{T}_{\lambda} \frac{\Omega}{4\pi} \ell\right]_{\text{exp}}}{\left[X_{\text{NO,sd}} \cdot \frac{p f_{\text{B}}}{T} \cdot \frac{1}{\sum Q_{ul}} \cdot \frac{\mathcal{N}_{\text{A}}}{c\mathcal{R}_{\text{u}}} \cdot \frac{1}{\Delta\nu_{\text{L}}} \cdot B_{12} \sum A_{ul} \cdot \Gamma \cdot \mathcal{E}_{\text{c}} \mathcal{T}_{\lambda} \frac{\Omega}{4\pi} \ell\right]_{\text{num}}}, \tag{A.8}$$

where constants between the experiments and the simulations cancel each other, such that:

$$C_{\text{opt}} = \frac{X^{\text{exp}}_{\text{NO,sd}}}{X^{\text{num}}_{\text{NO,sd}}} \cdot \left(\frac{\mathcal{E}_{\text{c}} \mathcal{T}_{\lambda} \Omega \ell}{\sum Q_{ul}}\right)_{\text{exp}} \cdot \left(\frac{\sum Q_{ul}}{\mathcal{E}_{\text{c}} \mathcal{T}_{\lambda} \Omega \ell}\right)_{\text{num}} \tag{A.9}$$

where T can be cancelled as it is measured experimentally, compared to predictions, and shown to be consistent; therefore $f_{\text{B}}(T)$ is also considered constant; p is also cancelled as the pressure is maintained constant throughout the experiments; B_{12} and A_{21} can be cancelled as they are constants relating to the LIF model chosen to model experiments; $\Delta\nu_{\text{L}}$ is measured experimentally and specified in LIFSim; and Γ is assumed perfectly modelled by LIFSim. Furthermore, assuming that $X^{\text{exp}}_{\text{NO,sd}} = X^{\text{num}}_{\text{NO,sd}}$ through the assumption that there is negligible NO reburn, and assuming that the major quenching species are properly modelled through simulations, such that $\sum Q^{\text{exp}}_{ul} = \sum Q^{\text{num}}_{ul}$, C_{opt} becomes fully independent of the flame condition, as well as the LIF model employed. It is a coefficient representing a conversion between the experimental and numerical optical parameters, encompassing the collection solid angle, the laser path length, the transmissivity of the optics, and the camera sensitivity:

$$C_{\text{opt}} = \left(\mathcal{E}_{\text{c}} \mathcal{T}_{\lambda} \Omega \ell\right)_{\text{exp}} \cdot \underbrace{\left(\frac{1}{\mathcal{E}_{\text{c}} \mathcal{T}_{\lambda} \Omega \ell}\right)_{\text{num}}}_{\sim 1}. \tag{A.10}$$

A.4 Uncertainty analysis

Uncertainty calculations were performed for each calibration technique under both assumptions on $F_{\text{interf.-LIF}}(\lambda)$. The major terms driving the uncertainty are presented in the following section. Calculations were performed for each seeded and unseeded flame at $z = 3\,\text{mm}$. For the sake of conciseness, only some results are shown below for the Phi0.9_Tad2130K_O21 flame.

A.4.1 Uncertainty on the experimental boundary conditions

Each boundary condition uncertainty specified in Tab. A.1 was calculated as follows:

- $\delta(p)$, $\delta(T_{\text{in}})$, and $\delta(T_{\text{wall}})$ stem from the experimental equipment;
- $\delta(\mathcal{L})$, $\delta(u_{\text{in}})$, and $\delta(\text{d}u_{\text{in}}/\text{d}z)$ are extracted from the post-processing of velocity measurements; and
- $\delta(X_{\text{NO,sd}})$, $\delta(\phi)$, $\delta(X_{\text{O}_2})$, and $\delta(X_{\text{Ar}})$ are calculated based on the number of MFCs used, their flow rates, and accuracy.

The uncertainty in $\delta(X_{\text{NO,sd}})$, $\delta(\phi)$, $\delta(X_{\text{O}_2})$, and $\delta(X_{\text{Ar}})$ is reduced when a minimal number of MFCs are used (as little as two MFCs controlling the fuel and air streams in an unseeded undiluted flame), and their individual flow rate is maximised since it is weighted by the uncertainty of the DryCal Piston calibrator, such that $\delta(\dot{m}_g) = \epsilon_{\text{DC}} \cdot \dot{m}_g$, with $\epsilon_{\text{DC}} = 0.4\%$.

A.4.2 Uncertainty on $F_{\text{NO-LIF}}(\lambda)$

A.4.2.1 Assuming constant $F_{\text{interf.-LIF}}(\lambda)$

The uncertainty on the averaged profile of $F_{\text{NO-LIF}}(\lambda)$ for an unseeded and seeded flames results from the contribution of the random and systematic errors. The first term encompasses experimental scatter and is reduced by the number of images captured and the number of flames performed for each condition, leading to a $\frac{\delta_{\text{rand}}(F_{\text{NO-LIF}})}{F_{\text{NO-LIF}}} \sim 3{-}4\%$.

The systematic uncertainty results from errors in the boundary conditions of the flames propagated to a fluorescence signal. Systematic errors in the photodiodes, the camera, and the long-pass filter are nil as they are assumed to have a linear effect on the signal captured and, thus, cancel through the calculation of $F_{\text{NO-LIF}}$. Hence,

$$\frac{\delta_{\text{sys}}(F_{\text{NO-LIF}})}{F_{\text{NO-LIF}}} = \left[\sum_{\text{BC}_j} \left(\text{L.S.}(\text{BC}_j)|_{F^{\text{num}}_{\text{NO-LIF}}} \cdot \frac{\delta_{\text{sys}}(\text{BC}_j)}{\text{BC}_j} \right)^2 \right]^{1/2}, \tag{A.11}$$

where $\text{L.S.}(\text{BC}_j)|_{F^{\text{num}}_{\text{NO-LIF}}}$ is the logarithmic sensitivity (L.S.) of each boundary condition propagated to a fluorescence signal using Cantera and LIFSim and evaluated at $z = 3$ mm. Each term composing Eq. (A.11) can be found in Fig. A.9, where their L.S. (top), uncertainties (middle), and uncertainty-weighted L.S. (bottom) are shown. Results are presented for the unseeded and seeded (50 ppm) flames. The root-square-sum (RSS) of the terms leads to $\frac{\delta_{\text{sys}}(F_{\text{NO-LIF}})}{F_{\text{NO-LIF}}} \sim 3\% - 17\%$.

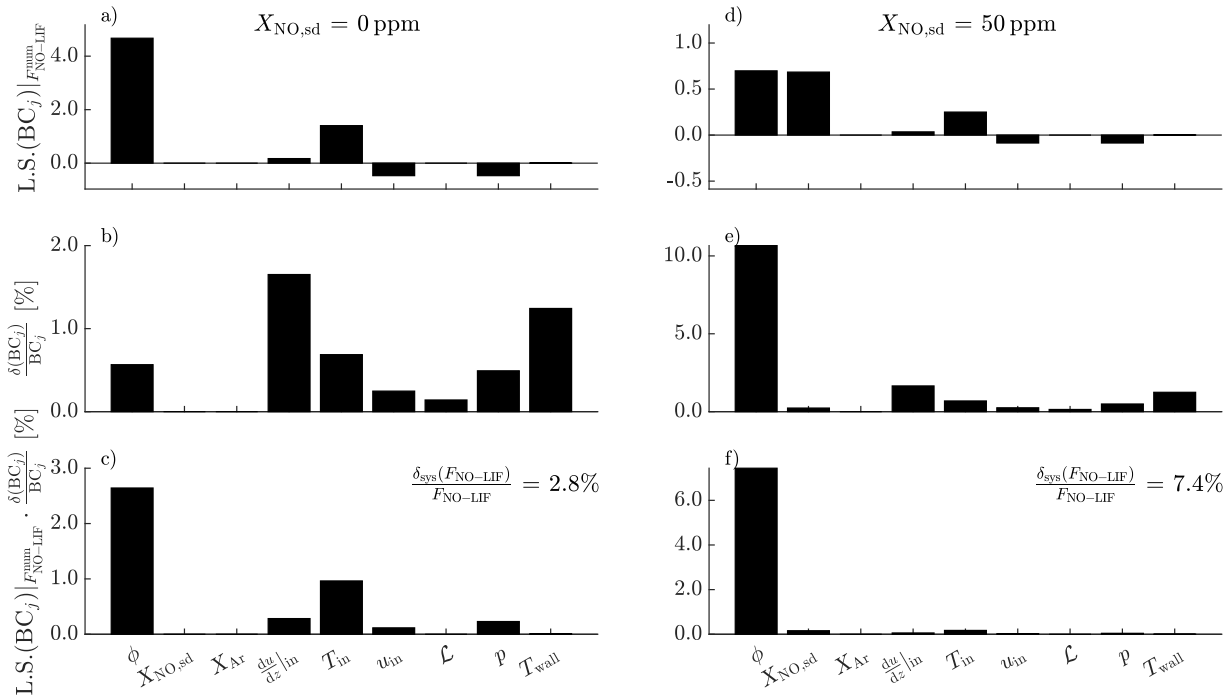

Figure A.9: L.S. (top), uncertainty (middle), and uncertainty-weighted L.S. (bottom) of the terms involved in the calculation of $\frac{\delta_{\text{sys}}(F_{\text{NO-LIF}})}{F_{\text{NO-LIF}}}$, for the unseeded (left) and seeded (right) Phi0.9_Tad2130K_O21 flames evaluated at $z = 3$ mm, assuming constant $F_{\text{interf.-LIF}}(\lambda)$, using the CRECK thermochemical model.

For all flames, three parameters are driving the uncertainty: the equivalence ratio, the seeded NO molar fraction, and the argon molar fraction (when applicable). For these terms, the uncertainty is larger for flames performed with more MFCs and with low flow rates, such as seeding the flame with low levels of NO, or using a diluent.

The total uncertainty for each unseeded and seeded averaged $F_{\text{NO-LIF}}(\lambda)$ profiles assuming constant $F_{\text{interf.-LIF}}(\lambda)$ results from the RSS of the random and systematic uncertainties, and is plotted in Fig. III.10b. It is calculated at $\epsilon_{F_{\text{NO-LIF,nsct}}}|_{\text{constant interf.-LIF}} \sim 4 - 18\%$, depending on the seeded level.

A.4.2.2 Assuming non-constant $F_{\text{interf.-LIF}}(\lambda)$

The uncertainty in $F_{\text{NO-LIF}}(\lambda)$ assuming non-constant $F_{\text{interf.-LIF}}(\lambda)$ is calculated at λ_{on}. Similar to the previous calculation, it results from both random and systemic terms.

The random error in $F_{\text{NO-LIF}}$ results from the experimental scatter and is reduced by the number of measurements performed for each flame condition. Unlike the previous methodology, it is hardly reduced by the number of images captured at each wavelength as only 120 laser shots are generated, as opposed to 5,000 in the technique assuming constant $F_{\text{interf.-LIF}}(\lambda)$. It leads to $\frac{\delta_{\text{rand}}(F_{\text{NO-LIF}})}{F_{\text{NO-LIF}}} \sim 3\%$.

The systematic term results from the propagation of the errors in the experimental boundary conditions on the fluorescence of an unseeded flame, as well as the error in $F_{\text{interf.-LIF}}(\lambda)$. For the latter, it is assumed that the uncertainty is a direct representation of the uncertainties in $F_{\text{NO-LIF,sd}}(\lambda)$ and $F_{\text{NO-LIF,nsct+sd}}(\lambda)$. Thus, it is calculated as the RSS of the residuals between $F_{\text{interf.-LIF}}(\lambda)$ and $F_{\text{interf.-LIF}}(\lambda)|_{\text{smoothed}}$, see Fig. III.8, and is reduced by the number of points in the spectral range on which it is fitted. Similar to the previous assumption, the systematic errors in the photodiodes, the camera, and the long-pass filter are assumed nil. Hence, $\frac{\delta_{\text{sys}}(F_{\text{NO-LIF}})}{F_{\text{NO-LIF}}} \sim 8\%$ and results from the RSS of the terms presented in Fig. A.10.

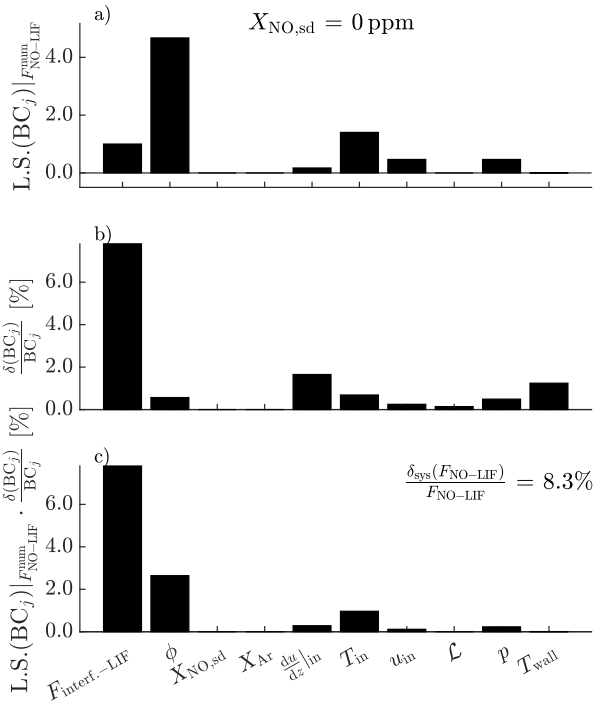

Figure A.10: L.S. (top), uncertainty (middle), and uncertainty-weighted L.S. (bottom) of the terms involved in the calculation of $\frac{\delta_{\text{sys}}(F_{\text{NO-LIF}})}{F_{\text{NO-LIF}}}$ for the Phi0.9_Tad2130K_O21 flame evaluated at $z = 3$ mm, assuming non-constant $F_{\text{interf.-LIF}}(\lambda)$, using the CRECK thermochemical model.

The total uncertainty for each unseeded averaged $F_{\text{NO-LIF}}(\lambda)$ profiles assuming non-constant $F_{\text{interf.-LIF}}(\lambda)$ is calculated as the RSS of the random and systematic uncertainties, and is plotted in Fig. III.11b. It is evaluated as $\epsilon_{F_{\text{NO-LIF,nsct}}}|_{\text{non-constant interf.-LIF}} \sim 9\%$.

A.4.3 Uncertainty on $F_{\text{NO-LIF,nsct}}/C_{\text{opt}}$

The uncertainty in $F_{\text{NO-LIF,nsct}}/C_{\text{opt}}$ results from the RSS of the random and systematic errors associated with the measurement and calculation of $F_{\text{NO-LIF,nsct}}$ and C_{opt}.

The random error is composed of the experimental scatter in the measurement of $F^{\text{exp}}_{\text{NO-LIF,nsct}}$ and $F^{\text{exp}}_{\text{NO-LIF,sd}}$, and is reduced by the number of measurements performed per flame condition. It leads to $\frac{\delta_{\text{rand}}(F_{\text{NO-LIF}}/C_{\text{opt}})}{F_{\text{NO-LIF}}/C_{\text{opt}}} \sim 0.1\%$ and 0.6% under the assumption of constant and non-constant $F_{\text{interf.-LIF}}(\lambda)$, respectively.

The systematic uncertainty encompasses the systematic error in the measurement of $F^{\text{exp}}_{\text{NO-LIF,nsct}}$ and C_{opt}. The error in $F^{\text{exp}}_{\text{NO-LIF,nsct}}$ is calculated according to the assumption formulated on $F_{\text{interf.-LIF}}(\lambda)$, as discussed previously, and is mostly driven by the propagation of the boundary condition uncertainties on $F^{\text{num}}_{\text{NO-LIF}}$. The systematic error in C_{opt} results from errors in both $F^{\text{num}}_{\text{NO-LIF,sd}}$ and $F^{\text{exp}}_{\text{NO-LIF,sd}}$. The quantification of the systematic error in $F^{\text{num}}_{\text{NO-LIF,sd}}$ would require an extensive investigation of the parameters used in the thermochemical model, Cantera, and LIFSim and was not performed in this work. Instead the scatter in the determination of C_{opt} was assumed to be representative of the combined uncertainty in $F^{\text{num}}_{\text{NO-LIF,sd}}$ and $F^{\text{exp}}_{\text{NO-LIF,sd}}$. Hence, $\frac{\delta_{\text{sys}}(F_{\text{NO-LIF}}/C_{\text{opt}})}{F_{\text{NO-LIF}}/C_{\text{opt}}} \sim 5\%$ and 11% under the assumption of constant and non-constant $F_{\text{interf.-LIF}}(\lambda)$, respectively.

The RSS of the random and systematic uncertainties leads to $\epsilon_{F_{\text{NO-LIF,nsct}}/C_{\text{opt}}}|_{\text{constant interf.-LIF}} \sim 5.5\%$ and $\epsilon_{F_{\text{NO-LIF,nsct}}/C_{\text{opt}}}|_{\text{non-constant interf.-LIF}} \sim 12\%$.

A.4.4 Uncertainty on $X_{\text{NO,nsct}}$

A.4.4.1 Using the linear extrapolation calibration technique C_{lin}

A.4.4.1.1 Assuming constant $F_{\text{interf.-LIF}}(\lambda)$

The uncertainty on $X_{\text{NO,nsct}}$ results from the linear fit performed between $F_{\text{NO-LIF}}$ and $X_{\text{NO,sd}}$. To account for the uncertainty in $F_{\text{NO-LIF}}$, the fit is performed using a Monte-Carlo (MC) methodology. The averaged $F_{\text{NO-LIF}}$ is varied within its uncertainty range, considering a uniform distribution and assuming no uncertainty in $X_{\text{NO,sd}}$[2]. The fit is performed 1,000 times and the resulting $X_{\text{NO,nsct}}$ is extracted through Eq. (III.54). The 1,000 calculations of $X_{\text{NO,nsct}}$ follow a normal distribution that is fitted to obtain the nominal value (50% of the cumulative distribution function) and its uncertainty (95% confidence interval on the cumulative distribution function), as seen in Fig. A.11.

Using three seeding levels, this calibration technique leads to $\epsilon_{X_{\text{NO,nsct}}}|_{C_{\text{lin,constant interf.-LIF}}} \sim 6\%$, as displayed through the shaded area in Fig. III.10b. An evaluation of the uncertainty was also performed by varying the number of seeded levels. An uncertainty of $\sim$15% was found for one

[2]The uncertainty in $X_{\text{NO,sd}}$ is already taken into account in the uncertainty of $F_{\text{NO-LIF}}$.

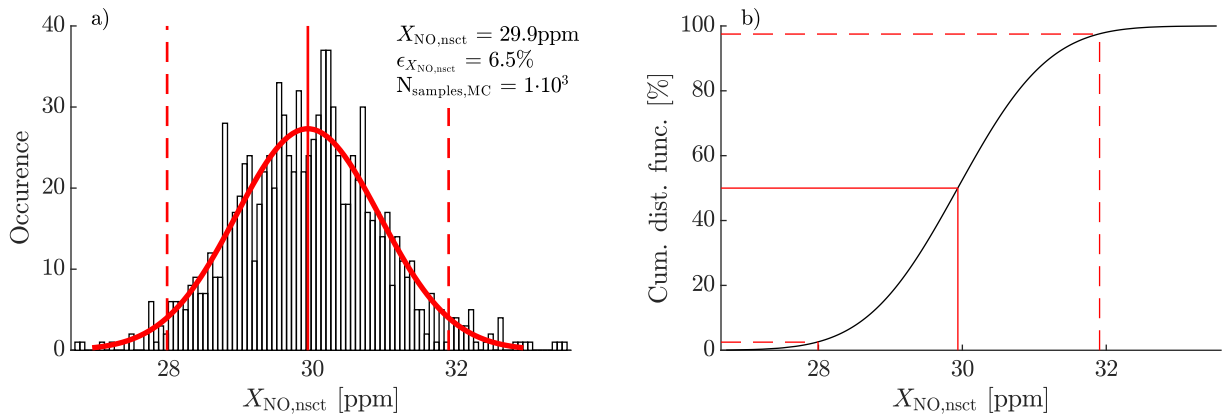

Figure A.11: Distribution of $X_{\mathrm{NO,nsct}}$ from 1,000 fits following a MC sampling technique for the flame Phi0.9_Tad2130K_O21 at $z = 3$ mm.

seeding level (25 ppm) and ∼7% for two levels (25 and 50 ppm). It is evident that a larger number of seeding levels will lead to a more certain extrapolation, hence, reducing the uncertainty on $X_{\mathrm{NO,nsct}}$.

A.4.4.1.2 Assuming non-constant $F_{\text{interf.-LIF}}(\lambda)$

Due to the simplification that can be performed using C_{bckgd} instead of the explicit calculation of C_{lin}, see Eq. (III.56), a specific uncertainty calculation is performed for this method.

The uncertainty in C_{bckgd} is assumed equivalent to the the uncertainty in $F_{\text{interf.-LIF}}(\lambda)$. As performed in Section A.4.2.2, it results from the RSS of the residuals between $F_{\text{interf.-LIF}}(\lambda)$ and its smoothed profile, and is assumed to represent the uncertainties in both $F_{\text{NO-LIF,sd}}(\lambda)$ and $F_{\text{NO-LIF,nsct+sd}}(\lambda)$.

Hence, assuming no uncertainty in $X_{\mathrm{NO,sd}}$, the uncertainty in $X_{\mathrm{NO,nsct}}$ is calculated as the RSS of the error in $F_{\text{interf.-LIF}}(\lambda)$ (systematic) and the scatter in the calculation of $X_{\mathrm{NO,nsct}}$ that is reduced by the number of flames performed. Thus, it leads to $\epsilon_{X_{\mathrm{NO,nsct}}}|_{C_{\text{lin,non-constant interf.-LIF}}}$∼8.5%, and is plotted through the shaded area of Fig. III.11c.

A.4.4.2 Using the optical calibration technique C_{opt}

As discussed previously, the calculation of this uncertainty is delicate as it would require the calculation of the uncertainty in the thermochemical model, Cantera, and LIFSim. Additionally, the calculation of $X_{\text{NO-LIF,nsct}}$ through the assumption that $f_{\mathrm{LIF}}^{\mathrm{exp}} = f_{\mathrm{LIF}}^{\mathrm{num}}$ is only valid if the thermochemical model can accurately predict the flame speed and main species concentrations. Hence, the uncertainty in $X_{\text{NO-LIF,nsct}}$ must include a term representing the inaccuracy of the model in predicting the kinetics of the flame, such as its position. A linear effect is assumed between an inaccurate prediction of the flame front position and the fluorescence generated at a given point of the do-

main. Hence, a numerical flame that is predicted downstream of its experimental position will lead to a lower predicted fluorescence, assuming a constant slope post-flame. Similarly, a numerical flame that is predicted upstream of the experimental flame will lead to a stronger predicted fluorescence. Thus, a systematic uncertainty on the numerical fluorescence is calculated as the delta in the flame front position between the numerical and experimental profiles. A systematic uncertainty is also present in the measurement of $F_{\text{NO-LIF,nsct}}/C_{\text{opt}}$ as discussed previously. Therefore, the systematic uncertainty in $X_{\text{NO-LIF,nsct}}$ is calculated as the RSS of $\epsilon_{F_{\text{NO-LIF,nsct}}/C_{\text{opt}}}$ and $\frac{\delta(z_{\text{f}})}{z_{\text{f}}}$ defined as the relative error of the numerical flame front position (z_{f}) to the experimental one. It leads to $\frac{\delta_{\text{sys}}(X_{\text{NO-LIF,nsct}})}{X_{\text{NO-LIF,nsct}}} \sim 6.5\%$ and 12.5% under the assumption of constant and non-constant $F_{\text{interf.-LIF}}(\lambda)$, respectively, and with $\frac{\delta(z_{\text{f}})}{z_{\text{f}}} \sim 4\%$ using the GRI thermochemical model. This points at the importance of choosing a thermochemical model that can the most accurately reproduce the flame kinetics to limit the propagation of uncertainties.

The random uncertainty results only from the scatter in $F_{\text{NO-LIF,nsct}}/C_{\text{opt}}$ and is calculated as mentioned above, leading to $\frac{\delta_{\text{rand}}(X_{\text{NO-LIF,nsct}})}{X_{\text{NO-LIF,nsct}}} \sim 0.1\%$ and 0.6% assuming constant and non-constant $F_{\text{interf.-LIF}}(\lambda)$, respectively.

The total uncertainty is calculated as the RSS of both random and systematic errors, such that $\epsilon_{X_{\text{NO,nsct}}}|_{C_{\text{opt}},\text{constant interf.-LIF}} \sim 6.5\%$, and $\epsilon_{X_{\text{NO,nsct}}}|_{C_{\text{opt}},\text{non-constant interf.-LIF}} \sim 13\%$.

A.4.5 Summary of uncertainties

Table A.3 presents the uncertainty calculation for each flame condition, seeding, calibration technique, and assumption.

Table A.3: Random, systematic, and total uncertainties of some keys experimental results using the different quantification techniques. All values are presented in %.

Flame		**Phi0.7_Tad1830K_O21**		**Phi0.9_Tad2130K_O21**				**Phi0.9_Tad2500K_O40**	
X_{sd} **[ppm]**		**0**	**50**	**0**	**25**	**50**	**75**	**0**	**150**
$\epsilon_{F_{\text{NO-LIF,nsct}}\vert\text{constant interf.-LIF}}$	**# samples**	**2**	**2**	**6**	**3**	**4**	**5**	**2**	**2**
	rand	0.7	0.6	2.8	4.3	4.0	4.0	0.7	4.1
	sys	3.8	19.2	2.8	17.2	7.4	2.8	2.1	1.4
	total	3.9	19.2	4.0	17.8	8.5	4.8	2.2	4.4
$\epsilon_{F_{\text{NO-LIF,nsct}}\vert\text{non-constant interf.-LIF}}$	**# samples**	**-**	-	**6**				**-**	-
	rand	-	-	3.1				-	-
	sys	-	-	8.3				-	-
	total	-	-	8.9				-	-
$\epsilon_{F_{\text{NO-LIF,nsct}}/C_{\text{opt}}\vert\text{constant interf.-LIF}}$	**# samples**	**2**		**6**				**2**	
	rand	0.9		0.1				0.4	
	sys	5.9		5.3				5.0	
	total	6.0		5.4				5.1	
$\epsilon_{F_{\text{NO-LIF,nsct}}/C_{\text{opt}}\vert\text{non-constant interf.-LIF}}$	**# samples**	**-**	-	**6**				**-**	-
	rand	-	-	0.6				-	-
	sys	-	-	11.4				-	-
	total	-	-	11.5				-	-
$\epsilon_{X_{\text{NO,nsct}}\vert C_{\text{lin,constant interf.-LIF}}}$	**# seeding levels**	**-**	**1**	**-**	**1**	**2**	**3**	**-**	**1**
	total	-	7.8	-	14.7	6.9	6.3	-	2.7
$\epsilon_{X_{\text{NO,nsct}}\vert C_{\text{lin,non-constant interf.-LIF}}}$	**# seeding levels**	**-**	-	**-**	**1**	**2**	**3**	**-**	-
	rand	-	-	-	3.2	4.5	3.9	-	-
	sys	-	-	-	6.9	7.2	7.5	-	-
	total	-	-	-	7.6	8.4	8.5	-	-
$\epsilon_{X_{\text{NO,nsct}}\vert C_{\text{opt,constant interf.-LIF}}}$	**# samples**	**2**		**6**				**2**	
	rand	0.9		0.1				0.4	
	sys	6.1		6.5				11.9	
	total	6.2		6.5				11.9	
$\epsilon_{X_{\text{NO,nsct}}\vert C_{\text{opt,non-constant interf.-LIF}}}$	**# samples**	**-**	-	**6**				**-**	-
	rand	-	-	0.6				-	-
	sys	-	-	12.5				-	-
	total	-	-	12.6				-	-

References

[1] P. H. Paul, J. A. Gray, J. L. Durant, and J. W. Thoman. "A model for temperature-dependent collisional quenching of NO $A^2\ \Sigma^+$". In: *Applied Physics B Photophysics and Laser Chemistry* 57.4 (1993), pp. 249–259.

[2] P. H. Paul, C. Carter, J. A. Gray, J. L. Durant, J. Thomson, and M. Furlanetto. *Correlations for the NO $A^2\Sigma^+$ (ν'=0) electronic quenching cross-section*. Tech. rep. Sandia National Lab. (SNL-CA), Livermore, CA (United States), 1995.

[3] A. Y. Chang, M. D. DiRosa, and R. K. Hanson. "Temperature dependence of collision broadening and shift in the NO A ← X(0, 0) band in the presence of argon and nitrogen". In: *Journal of Quantitative Spectroscopy and Radiative Transfer* 47.5 (1992), pp. 375–390.

[4] M. D. Di Rosa and R. K. Hanson. "Collision-broadening and -shift of NO γ(0,0) absorption lines by H_2O, O_2, and NO at 295K". In: *Journal of Molecular Spectroscopy* 164.1 (1994), pp. 97–117.

[5] M. D. DiRosa. "High-resolution line shape spectroscopy of transitions in the gamma bands of nitric oxide". PhD thesis. 1996.

[6] P. A. Berg, G. P. Smith, J. B. Jeffries, and D. R. Crosley. "Nitric oxide formation and reburn in low-pressure methane flames". In: *Symposium (International) on Combustion* 27 (1998), pp. 1377–1384.

[7] G. Bagheri, E. Ranzi, M. Pelucchi, A. Parente, A. Frassoldati, and T. Faravelli. "Comprehensive kinetic study of combustion technologies for low environmental impact: MILD and OXY-fuel combustion of methane". In: *Combustion and Flame* 212 (2020), pp. 142–155.

[8] Y. Song et al. "The sensitizing effects of NO_2 and NO on methane low temperature oxidation in a jet stirred reactor". In: *Proceedings of the Combustion Institute* 37 (2019), pp. 667–675.

[9] G. P. Smith et al. "GRI-Mech 3.0". In: (1999).

[10] University of California at San Diego. *Chemical-Kinetic Mechanisms for Combusiton Applications*. 2016.

Appendix B. Supplementary Materials to Chapter IV

B.1 Experimentally-measured boundary conditions

Table B.1 reports the experimental conditions used to perform simulations of quasi-1D stagnation flames.

Table B.1: Flame boundary conditions

O_2-to-N_2*	X_{Ar}**	T_{ad} [K]	$\mathcal{L}$ [mm]	T_{in} [K]	u_{in} [ms^{-1}]	du/d$z|_{in}$ [s^{-1}]	T_{wall} [K]
0.21	0.0000	2130	7.12	291.3 ± 2	0.545 ± 0.001	156.4 ± 2.6	402.3 ± 5
0.21	0.1580	2000	7.09	290.6 ± 2	0.365 ± 0.001	91.2 ± 1.1	372.0 ± 5
0.21	0.2560	1900	7.10	291.1 ± 2	0.274 ± 0.001	57.3 ± 0.9	360.5 ± 5
0.40	0.6430	2000	7.43	291.7 ± 2	0.319 ± 0.001	81.7 ± 1.6	362.0 ± 5
0.40	0.6032	2100	7.26	291.4 ± 2	0.471 ± 0.001	121.1 ± 1.2	381.5 ± 5
0.40	0.5556	2200	7.30	291.4 ± 2	0.640 ± 0.001	175.2 ± 1.9	402.9 ± 5
0.40	0.4965	2300	6.91	292.0 ± 2	0.907 ± 0.002	245.7 ± 2.2	421.8 ± 5
0.40	0.4185	2400	6.91	291.9 ± 2	1.216 ± 0.002	333.9 ± 3.5	462.1 ± 5
0.40	0.3085	2500	6.84	291.9 ± 2	1.575 ± 0.003	472.7 ± 5.4	501.9 ± 5

* Defined in Eq. (IV.1); ** Defined in Eq. (IV.2)

B.2 Calibration of the optical constant C_{opt}

Following the NO-LIF methodology used for NO concentration measurements, as reported in Section IV.3, the experimental signals of both a seeded flame and an unseeded flame, $F_{\mathrm{NO,exp}_{\mathrm{seeded}}}$ and $F_{\mathrm{NO,exp}_{\mathrm{unseeded}}}$ respectively, are collected. The seeding remains below 300 ppm such that the consumption of seeded NO through the flame zone remains negligible [1]. The collected signals are subtracted from one another, such that the remaining signal $F_{\mathrm{NO,exp}_{\mathrm{net}}}$ is only proportional to the known concentration of NO $\left(n^{\circ}_{\mathrm{NO,known}}\right)$:

$$F_{\mathrm{NO,exp}_{\mathrm{seeded}}} = F_{\mathrm{NO,exp}_{\mathrm{known}}} + F_{\mathrm{NO,exp}_{\mathrm{produced}}} \tag{B.1}$$

$$F_{\mathrm{NO,exp}_{\mathrm{unseeded}}} = F_{\mathrm{NO,exp}_{\mathrm{produced}}} \tag{B.2}$$

$$F_{\mathrm{NO,exp}_{\mathrm{net}}} = F_{\mathrm{NO,exp}_{\mathrm{seeded}}} - F_{\mathrm{NO,exp}_{\mathrm{unseeded}}} = F_{\mathrm{NO,exp}_{\mathrm{known}}} \tag{B.3}$$

Similar to the experiments, simulations are performed by virtually seeding the flame with an experimentally-known concentration of NO. The numerical NO profiles are transformed into LIF signal using the two-level LIF:

$$F_{\mathrm{NO,num_{net}}} = C_{\mathrm{opt}} \cdot f_{\mathrm{LIF}}\left(f_{\mathrm{B}}, \lambda, \Delta\nu_{\mathrm{L}}, \Gamma, B_{12}, A_{21}, Q_{21}\right) \cdot n^{\circ}_{\mathrm{NO,known}} \tag{B.4}$$

where f_{LIF} is the number of photons emitted per unit molecule of NO, $f_{\mathrm{B}}\left(T\right)$ is the Boltzmann fraction of NO molecules in the excited state, λ is the laser wavelength, $\Delta\nu_{\mathrm{L}}$ is the spectral width of the laser, $\Gamma\left(\Delta\nu_{\mathrm{L}}, T, P, X_i\right)$ is the dimensionless overlap fraction, B_{12} is the Einstein constant of photon absorption, A_{21} is the rate constant of spontaneous emission, $Q_{21}\left(T, P, X_i\right)$ is the rate constant of non-radiative collisional quenching, and $n^{\circ}_{\mathrm{NO,known}}\left(T, P, X_{\mathrm{NO}}\right)$ is the number density of NO molecules. Table B.2 presents the LIF constants used to calculate the numerical NO-LIF signal.

The direct comparison of $F_{\mathrm{NO,num_{net}}}$ and $F_{\mathrm{NO,exp_{net}}}$ allows the determination of the optical calibration coefficient (C_{opt}), by fitting the numerical and experimental profiles using a least-square fit. The calibration coefficient is fitted in the post-flame region, being the region of interest of this study. Figure B.1 shows an example of the signal-fitting to obtain C_{opt}.

The calibration has been performed approximately 50 times on different flame conditions and using different levels of seeding, leading to an average $\overline{C_{\mathrm{opt}}}$ of $2.56 \cdot 10^{-6}$ m, as shown on Fig. B.2. The coefficient has a low uncertainty ($\sim 2.90\%$) and confirms the independence of the seeding level and the flame condition on the calibration technique.

Table B.2: NO-LIF constants used the two-level LIF model in Eq. (B.4)

Parameter	Function	Constants				Units
		c_1	c_2	c_3	c_4	
f_{B}	$c_1 e^{+c_2/T} + c_3 e^{+c4/T}$	-0.2822	-1799	0.2183	-408.4	[-]
λ_{on}		226.0345				[nm]
λ_{off}		226.047				[nm]
$\Delta\nu_{\mathrm{L}}$		0.25				[cm^{-1}]
Γ		0.86				[-]
B_{12}		$2.38{\cdot}10^{9}$				[$\mathrm{m}^2\mathrm{J}^{-1}\mathrm{s}^{-1}$]
A_{21}		$5.72{\cdot}10^{6}$				[s^{-1}]
Q_{21}	$\sum X_k Q_k$					[s^{-1}]
Q_k	$\sigma_k \left(\frac{N}{V}\right) \sqrt{\frac{8k_B T}{\pi\mu_k}}$					[s^{-1}]
μ_k	$\frac{m_k m_{\mathrm{NO}}}{m_k + m_{\mathrm{NO}}}$					[kg]
σ_k from [2]						[$\mathrm{Å}^2$]

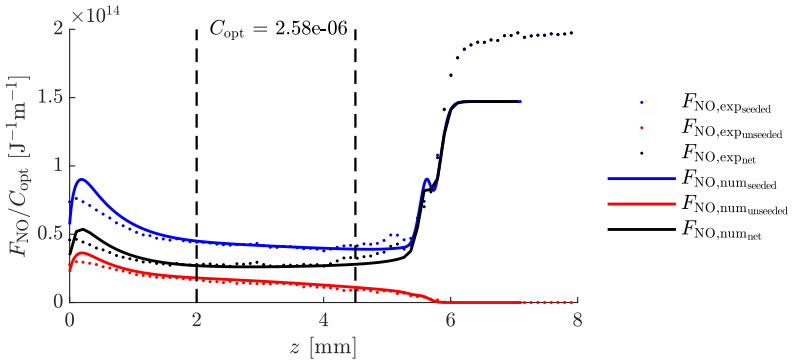

Figure B.1: Calibration obtained for the methane-air flame at $T_{\mathrm{ad}} = 2130\,\mathrm{K}$ with 50 ppm seeding, using the GRI mechanism

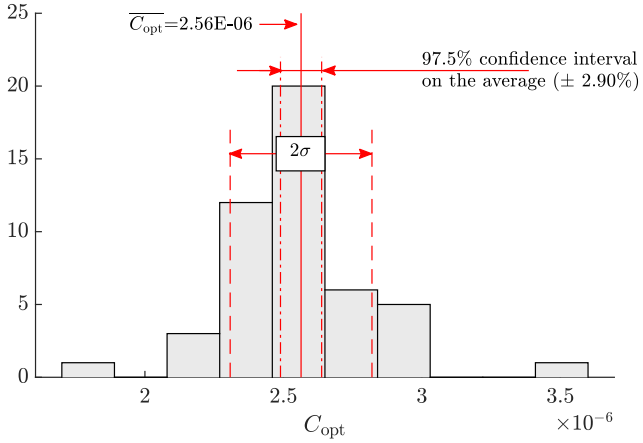

Figure B.2: Distribution of measured C_{opt}, with $\overline{C_{\mathrm{opt}}} = 2.56\text{E-}6$, and $1\sigma = 2.56\text{E-}7$.

B.3 Uncertainty calculation

Total uncertainty of the NO slope ratio $\sigma_{\left(\mathrm{d}F_{\mathrm{NO,num}}/\mathrm{d}z\right)/\left(\mathrm{d}F_{\mathrm{NO,exp}}/\mathrm{d}z\right)=1}$, illustrated in Fig. IV.4, is a combination of the experimental and the numerical uncertainties. They are evaluated at the reference location $z = 3.5$ mm. The total uncertainty on the NO slope is thus defined as follows:

$$\sigma_{\left(\mathrm{d}F_{\mathrm{NO,num}}/\mathrm{d}z\right)/\left(\mathrm{d}F_{\mathrm{NO,exp}}/\mathrm{d}z\right)=1} = \left(\left(\overline{\sigma_{\mathrm{d}F_{\mathrm{NO}}/(C_{\mathrm{opt}}\cdot\mathrm{d}z)_{\mathrm{exp,LIF}}}}\right)^2 + \left(\sigma_{\mathrm{d}F_{\mathrm{NO}}/(C_{\mathrm{opt}}\cdot\mathrm{d}z)_{\mathrm{num,BC}}}\right)^2\right)^{1/2} \tag{B.5}$$

B.3.1 Numerical uncertainties

The numerical uncertainties represent the impact of the calculated boundary conditions on the numerical solutions. They are calculated by performing a brute-force sensitivity analysis of the numerical boundary conditions x_j on each of the simulated flames. The resulting logarithmic sensitivity L.S.(x_j) is weighted by the uncertainty of each of the boundary conditions parameters $\sigma(x_j)$ such that the impact on the NO slope $\mathrm{d}F_{\mathrm{NO}}/\left(C_{\mathrm{opt}}\cdot\mathrm{d}z\right)$ can be evaluated as follows:

$$\sigma_{\mathrm{d}F_{\mathrm{NO}}/(C_{\mathrm{opt}}\cdot\mathrm{d}z)_{\mathrm{num,BC}}} = \left(\sum\left[\mathrm{L.S.}(x_j)\cdot\sigma(x_j)\right]^2\right)^{1/2} \tag{B.6}$$

The logarithmic sensitivity for each parameter and each flame is shown in Fig. B.3. One can see that the dilution of argon is the most sensitive boundary parameter on the slope of NO post-flame. As expected, a small change in X_{Ar} leads to a larger uncertainty for the most diluted flames, resulting in the largest numerical uncertainties for the flames at low temperature.

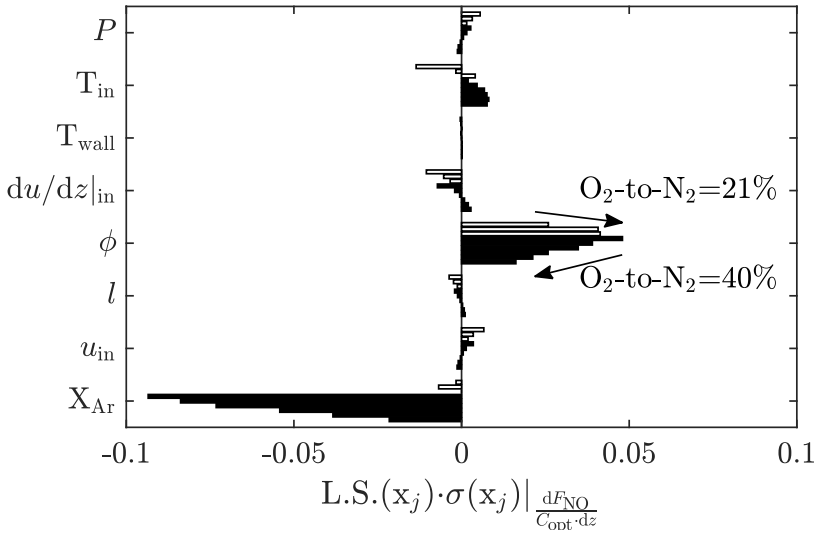

Figure B.3: Logarithmic sensitivity of $\mathrm{d}F_{\mathrm{NO}}/\left(C_{\mathrm{opt}}\cdot\mathrm{d}z\right)$ for each flame with O_2-to-$N_2 = 21\%$ (white) and O_2-to-$N_2 = 40\%$ (black). Increasing T_{ad} goes in the direction of the arrows.

B.3.2 Experimental uncertainty: NO-LIF

The experimental uncertainty $\sigma_{\mathrm{dNO/d}z_{\mathrm{exp,LIF}}}$, for each profile, consists of the camera calibration coefficient uncertainty $\Delta C/C$, the image signal variation $\Delta S/S$, the laser energy variation $\Delta E_{\mathrm{L}}/E_{\mathrm{L}}$, the NO concentration calibration coefficient uncertainty $\Delta C_{\mathrm{opt}}/C_{\mathrm{opt}}$, and the NO profile linear regression uncertainty $\Delta f/f$, such that:

$$\sigma_{\mathrm{d}F_{\mathrm{NO}}/(C_{\mathrm{opt}}\cdot\mathrm{d}z)_{\mathrm{exp,LIF}}} = \left(\left(\frac{\Delta C}{C}\right)^2 + \left(\frac{\Delta S}{S}\right)^2 + \left(\frac{\Delta E_{\mathrm{L}}}{E_{\mathrm{L}}}\right)^2 + \left(\frac{\Delta C_{\mathrm{opt}}}{C_{\mathrm{opt}}}\right)^2 + \left(\frac{\Delta f}{f}\right)^2\right)^{1/2} \tag{B.7}$$

Results presented in Fig. IV.4 have been averaged based on the sample size N_{s}, reducing the uncertainty as follows:

$$\overline{\sigma_{\mathrm{d}F_{\mathrm{NO}}/(C_{\mathrm{opt}}\cdot\mathrm{d}z)_{\mathrm{exp,LIF}}}} = \frac{\left\langle \sigma_{\mathrm{d}F_{\mathrm{NO}}/(C_{\mathrm{opt}}\cdot\mathrm{d}z)_{\mathrm{exp,LIF}}} \right\rangle_{1\rightarrow N_{\mathrm{s}}}}{(N_{\mathrm{s}})^{1/2}} \tag{B.8}$$

This resulting uncertainty is applied on the averaged profiles shown in the NO-LIF figures of Section IV.4.

B.4 Measured profiles

Figures B.4−B.6 show the measured profiles of Particle Tracking Velocimetry (PTV), Multi-line NO-LIF thermometry, and Planar LIF for the nine flames performed in this study.

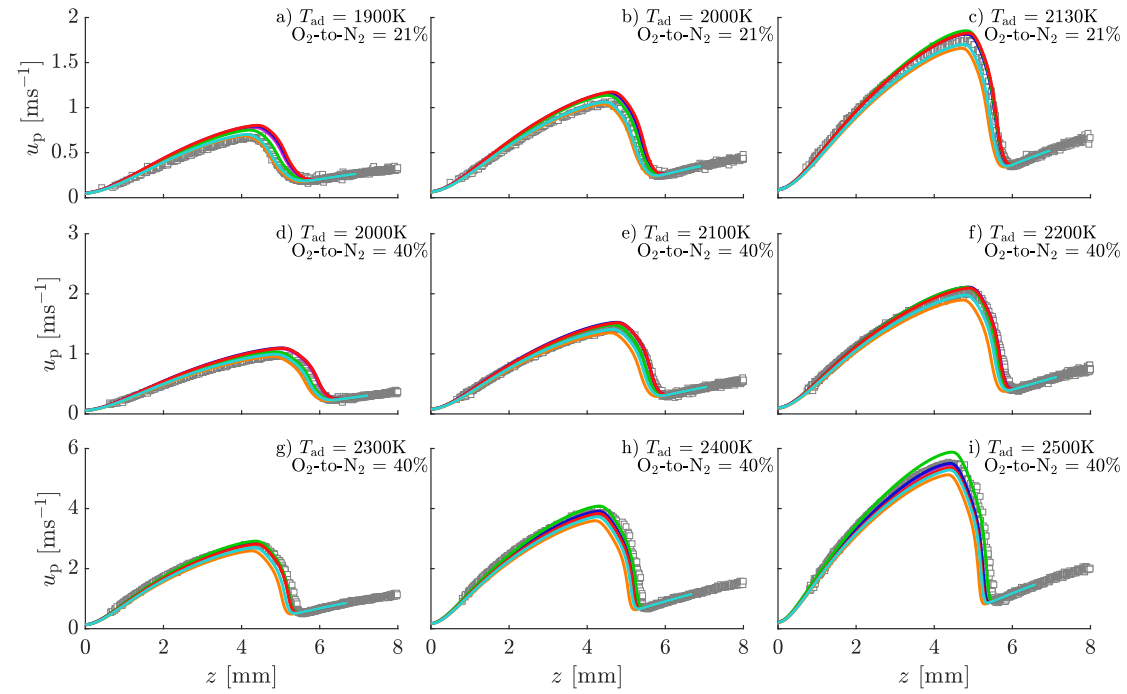

Figure B.4: Velocity profiles for methane-air-argon flames. Measured (▫) and simulated (—) profiles are illustrated. Different thermochemical models are shown: GRI (—), SD (—), CRECK (—), NUIG (—), DTU (—) and KON (—).

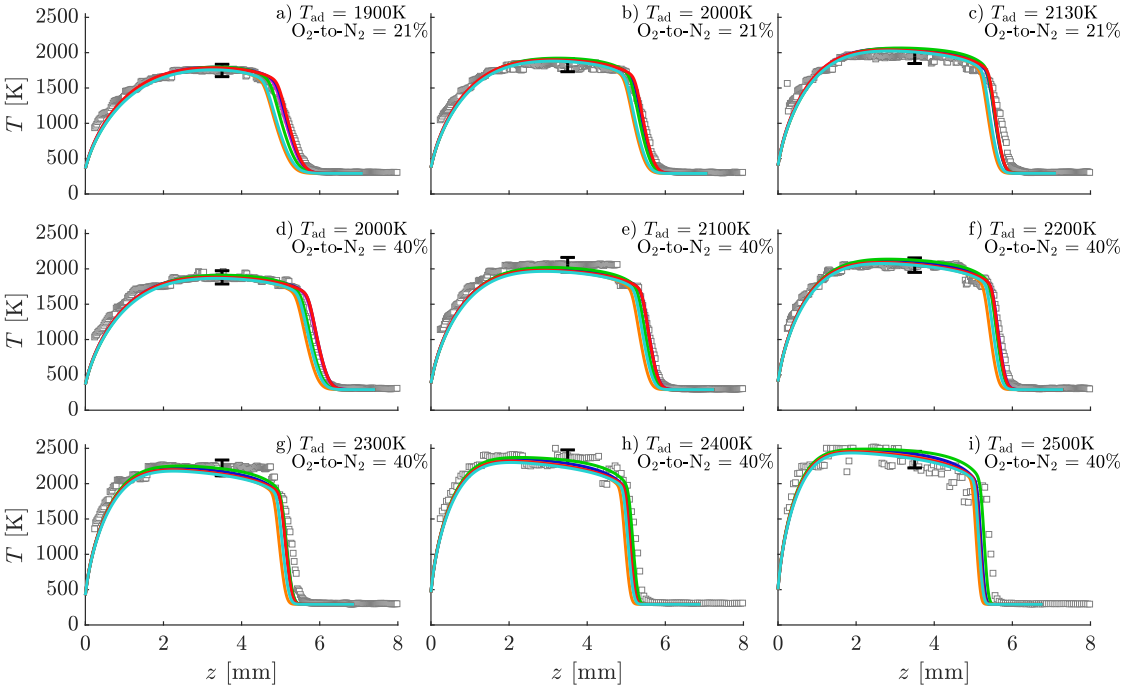

Figure B.5: Temperature profiles for methane-air-argon flames. Measured (▫) and simulated (—) profiles are illustrated. Different thermochemical models are shown: GRI (—), SD (—), CRECK (—), NUIG (—), DTU (—) and KON (—).

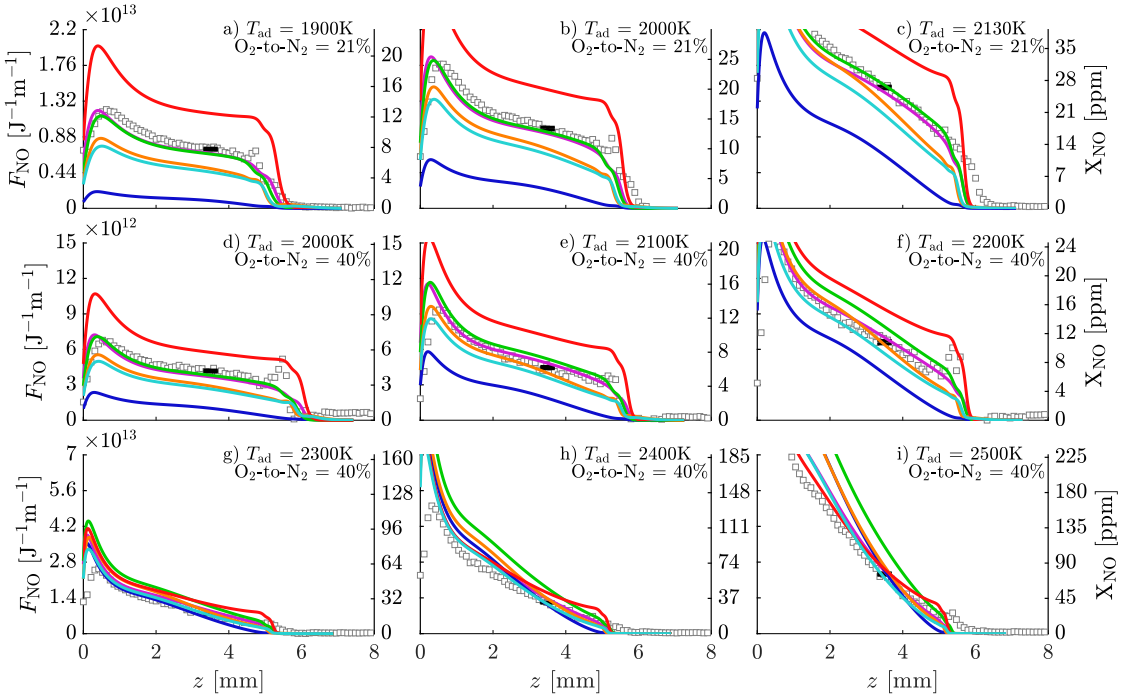

Figure B.6: NO profiles for methane-air-argon flames. Measured (▫) and simulated (—) profiles are illustrated. Different thermochemical models are shown: GRI (—), SD (—), CRECK (—), NUIG (—), DTU (—) and KON (—).

References

[1] P. A. Berg, G. P. Smith, J. B. Jeffries, and D. R. Crosley. “Nitric oxide formation and reburn in low-pressure methane flames”. In: *Symposium (International) on Combustion* 27 (1998), pp. 1377–1384.

[2] M. Tamura, P. A. Berg, J. E. Harrington, J. Luque, J. B. Jeffries, G. P. Smith, and D. R. Crosley. “Collisional quenching of CH(A), OH(A), and NO(A) in low pressure hydrocarbon flames”. In: *Combustion and Flame* 114 (1998), pp. 502–514.

Appendix C. Supplementary Materials to Chapter V

C.1 Experimentally-measured boundary conditions and full set of experimental data

Table C.1 reports the experimental conditions used to perform simulations of quasi-1D stagnation flames. The complete set of experimentally-determined boundary conditions and the full set of experimental data are presented in the attached Excel file.

Table C.1: Flame boundary conditions

ϕ	$X_{\mathrm{Ar}}{}^{*}$	T_{ad} [K]	$\mathcal{L}$ [mm]	T_{in} [K]	u_{in} [ms^{-1}]	du/d$z|_{\mathrm{in}}$ [s^{-1}]	T_{wall} [K]
1.0	0.6281	1600	8.04	291.8	0.680	169.6	383.0
1.0	0.5832	1700	7.89	290.3	0.887	206.8	386.8
1.0	0.5334	1800	7.82	290.5	1.098	260.6	402.0
1.0	0.4772	1900	7.80	291.0	1.389	324.7	434.0
1.0	0.4124	2000	7.85	291.8	1.725	427.7	454.6
1.0	0.3356	2100	7.91	291.5	2.067	584.2	493.0
1.0	0.2413	2200	8.07	291.6	2.537	735.3	501.6
1.0	0.1850	2250	7.71	291.8	3.289	798.0	527.0
1.0	0.1205	2300	7.42	291.9	3.822	886.5	540.0

* Defined in Eq. (V.1)

C.2 Calibration of the optical constant C_{opt}

The optical calibration coefficient, C_{opt}, used in Eq. (V.4), encompasses the camera sensitivity, the optical transmissivity of the experimental setup, and the laser average intensity. It allows for direct comparison of experimental results in LIF units of any experimental campaign, regardless of the experimental methodology and flame conditions. The advantage of this technique, unlike the usual technique that requires seeding flames at different levels of NO concentration to infer the NO produced by the flame, is that the C_{opt} calibration process needs to be performed only once and can be applied on all LIF results using the same experimental setup. This calibration coefficient is

obtained independently of the flame condition (except if NO re-burn occurs within the flame), of the level of seeding performed for the calibration, and is independent of the thermochemical model used. The use of C_{opt} minimises the assumptions and uncertainty linked to the NO measurements, while saving on experimental time and gas-cylinder consumption.

Following the NO-LIF methodology used for NO concentration measurements, as reported in Section V.3.3, the experimental signals of both a seeded flame and an unseeded flame, $F_{\mathrm{NO,exp}_{\mathrm{seeded}}}$ and $F_{\mathrm{NO,exp}_{\mathrm{unseeded}}}$ respectively, are collected. The amount of seeded NO is chosen to be as close as possible to the native concentration, while remaining below the NO re-burn threshold such that the consumption of seeded NO through the flame zone remains negligible [1]. The collected signals are subtracted from one another, such that the remaining signal $F_{\mathrm{NO,exp}_{\mathrm{net}}}$ is only proportional to the known concentration of NO $\left(n^{\circ}_{\mathrm{NO,known}}\right)$:

$$F_{\mathrm{NO,exp}_{\mathrm{seeded}}} = F_{\mathrm{NO,exp}_{\mathrm{known}}} + F_{\mathrm{NO,exp}_{\mathrm{produced}}} \tag{C.1}$$

$$F_{\mathrm{NO,exp}_{\mathrm{unseeded}}} = F_{\mathrm{NO,exp}_{\mathrm{produced}}} \tag{C.2}$$

$$F_{\mathrm{NO,exp}_{\mathrm{net}}} = F_{\mathrm{NO,exp}_{\mathrm{seeded}}} - F_{\mathrm{NO,exp}_{\mathrm{unseeded}}} = F_{\mathrm{NO,exp}_{\mathrm{known}}} \tag{C.3}$$

and removes the contribution of the flame chemiluminescence, the interfering LIF signal from species like O_2 for example, and the flame-nascent NO.

Similar to the experiments, simulations are performed by virtually seeding the flame with an experimentally-known concentration of NO. The numerical NO profiles are transformed into LIF signal using LIFSim [2]:

$$F_{\mathrm{NO,num}_{\mathrm{net}}} = f_{\mathrm{LIF}}\left(f_{\mathrm{B}}, \lambda, \Delta\nu_{\mathrm{L}}, \Gamma, B_{12}, A_{21}, Q_{21}, I\right) \cdot n^{\circ}_{\mathrm{NO,known}} \tag{C.4}$$

where f_{LIF}, obtained using LIFSim [2], is the number of photons emitted per unit molecule of NO, per unit volume, and per laser energy, and is a function of; $f_{\mathrm{B}}\left(T\right)$ the Boltzmann fraction of NO molecules in the excited state, λ the laser wavelength, $\Delta\nu_{\mathrm{L}}$ the spectral width of the laser, $\Gamma\left(\Delta\nu_{\mathrm{L}}, T, p, X_i\right)$ the dimensionless overlap fraction, A_{21} and B_{12} the Einstein coefficients for spontaneous emission and photon absorption, respectively, $Q_{21}\left(T, p, X_i\right)$ the rate constant of non-radiative collisional quenching, and I the average energy density. $n^{\circ}_{\mathrm{NO,known}}\left(T, P, X_{\mathrm{NO}}\right)$ is the number density of seeded NO molecules. Table C.2 presents the LIF constants used to calculate the numerical NO-LIF signal.

The direct comparison of $F_{\mathrm{NO,num}_{\mathrm{net}}}$ and $F_{\mathrm{NO,exp}_{\mathrm{net}}}$ allows the determination of the optical calibration coefficient (C_{opt}), by fitting the numerical and experimental profiles using a least-square

Table C.2: Parameters used to obtain f_{LIF} in Eq. (C.4) using LIFSim

Parameter	Notation	Value	Units	Source
LIFSim version		E 3.17		
Target molecule		NO		
Online excitation wavelength	λ_{on}	226.0345	[nm]	Experimental condition
Offline excitation wavelength	λ_{off}	226.0470	[nm]	Experimental condition
Laser energy density	I	10	[mJ.cm^2]	LIFSim default value
Laser pulse duration	Δt	3	[ns]	Laser manufacturer
HWHM of laser instrument Gauss function	$\Delta\nu_{\mathrm{L,Gauss}}$	0.396	[cm^{-1}]	Experimentally measured
HWHM of laser instrument Lorentz function	$\Delta\nu_{\mathrm{L,Loren}}$	0.168	[cm^{-1}]	Experimentally measured
Minimum detection wavelength	λ_{min}	220	[nm]	
Maximum detection wavelength	λ_{max}	340	[nm]	
Detection resolution	$\Delta\lambda$	0.05	[cm^{-1}]	
HWHM of detection instrument Gauss function	$\Delta\nu_{\mathrm{det,Gauss}}$	100	[cm^{-1}]	LIFSim default value
HWHM of detection instrument Lorentz function	$\Delta\nu_{\mathrm{det,Loren}}$	10	[cm^{-1}]	LIFSim default value
Detection instrument transmissivity	τ_λ	λ-dependent	[-]	Long-pass filter manufacturer:
Pressure	p	1	[bar]	Experimental condition
Temperature	$T(z)$	z-dependent	[K]	Numerical solution
Composition	$X(z)$	z-dependent	[-]	Numerical solution
Quenching cross-section	σ_{M}	specie-dependent*	[Å^2]	[3, 4]
Collisional width coefficient	2γ	specie-dependent**	[cm^{-1}.atm^{-1}]	[5–7]
Collisional shift coefficient	δ	specie-dependent**	[cm^{-1}.atm^{-1}]	[5–7]

* Species included: N_2, O_2, CO_2, CO ,H_2O, CH_4, C_2H_6, C_3H_8, C_2H_4, C_2H_2, NO, NO_2, N_2O, NH_3, NH, H_2, O, H, OH, CH, He, Ne, Ar, Kr, Xe

** Species included: N_2, O_2, H_2O, Ar, CO_2, CO, CH_4

fit, such that the following equation applies:

$$\frac{F_{\mathrm{NO,exp_{net}}}}{C_{\mathrm{opt}}} = F_{\mathrm{NO,num_{net}}} \tag{C.5}$$

The calibration coefficient is fitted in the post-flame region, being the region of interest of this study. Figure C.1 shows an example of the signal-fitting to obtain C_{opt}.

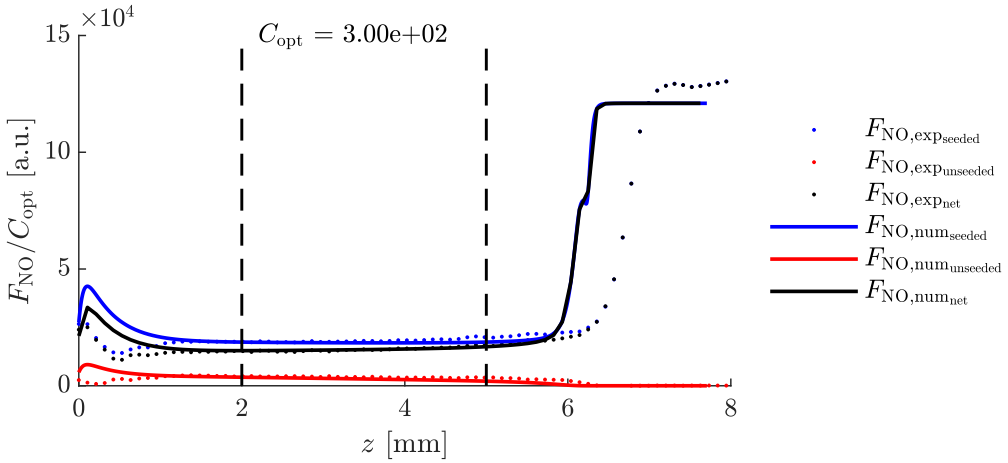

Figure C.1: Calibration obtained for the methane-air flame at $T_{\mathrm{ad}} = 2000$ K with 10 ppm seeding, using the GDF mechanism

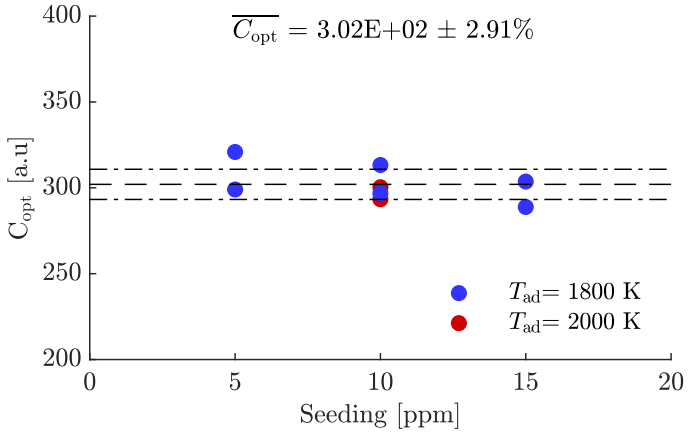

Figure C.2: C_{opt} obtained for the different flame conditions and levels of seeding.

The calibration has been performed 8 times on different flame conditions and using different levels of seeding, leading to an average $\overline{C_{\text{opt}}}$ of $3.02 \cdot 10^2$ a.u. $\pm 2.91\%$, as shown in Fig. C.2.

C.3 Estimate of the NO-LIF profiles in ppm

As discussed in Section V.3.3, the data are presented in LIF units instead of as NO concentrations, to minimise the assumptions and uncertainties associated with the limited knowledge of the temperature and quenching specie concentration fields at each point of the flame domain. However, an estimate of this concentration is given for each profile, valid in the hot flow region, and is performed as follows. A reference mechanism is used to assume the concentration and temperature of the quenching species at each point of the domain. Using LIFSim as presented in the C_{opt} methodology, the NO-LIF profile ($F_{\text{NO,num}}$) for this reference model is obtained from the molar concentration profile of NO ($X_{\text{NO,num}}$). A transformation [a.u.→ppm] is obtained through α at several points of the domain following Eq. (C.6).

$$\frac{F_{\text{NO,num}}}{X_{\text{NO,num}} \cdot \alpha} = 1 \tag{C.6}$$

with $X_{\text{NO,num}}$ in [ppm], $F_{\text{NO,num}}$ in [a.u.], and α in [a.u.ppm^{-1}]. α encompasses the LIF constants of each quenching specie and their temperature, as well as the uncertainties associated with these constants. Therefore, α can be applied to experimental results without an *a priori* knowledge of the full composition of the flame. It however carries uncertainty due to the potential inaccuracy of the LIF model in describing the quenching coefficients. Consequently, it is only presented as indicative in this study, as it would require further uncertainty calculation to accurately evaluate the uncertainty of this transformation.

C.4 Uncertainty calculation

The uncertainty calculation performed for the velocity and NO-LIF measurements are presented in this section. This calculation is a combination of the numerical uncertainty and the experimental uncertainty related to the measurement. Only the experimental uncertainty is presented on the measurement results (*e.g.,* Fig. V.5). However, when measurements and simulations are compared to one another through the use of ratios (*e.g.,* Fig. V.3 or Fig. V.6), the total uncertainty encompassing the numerical and experimental uncertainty is presented through the use of the grey shaded area. The total uncertainty for a measurement M is calculated following Eq. (C.7).

$$\sigma_{\text{(M,num)/(M,exp)=1}} = \sqrt{\left(\overline{\sigma_{\text{M,exp}}}\right)^2 + \left(\sigma_{\text{M,num,BC}}\right)^2} \tag{C.7}$$

C.4.1 Numerical uncertainty

The numerical uncertainty represents the uncertainty of the experimentally-measured boundary conditions propagated through the simulations. It is calculated by performing a brute-force sensitivity analysis of the numerical boundary conditions x_j on each of the simulated flames. The resulting logarithmic sensitivity L.S.(x_j) is weighted by the uncertainty of each of the boundary condition parameters $\sigma(x_j)$. Therefore, the impact on the measurement of interest (M) can be evaluated according to Eq. (C.8). It applies to the reference flame speed ($S_{\text{u,ref}}$), the concentration of NO in the flame-front ($X_{\text{NO,FF}}$), the concentration of NO in the post-flame region ($X_{\text{NO,PF}}$), and the NO concentration slope in the post-flame region ($\mathrm{d}X_{\text{NO}}/\mathrm{d}z$).

$$\sigma_{\text{M,num,BC}} = \sqrt{\sum \left[\text{L.S.}(x_j) \cdot \sigma(x_j)|_{\text{M}}\right]^2} \tag{C.8}$$

The logarithmic sensitivity for each boundary condition parameter and each flame is shown in Fig. C.3. One can see that the dilution of argon is the most sensitive boundary parameter on both measurements due to its strong effect on flame temperature. As expected, a small change in X_{Ar} leads to a larger uncertainty for the most diluted flames, resulting in the largest numerical uncertainties for the flames at low temperature.

C.4.2 Experimental uncertainty

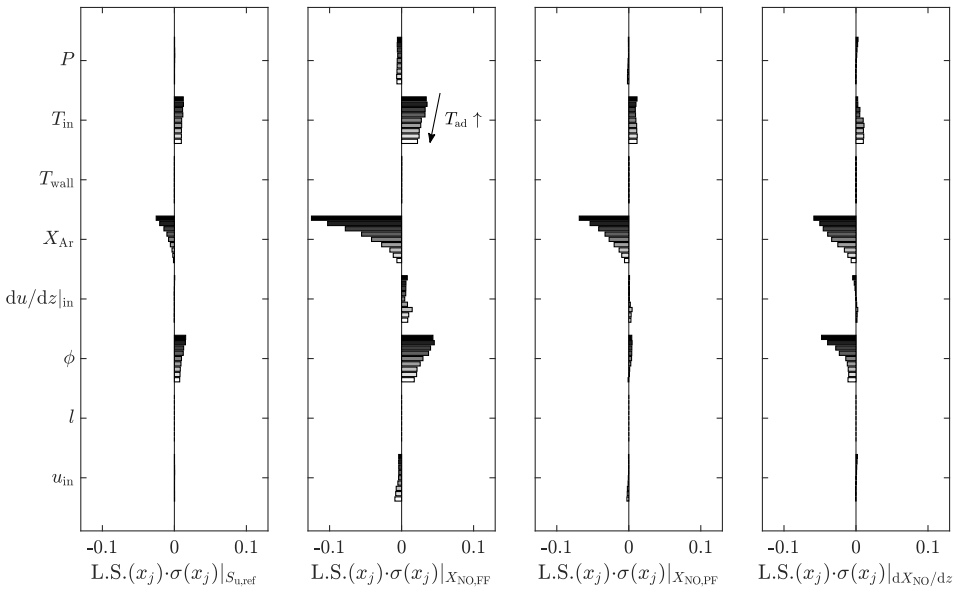

Figure C.3: Logarithmic sensitivity of the different measurements performed in this study, for each flame using a gradient in colour from $T_{\text{ad}} = 1600\,\text{K}$ (black) to $T_{\text{ad}} = 2300\,\text{K}$ (white).

C.4.2.1 Velocity measurement uncertainty

The experimental PTV uncertainty consists of the camera (CCD) calibration coefficient uncertainty $\Delta C_{\text{CCD}}/C_{\text{CCD}}$, the laser repetition rate uncertainty $\Delta f/f$, the error in the differentiation scheme E_{diff}, and the curve-fitting function uncertainty of low velocity region $E_{u_{\text{p}}}$, and is calculated following :

$$\sigma_{\text{M,exp,PTV}} = \sqrt{\left(\frac{\Delta C_{\text{CCD}}}{C_{\text{CCD}}}\right)^2 + \left(\frac{\Delta f}{f}\right)^2 + \left(E_{\text{diff}}\right)^2 + \left(E_{u_{\text{p}}}\right)^2} \tag{C.9}$$

C.4.2.2 NO-LIF measurement uncertainty

For each NO-LIF profile presented in Fig. V.5, the experimental NO-LIF uncertainty consists of the camera (ICCD) calibration coefficient uncertainty $\Delta C_{\text{ICCD}}/C_{\text{ICCD}}$, the image signal variation $\Delta S/S$, the laser energy variation $\Delta E_{\text{L}}/E_{\text{L}}$, the NO concentration calibration coefficient uncertainty $\Delta C_{\text{opt}}/C_{\text{opt}}$, and the post-flame NO profile linear regression uncertainty $\Delta R/R$ such that:

$$\sigma_{F_{\text{NO}},\text{exp,LIF}} = \sqrt{\left(\frac{\Delta C_{\text{ICCD}}}{C_{\text{ICCD}}}\right)^2 + \left(\frac{\Delta S}{S}\right)^2 + \left(\frac{\Delta E_{\text{L}}}{E_{\text{L}}}\right)^2 + \left(\frac{\Delta C_{\text{opt}}}{C_{\text{opt}}}\right)^2 + \left(\frac{\Delta R}{R}\right)^2} \tag{C.10}$$

For each local measurement M ($X_{\mathrm{NO,FF}}$,$X_{\mathrm{NO,PF}}$, and $\mathrm{d}X_{\mathrm{NO}}/\mathrm{d}z$), the uncertainty of the scatter in data-points $\Delta\epsilon/\epsilon$ is also calculated and added to $\sigma_{F_{\mathrm{NO}},\mathrm{exp,LIF}}$ through the square-root sum.

$$\sigma_{\mathrm{M,exp,LIF}} = \sqrt{\left(\sigma_{F_{\mathrm{NO}},\mathrm{exp,LIF}}\right)^2 + \left(\frac{\Delta\epsilon}{\epsilon}\right)^2} \tag{C.11}$$

Results presented in Fig. V.5 are an average of the two measurements ($N_\mathrm{s} = 2$) performed for each flame condition, reducing the uncertainty as follows:

$$\overline{\sigma_{F_{\mathrm{NO}},\mathrm{exp,LIF}}} = \frac{\left\langle \sigma_{F_{\mathrm{NO}},\mathrm{exp,LIF}} \right\rangle_{1\rightarrow N_\mathrm{s}}}{\sqrt{N_\mathrm{s}}} \tag{C.12}$$

This resulting uncertainty is applied on the averaged profiles shown in the NO-LIF figures of Section V.4.3.

C.5 NO-LIF Data extraction methodology

The extraction of the parameters presented in Fig. V.6 is performed using an algorithm in order to ensure consistency in the comparison of the results. Three parameters are extracted: the flame-front NO, $F_{\mathrm{NO,FF}}$, the post-flame NO, $F_{\mathrm{NO,PF}}$, and the slope of post-flame NO, $\mathrm{d}F_{\mathrm{NO}}/\mathrm{d}z$.

The first parameter to be calculated is $\mathrm{d}F_{\mathrm{NO}}/\mathrm{d}z$ as it is used in the calculation of the other two parameters. For each numerical profile and experimental profile, $\mathrm{d}F_{\mathrm{NO}}/\mathrm{d}z$ is calculated using a linear fit on the NO-LIF data-points in the post-flame region. The post-flame region Δz_{PF} is defined according to the flame position of each profile and ends at the same axial location for each flame, such that $\Delta z_{\mathrm{PF}} = [1.5\mathrm{mm}, z_\mathrm{f} - 1.5\mathrm{mm}]$ as shown in Fig. C.4. Note that z_f is defined at the minimum velocity, upstream of the reaction zone, of each profile (see Fig. V.2a). Therefore, the post-flame NO slope measurement is independent of the flame position misprediction between the models and the experiments.

The measurement of the flame-front NO-LIF signal is challenging due to the shape of the profiles, especially at high temperature where the flame-front NO is almost non-existent compared to the post-flame NO (see Fig. V.5i). Therefore, the use of an algorithm allows the extraction of the parameter consistently. This method allows a relative comparison from flame to flame and to have an overall understanding of the thermochemical models behaviour compared to the measurements, despite not being necessarily representative of the true absolute NO-LIF signal of the flame-front region. The flame-front NO is also calculated according to the flame position of each profile and is, therefore, independent of the velocity profiles. $F_{\mathrm{NO,FF}}$ is calculated as the intercept of the linear fit of the post-flame NO region and an axial location z_{FF} dependent on the flame position, such

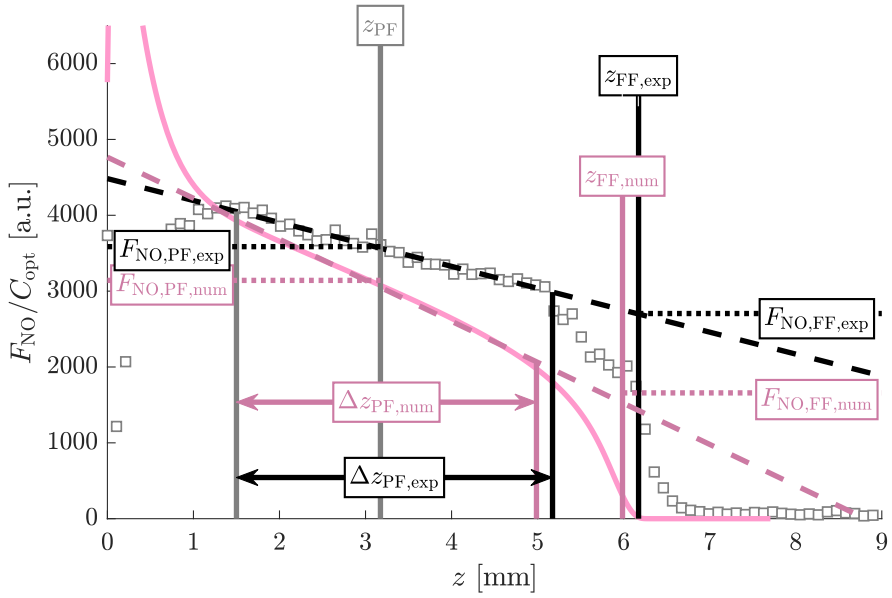

Figure C.4: Definition of the axial locations at which the NO-LIF parameters have been calculated. The NO-LIF profile is displayed for the flame at $T_{ad} = 2000$ K for experiments (black squares) and GDF mechanism (pink line). The dashed line represents $\mathrm{d}F_{NO}/\mathrm{d}z$.

that $z_{FF} = z_f - 0.5$mm. Using the linear fit determined for $\mathrm{d}F_{NO}/\mathrm{d}z$ eliminates the fluctuation of the NO-LIF measurements and allows a consistent comparison between each numerical and experimental profile for each flame condition.

Finally, the post-flame absolute NO signal is extracted at the same axial location for the experimental and numerical profiles, regardless of their disagreement in the velocity profiles. Therefore, $F_{NO,PF}$ carries the consequences of the velocity profiles mispredictions by the models. Similarly to the previous parameter, $F_{NO,PF}$ is extracted from the fit of F_{NO} versus z, eliminating the fluctuations of the NO-LIF measurements, at a given location z_{PF} for which the experimental profile is used for the calculation, such that $z_{PF} = z_{f,exp} - 3.5$mm.

C.6 Base chemistry impact on NO pathway contribution

As presented in Section V.8, the differences in branching ratios and fluxes between the two mechanisms, GDF and SD*, can be quantified by identifying the share of NO produced through the different NO-forming pathways.

Following literature, the formation pathways are identified according to how N_2 breaks-down to later form NO. As a consequence, NO formed through the reaction of N_2 into N or NO is labeled as thermal, while the oxidation of N_2 to NNH to form NO is labeled as belonging to the NNH pathway. Given that the share of the N_2O pathway is non-existent in these conditions, as the

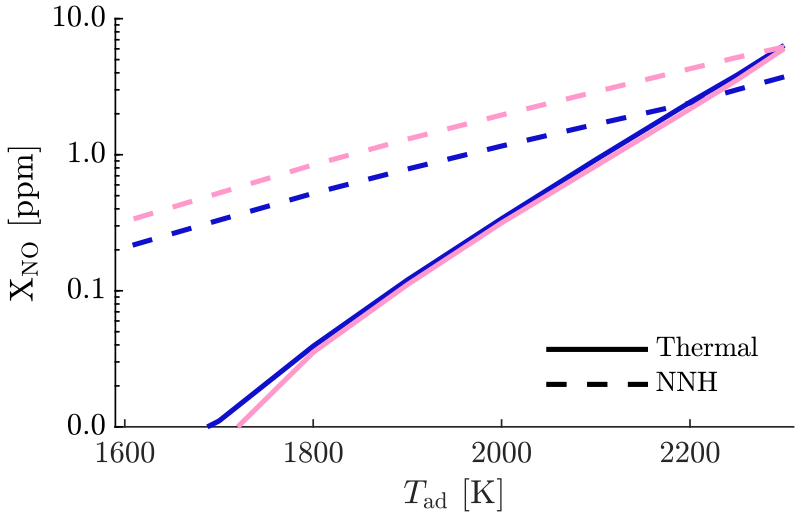

Figure C.5: NO concentration resulting from the thermal pathway and the NNH pathway, calculated using an RPA performed on each flame condition from 1600 K to 2300 K, at 3.5 mm from z_f, using GDF (—) and SD* (—) mechanisms. Note the logarithmic scale used in the figure.

net flux between N_2 to N_2O is negative (for all temperatures considered), any NO formed through $N_2 \rightarrow NNH \rightarrow N_2O \rightarrow NO$ is still labeled as from the NNH pathway.

Figure C.5 presents the concentration of NO formed through the two identified pathways for all adiabatic flame temperature conditions for GDF and SD*, at the same location as the previous RPA analyses. For both mechanisms, the NO formed through the thermal pathway is similar for the entire range of temperature, despite the stronger branching of $N_2 \rightarrow N/NO$ for SD* than for GDF, observed in Fig. V.12. This is because SD* predicts less overall NO production than GDF (as observed in Fig. V.11). In contrast, SD* consistently predicts less NO production through the NNH pathway compared to GDF. This shows that, despite the same NO_x sub-chemistry, both mechanisms have significant differences in the share of contribution of the NO producing pathways.

C.7 Radical pool profiles

C.7.1 Comparison of all 11 thermochemical models used in Section V.8

Fig. C.6 presents the concentration of O, H, OH, and NO of all modified thermochemical models for the hydrogen flame at $T_{ad} = 2300$ K to complete the figure presented in Section V.8 (Fig. V.13). Despite the use of the same NO_x sub-chemistry, the prediction of NO concentrations remain variable, especially in the post-flame region. The large disagreements between the models for a given radical profile at a given axial location seems to be at the origin of the observed discrepancies in the NO profiles.

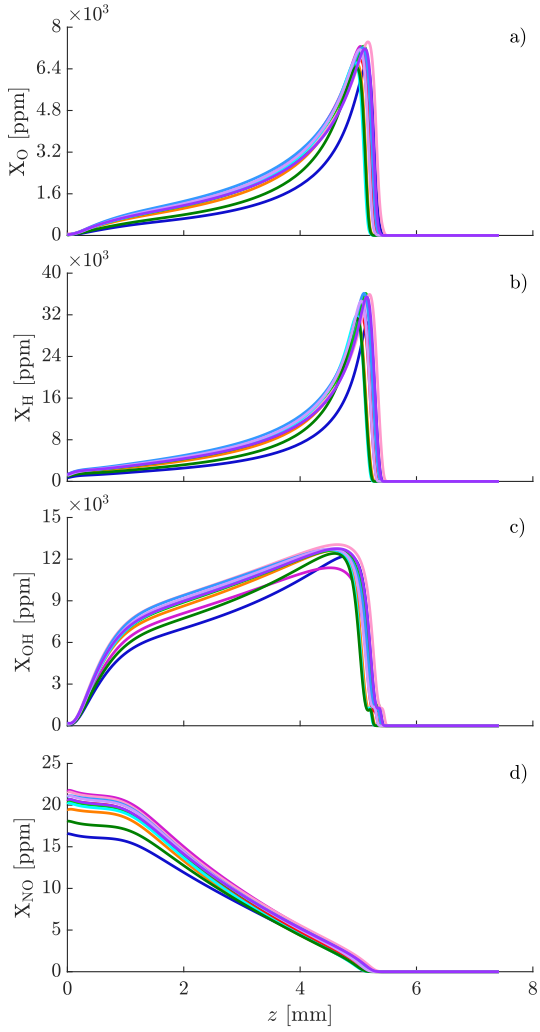

Figure C.6: Numerical profiles of a) O, b) H, c) OH, and d) NO molar fraction for the flame at $T_{ad} = 2300$ K using the different modified thermochemical models. The legend follows the colour-scale presented in Tab. V.1.

C.7.2 Comparison between a methane flame and a hydrogen flame

A comparison in the radical pool concentrations for O, H, and OH atoms are presented in Fig. C.7, as well as the concentration of NO between two flames. The comparison is performed on flames of the former study (see Fig. IV.3) in a methane-air flame, and the present study in hydrogen-air flames (see Fig. V.5e). While flames have an equivalence ratio of 0.9 and 1, respectively, the adiabatic temperature is the same, $T_{ad} = 2000\,\mathrm{K}$, as well as for the oxygen content in air, O_2-to-$N_2 = 0.21$. To perform this comparison between methane and hydrogen, the original version of CRECK (not altered to remove the carbon-containing reactions and species) was used.

This figure proves that the radical chemistry in these two types of flame is widely different. In hydrocarbon flames, the concentration of radicals available in the flame-front region is significantly lower than for a hydrogen flame, especially for the H atom. Therefore, modelling errors in its concentration would have a greater impact on hydrogen flames than on hydrocarbon flames.

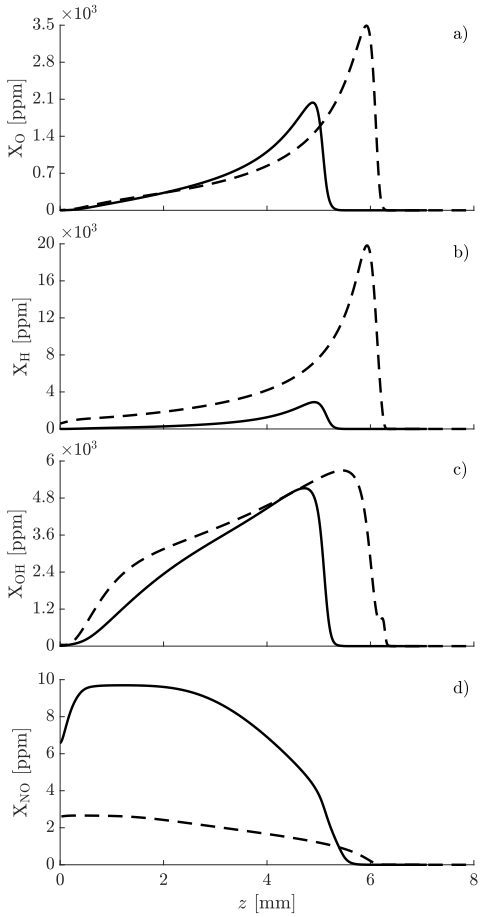

Figure C.7: Numerical profiles of a) O, b) H, c) OH, and d) NO molar fraction for a methane flame (—) and a hydrogen flame (- -) at $T_{ad} = 2000\,\mathrm{K}$ using the original version of the CRECK mechanisms.

References

[1] P. A. Berg, G. P. Smith, J. B. Jeffries, and D. R. Crosley. "Nitric oxide formation and reburn in low-pressure methane flames". In: *Symposium (International) on Combustion* 27 (1998), pp. 1377–1384.

[2] W. G. Bessler, C. Schulz, S. Volker, and J. W. Daily. "A versatile modeling tool for nitric oxide LIF spectra". In: *Proceedings of the Third Joint Meeting of the U.S. Sections of The Combustion Institute*. Chicago, 2003, P105.

[3] P. H. Paul, J. A. Gray, J. L. Durant, and J. W. Thoman. "A model for temperature-dependent collisional quenching of NO $A^2\ \Sigma^+$". In: *Applied Physics B Photophysics and Laser Chemistry* 57.4 (1993), pp. 249–259.

[4] P. H. Paul, C. Carter, J. A. Gray, J. L. Durant, J. Thomson, and M. Furlanetto. *Correlations for the NO $A^2\Sigma^+$ (ν'=0) electronic quenching cross-section*. Tech. rep. Sandia National Lab. (SNL-CA), Livermore, CA (United States), 1995.

[5] A. Y. Chang, M. D. DiRosa, and R. K. Hanson. "Temperature dependence of collision broadening and shift in the NO A $\leftarrow$ X(0, 0) band in the presence of argon and nitrogen". In: *Journal of Quantitative Spectroscopy and Radiative Transfer* 47.5 (1992), pp. 375–390.

[6] M. D. Di Rosa and R. K. Hanson. "Collision-broadening and -shift of NO γ(0,0) absorption lines by H_2O, O_2, and NO at 295K". In: *Journal of Molecular Spectroscopy* 164.1 (1994), pp. 97–117.

[7] M. D. DiRosa. "High-resolution line shape spectroscopy of transitions in the gamma bands of nitric oxide". PhD thesis. 1996.